



A University of Sussex PhD thesis

Available online via Sussex Research Online:

<http://sro.sussex.ac.uk/>

This thesis is protected by copyright which belongs to the author.

This thesis cannot be reproduced or quoted extensively from without first obtaining permission in writing from the Author

The content must not be changed in any way or sold commercially in any format or medium without the formal permission of the Author

When referring to this work, full bibliographic details including the author, title, awarding institution and date of the thesis must be given

Please visit Sussex Research Online for more information and further details



SEARCHES FOR CHARGINO AND NEUTRALINO
PRODUCTION IN DECAYS TO THREE-LEPTON
FINAL STATES VIA INTERMEDIATE BOSONS
USING $\sqrt{s} = 13$ TEV PROTON-PROTON
COLLISIONS WITH THE ATLAS DETECTOR

Fabrizio Trovato

*A thesis submitted in fulfilment of the requirements
for the degree of Doctor of Philosophy*

in the

School of Mathematical and Physical Sciences
Department of Physics and Astronomy

Submission date: 17th December 2020

I, Fabrizio Trovato, hereby declare that this thesis has not been and will not be, submitted in whole or in part to another university for the award of any other degree.

Brighton,

17th December 2020

Fabrizio Trovato

University of Sussex

School of Mathematical and Physical Sciences

Department of Physics and Astronomy

DOCTORAL THESIS

Searches for chargino and neutralino production in decays
to three-lepton final states via intermediate bosons using
 $\sqrt{s}=13$ TeV proton-proton collisions
with the ATLAS detector

by Fabrizio Trovato

ABSTRACT

Searches for production of charginos and neutralinos as predicted by Supersymmetry in three-lepton final states are presented. The analyses use data collected by the ATLAS detector at 13-TeV proton-proton collisions between 2015-2018 for a total of 139 fb^{-1} . The targeted simplified models are those for the production of the lightest chargino and the next-to-lightest neutralino decaying to the lightest neutralino and Standard Model bosons, WZ or Wh , subsequently decaying leptonically to yield three leptons in the final states. No significant deviation with respect to the Standard Model predictions is observed, and results are interpreted as exclusion limits on the considered simplified models. Masses of the lightest chargino and the next-to-lightest neutralino up to 640 GeV are excluded at 95% CL for the WZ model, while in the case of Wh model, masses up to 180 GeV are excluded.

ACKNOWLEDGEMENTS

A PhD can be full of surprises, as well as laughter, marvellous achievements but also inevitable low moments. Now that I am just about to submit this thesis, my mind can't help but think of all the people that have made this journey possible.

Firstly, I want to thank my supervisor, Antonella De Santo, for being such an incredible inspiration and support. She has given me time and motivation to grow, as a physicist and as a person, and I could not be more grateful and honoured for the great time spent working together. I hope I made her proud. I would also like to thank my second supervisor, Fabrizio Salvatore, whose knowledge and infinite kindness have made many of my days at Sussex.

I would like to thank Batool Safarzadeh for being always on my side, even when I could not see it, and for helping me going through most of the work in this thesis. And thanks also to Nicola Abraham and Nicky Santoyo, who have supported me at the beginning of my PhD with the most valuable advice and/or some drinks in R1. I would also like to thank Benedict Allbrooke, for patiently mentoring me during my qualification task, and all the other members of the Sussex group: Alex, Iacopo, Kate, Lily, Tom, and Mark, who I am looking forward to working with in the near future. All of you have made me feel at home.

I am also grateful to all the ATLAS SUSY group, and all the people involved in the three-lepton analyses, particularly Peter Tornambé, Jeanette Lorenz, Alberto Cervelli, Tina Potter, Sara Alderweireldt and Jeff Dandoy, for the fruitful physics talks and the incredible support.

I would like to thank all the people in the 4A26 office, who have made my days at Sussex such an enjoyable time: Mario Grandi, Ioannis, Marco, Meirin, Ondra, Fabio, Fab Miano (who let me use his thesis latex template!), Giuseppe and Sam.

My time in Brighton has been incredible, thanks to the many people I've met along the way. A huge thank you to Andrea and Pippa, for being such a cheerful presence in my first year. Thank you also to Dani, Chinmay and Ash, for being there during one of the most difficult moments of my journey. And thank you to Paolo, who is always able to cheer me up.

Also, a big thank you to my friends back in Catania: Salvo, Luca, Federico, Angelo, Luigi and Andrea, for always being with me beside the distance. Thank you also to all my friends from my days at the University of Catania (Michele, Miriam, Ruggero, Nicolò, Valeria, Laura, Paola, Giulia, Giulia, Stefano, Silvia, Jessica, Letizia, Nicola, Mimmo, Ferdinanda and many, many more!). Among all, a big thanks to Mario Spina, who I have shared with more than ten years (since laboratory at year 1!) in physics, and thanks to Lucia for being always such a caring friend.

I am grateful to Santo, who has motivated me during the last years of my PhD, and reminds me every day how insignificant distance can be. And a special thanks to Lorena, who has truly believed in me since the very first moments. Such a friendship is rare, I was just lucky to find it.

My family has been the best support during these years. Thank you to my sister Angela, my niece Ylenia and my nephew Giovanni, whose love is an amazing and constant source of motivation.

I can attempt to describe (part of) the Universe, but no words can do justice to the support, sacrifice and immense love I've received from my parents. I am grateful to them, they have taught and pushed me to follow my dreams, always. This thesis is for them.

Finally, thank you to Leon, one of the best people I know. He's supported me with infinite patience, particularly during these last months. Every day, I feel lucky to have him by my side.

PREFACE

The content of this thesis reflects the work I have done over the period of my PhD at the University of Sussex, as member of the ATLAS Collaboration at CERN, Geneva. The ATLAS experiment addresses a vast physics program which comprises both searches for new physics and precision measurements of Standard Model processes and properties of elementary particles. Collaborative tools and resources are available to ATLAS collaborators, which were used to obtain the results presented in this thesis.

I have been involved in the ATLAS SUSY group since the start of my PhD, working on searches for charginos and neutralinos in three-leptons final states. I have contributed to two rounds of analysis, a first one based on the first 36.1 fb^{-1} of data collected by the ATLAS experiment at $\sqrt{s} = 13 \text{ TeV}$ proton-proton collisions, and the analysis of the full Run-2 dataset (139 fb^{-1}). These analyses I have performed as a main analyser, alongside other physicists working in the same analysis groups where the presented work was conducted. I made leading contribution to various aspects of the analyses, such as the optimisation of regions sensitive to the targeted SUSY scenarios, the estimation of the main sources of Standard Model background in the analyses and the statistical interpretation of the results.

In order to become author within ATLAS, I have performed a technical task in view of the future upgrades of the ATLAS detector, beneficial for the entire physics program of the collaboration. This is presented in [Appendix A](#).

CONTENTS

1	Introduction	1
2	Theoretical framework	3
2.1	The Standard Model	4
2.1.1	Fundamental forces and symmetries	7
2.1.2	The Brout-Englert-Higgs mechanism	12
2.1.3	Limitations of the SM	14
2.2	Supersymmetry	17
2.2.1	The MSSM	19
2.2.2	Phenomenology of the MSSM at colliders	25
2.3	Electroweak SUSY searches	29
2.3.1	State of art of three-lepton searches for $\tilde{\chi}_1^\pm \tilde{\chi}_2^0$ via WZ/Wh bosons	31
3	The ATLAS detector at the Large Hadron Collider	37
3.1	The Large Hadron Collider	37
3.1.1	The acceleration complex	38
3.1.2	The LHC parameters	38
3.1.3	The LHC detectors	39
3.2	The ATLAS detector	41
3.2.1	The ATLAS coordinate system and some key variables	42
3.2.2	The magnet system	43
3.2.3	The Inner Detector	44

3.2.4	The calorimetry system	46
3.2.5	The Muon Spectrometer	49
3.2.6	The trigger and data acquisition system	51
4	Event generation, reconstruction and object definitions	55
4.1	Event flow in ATLAS	55
4.2	Event generation	56
4.2.1	The generators in ATLAS	59
4.2.2	Underlying events and pile-up	60
4.3	ATLAS simulation and digitisation	61
4.3.1	The ATLAS fast simulation	61
4.4	Object reconstruction	62
4.4.1	Track and vertex reconstruction	62
4.4.2	Electrons	64
4.4.3	Muons	68
4.4.4	Jets	70
4.4.5	<i>b</i> -tagged jets	72
4.4.6	Taus	73
4.4.7	Missing transverse momentum	74
4.4.8	Overlap Removal	75
4.5	Event quality cuts	76
4.6	Analysis objects	76
5	Analysis strategy for EWK SUSY searches with three-lepton final states	79
5.1	Data and simulated samples	79
5.1.1	SUSY signals	79
5.1.2	Trigger strategy and data quality	81
5.1.3	Standard Model backgrounds	82
5.2	Strategy for the event selection	83
5.2.1	Selection variables	84
5.3	Background estimation	87
5.3.1	Data-driven estimation of FNP backgrounds	87
5.3.2	Normalisation of irreducible background	90

5.3.3	Validation of the background estimation	91
5.4	Systematic uncertainties	91
5.4.1	Detector-level uncertainties	92
5.4.2	Theory uncertainties	93
5.5	Statistical analysis of results	94
5.5.1	Hypothesis test	94
6	Results of $\tilde{\chi}_1^\pm \tilde{\chi}_2^0$ searches with three-lepton and E_T^{miss} final states	98
6.1	Early Run-2 analysis searching for $\tilde{\chi}_1^\pm \tilde{\chi}_2^0$ via Wh	98
6.2	Full Run-2 analysis searching for $\tilde{\chi}_1^\pm \tilde{\chi}_2^0$ via WZ/Wh	109
6.2.1	Event selection	109
6.2.2	Standard Model background estimation	117
6.2.3	Systematic uncertainties	124
6.2.4	Background-only fit results	126
6.2.5	Results and statistical interpretation	128
7	Conclusions and outlook	138
A	Performance of the Hardware-based Tracking for Trigger upgrade for ATLAS	141
A.1	The LHC and ATLAS upgrades for high-luminosity	141
A.2	ATLAS TDAQ architecture for the Phase-II upgrade	142
A.3	The Hardware-based Tracking for Trigger for the HL-LHC	144
A.3.1	Track fitting in HTT	145
A.3.2	Reduction of storage space needed by track-fitting step	146
A.3.3	Exploring the low- p_T range	153
A.4	Conclusions	158
	List of Acronyms	160
	List of Figures	165
	List of Tables	177
	Bibliography	181

1 | INTRODUCTION

Until the beginning of the 20th century, atoms were considered indivisible particles. More than a century after, the physics of the elementary particles is completely transformed. Atoms are not indivisible but, like everything in Nature, are composed by subatomic, more fundamental components. The Standard Model (SM) is the theory that describes the physics of the elementary particles and their interactions. Experimental evidence is consistent with the SM predictions, such as the precise measurements in the so-called electroweak sector by the experiments at Large Electron-Positron collider (LEP), and the discovery of the Higgs boson by the ATLAS and CMS experiments at Large Hadron Collider (LHC).

However, despite its incredible experimental successes, the SM is not the ultimate theory of particles. Many of its extensions postulate solutions to some critical limitations of the theory, particularly the effects of high-energy renormalisation on physical observable, such as the mass of the Higgs boson, and the unknown nature of the Dark Matter. Supersymmetry is one of the most established Beyond the Standard Model (BSM) theories, which extends the particle content of the SM by introducing a fermion-boson symmetry. The new particle states should have a mass around 1 TeV scale.

The analyses in this thesis search for supersymmetry produced via electroweak modes with LHC proton-proton collisions at $\sqrt{s} = 13$ TeV, at a scale where possible hints of supersymmetry can appear. The targeted dataset is the one collected by the ATLAS experiment between the years 2015 and 2018, corresponding to 139 fb^{-1} . The targeted final states are those with three leptons and missing transverse momentum.

This thesis is structured as follows. In Chapter 2, the SM framework and its shortcomings are briefly presented, then the supersymmetrical extension of the SM is discussed, along with its phenomenology at the LHC and the state of art of searches for electroweak supersymmetry. Chapter 3 presents the experimental apparatus, the LHC and the ATLAS detector. In Chapter 4, the main features of the generation steps of the simulations used in the analyses are briefly described, as well as the algorithms used for the reconstruction of physics objects from hits in the detectors. In Chapter 5 the analysis strategy for the three-lepton searches is discussed, presenting the strategies for the optimisation of the searches, the techniques for the estimation of the SM backgrounds and the statistical interpretation of the results. In Chapter 6, the results of the analyses are then presented. Finally, conclusions are drawn in Chapter 7.

In this thesis, natural units $\hbar = c = 1$ are used.

2 | THEORETICAL FRAMEWORK

The [SM](#) is the theoretical framework that describes the physics of known elementary particles and their interactions. Despite its many successes, the [SM](#) presents several limitations, such as the non-natural radiative corrections to the Higgs boson mass at energies up to the Planck mass scale. In order to respond to such limitations, [BSM](#) theories aim to provide valid extensions to the [SM](#) at high energy.

Supersymmetry is one of the best established [BSM](#) extensions. It postulates the existence of a new symmetry, linking fermions to bosons and introducing additional particles, effectively doubling the particle content of [SM](#). Production and detection of these new particles would open a window on a whole new range of phenomena to be tested experimentally.

In Section [2.1](#), a brief description of the main features of the [SM](#) is presented. In Section [2.2](#), the supersymmetry extension of the [SM](#) is described concisely, with particular emphasis on the minimal supersymmetric Standard Model. Finally, Section [2.3](#) presents an overview of current experimental results from the search for Electroweak ([EWK](#)) supersymmetry signals at the [LHC](#), relevant for the studies presented in this thesis.

2.1 The Standard Model

The SM presents a coherent description of elementary particles' interactions via three of the four known fundamental forces [1]. Its particle content is shown in Figure 2.1.

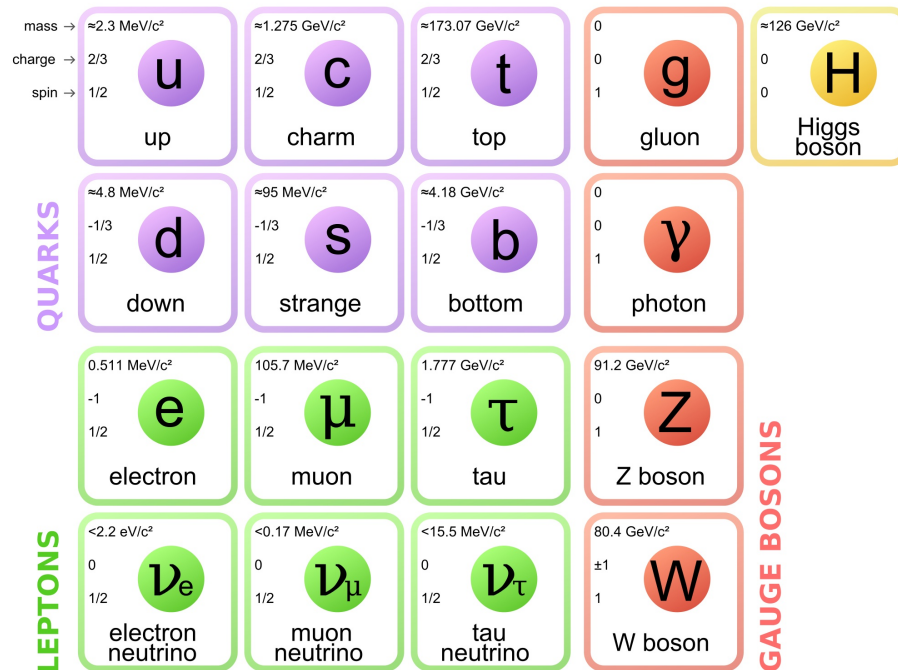


Figure 2.1: Particle content of the SM. The six quarks (u, d, s, c, b and t) are shown in purple, the six leptons ($e, \mu, \tau, \nu_e, \nu_\mu$ and ν_τ) displayed in green, while the gauge bosons (g, γ, Z and W) and Higgs boson (H) are shown in red and yellow, respectively. Values of masses, electric charge and spin are also given for each particle. [2]

Particles in the SM can be grouped into two different categories. The first one comprises particles with an integer value of the spin, the *bosons*. These are the spin-1 *gauge bosons* (g, γ, Z and W), associated with the considered fundamental interactions, as well as an additional spin-0 boson, the so-called *Higgs boson*, associated with the mechanism that ensures that elementary particles in the SM have non-zero masses. The second group of particles in the SM includes the matter particles, which are all spin-1/2 *fermions*, separated into *leptons* and *quarks*.

Chirality is an important quantum number which characterises particles in the SM. It is conceptually defined as a generalisation of *helicity*, namely the projection of a particle's spin along the direction of its motion. A particle's chirality is defined in terms of how its state transforms under a Poincaré rotation of the group $SU(2)$, and is invariant under a boost from one inertial reference frame to another. Depending on their

chirality, particles can be either *left-handed* or *right-handed*.

As mentioned, of the four fundamental forces of nature, only three are included in the **SM** framework: the *weak* force, responsible, for example, for β -decays; the *electromagnetic* force, described by Maxwell's equations; and the *strong* force, which is responsible for the nuclear force¹. The four gauge bosons in the **SM** are associated with these three fundamental forces. The light particle, the photon γ , is the massless mediator of the electromagnetic force. It interacts with particles which carry an *electric charge*. The gluons g are the massless carriers of the strong interaction, and thus couple with particles carrying a *colour charge*, which can assume three values (labelled as *red*, *green*, or *blue*). The W^\pm and the Z bosons are the force carriers associated with the weak interaction, which is short-range, and the W^\pm and the Z bosons have masses as shown in Figure 2.1, namely close to the *electroweak scale* of $O(100 \text{ GeV})$. The interactions mediated by the W boson, referred to as *charged currents*, involve only left-handed fermions with electric charge differing by one unit. This is not the case for the interactions mediated by the Z boson, the so-called *neutral currents*. It is convenient to organise particles interacting via the weak force into *doublets*, which are the eigenstates of rotation in the $SU(2)$ group. As it will be further discussed in Section 2.1.1, the formalism of the weak interaction is developed by using the algebra of the $SU(2)$ group, whose generators can be written as a function of the *Pauli's matrices* σ_i , the rotation generators in two-dimensional spaces. The weak isospin, the charge of the weak interaction, is defined as the eigenvalue T_3 corresponding to the application of $\sigma_3/2$ to $SU(2)$ states. The so-called Higgs mechanism and the Higgs boson will be discussed in more detail in Section 2.1.2.

The physics of fermions is described by the *Dirac equation*, which predicts the existence of an *antiparticle* for each fermion in the **SM**. Antiparticles have electric charge opposite to their corresponding particle, but have the same values of spin and mass.

The charged leptons are fermions which exist in three distinct *flavours*: the *electron* e , the *muon* μ , and the *tau* τ . Each of the three charged leptons is accompanied by an electrically neutral *neutrino* of the same flavour. Three additive quantum numbers, called *lepton numbers* (L_e , L_μ and L_τ), one for each flavour, are separately conserved

¹ The fourth fundamental interaction, *gravity*, is not included in the **SM**, but it is the subject of Einstein's *general relativity* [3], and a viable quantum theory of gravity remains to be developed.

in the SM. Each lepton number is +1 for particles in the relevant lepton flavour *family*, −1 for the corresponding antileptons, and zero otherwise. This implies that no SM process allows net change in the flavour of involved leptons. All the leptons carry weak isospin.

$SU(2)$ doublets of leptons can be constructed in correspondence to the lepton flavour families:

$$\begin{pmatrix} \nu_e \\ e^- \end{pmatrix}, \quad \begin{pmatrix} \nu_\mu \\ \mu^- \end{pmatrix}, \quad \text{and} \quad \begin{pmatrix} \nu_\tau \\ \tau^- \end{pmatrix}. \quad (2.1)$$

The main properties of leptons are summarised in Table 2.1.

Name	Symbol	Spin	Electric charge/ e	Mass [GeV]	L_e	L_μ	L_τ
Electron	e^-	1/2	−1	0.0005	1	0	0
Electron neutrino	ν_e	1/2	0	$< 1.1 \cdot 10^{-9}$	1	0	0
Muon	μ^-	1/2	−1	0.1134	0	1	0
Muon neutrino	ν_μ	1/2	0	$< 1.9 \cdot 10^{-4}$	0	1	0
Tau	τ^-	1/2	−1	1.77	0	0	1
Tau neutrino	ν_τ	1/2	0	$< 1.82 \cdot 10^{-2}$	0	0	1

Table 2.1: Summary of the main properties of the SM leptons. [4]

Quarks, with gluons, are the microscopic constituents of atomic nuclei. They carry a colour charge, an electric charge, and weak isospin, and are hence subject to each of the fundamental forces in the SM. In particular, due to the structure of the strong interaction, quarks are not detectable as isolated particles (*confinement*), but they aggregate into colourless states, known as *hadrons* (these can be three-quark states, known as *baryons*, or quark-antiquark states, known as *mesons*). Similarly to the leptons, quarks are organised into families, or *generations*, again arranged into $SU(2)$ doublets:

$$\begin{pmatrix} u \\ d \end{pmatrix}, \quad \begin{pmatrix} c \\ s \end{pmatrix}, \quad \text{and} \quad \begin{pmatrix} t \\ b \end{pmatrix}. \quad (2.2)$$

The values of the electric charge of the quarks is fractional: the up-type quarks (*up*, *charm*, *top*) have a positive charge $+2/3 e$, whilst the down-type quarks (*down*, *strange*, *bottom*) have charge $-1/3 e$, where e is the magnitude of the electron charge. Quarks carry an additive quantum number, the *baryon number* B , which is conserved

in the SM. For all the quarks, the baryonic number is $+1/3$, and $-1/3$ for antiquarks. A summary of the main properties of quarks is shown in Table 2.2.

Name	Symbol	Spin	Electric charge/ e	Mass [GeV]	Baryon number
Down	d	$1/2$	$-1/3$	0.00467	$1/3$
Up	u	$1/2$	$+2/3$	0.00217	$1/3$
Strange	s	$1/2$	$-1/3$	0.093	$1/3$
Charm	c	$1/2$	$+2/3$	1.27	$1/3$
Bottom	b	$1/2$	$-1/3$	4.18	$1/3$
Top	t	$1/2$	$+2/3$	172.9	$1/3$

Table 2.2: Summary of the main properties of the SM quarks. [4]

2.1.1 Fundamental forces and symmetries

The formalism of the SM is that of Quantum Field Theory (QFT) [5], which applies quantisation of continuous fields in order to express interactions and particles as quantum field fluctuations above the vacuum state. The quantity that describes the state of a field in a given point of the spacetime is called *lagrangian*, \mathcal{L} , whose expression depends on the space coordinates \mathbf{q} , the velocities $\dot{\mathbf{q}}$, and time t . The equations of motion, the *Euler-Lagrange equations*, can be derived from \mathcal{L} after applying the principle of least action, and are written as:

$$\frac{d}{dt} \frac{\partial \mathcal{L}}{\partial \dot{\mathbf{q}}} - \frac{\partial \mathcal{L}}{\partial \mathbf{q}} = 0. \quad (2.3)$$

In the formalism of the SM, a very important role is played by *symmetries*. The lagrangian of a system is *symmetric* if its form does not change after a specific transformation of the field. Through the Noether's theorem [6], each symmetry of the system corresponds to a conserved quantity or *charge*.

2.1.1.1 Quantum Electrodynamics

The electromagnetic force is described by the theory of Quantum Electrodynamics (QED), whose main ideas are briefly presented in this section. The lagrangian of a free

massless fermion, described through a *Dirac spinor* ψ , is

$$\mathcal{L}(x) = i\bar{\psi}(x)\gamma^\mu\partial_\mu\psi(x), \quad (2.4)$$

where x is the four-vector of the space-time coordinates and the γ^μ are the anti-commuting *Dirac matrices*. The lagrangian in Equation 2.4 is symmetric under a *global* phase transformation of the Dirac spinor in the symmetry group $U(1)$:

$$\psi(x) \xrightarrow{U(1)} \psi'(x) = e^{i\theta}\psi(x), \quad (2.5)$$

where θ is the generator of the transformation. Normally, if the transformation is *local* ($\theta = \theta(x)$), the symmetry is broken, due to the presence of partial derivatives of the field ψ in the lagrangian. The *gauge principle* imposes that the $U(1)$ phase transformation preserve invariance also under a local transformation. In order to achieve this, two quantities are introduced: a spin-1 *vector field* $A_\mu(x)$, which under $U(1)$ transforms as

$$A_\mu(x) \xrightarrow{U(1)} A'_\mu(x) = A_\mu(x) - \frac{1}{e}\partial_\mu\theta, \quad (2.6)$$

and a *covariant derivative* D_μ ,

$$D_\mu\psi(x) \equiv \left[\partial_\mu + ieA_\mu(x) \right] \psi(x), \quad (2.7)$$

which behaves like a Dirac spinor under transformations of the $U(1)$ group. The quantity e is the strength of the interaction term, or *coupling*. The core of the local gauge principle is to replace the partial derivative in the lagrangian in Equation 2.4 with the covariant derivative in Equation 2.7, leading to a locally-symmetric lagrangian under phase transformations of the $U(1)$ group:

$$\mathcal{L}(x) = i\bar{\psi}(x)\gamma^\mu D_\mu\psi(x) = i\bar{\psi}(x)\gamma^\mu\partial_\mu\psi(x) - eA_\mu(x)\psi(x). \quad (2.8)$$

Equation 2.8 shows that the local gauge invariance of the lagrangian of a free fermionic particle can be respected if a coupling term $-eA_\mu(x)\psi(x)$ between the fermion and the vector field A_μ is introduced. The field A_μ is interpreted as the field of the photon γ , while the parameter e is the electric charge. As it will be presented in the follow-

ing sections, the use of the local gauge principle can be extended also to the formalism to describe all the other fundamental forces in the SM.

QED gives some of the most successfully tested predictions of the SM. The magnetic moments of the electron and muon are sensitive to QED-loop corrections, which give rise to anomalies with respect to the classical electrodynamics expectations. The measured values of the anomalies of the electron [7] and the muon [8] agree with the theoretical prediction from QED up to twelve significant figures. In the case of the muon, the measured magnetic moment anomaly, $\alpha_\mu^{\text{QED}} = (116584718.92 \pm 0.03) \times 10^{-11}$, is in agreement within the 10^{-14} order with the value as expected from QED calculations, $\alpha_\mu^{\text{Exp}} = (11659209.1 \pm 5.4 \pm 3.3) \times 10^{-10}$ [4]. Possible deviations from the SM predictions are explainable by considering additional one-loop diagrams, shown in Figure 2.2, involving supersymmetric particles, whose properties will be discussed in Section 2.2.

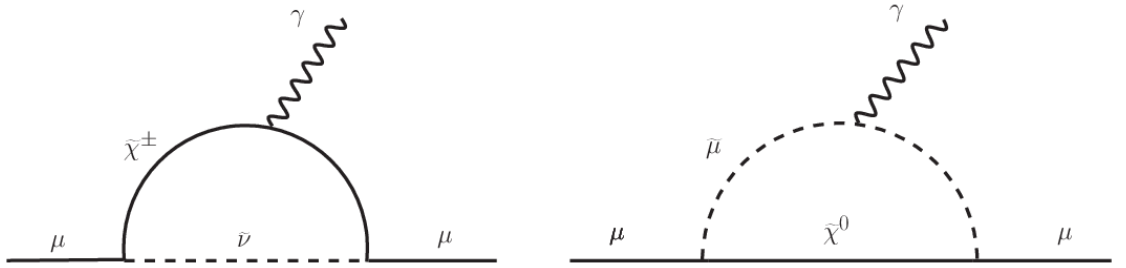


Figure 2.2: One-loop supersymmetric contributions to the anomalous magnetic momentum of the muon, involving chargino and sneutrino (left) and neutralino and smuon (right). [9]

2.1.1.2 Quantum Chromodynamics

Quantum Chromodynamics (QCD) is the theoretical framework which describes the strong interaction. The symmetry group which regulates the QCD interactions is $SU(3)$, whose local gauge transformation has the form:

$$U = \exp \left\{ i \frac{\lambda^a}{2} \theta_a \right\}, \quad (2.9)$$

where $\frac{\lambda^a}{2}$ are the eight $SU(3)$ generators. Similarly to QED, the structure of QCD is based on the application of the gauge principle to the lagrangian of a free Dirac spinor,

such that coupling terms with new interaction bosons are coherently included. The local invariance under $SU(3)$ introduces eight new vector fields which couple with the fermions, along with a covariant derivative which transforms like the fermion field under $SU(3)$. The new fields are associated with the mediators of the strong interaction, the gluons. The strength of the interaction is represented by the strong coupling α_s , in analogy to the QED coupling e appearing in Equation 2.8.

A crucial difference between QCD and QED is given by the non-abelian nature of the $SU(3)$ symmetry group, meaning that the generators do not commute with each other. For this reason, differently from the photons, the gluons can self-interact, leading to additional loop contributions in the Feynman propagators. As a consequence, the value of the strong coupling α_s changes significantly depending on the energy scale at which the interaction is considered. At energies comparable to the *hadronisation scale* (≈ 1 GeV), the strong coupling is $\alpha_s \approx 1$, and interacting particles experience the phenomenon of so-called *confinement*, which causes the aggregation of coloured particles into colourless hadrons. On the other hand, the strong coupling between particles become asymptotically weaker as the energy of the interaction increases, so that coloured particles reach *asymptotic freedom* and at asymptotically high energies come into existence as isolated states.

2.1.1.3 Electroweak unification

As discussed in Section 2.1, one of the main characteristics of the weak force is the dependency of the interaction on the left-handed and right-handed chirality of the particles. For this reason, it is useful to represent the left-handed fermions as $SU(2)$ doublets, and the right-handed particles as $U(1)$ singlets, written as:

$$\psi_1(x) = \begin{pmatrix} \nu^e \\ e^- \end{pmatrix}_L, \quad \psi_2(x) = (e^-)_R, \quad \psi_3(x) = (\nu_e)_R, \quad (2.10)$$

where $\psi_1(x)$ is a $SU(2)$ doublet with left-handed elements, $\psi_2(x)$ and $\psi_3(x)$ are $U(1)$ singlets. The symbols e^- and ν_e represent two particle spinors which differ from one unit of electric charge, whose left-handed components can interact via charged currents. For simplicity, the states in 2.10 are written only for the first family of leptons:

the same structure is maintained for the other leptons and the quarks.

In the electroweak unification theory [10, 11, 12], all ψ_1 , ψ_2 and ψ_3 can be transformed by a phase rotation in $U(1)$, but only ψ_1 has the structure to transform under $SU(2)$. The overall symmetry group of the interaction is given by the product $SU(2) \otimes U(1)$. With a formalism analogous to the one for QED and QCD, the application of the local-gauge invariance to $SU(2) \otimes U(1)$ introduces vector fields in the same number as the generators of the symmetry group. In particular, three vector fields ($W_\mu^i (i = 1, 2, 3)$) are introduced for the $SU(2)$, and one (B_μ) for $U(1)$. In addition, the local gauge invariance introduces the couplings g and g' of the fermions to four vector fields, $W_\mu^i (i = 1, 2, 3)$ and B_μ , respectively.

The two vector fields W_μ^1 and W_μ^2 combine together to give rise to states associated with the SM W^\pm bosons:

$$W_\mu = \frac{W_\mu^1 + iW_\mu^2}{\sqrt{2}}, \quad W_\mu^\dagger = \frac{W_\mu^1 - iW_\mu^2}{\sqrt{2}}. \quad (2.11)$$

The vector fields W_μ^3 and B_μ are both electrically neutral and mix with each other via a rotation matrix with rotation angle given by the *Weinberg angle* θ_W :

$$\begin{pmatrix} W_\mu^3 \\ B_\mu \end{pmatrix} = \begin{pmatrix} \cos\theta_W & \sin\theta_W \\ -\sin\theta_W & \cos\theta_W \end{pmatrix} \begin{pmatrix} Z_\mu \\ A_\mu \end{pmatrix}. \quad (2.12)$$

The fields Z_μ and A_μ correspond to the Z boson and the photon γ of the SM.

The electroweak unification relation connects the $SU(2) \otimes U(1)$ couplings g and g' to the $U(1)$ coupling e :

$$g \sin\theta_W = g' \cos\theta_W = e. \quad (2.13)$$

Finally, the Gell-mann-Nishijima relation defines the *hypercharge* Y , from the electric charge Q and the third component of the weak isospin T_3 [13, 14], as:

$$Y = 2(Q - T_3). \quad (2.14)$$

In conclusion, the overall symmetry group of the **SM** is given by the product of the groups of the electroweak unification theory and **QCD**:

$$SU(3)_C \otimes SU(2)_L \otimes U(1)_Y, \quad (2.15)$$

where C indicates the colour charge, L refers to the left-handed chirality of the particles, and Y is the hypercharge.

2.1.2 The Brout-Englert-Higgs mechanism

Up to this point, all the particles in the **SM** are assumed to be massless, since a mass term would explicitly violate the local gauge invariance. However, experiments show that most of the particles in the **SM** possess a non-zero mass, as seen in Tables 2.1 and 2.2. The Brout-Englert-Higgs (**BEH**) mechanism [15, 16, 17] provides a solution to this issue. The **BEH** mechanism considers the locally gauge-invariant lagrangian

$$\mathcal{L}_S = (D_\mu \phi)^\dagger D^\mu \phi - V(\phi), \quad \text{where } V(\phi) = -\mu^2 \phi^\dagger \phi - h(\phi^\dagger \phi)^2, \quad (2.16)$$

where μ^2 and h are parameters that define the shape of the potential, and D_μ is the $SU(2)_L \otimes U(1)_Y$ covariant derivative. The $\phi(x)$ are $SU(2)_L$ doublets of complex scalars of the form:

$$\phi(x) = \begin{pmatrix} \phi^+(x) \\ \phi^0(x) \end{pmatrix}. \quad (2.17)$$

For $\mu^2 < 0$, the potential $V(\phi)$ assumes the characteristic “mexican-hat” shape, as shown in Figure 2.3. The minimum of the potential corresponds to an infinite set of points lying on the circle at the “bottom” of the potential in the complex plane $\{\text{Re}\phi, \text{Im}\phi\}$. The system will “choose” to occupy one random point at the minimum of the potential, corresponding to the *vacuum expectation value* $V(\phi_0) = -\mu^2/h\sqrt{2} \equiv v/\sqrt{2}$, where ϕ_0 is the complex scalar spinor that minimises the potential. The choice does not explicitly break the symmetry, which remains hidden. The phenomenon is referred to as *spontaneous symmetry breaking*. As a consequence of the spontaneous symmetry breaking, the system is bound to move around the chosen vacuum expectation value. Excitations around the minimum lead to phase rotations of $\theta^i(x)$

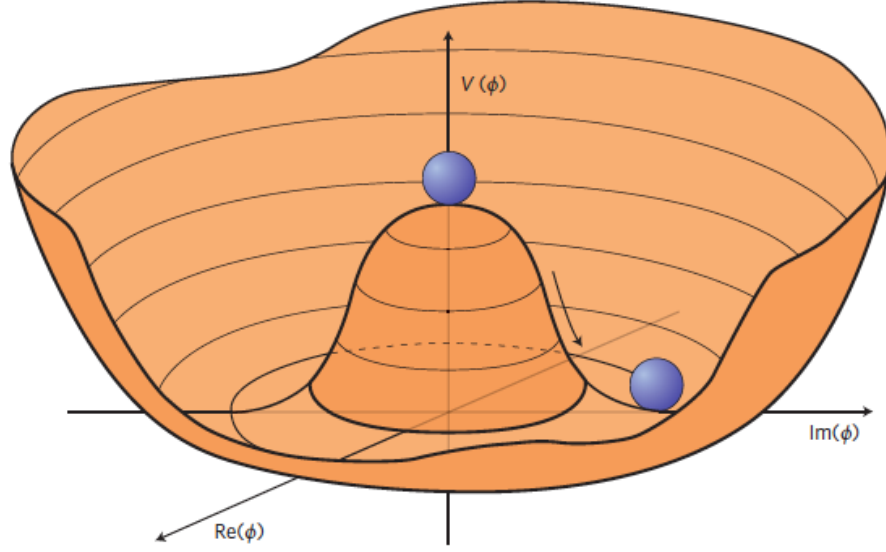


Figure 2.3: The complex scalar potential $V(\phi)$ in the Brout-Englert-Higgs mechanism, shown in function of the real and imaginary components of the complex scalar field ϕ . The potential presents a set of vacuum expectation values, lying on the same complex plane. [18]

along points at the same minimum value $V(\phi_0)$ and excitations $H(x)$ along the curve of the potential. Taking into account the excitations around the chosen minimum, the $SU(2)_L$ spinor of the complex scalar can be written as;

$$\phi(x) = \exp\left\{i\frac{\sigma_i}{2}\theta^i(x)\right\} \frac{1}{\sqrt{2}} \begin{pmatrix} 0 \\ v + H(x) \end{pmatrix} \quad (i = 1, 2, 3), \quad (2.18)$$

where $\theta^i(x)$ is the parameter of the phase $SU(2)_L$ rotation in the complex plane generated by σ_i and $H(x)$ corresponds to the excitations along the curve of the potential $V(\phi)$.

By the imposed local gauge invariance, the potential is invariant under any phase rotation under $SU(2)_L$. Therefore, the gauge $\theta^i(x) = 0$ is a valid choice which does not lack generality. The spontaneous symmetry breaking in the BEH mechanism introduces thus only a massive excitation, associated to a newly introduced complex scalar field $H(x)$. This is conventionally referred to as the *Higgs boson*. By replacing the spinor in Equation 2.18 inside the lagrangian in Equation 2.16, mass terms for the W and Z bosons are introduced, without explicitly breaking the gauge symmetry.

According to the BEH mechanism, the masses of the W and Z bosons are related

by the Weinberg angle θ_W , as follows:

$$M_W = M_Z \cos \theta_W = \frac{vg}{2}. \quad (2.19)$$

The BEH mechanism also introduces a mass term for the H boson. This gives a mass for the H boson proportional to the μ parameter of the potential in Equation 2.16:

$$M_H = \sqrt{-2\mu^2}. \quad (2.20)$$

The Higgs boson couples directly to all the massive particles of the SM. In particular, for gauge bosons, coupling to the Higgs boson are proportional to their squared masses, while couplings with fermions are linearly proportional to the values of the fermion masses.

The validity of the BEH mechanism was proven when, in 2012, a new scalar particle with mass approximately of 125 GeV was discovered by the ATLAS and CMS experiments at the LHC [19, 20, 21], and subsequently found to be consistent with the SM Higgs boson of the spontaneous symmetry breaking mechanism. The Higgs boson was initially observed in channels for the tree-level decays $H \rightarrow ZZ^* \rightarrow 4\ell$ and $H \rightarrow WW^* \rightarrow \ell\nu\ell\nu$, and the loop-decay into photons $H \rightarrow \gamma\gamma$. The reconstructed masses from the $H \rightarrow ZZ^* \rightarrow 4\ell$ and the $H \rightarrow \gamma\gamma$ decays in ATLAS and CMS, respectively, as obtained at the time of the first observation, are shown in Figure 2.4a and 2.4b, respectively.

2.1.3 Limitations of the SM

Despite its excellent predicting power, the SM presents several limitations, which motivate the search for signals from new BSM phenomena. In the following, some of the main motivations for BSM theories are briefly discussed.

Hierarchy problem and naturalness

One compelling motivation to look for BSM physics is the so-called *hierarchy problem*, which becomes manifest when the theory is extrapolated to high energy scales, up to the Planck mass scale $M_P = \sqrt{\frac{\hbar c}{G}}$ equal to 2.4×10^{18} GeV, where G is the gravitational

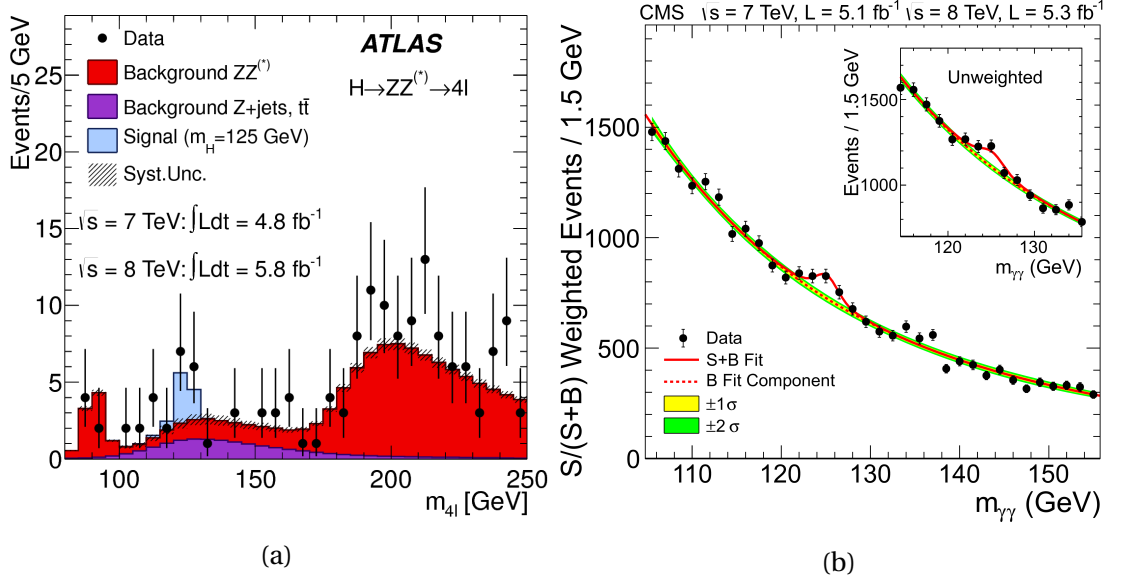


Figure 2.4: The reconstructed mass of the Higgs boson, at the time of its first observation in 2012. On the left, the distribution of the four-lepton invariant mass from the $H \rightarrow ZZ^* \rightarrow 4\ell$ decay, as observed by ATLAS. On the right, the analogous distribution from the $H \rightarrow \gamma\gamma$ channel as measured by CMS.[19, 20]

constant. The mass of the Higgs boson receives important high-order corrections from the one-loop couplings to fermion pairs, $f\bar{f}$, as shown in Figure 2.5.

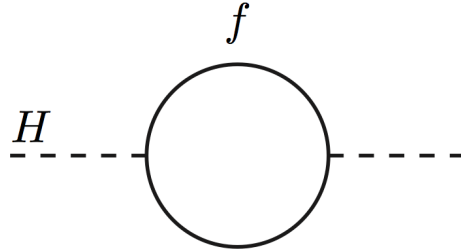


Figure 2.5: Fermionic one-loop correction to the mass of Higgs boson.

These corrections are proportional to the strength λ_f of the Higgs-fermion coupling and depend on the high energy cut-off Λ_{UV} . One can write them as:

$$\Delta M_H^2 = -\frac{|\lambda_f|^2}{8\pi^2} \Lambda_{UV}^2 + \dots, \quad (2.21)$$

where the quantity Λ_{UV} is the regulator of the theory, interpreted as the energy scale at which new physics might arise and the SM would lose full validity. Such corrections to the Higgs boson mass are not *natural*, in the sense that, if Λ_{UV} approaches M_P , the one-loop corrections increase enormously and become around thirty orders of magnitude larger than the measured mass of the Higgs boson.

Dark Matter

Dark matter constitutes approximately one quarter of the Universe [22]. Its origin is still unknown, but several experimental and observational results point clearly to its existence. One of the historical motivations for dark matter comes from the study of the rotation curves of spiral galaxies [23]. As shown in Figure 2.6, the observed data for the rotation curve of the spiral galaxy NGC-3198 can be explained only by assuming matter abundance not just in the core of the galaxy, as expected, but also in the halo.

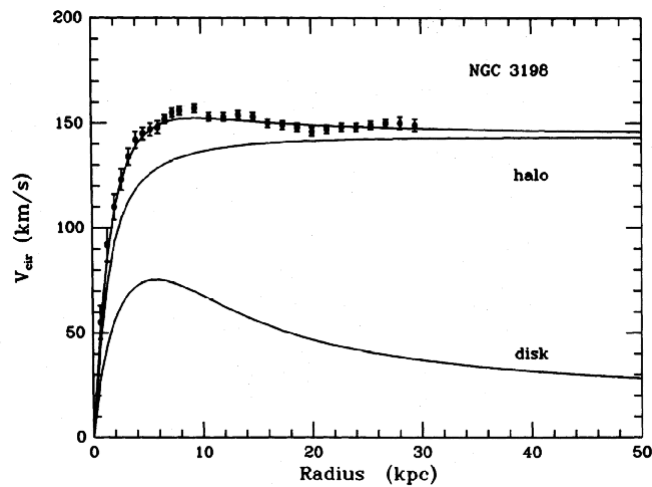


Figure 2.6: Rotation curves for the spiral galaxy NGC 3198. Observed data show agreement with the model which assumes a uniform distribution of matter across the core of the galaxy and the halo. [23]

Different models are used to characterise the nature of dark matter, and one of the most accredited models describes its constituents as Weakly Interacting Massive Particle (WIMP), yet eluding direct detection at dedicated experiments. Many BSM extensions bring about massive particles consistent with the WIMP assumption of dark matter, and therefore are good candidates to explain the unknown matter density of the universe.

Grand Unified Theories

The SM does not predict a unification of all the three fundamental interactions it describes. That is because of how the interaction couplings evolve depending on the energy scale. The *running* of the coupling constants is predicted by equations in the renormalisation group. As shown in Figure 2.7, in the SM couplings do not meet at any

energy scale, although a hint is seen of a possible unification at some very large energy scale.

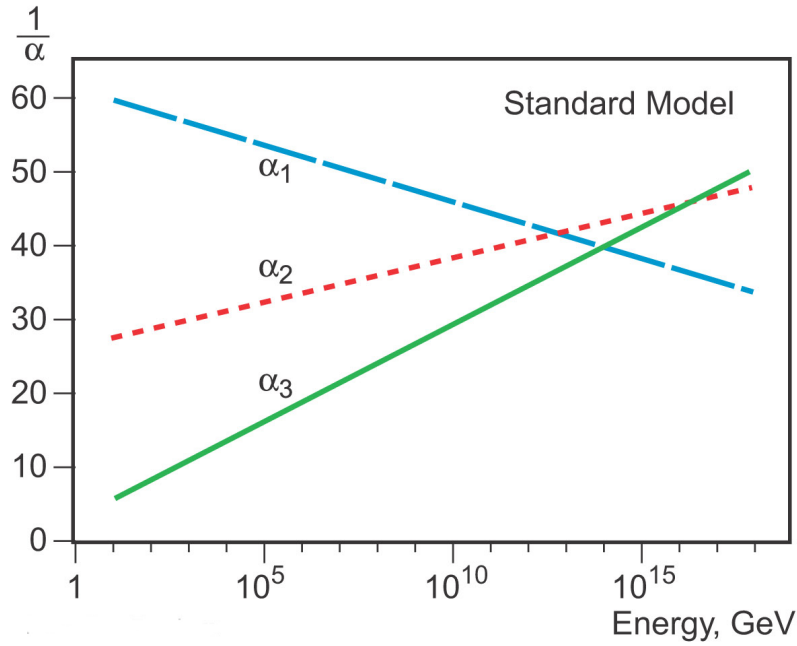


Figure 2.7: Running of the interaction couplings in the SM as a function of the energy scale, where α_1 corresponds to the electromagnetic force coupling, α_2 the strong force coupling and α_3 the weak force coupling. [24]

2.2 Supersymmetry

Supersymmetry (SUSY) is one of the most widely studied BSM theories that extend the particle content of the SM to include new particle states. The theory postulates the existence of *supersymmetric partners* of the SM particles, with the same quantum numbers except the spin, which differs by 1/2 between SM and SUSY counterparts. This corresponds to considering an operator \hat{Q} which transforms a fermion in a boson and viceversa [25, 26]:

$$\hat{Q}|\text{Fermion}\rangle = |\text{Boson}\rangle \quad \text{and} \quad \hat{Q}|\text{Boson}\rangle = |\text{Fermion}\rangle. \quad (2.22)$$

This has the effect of approximately doubling the particle content of the SM.

As an important consequence of the introduction of these new particles, SUSY can provide a good solution to the hierarchy problem. In the supersymmetric scenario,

in addition to the high-order corrections to the Higgs boson mass mentioned in Section 2.1.3, analogous corrections arise due to the one-loop diagrams involving the new scalar bosons, as shown in Figure 2.8.

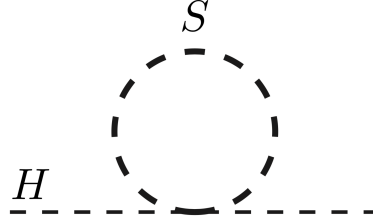


Figure 2.8: Bosonic one-loop correction to the mass of Higgs boson.

This gives rise to contributions of the form:

$$\Delta M_{\text{H}}^2 = \frac{\lambda_{\text{S}}}{16\pi^2} \Lambda_{\text{UV}}^2 + \dots, \quad (2.23)$$

where λ_{S} is the coupling of the Higgs boson to the new scalar particle and Λ_{UV} is the same energy scale cut-off as before. In **SUSY**, each correction Δm_{H}^2 from a fermionic loop as in Equation 2.21 is hence balanced by a contribution from a bosonic loop involving its supersymmetry partner, as in Equation 2.23. In the two terms, the contributions to Δm_{H}^2 proportional to Λ_{UV}^2 have opposite signs and, when added together, give an overall correction proportional to $(\lambda_{\text{S}} - |\lambda_{\text{f}}|^2)\Lambda_{\text{UV}}^2$, which cancels if the couplings of the fermion and the boson to the Higgs are such that $\lambda_{\text{S}} = |\lambda_{\text{f}}|^2$.

In the **SUSY** formalism, particles are grouped into *supermultiplets*. Each supermultiplet contains a **SM** particle and its **SUSY** counterpart [27], referred to as *supersymmetric partner*. A *chiral supermultiplet* contains a chiral state of a spin-1/2 particle, represented by a Weyl spinor, and two real scalar particles. Therefore, both the left-handed and the right-handed states of fermions in the **SM** are organised into two different chiral supermultiplets in association with two spin-0 particles, their supersymmetric partners. The supersymmetric partners of leptons and quarks are assigned the same name of their **SM** counterpart with an "s-" (standing for "scalar") as prefix: *sleptons* and *squarks* are the supersymmetric counterparts of leptons and quarks.

SM vector bosons are included in *gauge multiplets*, along with their spin-1/2 Weyl fermions **SUSY** partners, assumed massless in order not to break the gauge symmetry. The supersymmetric partners of the **SM** gauge bosons are called *gauginos*. Specifically,

the supersymmetric partners of the gluon, W_μ and B_μ boson fields are called *gluino*, *wino* and *binos*, respectively.

In order to avoid anomalies in the theory and to give mass to the up-type and down-type fermions separately, two chiral supermultiplets for the Higgs boson are introduced, H_u and H_d . Therefore, multiple Higgs bosons are postulated in the **SUSY** extension of the **SM**, as discussed later in Section 2.2.1.2. The supersymmetric partners of the Higgs bosons are called *higgsinos*. The two vacuum expectation values for the up-type and down-type Higgs supermultiplets, v_u and v_d , are connected to the vacuum expectation value v by the relation $v^2 = v_u^2 + v_d^2$. Often, their ratio $v_u/v_d = \tan \beta$ is considered.

2.2.1 The MSSM

The Minimal Supersymmetric Standard Model (**MSSM**) is the minimal extension of the **SM** to include supersymmetric partners and solve the hierarchy problem [28, 29]. It has 105 free parameters [30]. The **MSSM** is a grand unified theory. The running of the couplings as calculated in the **MSSM** is shown in Figure 2.9. Assuming all the contributions coming from particles in the **MSSM**, unification of couplings is achieved at energy scales of $10^{15} - 10^{16}$ GeV.

Table 2.3 shows the supermultiplets of the **MSSM**. For simplicity, only one generation for quarks and leptons is shown. Supermultiplets for the $SU(2)_L$ doublet for squarks-quarks and sleptons-leptons are labelled Q and L , while those for the right-handed $U(1)$ singlet are referred to as \bar{u} , \bar{d} and \bar{e} , for the up-quark, the down-quark and the electron, respectively. By convention, sparticles are labelled by the same symbols of their **SM** counterparts, with a tilde on top (e.g., \tilde{e} for the selectron).

2.2.1.1 Soft supersymmetry breaking

The supersymmetry operator \hat{Q} commutes with the four-momentum operator \hat{P}_μ , and thus the **SM** particles and their supersymmetric partner have the same masses. Nevertheless, if that were the case, the sparticles would have been already observed. Therefore, **SUSY** must be a *broken symmetry*, with the consequence that sparticles must

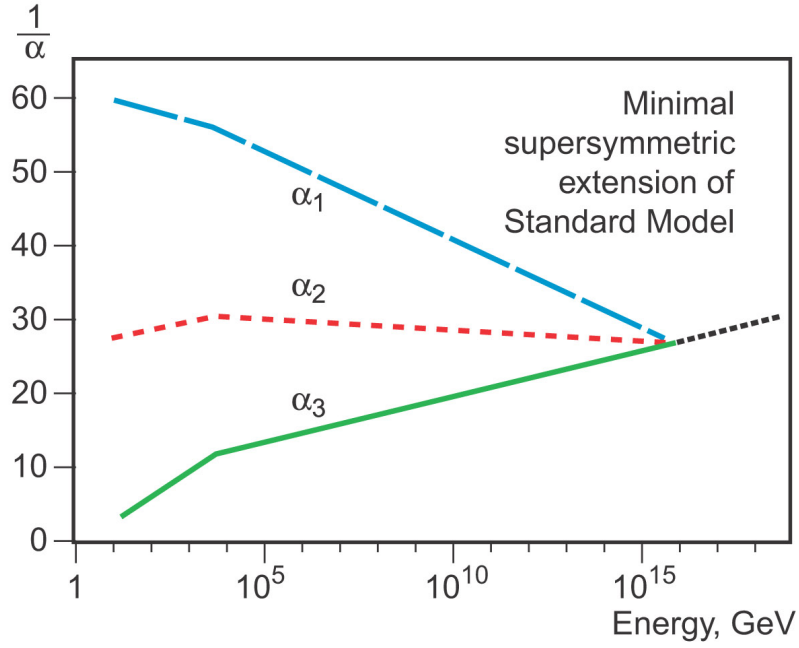


Figure 2.9: Running of the couplings in the [MSSM](#) as a function of the energy scale, where α_1 corresponds to the electromagnetic force coupling, α_2 the strong force coupling and α_3 the weak force coupling. [24]

Names and symbols	spin-0	spin-1/2	spin-1	
Squarks, quarks	Q	$(\tilde{u}_L, \tilde{d}_L)$	(u_L, d_L)	-
	\tilde{u}	(\tilde{u}_R)	(u_R)	-
	\tilde{d}	(\tilde{d}_R)	(d_R)	-
Sleptons, leptons	L	$(\tilde{e}_L, \tilde{\nu}_L)$	(e_L, ν_L)	-
	\tilde{e}	(\tilde{e}_R)	(e_R)	-
Higgs, higgsinos	H_u	$(\tilde{H}_u^+, \tilde{H}_u^0)$	(H_u^+, H_u^0)	-
	H_d	$(\tilde{H}_d^0, \tilde{H}_d^-)$	(H_d^0, H_d^-)	-
Gluginos, Gluons	-	\tilde{g}	g	
Winos, W bosons	-	$\tilde{W}^\pm, \tilde{W}^0$	W^\pm, W^3	
Bino, B boson	-	\tilde{B}	B	

Table 2.3: List of the supermultiplets in the [MSSM](#). Chiral and gauge multiplets are shown. In the case of leptons and quarks, only one generation is reported; two additional sets of chiral supermultiplets are to be considered to account for a total of three families of fermions and [SUSY](#) counterparts. [27]

have higher masses than their [SM](#) partners. However, depending on the masses of the sparticles, the coupling constants of the Higgs boson to fermions and scalars change, leading to the possible situation in which the condition $\lambda_S = |\lambda_f|^2$, necessary to solve the hierarchy problem, might not be satisfied. Therefore, if [SUSY](#) has to restore the naturalness of the corrections at the mass of the Higgs boson, it has to be *softly broken*.

The *soft* term $\mathcal{L}_{\text{soft}}$ for the symmetry breaking is added to the [SUSY](#) lagrangian $\mathcal{L}_{\text{SUSY}}$:

$$\mathcal{L} = \mathcal{L}_{\text{SUSY}} + \mathcal{L}_{\text{soft}}. \quad (2.24)$$

The soft term of the lagrangian ensures the breaking of the supersymmetry, but without inadvertently reintroducing terms proportional to Λ_{UV}^2 in the loop corrections to the Higgs mass. This condition is satisfied for masses of the sparticle of $O(\text{TeV})$. The general idea around the soft supersymmetry breaking is that the mechanism that breaks the symmetry occurs in a *hidden sector*, regulated by independent symmetry groups. The effect of the soft supersymmetry breaking is “communicated” to the visible sector by mediator carriers. Various options are considered for the nature of the mediators, such as gravity [31, 32], the gauge interaction [33] and extra-dimensions [34].

The soft supersymmetry breaking introduces new parameters in the [MSSM](#). A partial inventory of the parameters in the [MSSM](#) is shown in Table 2.4, where only the first generation of quarks and leptons have been listed.

Parameters	Description
M_1	Mass of bino
M_2	Mass of wino
M_3	Mass of gluino
$m_Q^2, m_L^2, m_{\bar{u}}^2, m_{\bar{d}}^2, m_{\bar{e}}^2$	Squared masses of left-handed (Q and L) and right-handed (\bar{u} , \bar{d} and \bar{e}) squarks and sleptons
$m_{H_u}^2, m_{H_d}^2$	Squared masses of the up-type and down-type Higgs chiral supermultiplets, H_u and H_d
μ, b	Mass parameter of Higgs and higgsino, μ and soft bilinear Higgs term, b
a_u, a_d, a_e	Trilinear couplings of the Higgs bosons to up-squark, down-squark and selectron (Figure 2.10)

Table 2.4: The [MSSM](#) parameters introduced by the soft [SUSY](#) breaking. Only first generation of scalar quarks and leptons are considered in this table.

2.2.1.2 The masses in the MSSM mass spectrum

In analogy to the [SM](#), the electroweak symmetry breaking is applied to all the sparticles through a more complex Higgs potential which takes into account the enhanced Higgs

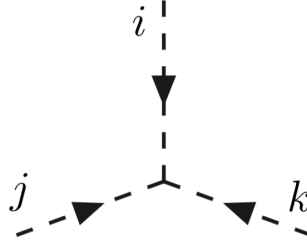


Figure 2.10: Scalar cubic coupling in the [MSSM](#). Interaction couplings a of Higgs bosons to squark and sleptons are part of the [MSSM](#) parameters. [27]

sector in the [MSSM](#). The consequence of the electroweak symmetry breaking is a mix of the masses of the particles to form mass eigenstates.

Higgs bosons When taking into account only the massive excitations in the Higgs potential around the vacuum expectation values, five degrees of freedom are left. These mix together to form five mass eigenstates of the Higgs bosons: h , H^0 , A^0 , H^+ , and H^- . By convention, h is the lightest neutral Higgs boson, consistent with the 125-GeV boson observed by ATLAS and CMS in 2012.

Charginos and neutralinos Winos, bino and higgsinos mix together to generate neutral and charged mass eigenstates. The charged higgsinos and winos mix to form two mass eigenstates called *charginos*, while the neutral higgsinos, the neutral wino and the bino mix into four mass eigenstates called *neutralinos*. Charginos and neutralinos are identified by the $\tilde{\chi}_i^\pm$ and $\tilde{\chi}_j^0$ symbols. The mass mixing is regulated by the matrix relations in Equation 2.25 and Equation 2.26, namely:

$$\begin{pmatrix} \tilde{\chi}_1^0 \\ \tilde{\chi}_2^0 \\ \tilde{\chi}_3^0 \\ \tilde{\chi}_4^0 \end{pmatrix} = \begin{pmatrix} M_1 & 0 & -c_\beta m_Z s_W & s_\beta m_Z s_W \\ 0 & M_2 & c_\beta m_Z c_W & -s_\beta m_Z s_W \\ -c_\beta m_Z s_W & c_\beta m_Z s_W & 0 & -\mu \\ s_\beta m_Z s_W & -s_\beta m_Z c_W & -\mu & 0 \end{pmatrix} \begin{pmatrix} \tilde{B}^0 \\ \tilde{W}^0 \\ \tilde{H}_u^0 \\ \tilde{H}_d^0 \end{pmatrix}, \quad (2.25)$$

and

$$\begin{pmatrix} \tilde{\chi}_1^\pm \\ \tilde{\chi}_2^\pm \end{pmatrix} = \begin{pmatrix} M_2 & \sqrt{2} m_W s_\beta \\ \sqrt{2} m_W c_\beta & \mu \end{pmatrix} \begin{pmatrix} \tilde{W}^\pm \\ \tilde{H}^\pm \end{pmatrix}. \quad (2.26)$$

Here c_β and s_β are shorthands for the $\cos \beta$ and $\sin \beta$, and similarly c_W and s_W are short forms for $\cos \theta_W$ and $\sin \theta_W$. Moreover, m_W and m_Z are the masses of the W and Z bosons, respectively. By convention, the indices of neutralinos and charginos are used to label particles in increasing order of their mass. Therefore, $\tilde{\chi}_1^0$ and $\tilde{\chi}_1^\pm$ are the lightest neutralino and chargino, respectively.

Squarks and sleptons Mixing occurs also in the case of squarks and sleptons. As seen for charginos and neutralinos, the mass-mixing are regulated by mass matrices whose terms provide corrections at the nominal mass of the sparticles. In the case of squarks and sleptons, the corrections depend on the squared value of the mass of the corresponding [SM](#) partner and specific mixing angles, thus becoming important for the heaviest quarks, bottom b and top t , and the heaviest lepton, the tau τ , but otherwise negligible. For illustration, the mass matrix for the scalar top quark can be written as:

$$m_{\tilde{t}}^2 = \begin{pmatrix} m_{Q_3}^2 + m_t^2 + \Delta_{\tilde{u}_L} & \nu(a_t^* \sin \beta - \mu y_t \cos \beta) \\ \nu(a_t \sin \beta - \mu^* y_t \cos \beta) & m_{\tilde{u}_3}^2 + m_t^2 + \Delta_{\tilde{u}_R} \end{pmatrix}, \quad (2.27)$$

where m_t^2 is the squared mass of the top quark, $m_{Q_3}^2$ and $m_{\tilde{u}_3}^2$ are the squared masses of the left-handed and right-handed third generation supermultiplets, $\Delta_{\tilde{u}_L}$ and $\Delta_{\tilde{u}_R}$ are mass corrections coming from quartic interaction with the Higgs bosons for the left-handed and the right-handed supermultiplets, respectively. Moreover, a_t and y_t are the trilinear coupling and the Yukawa coupling of the top-squark to the Higgs bosons, respectively. The off-diagonal elements of the matrix give negative contributions to the mass, reducing the mass of the top-squark. For this reason, the lightest stop \tilde{t}_1 is the lightest squark in the [MSSM](#). Similar, although in reduced magnitude, mixing effects occur in the case of the bottom-squark and tau-slepton.

2.2.1.3 R-parity

In the [SM](#), processes which break the conservation of the baryonic and leptonic numbers B and L can be only described through non-renormalisable terms. Therefore, the conservation of B and L is assumed for any possible process involving only [SM](#)

particles. On the other hand, all the **SUSY** non-gauge interactions are described by the *superpotential*

$$W_{\text{MSSM}} = \bar{u}_i y_u Q_i H_u - \bar{d}_j y_d Q_j H_d - \bar{e}_k y_e L_k H_d + \mu H_u H_d, \quad (2.28)$$

which admits extra renormalisable terms that can break the conservation of B and L . These terms are added to the superpotential as

$$W_{\Delta B/\Delta L} = \frac{1}{2} \lambda^{ijk} L_i L_j \bar{e}_k + \lambda^{ijk'} L_i Q_j \bar{d}_k + \mu^{i'} L_i H_u + \frac{1}{2} \lambda^{ijk'} \bar{u}_i \bar{d}_j \bar{d}_k, \quad (2.29)$$

where i, j and k are family indices, λ^{ijk} and $\lambda^{ijk'}$ are the trilinear couplings of sfermions, and $\mu^{i'}$ is the lepton-number-violating Higgs coupling.

At present, strong constraints exist on the possible violation of B and L , for example from the search for the evidence of proton decay [35]. Therefore, the conservation of B and L is introduced in the **MSSM** by imposing the conservation of a new quantity called *R-parity* [29], defined as:

$$R = (-1)^{3(B-L)+2s}, \quad (2.30)$$

where s is the spin of the particle, and B and L are the usual quantum numbers. *R-parity* takes the value $R = +1$ for all **SM** particles and all the Higgs bosons, and $R = -1$ for all the sparticles in the **MSSM**.

The conservation of *R-parity* at any interaction vertex ensures that B - and L -violating terms in Equation 2.29 are cancelled.

Some important phenomenological consequences are expected in the case of *R-parity* conservation:

- In collisions of **SM** particles, for example protons into protons, sparticles can be produced only in pairs;
- In the **MSSM**, sparticles can only decay into an odd number of other **MSSM** sparticles;
- The Lightest Supersymmetric Particle (**LSP**) is stable.

2.2.2 Phenomenology of the MSSM at colliders

The work described in this thesis focuses on the search for chargino and neutralino production at the LHC. In the following, particular emphasis will therefore be given to the sparticle production modes mediated by electroweak interactions. A more complete description of the production of squarks and gluinos via strong interaction can be seen, for example, in Ref. [27]. In the following sections, R-parity is assumed to be always conserved.

2.2.2.1 Production channels at hadronic colliders

Despite proton-proton collisions favouring the production of squarks and gluinos, with typical processes:

$$gg \rightarrow \tilde{g}\tilde{g}, \tilde{q}_i\tilde{q}_j^*, \quad gq \rightarrow \tilde{g}\tilde{q}_i, \quad q\bar{q} \rightarrow \tilde{g}\tilde{g}, \tilde{q}_i\tilde{q}_j^*, \quad qq \rightarrow \tilde{q}_i\tilde{q}_j, \quad (2.31)$$

production channels mediated by the electroweak interaction can still arise from hadronic initial states at a lower cross-section. Some electroweak SUSY production modes are shown in Figure 2.11.

In general, the SUSY production cross-sections increase with the centre of mass energy of the collisions and decreases with the masses of the sparticles. The behaviour of the production cross-sections as a function of the masses of the sparticle is shown in Figure 2.12, where initial states are those in proton-proton collisions at $\sqrt{s} = 13$ TeV. As it can be seen, for masses of charginos and neutralinos of the order $\mathcal{O}(100$ GeV) and masses of squarks and gluinos of $\mathcal{O}(1$ TeV), cross-section for the electroweak production of gauginos and sleptons become dominant with respect to the channels for the production of squarks and gluinos.

2.2.2.2 Sparticle decays

The strength of the coupling constants at the relevant vertex, as well as the mass spectrum of the involved sparticles, determines which are the favoured decay modes of the

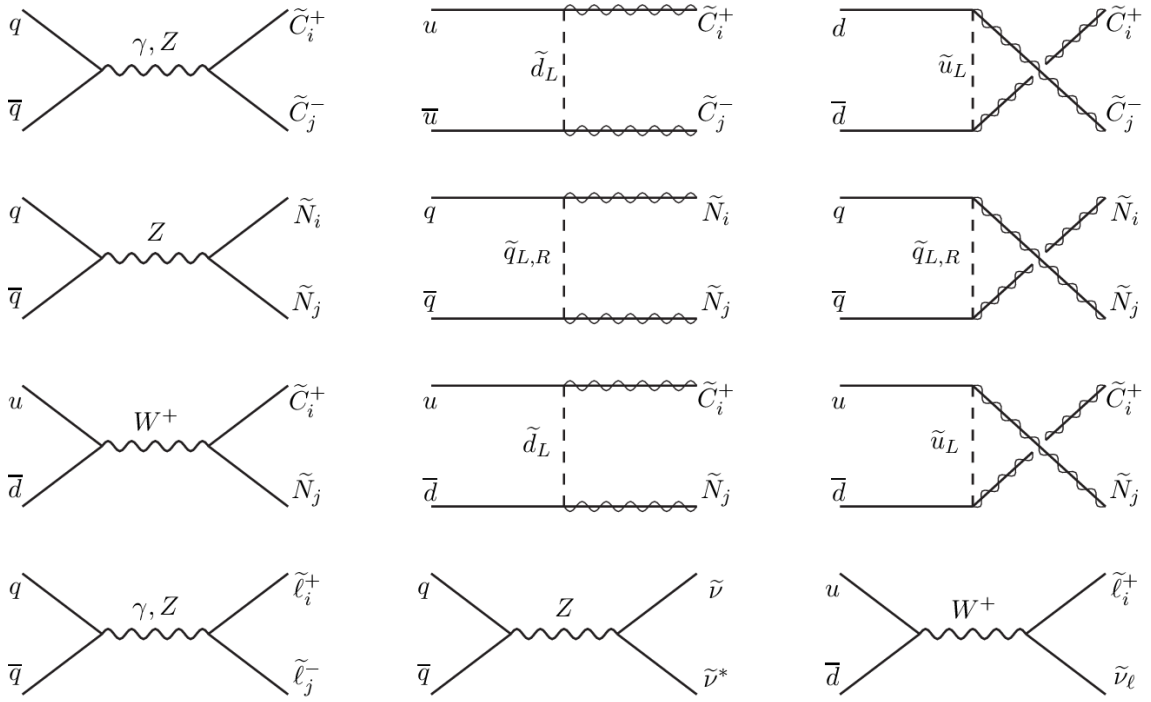


Figure 2.11: Channels for the production of gauginos and sleptons with hadronic initial states, with both contributions from s -channels mediated by gauge bosons and t -channels. In these diagrams, $\tilde{C}_i^\pm = \tilde{\chi}_i^\pm$ ($i=1, 2$) and $\tilde{N}_j^0 = \tilde{\chi}_j^0$ ($j=1, 2, 3, 4$). [27]

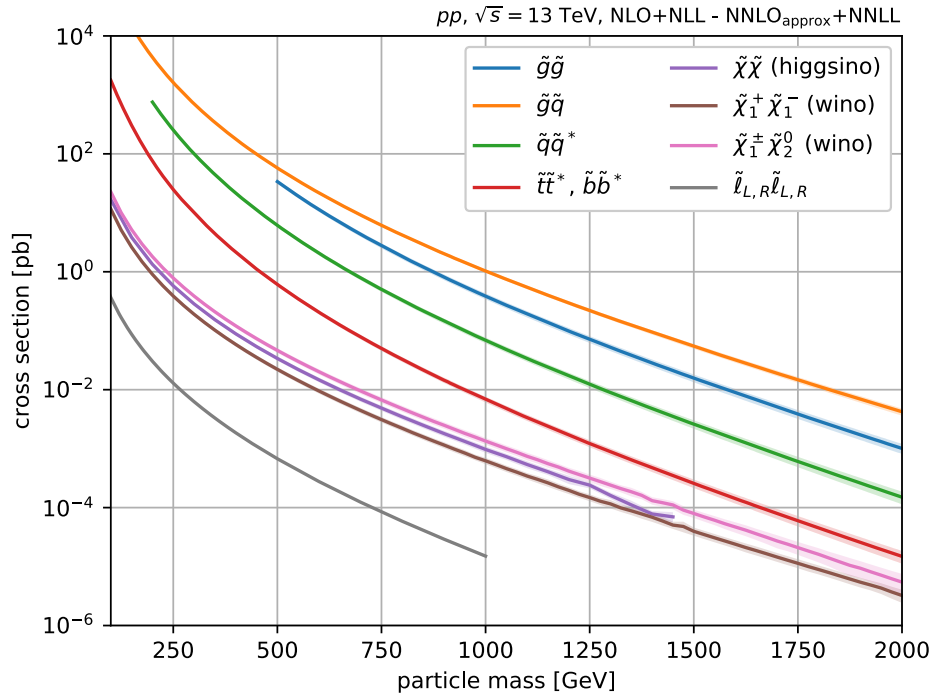


Figure 2.12: Typical cross-sections for the production of sparticles at the LHC as a function of their masses. The assumed centre of mass energy is $\sqrt{s} = 13$ TeV.

sparticles. In the specific case of the gauginos, the allowed decay modes are:

$$\tilde{\chi}_i^0 \rightarrow Z\tilde{\chi}_j^0, \quad W^\mp\tilde{\chi}_j^\pm, \quad h^0\tilde{\chi}_j^0, \quad \ell\tilde{\ell}, \quad \nu\tilde{\nu} \quad (2.32)$$

and

$$\tilde{\chi}_i^\pm \rightarrow W^\pm\tilde{\chi}_j^0, \quad Z\tilde{\chi}_j^\pm, \quad h^0\tilde{\chi}_j^\pm, \quad \ell\tilde{\nu}, \quad \nu\tilde{\ell}. \quad (2.33)$$

If sleptons are lighter than gauginos and higgsinos, the decays into sleptons are dominant, favouring in particular decays into the tau-slepton, the lightest slepton. Otherwise, the decays into [SM](#) gauge bosons and the lightest Higgs boson become dominant.

2.2.2.3 Electroweak SUSY simplified models

Together with the parameters of the [MSSM](#) shown in Table 2.4, parameters from the Higgs sectors such as $\tan\beta$ and the Yukawa couplings also characterise the production and decay modes of sparticles at the [LHC](#). From the point of view of the experiments, the large amount of free parameters is a big limitation: it would be very complicated, or in fact virtually impossible, to design a search able to test all the [MSSM](#) parameters at the same time. For this reason, a vast range of searches are performed using *simplified models* of the [MSSM](#) [36, 37], which correspond to specific choices of free parameters of the [MSSM](#), in order to restrict consideration to a specific production channel of sparticles and specific decays. In this way, the [MSSM](#) parameter-space is highly reduced, leaving just a few parameters to be tested by the experiment.

The simplified models considered in this thesis are the production of the lightest chargino $\tilde{\chi}_1^\pm$ and the next-to-lightest neutralino $\tilde{\chi}_2^0$. The simplified models considered assume decays into the [LSP](#) $\tilde{\chi}_1^0$ mediated by [SM](#) bosons. In the following, the $\tilde{\chi}_1^\pm$ and $\tilde{\chi}_2^0$ are assumed to be mostly winos, while the [LSP](#) $\tilde{\chi}_1^0$ is assumed bino-like. Various values of $\tan\beta$ lead to mass degenerate $\tilde{\chi}_1^\pm$ and $\tilde{\chi}_2^0$, according to the mixings in Equation 2.25 and 2.26. Further details on the chosen simplified models are discussed in what follows.

$\tilde{\chi}_1^\pm \tilde{\chi}_2^0$ decays via W and Z bosons

The first set of simplified models considered for analysis here assume $\tilde{\chi}_1^\pm$ and $\tilde{\chi}_2^0$ decays via intermediate gauge bosons W and Z , with 100% branching ratios for the $\tilde{\chi}_1^\pm \rightarrow W^\pm \tilde{\chi}_1^0$ and $\tilde{\chi}_2^0 \rightarrow Z \tilde{\chi}_1^0$ decays, followed by further decays of the Z and W bosons, according to the SM branching ratios. The corresponding diagram is shown in Figure 2.13. The simplified models permit a direct test of the masses M_1 and M_2 and of the gauge couplings of the gauginos to the gauge bosons. In what follows, this family of simplified models will be referred to as the “ WZ models”.

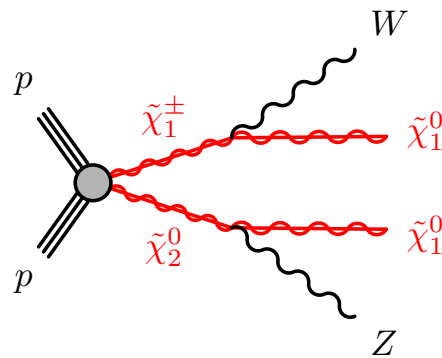


Figure 2.13: Diagram for the production of chargino and neutralino, with decays via W and Z bosons.

$\tilde{\chi}_1^\pm \tilde{\chi}_2^0$ decays via W and h bosons

This other set of simplified models model assumes $\tilde{\chi}_1^\pm$ and $\tilde{\chi}_2^0$ decays, still with a 100% branching ratio, via intermediate W boson and the lightest MSSM Higgs boson h , assumed to be SM-like with a mass of 125 GeV. The decays $\tilde{\chi}_1^\pm \rightarrow W^\pm \tilde{\chi}_1^0$ and $\tilde{\chi}_2^0 \rightarrow h \tilde{\chi}_1^0$ are followed by decays of the W and the h bosons, regulated by the usual SM branching ratios. The corresponding diagram of these models is shown in Figure 2.14. As in the case of decays via WZ bosons, these simplified models allow the exploration of mass parameters of bino M_1 and winos M_2 . Furthermore, the decay via W and h allows a direct test of the Higgs-higgsino-gaugino coupling. In what follows, these simplified models will be referred to as “ Wh models”.

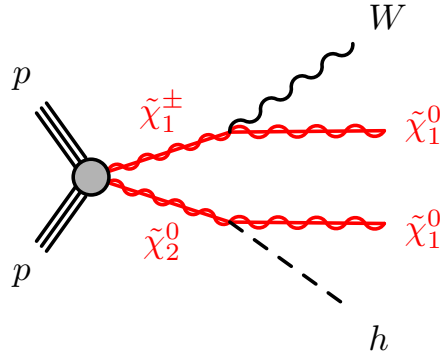


Figure 2.14: Diagram for the production of chargino and neutralino, with decays via W bosons and the Higgs boson h .

2.3 Electroweak SUSY searches

As mentioned in Section 2.2.2.1, the production of charginos and neutralinos becomes dominant at LHC if the masses of the gauginos and sleptons are of the order $O(100 \text{ GeV})$ and squarks and gluinos are heavier than 1 TeV. This is suggested by several experimental results, as discussed in the following.

Searches for the top-squark \tilde{t}_1 have been performed by the ATLAS [38, 39] and CMS [40, 41] collaborations, using proton-proton collision data collected between the years 2009 and 2012 at $\sqrt{s} = 8 \text{ TeV}$ and between the years 2015 and 2018 at $\sqrt{s} = 13 \text{ TeV}$ at the LHC. A summary of the results from the ATLAS collaboration, as of May 2020, is shown in Figure 2.15. These searches consider the $\tilde{t}_1 \rightarrow t\tilde{\chi}_1^0$ decay, and the top-squark masses of up to 1 TeV (for a massless LSP) are excluded at 95% CL.

Searches for the direct gluino production at proton-proton collisions were performed by the ATLAS [43] and CMS [44] collaborations. A summary of results from the ATLAS collaboration, also as of May 2020, is shown in Figure 2.16, for the total 2009-2018 dataset at $\sqrt{s} = 8 \text{ TeV}$ and $\sqrt{s} = 13 \text{ TeV}$. Limits are obtained assuming simplified models in which $\tilde{g} \rightarrow t\bar{t}\tilde{\chi}_1^0$. The searches exclude values of the mass of the gluino up to 2.2 TeV for massless LSP.

In summary, the current observed exclusion limits predict heavy \tilde{t}_1 and gluinos, with masses greater as large as 1 TeV or more. Therefore, searches for electroweak production of sparticles are strongly motivated.

Direct searches for sleptons and searches for charginos and neutralinos decaying

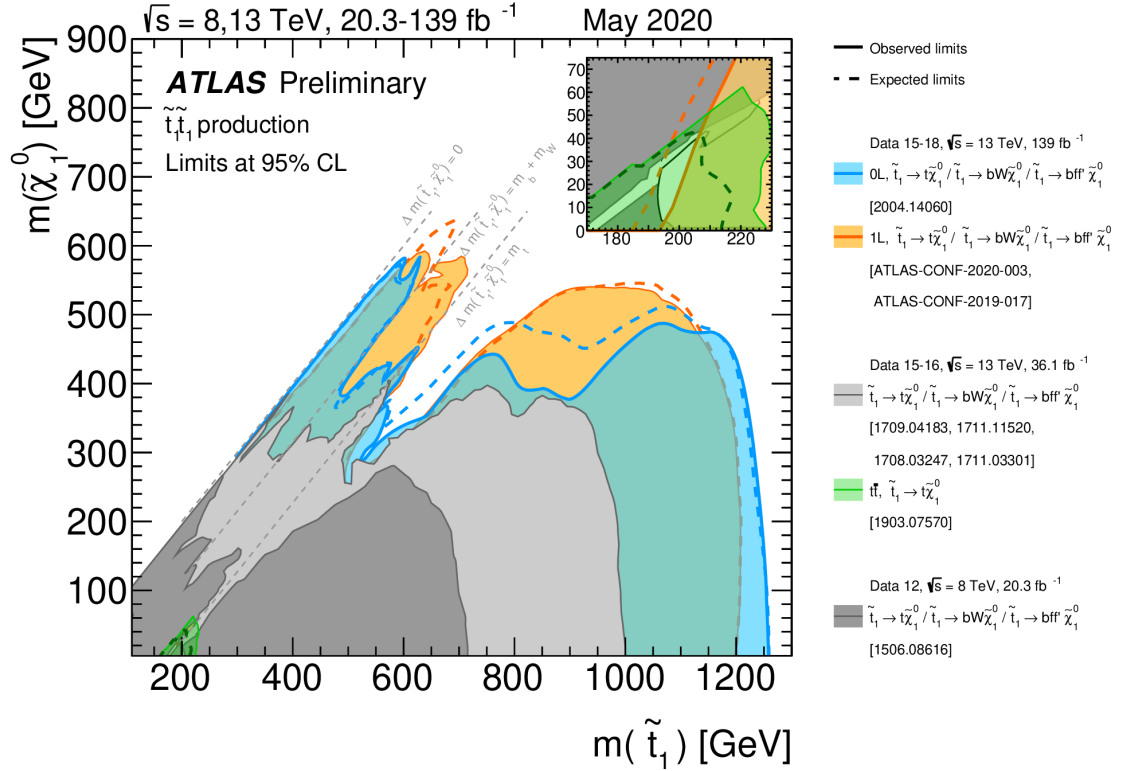


Figure 2.15: Observed and expected exclusion limits on the mass of the top-squark. The dataset corresponds to 20.3 fb^{-1} data at $\sqrt{s} = 8 \text{ TeV}$ and 139 fb^{-1} data at $\sqrt{s} = 13 \text{ TeV}$ in proton-proton collisions at the LHC, recorded by the ATLAS experiment. Limits are set at the 95% of confidence level. [42]

via sleptons have been explored by the ATLAS [45] and the CMS [46] collaborations. Current limits (as of May 2020) on the masses of sleptons are set by the searches for direct production of sleptons with data of proton-proton collision at $\sqrt{s} = 13 \text{ TeV}$ by the ATLAS experiment. The corresponding exclusion limits are shown in Figure 2.17. Under the assumed decay of sleptons into two leptons and two $\tilde{\chi}_1^0$, ATLAS excludes slepton masses up to approximately 700 GeV (for a massless LSP). Searches for direct production of tau-sleptons have also been performed [47, 48], providing exclusion limits on the mass of the tau-slepton up to 400 GeV.

In addition, searches for $\tilde{\chi}_1^\pm \tilde{\chi}_2^0$ decaying via intermediate sleptons have been performed by the ATLAS [49, 50] and the CMS [51, 52] collaborations. A summary of the results from the ATLAS collaboration, as of July 2019, prior to the work performed in this thesis, is shown in Figure 2.18, where results from analyses of data of proton-proton collisions at $\sqrt{s} = 8 \text{ TeV}$ and $\sqrt{s} = 13 \text{ TeV}$ are included. Such limits exclude masses for the $\tilde{\chi}_1^\pm \tilde{\chi}_2^0$ decaying via sleptons up to 1.1 TeV.

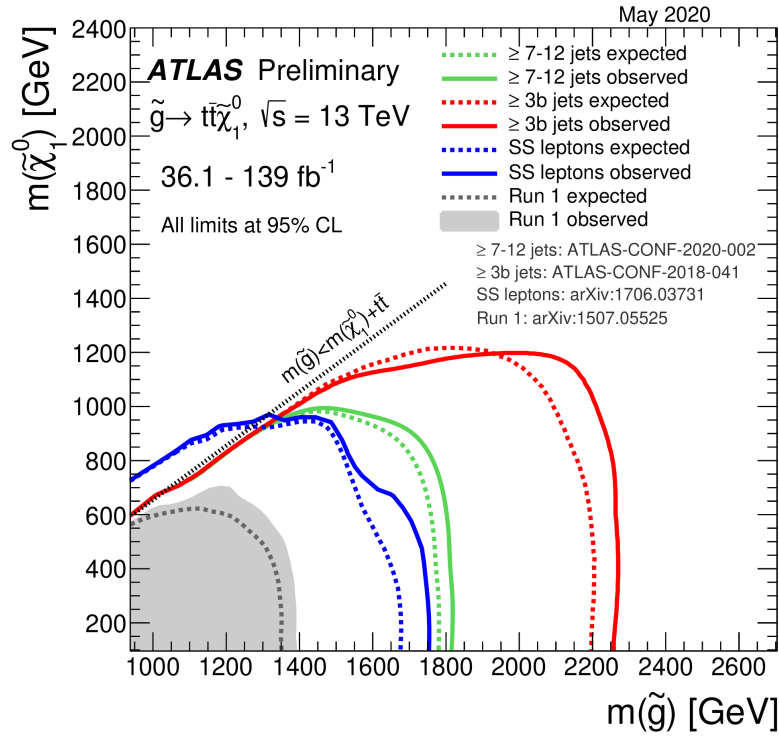


Figure 2.16: Observed and expected exclusion limits on the masses of the gluino. The dataset corresponds to 20.3 fb^{-1} data at $\sqrt{s} = 8 \text{ TeV}$ and 139 fb^{-1} data at $\sqrt{s} = 13 \text{ TeV}$ in proton-proton collisions at the LHC, recorded by the ATLAS experiment. Limits are set at the 95% of confidence level. [42]

2.3.1 State of art of three-lepton searches for $\tilde{\chi}_1^\pm \tilde{\chi}_2^0$ via WZ/Wh bosons

Limits prior to work presented in this thesis on the masses of the sleptons and on the decay of $\tilde{\chi}_1^\pm \tilde{\chi}_2^0$ via sleptons motivate the focus on the searches for $\tilde{\chi}_1^\pm \tilde{\chi}_2^0$ via intermediate bosons. As a reminder, decays mediated by SM bosons are expected to become dominant for heavy sleptons. In what follows, results of searches for simplified models for the decays of $\tilde{\chi}_1^\pm$ and $\tilde{\chi}_2^0$ via intermediate SM bosons are discussed, which set the scene to the searches described in this thesis. Emphasis is given to the channel where the SM bosons decay into light leptons (electrons and muons).

Simplified models for $\tilde{\chi}_1^\pm$ and $\tilde{\chi}_2^0$ decaying via intermediate SM bosons had been explored by the ATLAS and CMS collaborations with 8-TeV proton-proton collision [53, 54], and with proton-proton collision data at $\sqrt{s} = 13 \text{ TeV}$ collected during the years 2015 and 2016 [50, 52]. The observed and expected exclusion limits shown in Figure 2.19 are for the Wh models as provided by the ATLAS collaboration with data at

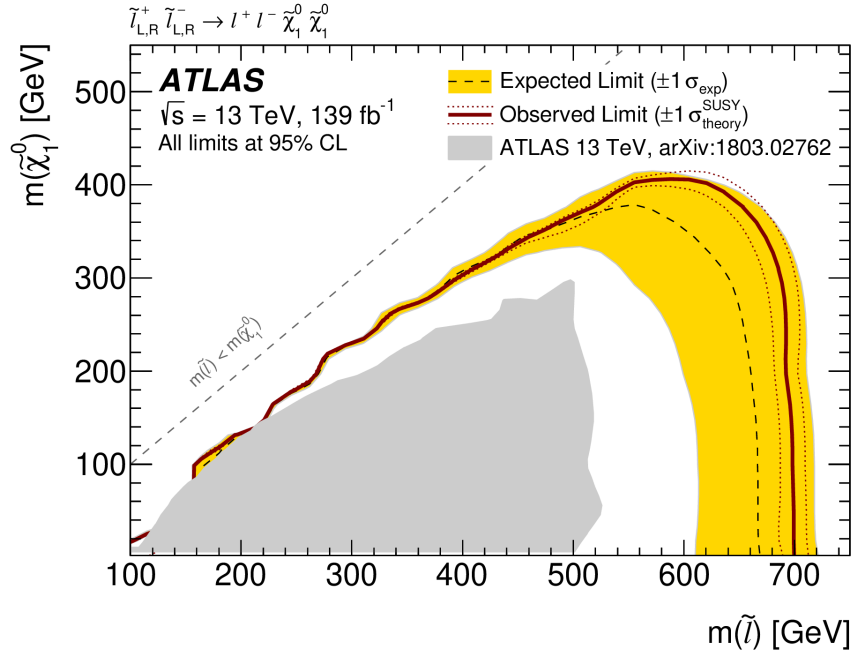


Figure 2.17: Observed and expected exclusion limits on the masses of sleptons. The dataset corresponds to 139 fb^{-1} data at $\sqrt{s} = 13 \text{ TeV}$ in proton-proton collisions at the LHC, recorded by the ATLAS experiment. Limits are set at the 95% of confidence level. [45]

$\sqrt{s} = 8 \text{ TeV}$ [53]. Exclusion limits were obtained by a statistical combination of three channels: three light leptons (electrons and muons), one hadronically-decaying τ plus two light leptons and two hadronically-decaying τ plus one light lepton in the final states. The analysis excludes mass values up to approximately $m_{\tilde{\chi}_2^0, \tilde{\chi}_1^\pm} = 150 \text{ GeV}$.

In Figure 2.20, the results of the search for $\tilde{\chi}_1^\pm \tilde{\chi}_2^0$ production via WZ model by the ATLAS collaboration are presented. The analyses targeted proton-proton collision data at $\sqrt{s} = 13 \text{ TeV}$ collected during the years 2015 and 2016 [50]. The observed and exclusion limits are shown as a statistical combination of the three lepton and two lepton channels. The results excluded masses up to approximately $m_{\tilde{\chi}_2^0, \tilde{\chi}_1^\pm} = 575 \text{ GeV}$.

A similar analysis was performed by the CMS collaboration [52]. The searches targeted proton-proton collision data collected at $\sqrt{s} = 13 \text{ TeV}$ during the years 2015 and 2016. A summary of the observed and expected exclusion limits as CMS are shown in Figure 2.21. For the Wh models, channels with one lepton plus two photons, two leptons and at least three leptons in the final states were considered. For the WZ model, channels with two leptons and three leptons in the final states were considered. Masses of $\tilde{\chi}_1^\pm \tilde{\chi}_2^0$ up to 500 GeV and 600 GeV were excluded, for the Wh and WZ models,

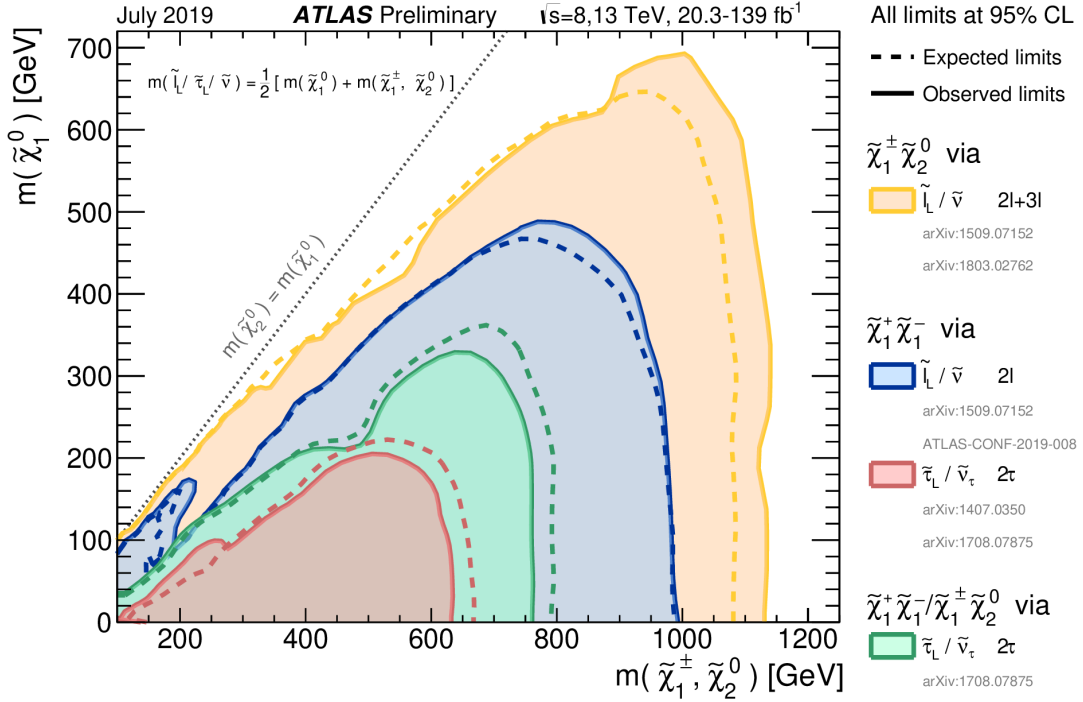


Figure 2.18: Observed and expected exclusion limits on the masses of charginos and neutralinos decaying via intermediate sleptons. The proton-proton collision data was recorded by the ATLAS experiment at $\sqrt{s} = 8$ TeV and $\sqrt{s} = 13$ TeV. All the limits but those for the $\tilde{\chi}_1^\pm \tilde{\chi}_2^0$ production are obtained by targeting channels with two leptons in the final states. Searches for $\tilde{\chi}_1^\pm \tilde{\chi}_2^0$ are presented as a combination of the three light lepton and two lepton channels. Limits are set at the 95% of confidence level. [42]

respectively.

Finally, results of searches for $\tilde{\chi}_1^\pm \tilde{\chi}_2^0$ decaying via intermediate SM bosons by the ATLAS experiment as of 2019, prior to publication of work presented in this thesis, are presented in Figure 2.22. In the plot, results for the WZ and Wh simplified models for the production of $\tilde{\chi}_1^\pm \tilde{\chi}_2^0$ are shown, along with a third model which assumes the production of $\tilde{\chi}_1^+ \tilde{\chi}_1^-$ decaying via two W bosons.

For the WZ models, the early Run-2 exclusion limits were obtained as a combination of results from the two lepton and three lepton channels. For the Wh models, channels with one lepton plus two b -jets and one leptons plus two photons had been considered for the overall combined exclusion limits. In both cases, searches showed good sensitivity at high values of the $\tilde{\chi}_1^\pm \tilde{\chi}_2^0$ mass, although with clear room for improvement, especially close to the kinematic edges where the intermediate bosons are on-shell.

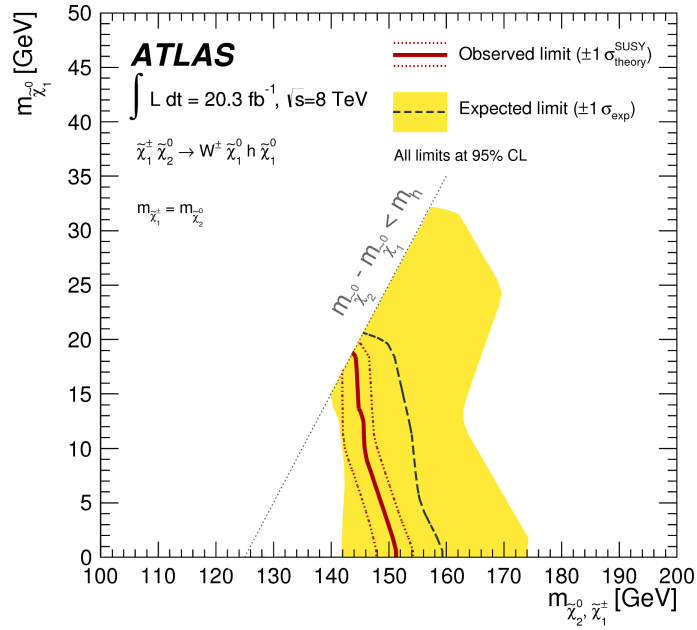


Figure 2.19: Observed and expected exclusion limits on the masses of $\tilde{\chi}_1^\pm$ and $\tilde{\chi}_2^0$ and $\tilde{\chi}_1^0$ for the Wh models. The dataset corresponds to 20.3 fb^{-1} data collected at $\sqrt{s} = 8 \text{ TeV}$ proton-proton collisions by the ATLAS experiment. Exclusion limits are obtained through a combination of channels with three light leptons, one leptonic τ and two light leptons and two leptonic τ and a light lepton. Limits are set at the 95% of confidence level. [53]

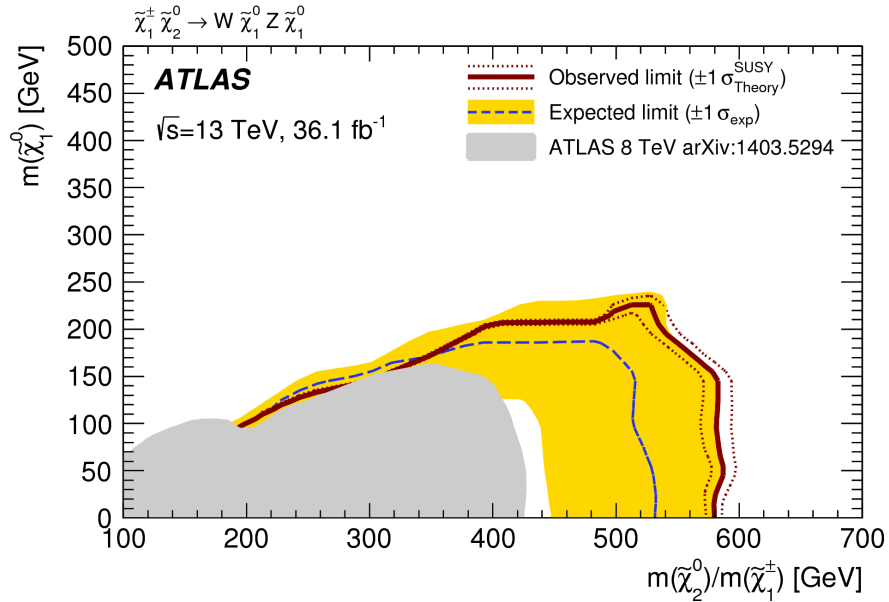


Figure 2.20: Observed and expected exclusion limits on the masses of $\tilde{\chi}_1^\pm$ and $\tilde{\chi}_2^0$ and $\tilde{\chi}_1^0$ for the WZ model. The dataset corresponds to 36.1 fb^{-1} of proton-proton collision data collected at $\sqrt{s} = 13 \text{ TeV}$ by the ATLAS experiment. Exclusion limits are obtained by combining the three-lepton and two-lepton channels. All limits are set at the 95% of confidence level. [50]

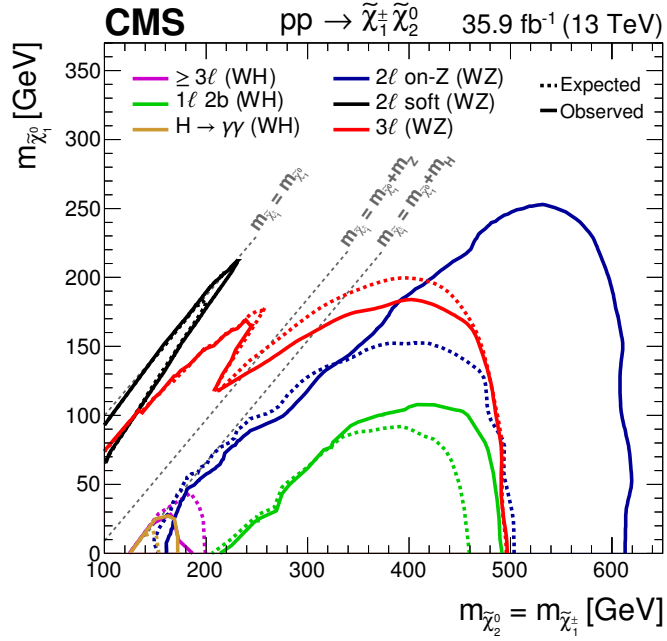


Figure 2.21: Observed and expected exclusion limits on the masses of $\tilde{\chi}_1^\pm$ and $\tilde{\chi}_2^0$ and $\tilde{\chi}_1^0$ for the Wh and the WZ models. The dataset corresponds to 35.9 fb^{-1} of proton-proton collision data collected at $\sqrt{s} = 13 \text{ TeV}$ by the CMS experiment. Exclusion limits are shown for channels with one lepton plus photons, the two leptons and at least three leptons in the final states, and the two-lepton and three-lepton channels, for the Wh and the WZ models, respectively. All limits are set at the 95% of confidence level. [52]

In this context, the three lepton channel can be particularly interesting to explore, since, as will be discussed, it can give access to regions of the parameter space not easily accessible by other channels.

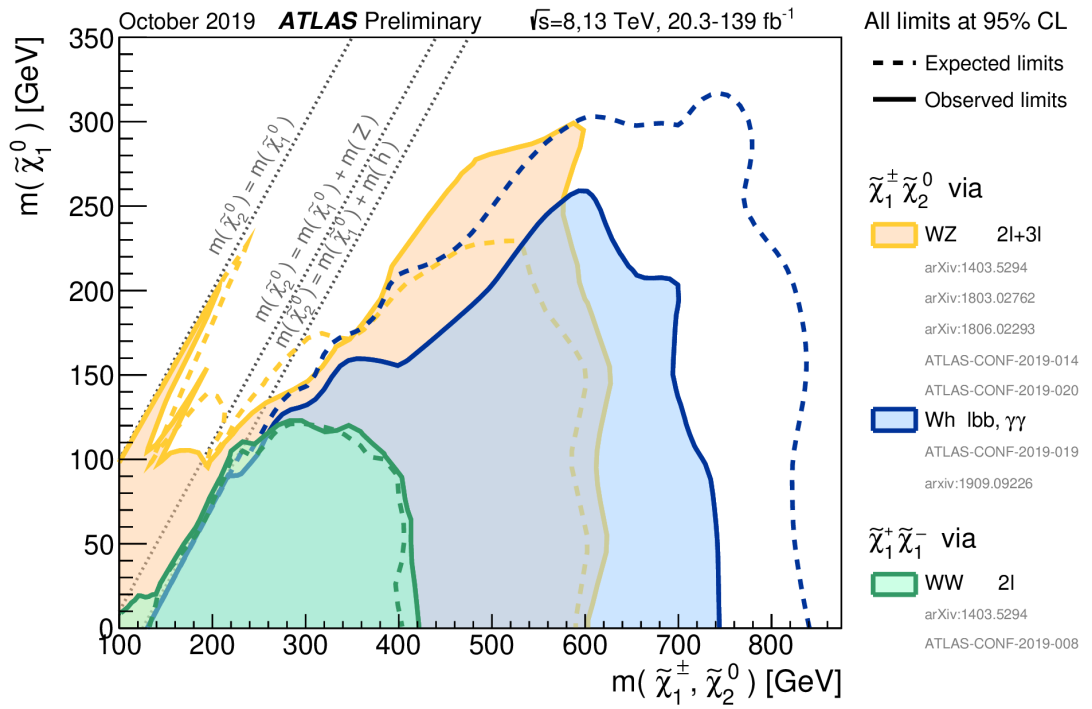


Figure 2.22: Summary of observed and exclusion limits on the masses of $\tilde{\chi}_1^\pm$ and $\tilde{\chi}_2^0$ and $\tilde{\chi}_1^0$ for the WZ , Wh and WW models. The datasets correspond to 36.1 fb^{-1} data collected in 13-TeV proton-proton collisions at the LHC by the ATLAS experiment. Limits are obtained by combining the three-lepton and two-lepton channels. Limits are set at the 95% of confidence level. [42]

3

THE ATLAS DETECTOR AT THE LARGE HADRON COLLIDER

This chapter describes the experimental setup of the [LHC](#) and the ATLAS detector, which have been used to collect the data used in this thesis.

3.1 The Large Hadron Collider

Over the past few decades, colliders have been used to explore new physics frontiers and perform precision measurements of known [SM](#) physics processes, playing a crucial role in the development of experimental particle physics. The [LHC](#) [55] is the most powerful circular particle accelerator ever constructed. It collides high-energy protons and, during special runs, heavy ions. It is located at the European Organization for Nuclear Research ([CERN](#)), across the French-Swiss border, near Geneva, between 75-140 m underground, on an inclined plane with respect to the ground level.

The [LHC](#) is composed of two 26.7-km rings in which particles are accelerated and made to travel along two opposite-direction circular beams. It accelerates approximately 2800 bunches of 10^{11} of protons per beam, with the bunches crossing every 25 ns. The accelerator is structured as a succession of arcs and straight segments, along which Radio-frequency ([RF](#)) elements are used for the acceleration, cleaning, injection and dumping of the beams. Series of dipoles and quadrupoles are used for the bending and the focusing of the beams. The 1232 cryostat dipoles used at the [LHC](#) operate in a superconducting regime, at a temperature of 1.9 K, and reach magnetic fields of 8.33 T.

So far, collisions at the LHC have been collected over two main data-taking periods, referred to as Run 1 (2010-2011, at 7 TeV; 2012, at 8 TeV) and Run 2 (2015-2018, at 13 TeV). They were interrupted by two long shutdown (LS) periods, during which planned upgrades and maintenance works were, or are being performed on the accelerators and the experiments. The first long shutdown (LS1) took place between 2012 and 2015, while the second long shutdown (LS2) is still in progress, with the machine expected to come back in full operation in 2021 for the start of the Run 3 data-taking period.

3.1.1 The acceleration complex

Protons used in the LHC are brought to the required energy in a sequence of accelerators, of which the LHC is the last step. In the first stage, the protons obtained from the ionisation of hydrogen atoms are accelerated by LINAC2, a linear RF acceleration system that feeds the protons into the Proton Synchrotron Booster (PSB), where they reach the energy of 1.4 GeV. In the next step, the Proton Synchrotron (PS) accelerates the protons to an energy of 25 GeV, before they are injected into the Super Proton Synchrotron (SPS), a 7-km circular accelerator that brings the protons to an energy of 450 GeV. Finally, protons are injected into the LHC where they reach the final energy of, currently, 6.5 TeV per beam. Schematics of the CERN acceleration complex is shown in Figure 3.1.

3.1.2 The LHC parameters

Together with its centre of mass energy, the luminosity \mathcal{L} is one of the parameters that describe the LHC performance. Its value is fixed by the technical characteristics of the collider. It is given by:

$$\mathcal{L} = \frac{N_1 N_2 f}{4\pi\sigma_x\sigma_y}, \quad (3.1)$$

where N_1 and N_2 are the number of particles in beams 1 and 2, respectively, f is the revolution frequency, and the σ_x and σ_y are the horizontal and vertical widths of the two beams.

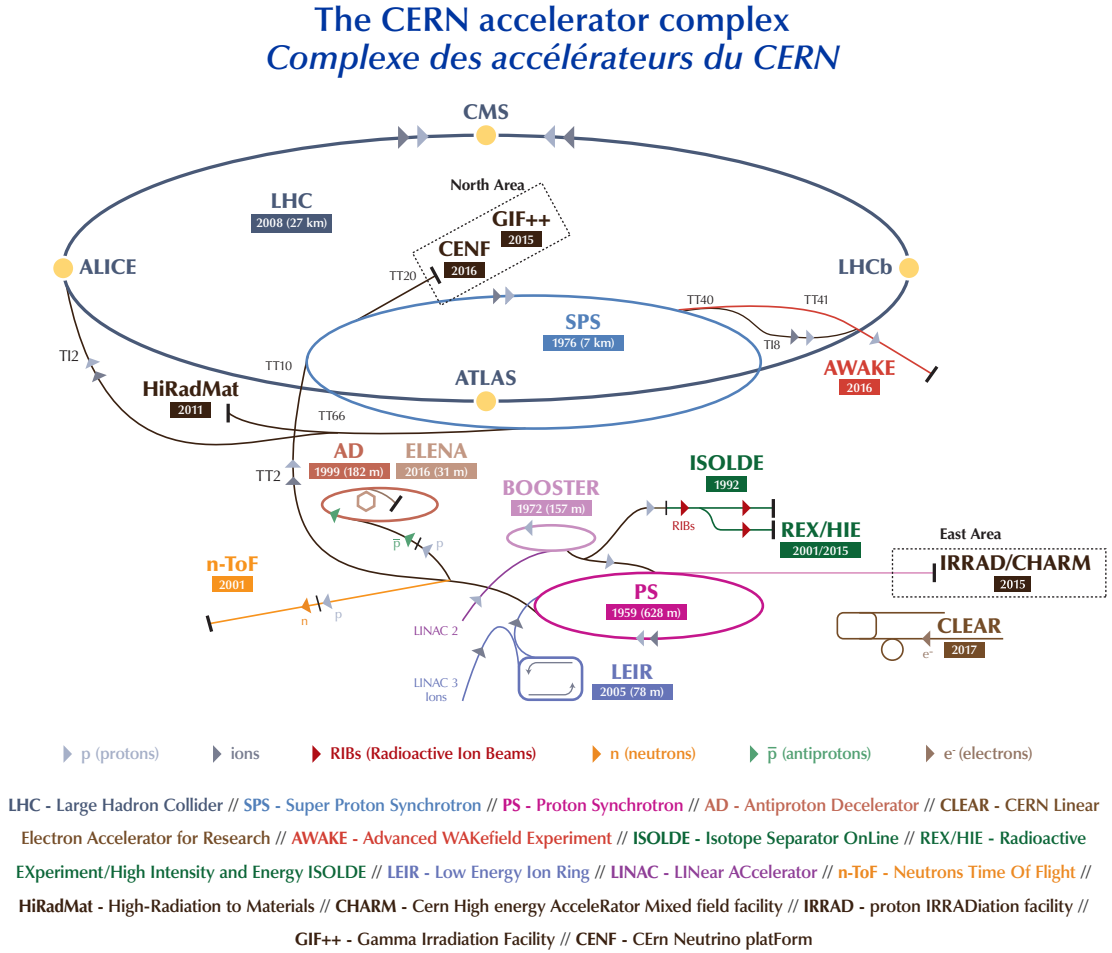


Figure 3.1: A schematic view of the CERN acceleration complex. [56]

The luminosity \mathcal{L} typically depends on time t and is connected the production rate $R(t)$ of a given process of cross section σ [57] as follows:

$$R(t) = \sigma \cdot \mathcal{L}(t). \quad (3.2)$$

Equation 3.2 serves as a definition of the instantaneous luminosity $\mathcal{L}(t)$. In 2018, the LHC set a record instantaneous luminosity peak of $2 \cdot 10^{34} \text{ cm}^{-2} \text{ s}^{-1}$ [58].

3.1.3 The LHC detectors

Four main experiments (plus other smaller ones, not mentioned here) are located along the LHC circumference. ATLAS (A Toroidal LHC Apparatus) [59] and CMS (Compact Muon Solenoid) [60] are general-purpose experiments whose physics programmes span a vast range of topics, from SM precision measurements to searches for BSM physics.

The LHCb (LHC-beauty) [61] physics programme focuses especially on measuring the properties of the B-mesons and their decays, to investigate CP violation and search for BSM physics in rare decays. ALICE (A Large Ion Collider Experiment) [62] is dedicated to the study of heavy ions collisions, focusing on the study of the quark-gluon plasma state of matter.

Cumulative integrated luminosity measured by the ATLAS experiment is shown in Figure 3.2 for the different years of data taking in Run 1 and Run 2. For the ATLAS experiment, luminosity measurements are obtained by the use of the Cherenkov radiation detector LUCID-2 [63]. LUCID-2 is composed of two modules, located on the LHC beam pipe, at equal distance from the ATLAS detector. Each module counts sixteen photomultipliers, arranged around the beam pipe and used as event counter detectors. The photomultipliers are provided with a thin quartz window, which serves as medium for the Cherenkov radiation emission. A dedicated algorithm is used to compute the integrated luminosity as a function of the counted events [64].

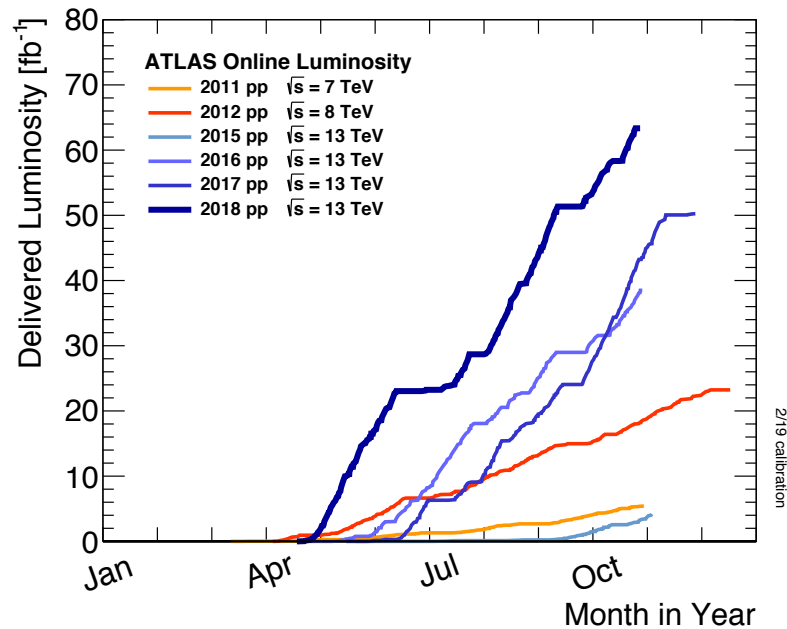


Figure 3.2: Cumulative integrated luminosity delivered to the ATLAS experiment during the data taking years in Run 1 and Run 2, as measured by the LUCID2 detector. [65]

3.2 The ATLAS detector

The ATLAS detector uses several techniques for the reconstruction and identification of different particles, including through fast detection and readout of signals, for rapid processing of the collision data. The granularity of sub-detectors is adequate for precise determination of event topology and the reconstruction of the key kinematic variables.

The ATLAS detector has a cylindrical symmetric geometry. The detector is 44-m long, with a height of 25 m and near-full 4π coverage. A schematic view of the detector is shown in Figure 3.3.

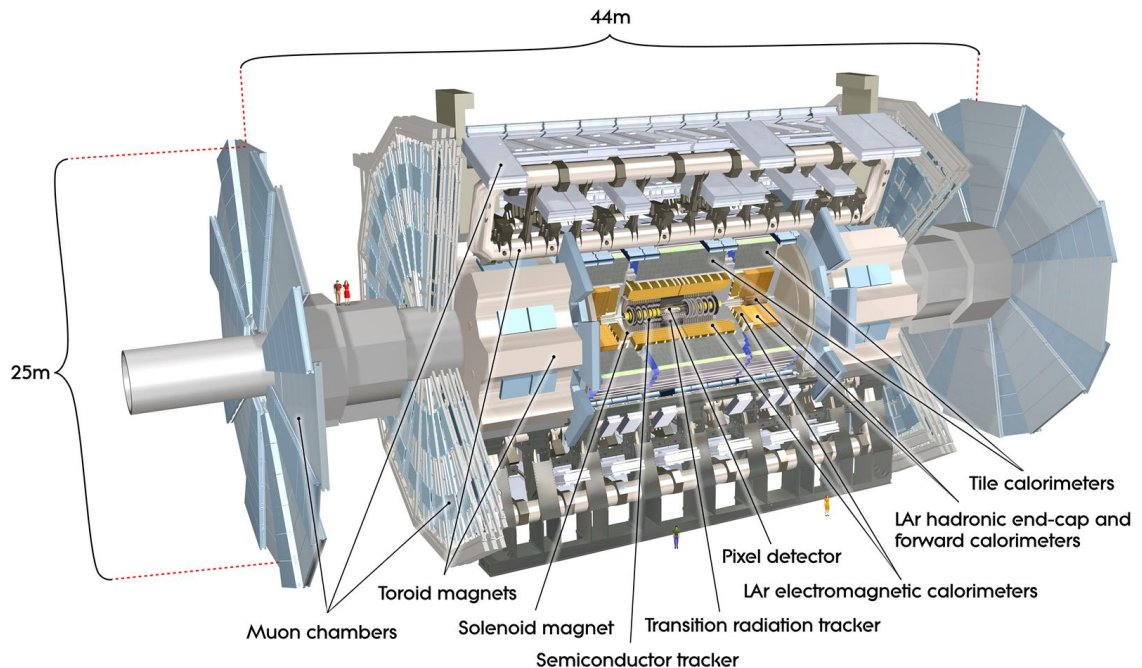


Figure 3.3: A schematic view of the main components of the ATLAS detector. [59]

Each of the sub-detectors is arranged in a coaxial cylindrical geometry around the beam-pipe, in the *barrel* region, or “closes” the cylinder at the two ends, in the so-called *end-cap* regions.

Overall, in Run 2 the data recording efficiency of the ATLAS detector was of approximately 94% of the integrated luminosity delivered by the LHC. This is shown in Figure 3.4.

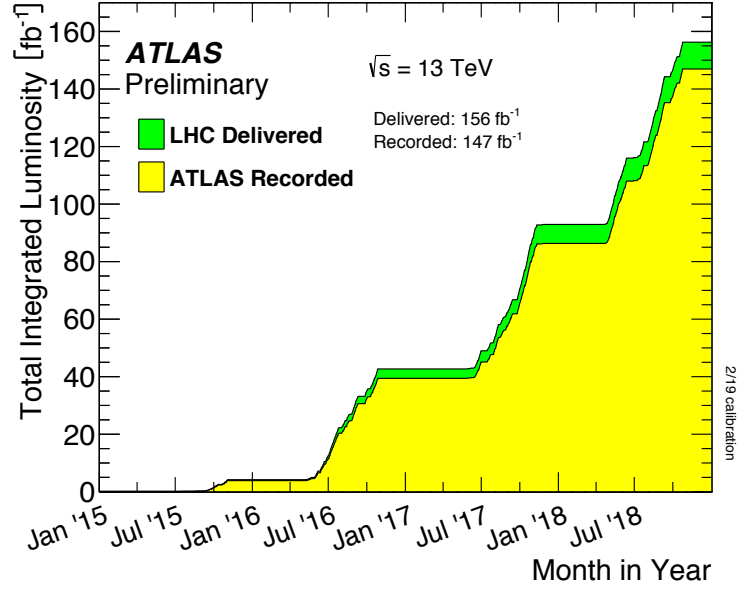


Figure 3.4: Delivered and recorded luminosity as measured by the ATLAS experiment during the LHC Run-2. [65]

3.2.1 The ATLAS coordinate system and some key variables

The origin of the coordinate system used by the ATLAS experiment coincides with the collision point at the centre of the detector, with the x axis pointing towards the centre of the LHC, the y axis pointing upwards and the z axis parallel to the beam in the anticlockwise direction. The azimuthal angle ϕ spans the $[0, 2\pi]$ range around the z axis, while the polar angle θ is measured from the positive direction of the z axis. The xy plane is referred to as the *transverse plane*. The transverse momentum is defined as:

$$p_T = \sqrt{p_x^2 + p_y^2}, \quad (3.3)$$

where p_x and p_y are the components of the momentum vector along the x and y axes of the ATLAS reference frame. The longitudinal component of the momentum, along the beam pipe direction, is p_z . Rapidity is defined as:

$$y = \frac{1}{2} \ln \left(\frac{E + p_z}{E - p_z} \right). \quad (3.4)$$

Rapidity differences Δy are Lorentz-invariant. For ultra-relativistic particles ($E \gg m$), such as it is usually the case for particles produced in LHC collisions, rapidity is well

approximated by the *pseudo-rapidity*,

$$\eta = -\ln\left(\tan\frac{\theta}{2}\right), \quad (3.5)$$

which for massless particles maintains the Lorentz-invariant properties of the rapidity.

Sometimes the angular distance between reconstructed objects is used, defined as

$$\Delta R = \sqrt{(\Delta\eta)^2 + (\Delta\phi)^2}. \quad (3.6)$$

Fundamental collisions occur within partons which compose the protons, as will be further discussed in Section 4.2. Therefore, the actual total energy at which the collisions occur is unknown. Nevertheless, conservation of momentum can be applied to the transverse momentum components of detected objects. Neglecting any small p_T component in the initial state, the missing transverse momentum is thus defined as:

$$\vec{p}_T^{\text{miss}} = - \sum_{i \in \text{visible}} \vec{p}_T^i, \quad (3.7)$$

where the index i runs over the visible particles reconstructed in the detector. The missing transverse energy E_T^{miss} is the magnitude of the missing momentum vector, i.e. $E_T^{\text{miss}} = |\vec{p}_T^{\text{miss}}|$.

3.2.2 The magnet system

The ATLAS magnet system plays a crucial role in the detection of charged particles. It is composed of four superconducting magnets and, like the detector, has a cylindrical geometry. The system is 26-m long and has a diameter of 22 m. A solenoid provides a longitudinal magnetic field of up to 2 T in the the inner detector volume. Additionally, a system of toroids spans the region occupied by the muon spectrometer, one in the barrel ($|\eta| < 1.4$) and two in the end-cap ($1.6 < |\eta| < 2.7$). The barrel and end-cap toroids provide a magnetic field of approximately 0.5 T and 1 T, respectively, while in the transition region ($1.4 < |\eta| < 1.6$) the magnetic field is a combination of the fields coming from the barrel and the end-cap toroids. A schematic representation of the ATLAS magnetic system is shown in Figure 3.5.

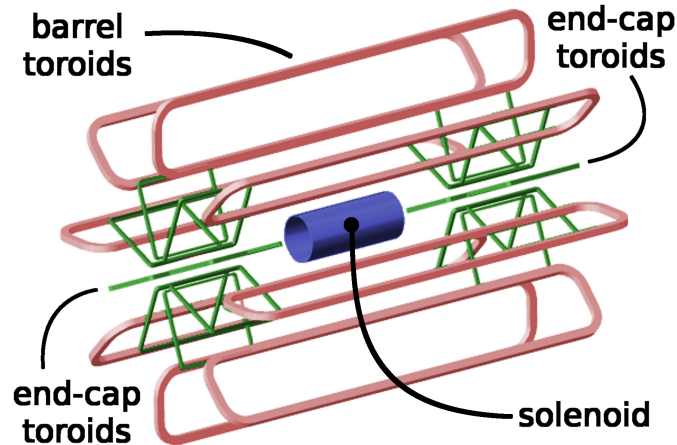


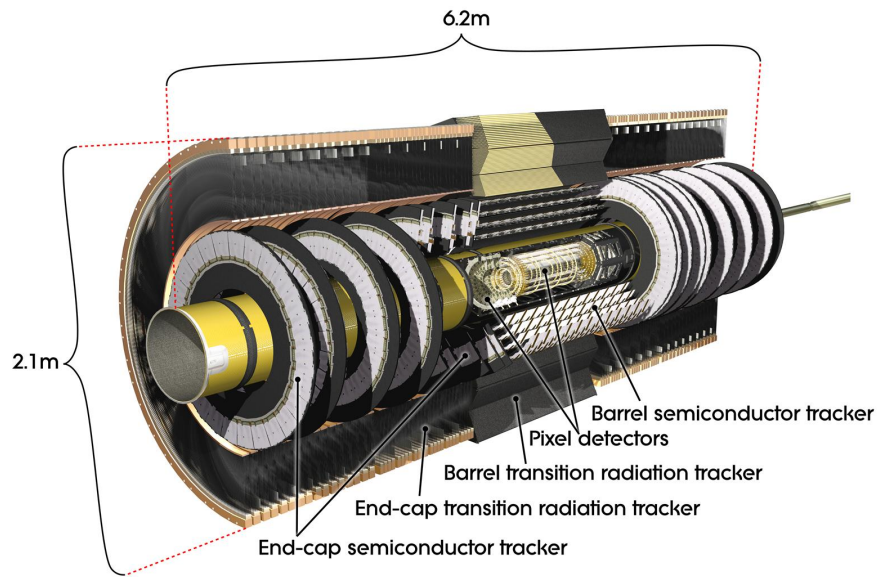
Figure 3.5: Schematic view of the magnet system of the ATLAS detector. [66]

3.2.3 The Inner Detector

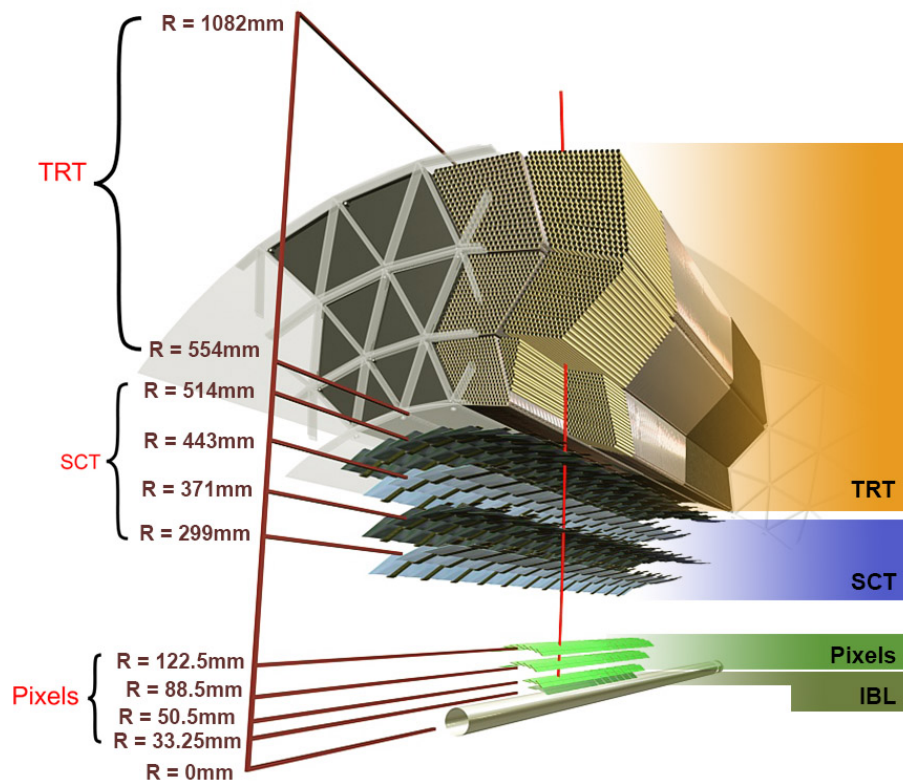
The innermost part of the ATLAS detector is occupied by the Inner Detector (**ID**), whose function is to reconstruct tracks of charged particles inside the solenoidal magnetic field. The **ID** is composed by three different parts. Just outside the beam-pipe, three layers of pixel detectors allow the fast reconstruction of vertices and tracks. The pixel detector is followed by the Semiconductor Tracker (**SCT**), comprising double-layer silicon strips, and finally by the Transition Radiation Tracker (**TRT**), which uses straw-shaped gas detection technology for the reconstruction of charged particles trajectories, based on the electromagnetic radiation emitted by particles when transitioning between two different media of different dielectric constants. The ATLAS **ID** provides precise measurements of the p_T of particles, for pseudorapidities covering $|\eta| < 2.5$. A sketch of the ATLAS **ID** is shown in Figure 3.6. More details on the individual **ID** components are given below.

3.2.3.1 Silicon Pixel Detector

The pixel detector comprises three barrel pixel layers and three pixel disks in the end-cap, for a total of 1456 modules in the barrel and 288 in the end-cap. Each pixel has a size of approximately $50 \times 400 \mu\text{m}^2$, providing the necessary granularity to distinguish vertices and track with a resolution of $10 \times 115 \mu\text{m}^2$. During **LS1**, an Insertable B-Layer (**IBL**) was added at a radius of 3.2 cm from the beam-pipe, providing a fourth pixel layer [68], in order to improve the precision of vertex reconstruction.



(a) Schematic view of the inner detector of the ATLAS detector. [59]



(b) Transverse view of the ATLAS inner detector, showing the position of the barrel modules. [67]

Figure 3.6: Digital-graphic representation of the ATLAS tracker detector.

3.2.3.2 Semiconductor Tracker

The ATLAS SCT is made of 60 m^2 of semiconductor material, arranged into four double-sided layers of silicon strips in the barrel, comprising 2112 modules, and nine double-sided layers in the end-cap, corresponding to additional 1976 modules. The strips have a width of about $80 \mu\text{m}$, allowing a position reconstruction of charged track with an accuracy of around $17 \mu\text{m}$.

3.2.3.3 Transition Radiation Tracker

The TRT is the outermost component of the ATLAS ID. Unlike the pixel detector and the SCT, the TRT is a gas detector, which uses layers of 4-mm diameter straw tubes, filled with $\text{Xe}(70\%)\text{CO}_2(27\%)\text{O}_2(3\%)$ gas. The straw tubes are surrounded by polypropylene, so that a particle would emit transition radiation when crossing a straw tube. The emission of transition radiation can in principle be used for the discrimination of electrons from heavier particles such as pions. In the barrel, 50000 straw tubes of 144-cm diameter are arranged along the direction parallel to the beam pipe. In the end-caps, 250000 straw tubes of 39-cm diameter are arranged on a wheel structure. On its own, the TRT measures particle tracks with a resolution of approximately $130 \mu\text{m}$.

3.2.4 The calorimetry system

The calorimeters allow the measurement of the energy of particles crossing the detector. A particle entering the calorimeters interacts with its active material. Two different calorimeters form the calorimetry system of the ATLAS detector: the Electromagnetic Calorimeter (ECal) and the Hadronic Calorimeter (HCal), with coverage up to $|\eta| < 4.9$, as shown schematically in Figure 3.7. The ATLAS detector exploits two different technologies to achieve good energy resolution, one based on Liquid Argon (LAr), for the ECal barrel calorimeter and end-cap calorimeters, and a steel sampling Tile Calorimeter (TileCal) for the HCal barrel.

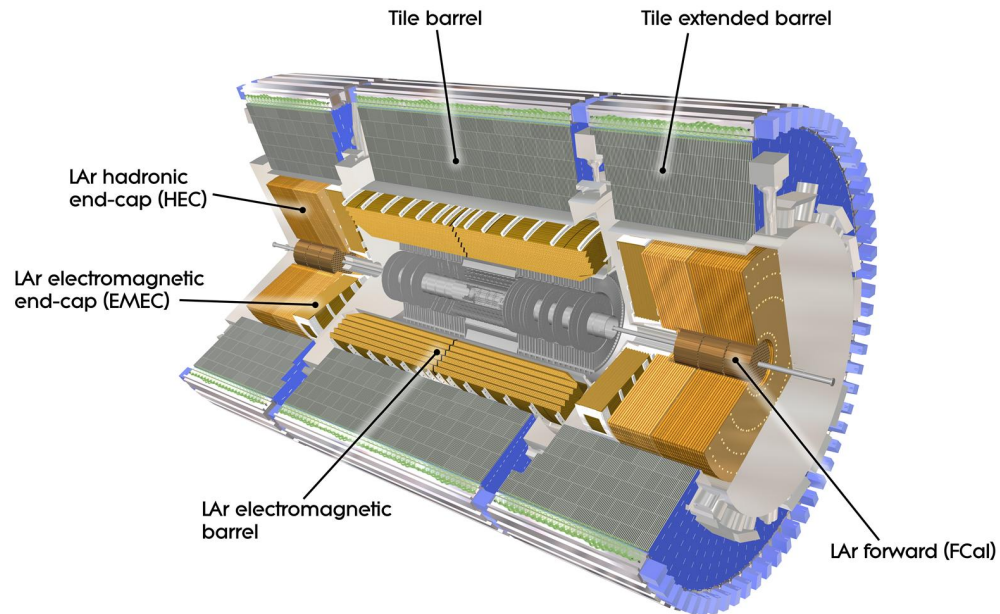


Figure 3.7: Schematic view of the calorimetry system of the ATLAS detector. [59]

3.2.4.1 The Electromagnetic Calorimeter

The region just outside the solenoid is occupied by the LAr electromagnetic calorimeter, which comprises a barrel and Electromagnetic End-cap Calorimeter (EMEC) components. It is composed by lead and LAr in a cryostat as passive-absorber material and active material, respectively. The barrel detector is divided into two parts, with a 4-mm gap at $\eta=0$, and covers a range of pseudorapidity up to $|\eta| < 1.475$. The modules in the barrel are split into three different layers, with changing segmentation, according to the $|\eta|$ area covered, to improve resolution. Components of the calorimetry layers are arranged in towers, defined as regions in $\Delta\eta \times \Delta\phi$. A sketch of the setup of the barrel modules of the ECal is shown in Figure 3.8.

The ECal end-cap is composed by two coaxial wheels, the inner one covering $2.5 < |\eta| < 3.2$ and the outer one spanning the region $1.375 < |\eta| < 2.5$. In terms of thickness, the barrel lead-LAr calorimeter is approximately 53 cm, corresponding to 22 radiation lengths (X_0), while the end-cap detectors have a total thickness of approximately 63 cm ($> 24 X_0$). The ECal towers are positioned in an accordion geometry, which ensures maximal coverage of the pseudorapidity-azimuthal plane.

Finally, a pre-sampler calorimeter is used for $|\eta| < 1.8$. It consists of an active LAr

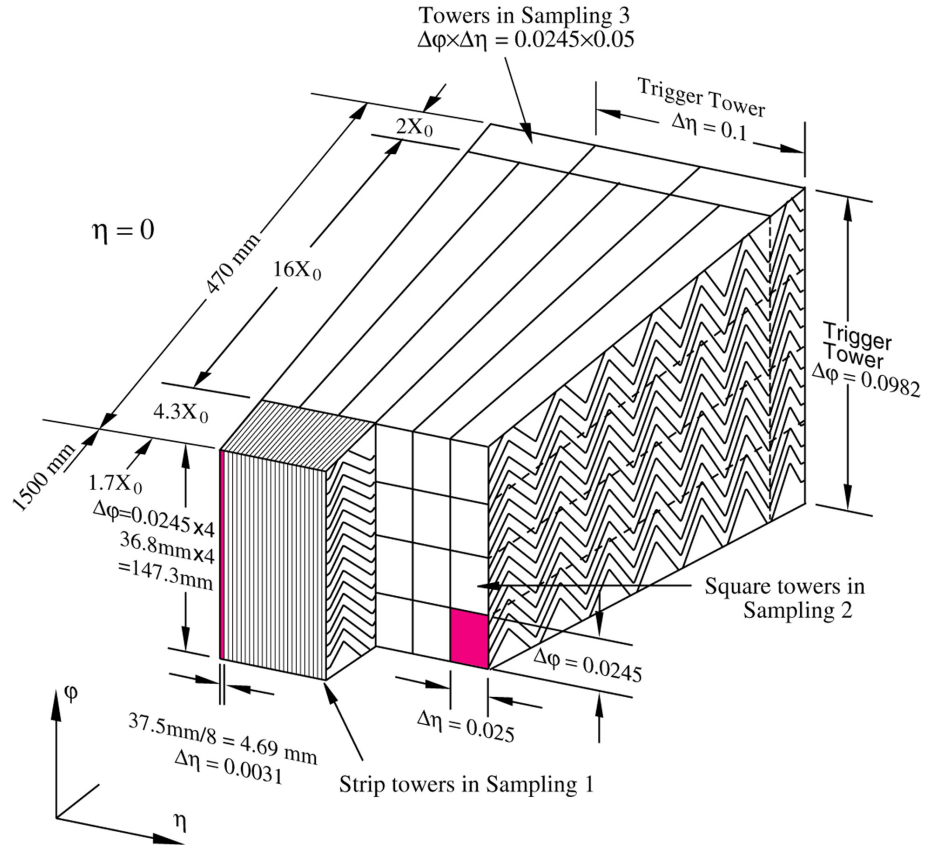


Figure 3.8: Sketch of the setup of the barrel module of the [ECal](#) of the ATLAS detector. Each of the modules is split into three different components with increasing granularity. [59]

layer, 1.1-cm thick, used to account for energy loss due to the material payload coming from the [ID](#) and the solenoid.

3.2.4.2 The Hadronic Calorimeter

Tile calorimeter The barrel part of the hadronic calorimeter is placed outside the electromagnetic calorimeter and covers a region up to $|\eta| < 1.0$. Two detectors extend the hadronic barrel calorimeter to the $0.8 < |\eta| < 1.7$ region. Across all the η region, steel is used as passive-absorber material, while scintillating tiles play the role of the active material for the collection of energy deposits. The overall thickness of the calorimeter is 1.97 m, corresponding to 9.7 interaction lengths at $\eta = 0$. TileCal provides good granularity of 0.1×0.1 in the pseudorapidity-azimuthal plane $\Delta\eta \times \Delta\phi$.

LAr end-cap calorimeters The Hadronic End-cap Calorimeter ([HEC](#)) is the component at high pseudorapidity of the [HCal](#). It comprises two wheels of LAr in a cryostat,

divided into a total of four layers and covering the $1.5 < |\eta| < 3.2$ region, therefore overlapping with the TileCal extended barrel, ensuring coverage by active material in the transition region between the barrel and the end-cap components of the HCal. Copper plates are used as passive-absorber material.

LAr forward calorimeters The Forward Calorimeter (FCal) is used to measure in the $3.1 < |\eta| < 4.9$ pseudorapidity region. It comprises three layers, which overall extend to up to 10 interaction lengths. The first layer is supported by copper plate, while the last two are modules made in tungsten, providing optimised measurements of hadronic interactions. As for the ECal and the other end-cap components of the calorimetry system, LAr is used as active material.

3.2.5 The Muon Spectrometer

The Muon Spectrometer (MS) is the outermost component of the ATLAS detector. It occupies the same volume as the magnetic system. The configuration of the toroids guarantees a magnetic field which is mostly orthogonal to the direction of the muon tracks.

A schematic view of the ATLAS muon system is shown in Figure 3.9. The system is structured in chambers used in offline tracking as well as additional chambers dedicated to triggering. Chambers are arranged into three layers in the barrel region, parallel to the beam direction, and three layers in the end-cap, perpendicular to the beam-pipe.

Precision tracking chambers

The 1088 Monitored Drift Tubes (MDTs) in the muon spectrometer extend over the $|\eta| < 2.7$ region. They consist of gas-based drift detectors, relying on the ionisation of a pressurised gas Ar/CO₂(93%:7%). Each tube has a diameter of 30 mm. While each of them allows precision spatial measurement with a resolution around 80 μm , the drift time for the ionised electrons to reach the walls of the tube is approximately 700 ns, making the MDTs not useful for fast tracking and trigger.

In the end-cap, the higher counting rates and the consequent radiation damage requires the use of a different kind of chambers to the MDTs. Cathod Strip Cham-

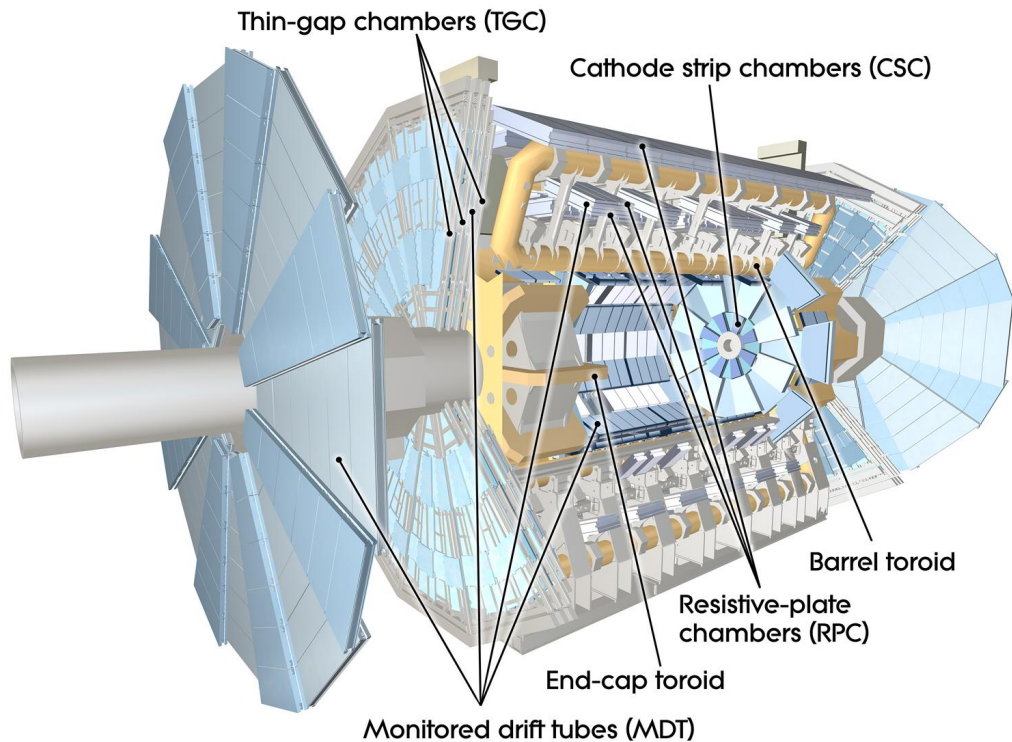


Figure 3.9: Schematic view of the muon system of the ATLAS detector. [59]

bers (CSCs) are used in the first end-cap layer, providing high spatial resolution for the tracking of muon passing through the forward region, as well as adequate radiation hardness and fast timing response. The CSCs consist of double disks of multiwire proportional chambers, oriented in the radial direction, filled with Ar/CO₂ (80%:20%). Their spatial resolution of 5 mm is worse than for the MDTs, but they provide a much faster response with a drift time of approximately 20 ns.

Trigger chambers

Different muon chambers are specifically dedicated to triggering purposes, for the selection of events of interest containing muons. These muon detectors, which cover the $|\eta| < 2.4$ region, are required to be robust against radiation damage, to have a fast timing response (< 50 ns), although their spatial resolution can be coarser. Additionally, they provide orthogonal coordinate measurements, which can be used together with those provided by the precision tracking chambers.

In the barrel, for $|\eta| < 1.05$ the muon triggering function is assigned to a set of Resistive Plate Chambers (RPCs). These are gas detectors with a principle of opera-

tion similar to that of multiwire chambers, but using electrode plates instead of wires. They are disposed over three different layers, and are used to trigger on muons with p_T between 6-35 GeV.

In the end-cap region, between $1.05 < |\eta| < 2.7$, the Thin Gap Chambers (TGCs) are used. These consist of multiwire chambers similar to the ones used in the RPCs, where the distance between the electrode plates is smaller than that interposed between the wires. With this configuration, the detector works in a quasi-saturated regime, in which the ionisation avalanches started by the incident particle are multiplicatively produced inside the detector. This allows for a faster timing response, and an improved granularity with respect to the RPCs. Furthermore, the TGCs are more resilient against radiation damage in the forward region.

3.2.6 The trigger and data acquisition system

The LHC provides collision events at a rate of 40 MHz, impossible to handle in terms of processing time and storage capacities. Therefore, some form of online data reduction is necessary. The trigger system of the ATLAS detector has the function to decrease the event rate to around 1 kHz by rapidly rejecting events that are not interesting for the physics goals of the experiment [69]. The ATLAS trigger system is composed of two levels [70]. The Level-1 (L1) is a hardware-based trigger, while the subsequent level is a software-based trigger, known as the High-Level Trigger (HLT). A sketch of the ATLAS Trigger and Data Acquisition (TDAQ) architecture, is shown in Figure 3.10.

3.2.6.1 The Level-1 trigger

The TDAQ L1 permits a first, fast selection of the events. It implements two hardware-based algorithms, L1Calo and L1Muon, which use information from the calorimeter system and the muon chambers, respectively. The L1 sends information to the Central Trigger Processor (CTP), which manages the handling of data from the the L1 to the HLT.

During the data taking, the data acquisition system records the hits from the ATLAS sub-detectors, starting the L1 algorithms. At an event rate of 40 MHz, there is not

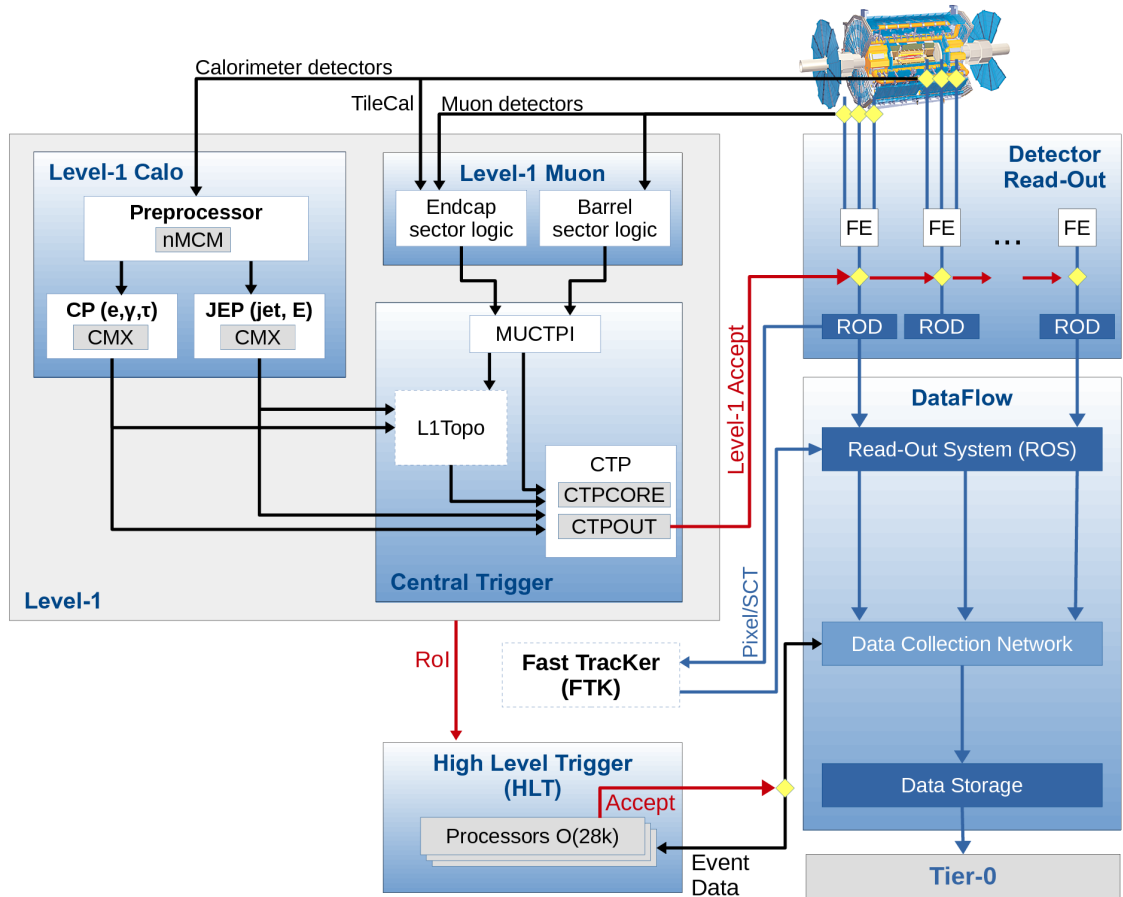


Figure 3.10: Schematic description of the ATLAS TDAQ system architecture used in Run 2. [70]

sufficient time to reconstruct physics objects. *Trigger objects* are generated from fast, coarse energy clusters in the calorimeters and from hits in the MS. The L1Calo sets energy thresholds in the calorimeters, while the L1Muon applies a selection based on information coming from the RPCs and the TGCs. In the case of L1Calo, calorimeter towers are used to apply energy thresholds, according to the chosen trigger selection in a given $|\eta|$ region. The clusters passing the energy thresholds are used to define so-called Region of Interest (RoI). The RoI are used to identify $\Delta\eta \times \Delta\phi$ L1 seeds, used by the HLT as targeted regions where to reconstruct physics object and apply the software-based trigger selection. Similarly, the L1Muon algorithm selects trigger objects from MS hits, and for which p_T is above the required threshold. Also in this case, RoIs are defined for muon triggers.

The calorimeter towers and muon segments are then passed to so-called L1Topo,

which applies a more precise reconstruction algorithm to extract topological and kinematic variables such as the missing transverse energy. Finally, the **CTP** takes all the **L1** information and decides which events pass the first level of trigger, and which are to be permanently rejected. The events with an **L1** pass are moved to the Read-Out Systems (**ROS**), as input information for the **HLT**. The event rate at the end of the **L1** step is approximately 100 kHz.

3.2.6.2 The High-Level Trigger

After passing the **L1** triggers, further skimming is applied by the **HLT** to bring down the event rate to 1 kHz. At this stage, information from the **ID** becomes available and it is used for trigger decisions. More sophisticated tower-clustering algorithms are used for precision reconstruction of energy deposits in the calorimeters. Information from the **MDTs** and **CSCs** are also added to the **L1** muon candidates for precision p_T reconstruction.

In the **ID**, two algorithms are used, the Fast Track Finder (**FTF**) and the precision tracking. The **FTF** is performed in the corresponding **RoI** seed defined by the **L1**. The precision tracking can be performed either in a corresponding **L1 RoI** or as full scan of the **ID** $|\eta|$ coverage. It relies on full reconstruction of the objects, thus including information from the calorimeters. It allows a complete and precise reconstruction of tracks and calorimetry variables such as E_T^{miss} .

Events selected by the **HLT** are stored in the *Data Storage* unit at the *Tier-0*, the others are permanently rejected. The final event rate at the end of the **HLT** is 1 kHz.

3.2.6.3 Trigger chains, menus and streams

The list of requirements of the **L1** and **HLT** is summarised in the so-called *trigger chain*. A trigger chain is labelled according to the naming conventions as follows. The naming of a trigger chain starts with "HLT_" and then continues with the list of the requirements of the **HLT** trigger, and, if applicable, it ends with the **L1** seed to the **HLT**. For example, the trigger chain labelled *HLT_2e17_lhvloose_nod0_L12EM15VHI* (one of those used in the analyses presented in this thesis) means that one is considering the **HLT** requirements labelled as *HLT_2e17_lhvloose*, indicating the presence of two electrons

with $p_T > 17$ GeV, and which are required to be identified as electrons by the likelihood algorithm "lhvlose", as described in Section 4.4.2. The HLT trigger receives an L1 seed *L12EM15VHI*, indicating the presence in the L1 trigger of two electromagnetic RoI with $E_T > 15$ GeV (*2EM15*), with E_T thresholds varying according to the η to account for energy loss effects (*V*). Finally, isolation of the hadronic core ("H") and the electromagnetic core (*I*) of the energy deposit is required.

For each signature, different trigger chains are available, which are distinguished by the requirements on the trigger objects. In some cases, triggers may still present too high a rate at the end of the HLT selection, resulting in streams of events which would be too busy and with rates higher than the desired 1 kHz. In such cases, an appropriate *prescale* is applied, such that only a fraction of randomly selected events passing the trigger selection is kept. None of the triggers used in the analyses described in this thesis have been pre-scaled.

Trigger chains are used to define *trigger menus*, the lists of trigger selections considered during the data-taking. Within a trigger menu, specific *trigger streams* can be defined: *main physics triggers*, used for physics analysis, to which no pre-scale is applied; *support triggers*, used for monitoring and performance measurements; *alternative triggers*, which use alternative reconstruction algorithms; *backup triggers*, which use tighter selection than the primary triggers; and *calibration triggers*, used for specific detector-calibration tasks. An *express stream* is used for quick quality checks of the recorded data. Finally, a special *debug stream* is filled with events for which an HLT decision could not be reached. These are then reprocessed offline and, if successful, will be retained in the main physics stream.

In view of future high-luminosity upgrades of the LHC, upgrades of the TDAQ system of the ATLAS experiment are foreseen. I made contributions to the performance studies of a tracking-based trigger, as part of my qualification as author of the ATLAS collaboration. This task is further detailed in Appendix A,

4 | EVENT GENERATION, RECONSTRUCTION AND OBJECT DEFINITIONS

This chapter introduces the different steps of a typical analysis using ATLAS data, from simulation to reconstruction and definition of relevant physics objects, as used in the analyses described in this thesis.

4.1 Event flow in ATLAS

The ATHENA framework [71] is used to manage all the necessary software for data analysis at ATLAS. ATHENA is based on the framework GAUDI [72], developed originally for the LHCb experiment. It incorporates tools and packages used for the software components of the trigger, the simulation algorithms, and the reconstruction of physics objects.

A schematic representation of the data flow in ATHENA is shown in 4.1. As described in Section 4.2, physics processes are first generated using Monte Carlo (MC) techniques. The outputs from the generation step are provided in the HepMC format [73]. The generated physics processes are passed through a simulation of the detector, as discussed in Section 4.3. Simulated hits from the detector are then digitised and provide so-called Raw Data Objects (RDO). Section 4.4 presents the reconstruction algorithms used to produce reconstructed samples. The outputs are then provided in the so-called Analysis Object Data (AOD) format. At this point, data is ready for physics analysis.

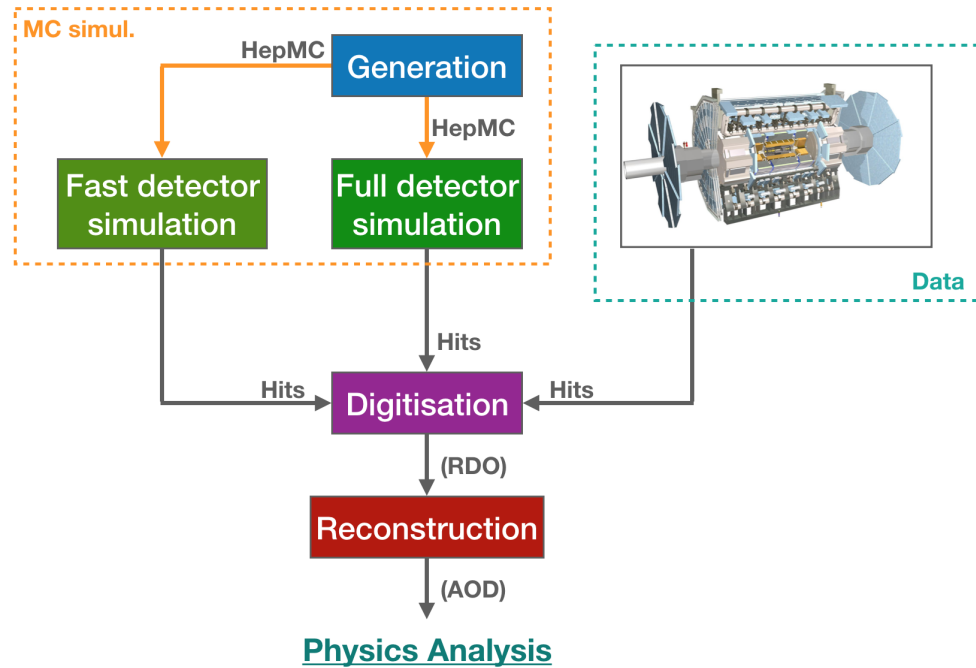


Figure 4.1: Schematic representation of the data flow in the ATLAS ATHENA framework prior to physics analysis.

4.2 Event generation

Proton-proton collisions at the LHC are dominated by the strong interaction and, in a “hard collision”, involve the *deep inelastic scattering* [74, 75] of *partons* inside the protons. Interacting partons can be either *valence quarks*, which determine the proton’s quantum numbers such as the electromagnetic charge and the baryon number, or originated from the *sea* of virtual quarks and gluons inside each of the protons.

The Parton Distribution Functions (PDF) describe the likelihood to find a parton with momentum fraction x of the parent proton momentum and value Q^2 of the transferred momentum squared. PDF have been measured indirectly by H1 [76], ZEUS [77] and other experiments through measurements of the deep inelastic scattering processes [78]. For illustration, the typical shape of a proton’s PDF are shown in Figure 4.2. For the calculation of cross-sections at different energy scales, the evolution of the PDF is described by the Dokshitzer-Gribov-Lipatov-Altarelli-Parisi (DGLAP) equations, detailed in Refs [79] and [80].

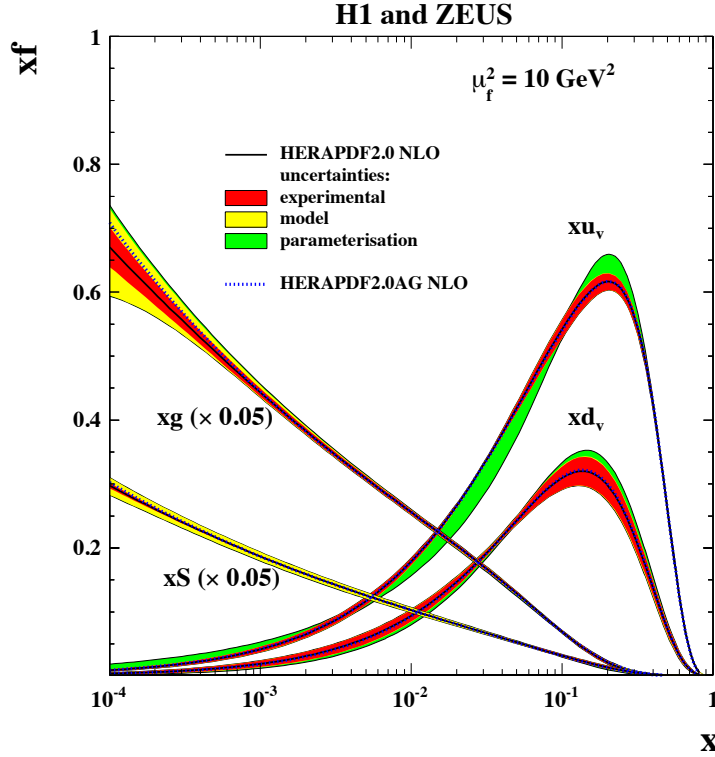


Figure 4.2: Proton PDF as measured by the H1 and ZEUS deep inelastic scattering experiments, at a scale of $\mu_f^2 = 10 \text{ GeV}^2$. The xu_v and xu_d represent the PDF of valence up-quarks and down-quarks. PDF for the gluons, xg , and the sea-quarks $xS = 2x(\bar{U} + \bar{D})$, are scaled down by a factor of 20. Experimental and modelling uncertainties are included. [78]

The total proton-proton interaction cross-section can be written as:

$$\sigma_{pp} = \sum_{a,b} \int_0^1 dx_a dx_b \int F_a(x_a, \mu_F) F_b(x_b, \mu_F) d\hat{\sigma}_{ab \rightarrow n}(\mu_F, \mu_R), \quad (4.1)$$

where

- The *factorisation scale* μ_F is the regulator needed to cure the infrared divergences of the theory, which arise due to the emission of massless particles from the initial states, while the *renormalisation scale* μ_R is the regulator of the ultraviolet divergences of the theory;
- $F_a(x_a, \mu_F)$ and $F_b(x_b, \mu_F)$ are the PDF of the interacting partons, a and b . They depend on the fractions of the proton momentum carried by the partons, x_a and x_b , respectively, and on μ_F ;

- $\hat{\sigma}_{ab \rightarrow n}(\mu_F, \mu_R)$ is the differential parton-parton cross-section, which depends on the μ_F and on μ_R .

Parton-parton interactions involving the highest transferred momentum Q^2 are referred to as *hard scattering* processes. Along with the hard scattering processes, other interactions at lower transferred momentum occur as *underlying events* between the partons not involved in the hard scattering. In addition to scatterings occurring simultaneously to the hard scattering, *pile-up* events are defined as overlapping proton-proton collisions other than those originating from the hard scattering interaction. They can happen in the same or in a different bunch-crossing, either slightly before or slightly after the main collision. Simulation techniques of underlying events and pile-up events are described in Section 4.2.2.

Hard scattering

At LHC, gluons and quarks involved in the hard scattering typically transfer a momentum larger than the hadronisation scale. Therefore, the cross-section of the parton-parton hard scattering is computed using the perturbation theory of the interaction, and it thus depends on *matrix elements*.

In general, the computation of the cross-sections takes into account the Feynman diagrams of the interaction. For the results shown in this thesis, dedicated PDF sets are provided to include parton momentum distribution, namely the NNPDF set [81, 82]. At the Leading Order (LO) calculation, only the tree-level diagrams are included, while possible *radiative corrections* are included as Next-to-Leading Order (NLO) matrix elements for one additional order of the perturbation, or, if two more orders of the perturbation are considered, Next-to-Next-Leading Order (NNLO). The precision of the calculation is typically at the Next-to-Leading-Logarithm (NLL) and in some cases at the Next-Next-to-Leading-Logarithm (NNLL). The radiative corrections model Initial State Radiation (ISR) and Final State Radiation (FSR) in the parton-parton interaction. The ISR is defined as the emission of gluons by the partons prior to the hard scattering. Similarly, gluons and quarks can be emitted by the final states of the hard scattering as FSR.

Parton-shower and hadronisation

Following the hard scattering, the typical value of the exchanged momentum between particles decreases. At this stage, the perturbation theory is not able to fully describe the physics of the interactions, and specific phenomenological models characterise the phenomena as *parton showers*, where continuous interactions of the form $g \rightarrow gg$, $g \rightarrow q\bar{q}$, $q \rightarrow qg$ occur in an avalanche starting from the final states of the hard scattering. Different algorithms are used to model parton-showers. These are based on Markov processes or *Markov chains*. A Markov chain is a stochastic method that can be used to describe the radiation of a gluon or gluon-gluon splitting at a factorisation scale μ_F from a given initial state at higher scale $\mu_F + d\mu_F$. Examples of parton-shower algorithms are the CKKW (Catani-Krauss-Kuhn-Webber) and the MLM (Michelangelo L. Mangano) algorithms [83, 84].

When the transferred momentum of interaction is close to the hadronisation scale, the remnant coloured particles start to feel the confinement of the strong interaction. At this energy scale, the phenomena are entirely described by phenomenological models. Instances of common models used in high-energy physics experiments are the *cluster hadronisation* [85] and the *Lund model* [86]. The parameters of the hadronisation models can be tuned to data. Some instances of model tuning are described in Refs. [87], [88] and [89].

4.2.1 The generators in ATLAS

The hard-scattering parton-parton collisions are modelled by the use of MC techniques, which makes use of the random sampling of events of the same process to extract physical properties and kinematics of the interaction products. Different generators are used in the ATLAS physics analysis. This section briefly describes the main features of those used to extract results presented in this thesis.

PYTHIA [90], SHERPA [91, 92] and HERWIG [93] are general-purpose generators used for LO calculation of the matrix elements. The SHERPA generator calculates the cross-sections up to the NLO accuracy, and also includes proper parton-shower modelling. In order to model the hadronisation, PYTHIA and HERWIG use the cluster hadronisation

model, whilst SHERPA uses the Lund model [86].

The MADGRAPH [94] generator can calculate matrix elements at LO accuracy, and up to the NLO with the aMC@NLO version. With POWHEG [95], it is possible to calculate matrix elements either at LO or NLO level of accuracy. MADGRAPH and POWHEG do not include any modelling for parton-shower and hadronisation. Therefore, they are interfaced with PYTHIA or HERWIG for the modelling of the parton showers and the hadronisation.

The EVTGEN [96] package is added to PYTHIA or HERWIG to improve the accuracy in the determination of the parton-shower modelling, implementing physics processes which are relevant for the description of the decays of B mesons.

In order to minimise statistical uncertainties for simulation of rare processes, a *generation filter* is often used to produce only those with specific characteristics, for instance the presence of a given number of leptons with a given threshold for their p_T . A *filter efficiency* is applied to simulated events as a weight, in order to account for the enhanced statistics.

4.2.2 Underlying events and pile-up

Generator like SHERPA and PYTHIA [97] already include underlying events in the simulation of processes, alongside the hard scattering. The methods described in previous sections are then used for the parton shower, hadronisation modelling and data tuning.

Pile-up events are generated independently and then overlaid to the hard scattering prior to reconstruction [98]. PYTHIA and MADGRAPH are used to simulate the pile-up events, accounting for the measured profile of the pile-up events in data. This is expressed as the mean number of interactions per bunch crossing $\langle \mu \rangle$. For Run-2 data, simulated samples for the ATLAS experiment were produced using three different pile-up simulations, to reflect the $\langle \mu \rangle$ distributions seen in data in different data-taking years, as shown in Figure 4.3.

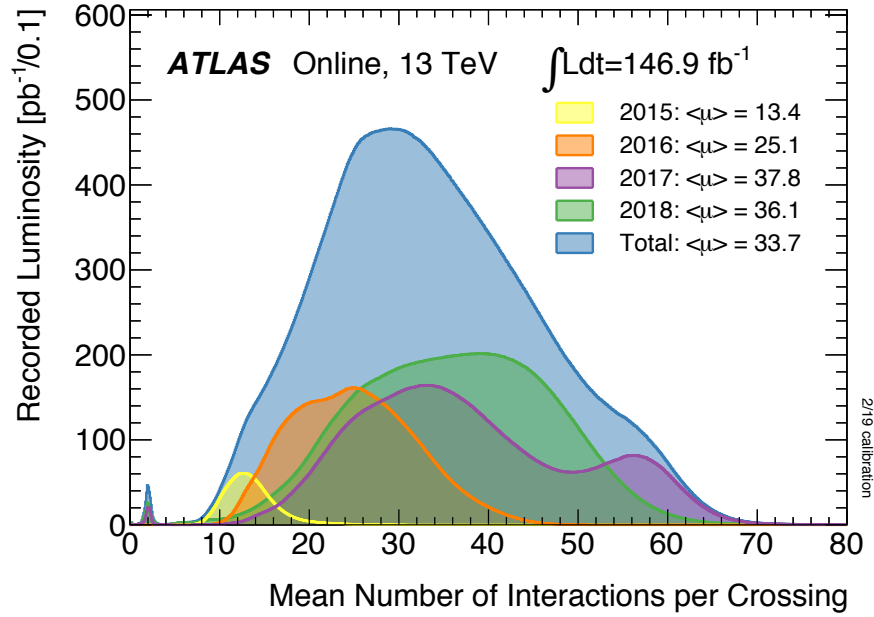


Figure 4.3: Distribution of the mean number of interactions per bunch crossing, $\langle \mu \rangle$, for the different years of data-taking in Run 2. [65]

4.3 ATLAS simulation and digitisation

The framework GEANT4 [99] is used for the detector simulation. Taking generated events as inputs, GEANT4 provides detailed simulation of the entire ATLAS detector, implementing a precise description of its full geometry, material distribution and services, as well as accurate simulations of the interaction of particle radiation with the sub-detectors.

The output of GEANT4 is in the identical format as that of actual data collected with the ATLAS detector. This is a file containing byte-stream of the particle interactions with the material of the detector. Files are then processed via *digitisation*, which converts byte-streams into C files, referred to as RDO, which can now be processed offline for event reconstruction.

4.3.1 The ATLAS fast simulation

ATLFastII (AFII) [100] is a fast simulation of the ATLAS detector. Instead of using the full detector simulation, the AFII uses the package FastCaloSim, which simplifies the calorimeter simulation. In FastCaloSim, calorimeter cells are described by cuboids and

shower development are parametrised by just considering only three particles: electrons, photons and pions. The use of the FastCaloSim the simulation time reduces by a factor 10 with respect to the full detector simulation. Detector hits from FastCaloSim are used to reconstruct basic particle kinematics, finding distributions similar to those extracted from full simulated hits. However, some discrepancies have been found, e.g. in the η distributions for jets, as better detailed in Ref. [100]. Therefore, the use of AFII is not recommended for all the simulations. Given the clear advantage of using AFII for the simulation of large amounts of events, as required for low cross-section processes, in this thesis, AFII has been used for the simulation of the SUSY signal samples.

4.4 Object reconstruction

Reconstruction algorithms combine detector hits to extract kinematic variables. Dedicated algorithms are used for the reconstruction of leptons, jets and missing transverse energy E_T^{miss} , with sophisticated procedures applied for the reconstruction of collision vertices and to "tag" jets originating from heavy flavour quarks.

4.4.1 Track and vertex reconstruction

Tracking algorithms

The New Tracking (NEWT) [101] algorithm is implemented in the ATHENA framework for the track reconstruction from detector hits in the ID.

There are two main algorithms used for the track reconstruction. They both use the same pattern-finding and ambiguity solving steps, but they differ by the way tracks are built in all the sub-detectors. In the case of the *inside-out* algorithm, the track reconstruction starts from the hits in the SCT, then by the use of Kalman filter [102] techniques, the nominal track is extrapolated and matched to hits in the TRT. Similarly, the *outside-in* algorithm starts the track reconstruction from hits in the TRT and extends the candidate tracks inwards to include hits from the innermost modules of the ID.

In the first step, ID hits are clustered together and combine via pattern-matching into ID track candidates. Possible ambiguities within the track candidate collection

arise from tracks sharing segments or from multiple tracks being very close. Ambiguities are solved by the use of a score-based algorithm, which favours tracks with more hits or hits on both sides of the [SCT](#) modules.

The Kalman filter, and the overall track-fitting procedure, is based on the assumption that tracks can be described as a linear dynamic system. Therefore, a linear correlation must exist between the positions of the hits in the [ID](#) and the kinematic variables that describe the kinematics and topology of the tracks. In the ATLAS reference frame, five variables are used to unequivocally describe a track:

- *impact parameter*, which measures how close the track extrapolation is to the origin of the reference system. The parameter d_0 is the distance measured from the origin of the axes to the closest track point, while z_0 is the longitudinal projection of d_0 along the z -axis;
- *angular variables*: the pseudorapidity η and the polar angle ϕ , defined from the point of the track the closest to the origin of the reference frame, described in [Section 3.2.1](#);
- the *curvature* q/p_T of a track, associated with a particle of transverse momentum p_T and its electric charge q .

In the analyses presented in this thesis, tracks with $p_T > 500$ MeV and $|\eta| < 2.5$ are selected. At least seven hits in the silicon detectors, including [SCT](#) and pixels, are required, with no more than one missing layer in the pixel detector and no more than two in the [SCT](#).

Vertex reconstruction

Reconstructed tracks are used to identify the *vertices* of the interactions. Reconstructed [ID](#) tracks are interpolated so that a common origin, or vertex, is found. Requirements on the number of tracks and impact parameter can be set to avoid contamination from underlying or pile-up events [\[103\]](#). All the vertex candidates must have at least two tracks associated with them, and only those with $|d_0| < 2$ mm and $|\Delta z_0 \sin \theta| < 3$ mm are selected.

Among all the vertex candidates, the *primary vertex* is defined as the main vertex of the collision, and it is associated with the hard scattering process. The primary vertex is identified as the one whose associated tracks give the highest sum of the squared transverse momenta.

4.4.2 Electrons

Electrons are associated with energy deposits in the [ECal](#) matching a reconstructed track in the [ID](#) [104, 105, 106, 107].

During Run 2, electron reconstruction was based on *topo-clusters* identified from calorimetry towers, with a substantial energy deposit with respect to noise coming from electronic and pile-up events [108]. The *topo-clusters* cover a region in η and ϕ , variable in size, which serves as [RoI](#) for the tracking reconstruction. Tracks are then extrapolated from the second layer of the *topo-cluster* to the outer hit in the [ID](#). Matched tracks are required to satisfy $|\eta| < 0.05$ and $-0.10 < q \cdot (\phi_{\text{track}} - \phi_{\text{cluster}}) < 0.05$, where q is the charge of the track, and ϕ_{track} and ϕ_{cluster} are the azimuthal angles of track and cluster, respectively. Moreover, in order to include Bremsstrahlung emission, *super-clusters* are also built, to include secondary clusters within a window of 3×5 calorimeter towers around the primary *topo-cluster*. Only *super-clusters* with energy above 1 GeV and a matching track in the corresponding [RoI](#) with at least four hits in the [SCT](#) are considered valid electron candidates.

The same reconstruction algorithm is also used for photons, defined as [ECal](#) clusters which do not match any [ID](#) track. In ambiguous cases, for instance when a track is matched but no hits from the innermost layers of the [ID](#) are found, they are kept in both the photon and electron candidate containers. Additional requirements are then applied to solve any ambiguity in the object reconstruction. This step is made in the *overlap removal* procedure described below.

Electron identification

Not all the reconstructed electrons are indeed *real* electrons. It can happen that matched cluster-track objects are originated from a jet, leptonic decays of hadronic particles in

the **ID**, or photon-conversion processes. All these alternatives are referred to as Fake or Non-Prompt (**FNP**) electrons. In what follows, in order to reduce contamination from **FNP** electrons, dedicated identification criteria are used on reconstructed electrons, as described below.

The identification of electrons is performed using a Likelihood (**LH**) approach, which combines evolution properties of the electromagnetic showers in both the longitudinal and transverse directions. The final electron **LH** is the product of all the Probability Density Function (**pdf**) associated with the relevant shower quantities:

$$L_{S(B)}(x) = \prod_i P_{S(B)}^i(x_i), \quad (4.2)$$

where x_i label the shower-development quantities used to calculate the **pdf** P . The electron **LH** is computed for both *signal* real electrons and *background* **FNP** electrons, labelled S and B , respectively. The **pdfs** are built from simulations of $Z \rightarrow e^+e^-$ for $E_T > 15$ GeV and $J/\Psi \rightarrow e^+e^-$ for $E_T < 15$ GeV. The discriminant is defined from the **LH** in 4.2, as the ratio between the $L_S(x)$ and the sum $L_S(x) + L_B(x)$.

Three operating points, or *working points*, are defined for the electron identification. The *Loose*, *Medium* and *Tight* working points apply a selection on the **LH** discriminant corresponding to given values of identification efficiencies. Loose corresponds to an average 93% of identification efficiency, Medium to 88% and Tight to 80%. All the working points require at least seven hits in the pixel detector and **SCT**, with the Medium and Tight requiring one hit in the innermost layer of the pixel detector. An additional working point, called *LooseAndBLayer*, uses the same discriminant value as the Loose working point, but requiring at least one hit in the **IBL**. Performances of the **LH** identification working points are shown in Figure 4.4.

Electron isolation

As for the identification, the use of isolation criteria suppresses contamination from **FNP** electrons in the final electron candidate collection. An electron satisfies the isolation requirement if the amount of energy and tracks around the nominal calorimeter cluster and track used for its identification is less than a given threshold, typically set by dedicated isolation working points.

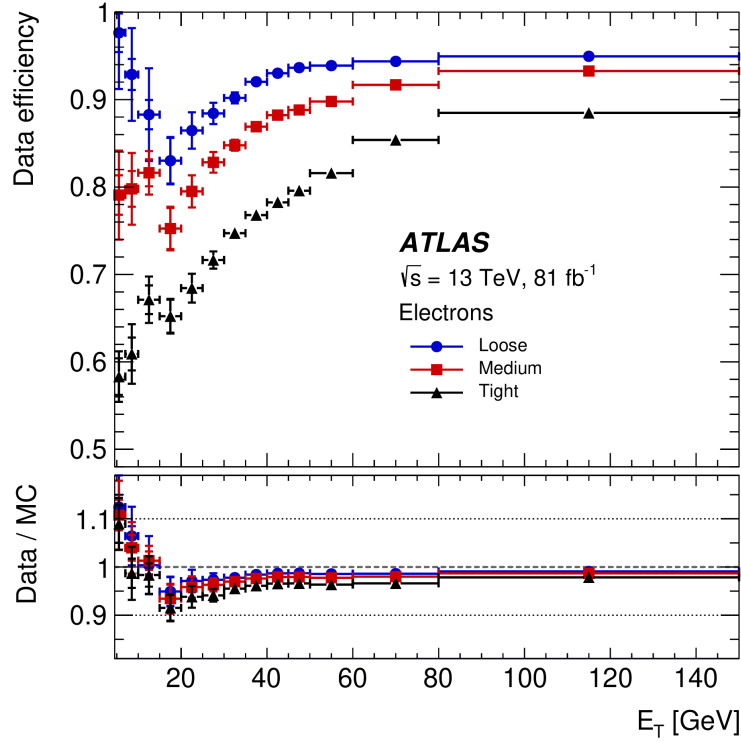


Figure 4.4: Performance of the working points for the LH-based identification of electrons. The upper panel shows efficiencies in data for the three working points: the Loose (blue) presents the highest efficiency with respect to the Medium (red) and Tight (tight). The lower panel shows the ratio between data and MC. Only data collected between 2015-2017 is used. Statistical and systematic uncertainties are considered. [108]

Two different variables are used for the isolation of the electrons, defined from calorimeter clusters and tracks separately. The variable E_T^{cone20} is defined as the sum of calorimeter deposits in the ECal within a cone of size $\Delta R = 0.2$ around the core of the topo-cluster reconstructing the electron, after subtracting the energy deposit associated with the electron itself, possible energy leakage from the nominal electromagnetic shower and energy deposits given by pile-up. Similarly, a $p_T^{\text{varcone20}}$ is defined around the electron track as the sum of p_T of tracks within a cone of $\Delta R = 0.2$ around the nominal track of the electron candidate. The vicinity of the electron track to those from other particle depends on p_T of the electron candidate. For this reason, in contrast to the calorimeter clusters, the size ΔR of the cone used in the track-isolation is not fixed, but varies with the p_T of the electron candidate:

$$\Delta R = \min\left(\frac{p_T}{10 \text{ GeV}}, 0.2\right). \quad (4.3)$$

Cuts on E_T^{cone20} and $p_T^{\text{varcone20}}$ define different working points for the electron isolation, as shown in Table 4.1.

Name	calo-isolation $E_T^{\text{cone20}} / p_T$	track-isolation $p_T^{\text{varcone20}} / p_T$
FCLoose	< 0.20	< 0.15
FCTight	< 0.06	< 0.06

Table 4.1: Working points for isolation of electrons used in the analyses described here. [108]

Figure 4.5 shows the efficiencies for the isolation algorithm for different choices of working points, where a fixed $\Delta R = 0.2$ for calorimeter isolation is used, while the radius of the cone for track isolation is set to $\Delta R = 0.2$, a part from the “Track $R_{\text{max}} 0.4$ ” working point, where a double-size cone is considered.

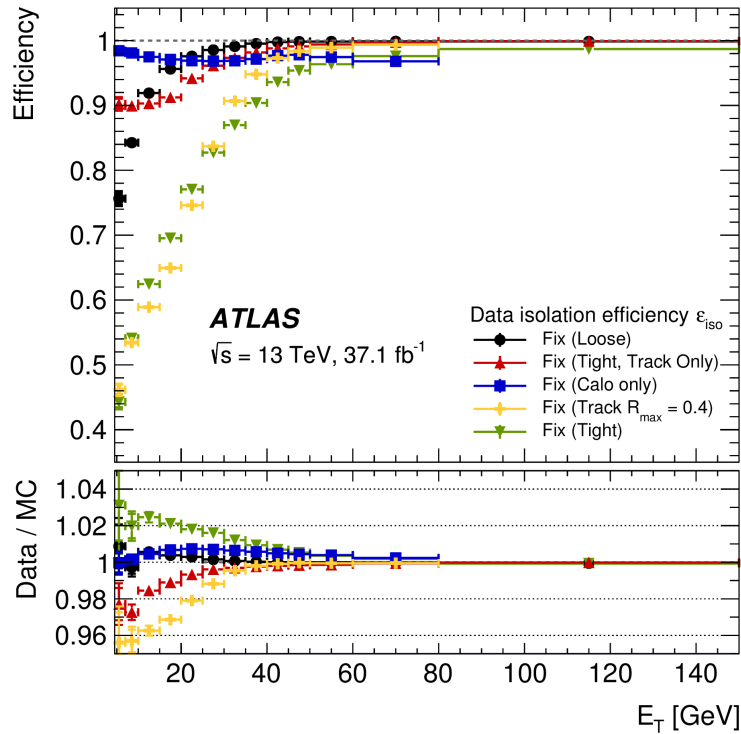


Figure 4.5: Performance of the working points for isolation of electrons. The upper panel shows efficiencies in data for different working points. The lower panel shows the ratio between data and MC. Only data collected between 2015-2016 is used, and only statistical uncertainties are shown. [106]

4.4.3 Muons

The reconstruction of muons is based on hits from both the **MS** and the **ID** [104, 109, 110]. Muon reconstruction algorithms run independently in the two sub-detectors, and only at a later stage the results are combined to fill the collection of muon candidates.

Hits in the middle layers of the **MDTs** are used to reconstruct *segments* via a Hough transform [111], in the cylindrical envelope around the beam-pipe. Hits from the **RPCs** and **TGCs** are then used to reconstruct the coordinates. The use of a linear χ^2 fit allows the reconstruction of the track from at least two segments, by extrapolating tracks from the hits in the middle layers to the outer and inner modules of the **MS**.

Muon tracks from hits in the modules of the **ID** are reconstructed via tracking algorithms, such as the inside-out and outside-in algorithms, described in Section 4.4.1. Candidate muon tracks are then matched to tracks reconstructed in the **MS**.

According to the outcome of the track-**MS** matching, four *types* of muons are defined:

- *Combined muons*: reconstructed by a global fit of hits in the **ID** and the **MS**, if candidate tracks are found in both. Most of the objects are reconstructed with an *outside-in* approach with fits starting from the hits in the **MS** and extrapolate the track inward to the **ID**. The collection of combined muons is highly pure in real muons.
- *Segment-tagged muons*: tracks reconstructed in the **ID** are extrapolated to the **MS** through a fit. A muon is reconstructed when an extended track matches a segment in the **MDTs** or **CSCs**.
- *Calorimeter-tagged muons*: **ID** tracks are matched to energy deposit in the calorimeter, compatible with a low-ionising particle. The collection of calorimeter-tagged muons recovers those muons passing through non-instrumented sections of the **MS**, typically used for services cables and connection for the innermost sub-detector.
- *Extrapolated muons*: only tracks in the **MS** are used. These are extrapolated inwards to the primary vertex, taking into account possible energy loss of the

muons in the calorimeters.

Muon identification

Similarly to the electrons, contamination from **FNP** muons typically arise from leptonic decays of light mesons. For such muons, the **ID** tracks do not match any **MS** segment. Therefore, in order to suppress the contamination from **FNP** muons, muon candidates are required to meet identification criteria. These are based on key muon quantities, such as: the q/p significance, depending on the ratio q/p of the muon and on the sum in quadrature of the uncertainties on q and p ; the quantity ρ' , defined as the difference of the muon p_T extracted from the **ID** and the **MS** separately and divided by the combined p_T of the muon; and the χ^2 of the global fit. Four working points are defined for muon identification:

- *Medium* muons are typically combined muons, with at least three hits in at least two layers of **MDTs**, at least one hit in $|\eta| < 0.1$, and q/p significance < 7 . In the $2.5 < |\eta| < 2.7$ region, extrapolated muons are considered to cover regions non-instrumented by the **ID**, requiring hits in at least three **MDTs** or **CSCs** layers.
- The *Loose* working point was optimised for searches for the Higgs boson decaying in four leptons. Muons passing the Loose working point are either Medium muons, or segment-tagged and calorimeter-tagged in the region $|\eta| < 0.1$.
- Furthermore, the *Tight* muons include combined muons which pass the Medium identification, but required to have at least four hits in the **MS** and a $\chi^2 < 8$. Cuts on the q/p significance and ρ' are in place to improve the purity of real muons.
- Finally, the *HighPt* working point was optimised for searches of heavy resonances decaying to muon pairs, such as the Z' . It selects combined muons with p_T above 100 GeV, and at least three hits in three **MS** stations. The use of the HighPt working point improves the muon identification efficiency by 30% for $p_T > 1.5$ TeV with respect to the other working points.

In all the above cases the **MC** samples $Z \rightarrow \mu^+ \mu^-$ and $J/\Psi \rightarrow \mu^+ \mu^-$ are used for the calibration of the identification algorithm.

Figure 4.6 shows the efficiencies for the muon identification working points, where the Tag-and-probe method is applied to target $Z \rightarrow \mu^+ \mu^-$ and $J/\Psi \rightarrow \mu^+ \mu^-$.

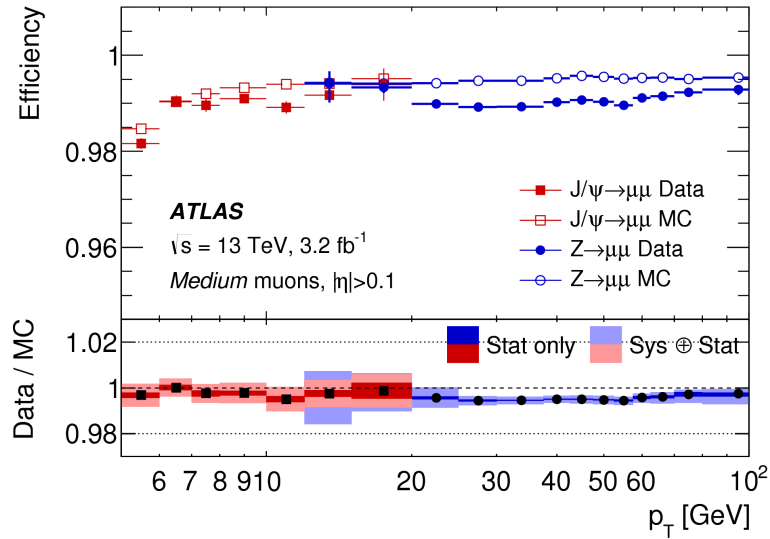


Figure 4.6: Performance of the working points for the identification of muons. Upper panel shows efficiencies in data and MC for the Medium working point. The lower panel shows ratio between data and MC. Only data collected in 2015 is used for a total of 3.2 fb^{-1} . Statistical and systematic uncertainties are considered. [110]

Muon isolation

Two algorithms are used for the isolation of the muons, in order to reduce the contamination from FNP muons. Similarly to the electrons, as described in Section 4.4.2, calorimeter-based and track-based isolation algorithms are used.

For the calorimeter-based isolation, calorimeter clusters are matched to the muon track in the ID. The energy E_t^{cone20} is defined as the energy inside a cone of dimension $\Delta R = 0.2$ drawn around the core energy deposit of the muon, and after subtracting the energy deposit of the muon itself. For the track-based isolation, the total transverse momentum $p_T^{\text{varcone20}}$ inside a cone drawn around the muon track, whose size varies according to the relation in 4.3. Cuts for two different working points are shown in Table 4.2.

4.4.4 Jets

As already seen for electrons in Section 4.4.2, jet reconstruction is based on topological clustering [107, 112, 113]. The construction of the topo-cluster for jets considers high

Name	calo-isolation $E_t^{\text{cone20}} / p_T$	track-isolation $p_T^{\text{varcone20}} / p_T$
FCLoose	< 0.3	< 0.16
FCTight	< 0.15	< 0.04

Table 4.2: Working points for isolation of electrons used in the analyses described here. [110]

energy deposits in the [HCal](#) and neighbouring cells. If a cell has energy greater than 500 MeV, it is used for a new clustering attempt as the central core of a topo-cluster. The final topo-clusters are then weighted by a Local Cluster Weight ([LCW](#)) [114], which calibrates the position of the cluster and applies a weight, accounting for the electromagnetic and hadronic development of the showers. The calibrated topo-clusters are then used as input for the jet algorithm, whose purpose is to identify which energy deposits are likely to originate from the same jet.

The [ANTIKT4EMTOPO](#) algorithm [115] is used as the default jet reconstruction algorithm in the ATLAS experiment. It is based on the distance between topo-clusters using the following metric:

$$d_{ij} = \min\left(\frac{1}{k_{T,i}}, \frac{1}{k_{T,j}}\right) \frac{\Delta R_{ij}}{R^2}, \quad (4.4)$$

where i and j are the indices of the two topo-clusters, $k_{T,i}$ and $k_{T,h}$ are the transverse momenta of the i -th and the j -th topo-clusters, and ΔR_{ij} is the ΔR between the two clusters. In the rapidity- ϕ plane, the radius parameter R corresponds to the size of the circle within the cells are clustered. In the analyses described in this thesis, the radius parameter is fixed at $R = 0.4$.

The general behaviour of the [ANTIKT4EMTOPO](#) algorithm is shown in the [Figure 4.7](#). Due to the dependency on the inverse of the momenta of the topo-clusters, clusters with highest momenta are prioritised in the identification of the jets, which usually have conical shapes. For clusters with low momentum, the [ANTIKT4EMTOPO](#) reconstruction would give a conical jet only for isolated topo-clusters. Otherwise, if a low-momentum cluster is close to a higher momentum cluster, possible overlaps between the two are assigned to the high momentum cluster, resulting in a non-conical shape for low momentum jets.

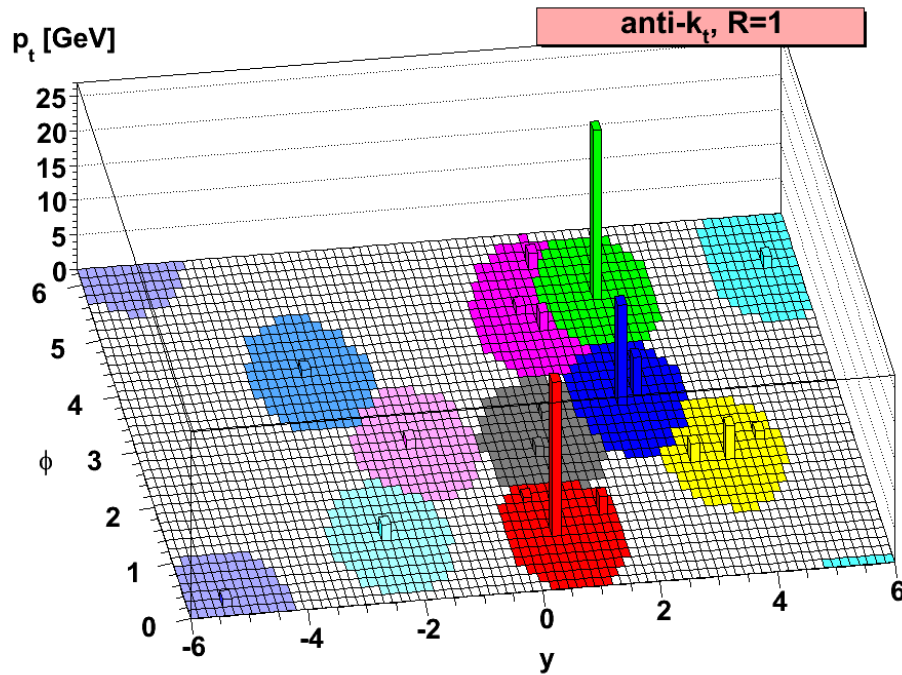


Figure 4.7: Pictorial representation of the general behaviour of the ANTIKT4EMTOPO algorithm, showing all the possible clustering configurations. Instances of clusters with high momentum and conical reconstructed shape are shown as blue and red cones. An example of isolated low-momentum clusters are represented in cyan and pink. Finally, an instance of a low-momentum cluster in proximity of a high-energy deposit is shown in magenta. [115]

Pile-up mitigation

Jets produced in underlying events and pile-up contribute to the transverse momentum distribution of jets in the analysis. The Jet Vertex Tagger (*JVT*) [116, 117] algorithm is exploited to suppress contribution from the pile-up jets. The *JVT* algorithm is based on Multi-Variate Analysis (*MVA*) techniques, whose inputs are a set of variables related to the topology and the kinematic of jets, to identify the jet tracks associated with the primary and secondary vertices. The output of the *JVT* algorithm is a *MVA* discriminant, which is used to distinguish between jets from hard scattering and those coming from underlying events and pile-up.

4.4.5 *b*-tagged jets

The main feature used to distinguish between *b*-jets and jets from light quarks, or *light jets*, is the presence of a displaced secondary vertex. In the case of *b*-jets, a second-

ary vertex is expected due to the decay of the b -hadrons, which travel a few hundred μm before decaying. The ATLAS b -tagging algorithms [118, 119, 120] are applied to reconstructed jets and are optimised for central jets with $|\eta| < 2.4$. Track impact parameters, secondary vertex positions and calorimeter deposits are all input variables to the b -tagging procedure, based on MVA techniques.

Likelihood-based taggers are used to provide a first level of discrimination. The IP2D and IP3D algorithms use the impact parameters of the jet tracks and pdfs based on distributions obtained from simulation of b -jets, c -jets and light-jets. The SV1 algorithm is used to identify secondary vertices in jets, scanning over all possible pairs of tracks in a jet and extrapolating them to a common secondary vertex via a χ^2 fit. Finally, the JETFITTER algorithm extracts decay paths from the tracks in a jet using a Kalman filter [102]. The JETFITTER algorithm identifies the common direction of the decay paths, which would correspond to the direction of the parent particle.

In a subsequent step, the discriminants from the low-level likelihood-based taggers IP2D and IP3D, outputs from SV1 and JETFITTER are inputted to a higher-level MVA-based algorithm. The MV2 algorithm is a Boosted Decision Trees (BDT) algorithm trained on simulation of $t\bar{t}$ processes for the "signal" (b -jets) and "background" (c -jets and light-jets). A specific version of the MV2 algorithm is used in this thesis, namely MV2c10. In this, the background training sample is composed by the 10% of c -jets, while the remaining 90% is made of light-jets. As shown in Figure 4.8, the MV2 algorithm shows clear discrimination power between all the different flavour categories considered.

4.4.6 τ aus

Specific algorithms for the reconstruction of hadronically decaying taus are used in ATLAS, while leptonically decaying taus are reconstructed as electrons or muons according to the procedures described in Section 4.4.2 and Section 4.4.3. Hadronically decaying taus leave energy deposits in the HCal. They are reconstructed from jet collections and identified by dedicated BDT algorithm, trained on signal taus from $Z \rightarrow \tau\tau$ simulated samples and light jet background from Z +jets.

The analyses described in this thesis do not target final states with hadronically

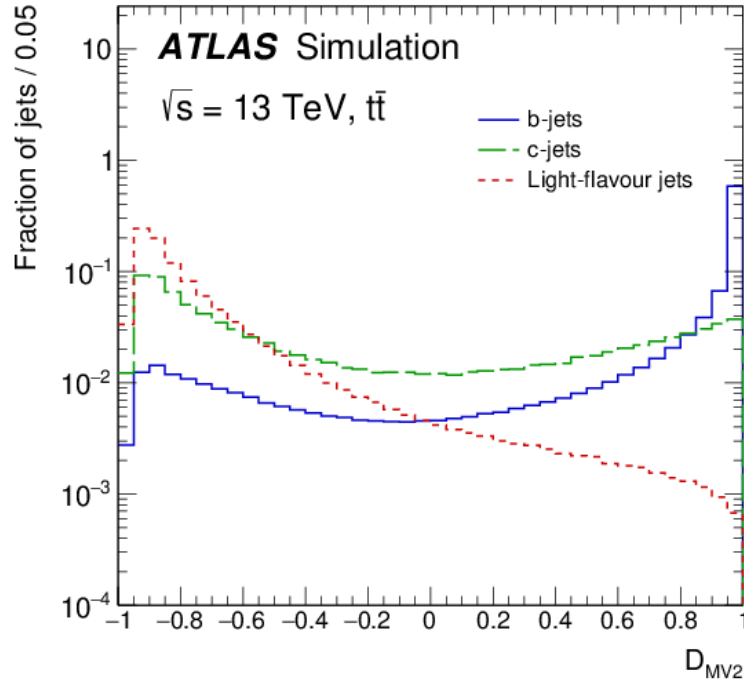


Figure 4.8: The fraction of jets as a function of the discriminant of the MV2, namely D_{MV2} . Distribution for the background c -jets (green) and light-jets (red) and the signal b -jets (blue) are shown. [120]

decaying taus, therefore a full description of their identification is not reported. Details can be found in the Refs. [121], [122] and [123].

4.4.7 Missing transverse momentum

Two different terms contribute to the final value of the transverse missing energy [124]. The *hard-term* is obtained by summing all the energy contributions originated from the reconstructed objects in the events, such as electrons, muons, photons, jets. In addition, a *soft-term* is considered to account for energy releases not reconstructed as a physical object, but associated to the hard-scattering process in the primary vertex. Hard-objects entering the E_T^{miss} calculation are required to be reconstructed and calibrated, no further criteria on the identification and isolation are required. In a general form, the E_T^{miss} can be expressed as an algebraical sum of several terms:

$$\begin{aligned}
 E_T^{\text{miss}} = & - \sum_{\text{electrons}} E_T^e - \sum_{\text{photons}} E_T^\gamma - \sum_{\text{tau}} E_T^\tau - \sum_{\text{muons}} E_T^\mu - \sum_{\text{jets}} E_T^{\text{jet}} \\
 & - \sum_{\text{unused tracks}} |\vec{p}_T|^{\text{track}} - \sum_{\text{unused CaloCells}} E_T^{\text{Cells}},
 \end{aligned} \tag{4.5}$$

where E_T^e , E_T^γ , E_T^τ are the transverse momentum extracted from calorimeter energy deposits for each electron, photon and hadronically decaying tau. Similarly, E_T^{jet} is the transverse energy term calculated for each reconstructed jet. The term E_T^μ is the total transverse energy of the each muon, calculated as sum of the p_T measured in the **MS** and the calorimeter muon energy deposit. The last two terms correspond to the scalar sum of the p_T of tracks and the sum of energy deposits in the calorimeter cells, which do not match any physics object.

4.4.8 Overlap Removal

Overlap between objects can occur for different reasons. Energy leakage from the **ECal** to the **HCal** and semileptonic in-jet decays are among the main causes, together with double-counting of physics objects arising from ambiguity in the object assignment at reconstruction level (e.g. the mentioned ambiguities between electron and photons). Specific *overlap removal* procedures are applied to reconstructed objects in order to resolve double-counting by looking at the vicinity of two objects. The effect of the overlap removal is to permanently reject physics objects considered too close to other reconstructed objects. The priority order for the discarding of the objects is decided based on the specific requirements of the physics analysis. In this thesis, the following criteria are used for the overlap removal and applied in the following priority order:

- first, if an electron and a muon share an **ID** track, they are both discarded;
- second, if the ΔR distance between a jet and an electron is less than 0.2, the jet is discarded;
- if the same situation as above occurs between a muon and a jet with less than three tracks with $p_T > 500$ MeV, the jet is removed from the object collection;
- finally, if an electron or muon is within $\Delta R=0.4$ of a jet candidate, the electron or muon is discarded;

4.5 Event quality cuts

Events in the simulated and data samples must satisfy a list of quality requirements. These assure a good quality of the data entering the physics analysis, suppressing events from non-collision background and vetoing inactive sections of the detector. An event can fail to pass this step for several reasons:

- corrupted hits due to errors in the [LAr](#) or Tile calorimeters;
- missing information for the full event reconstruction;
- presence of reconstructed muons coming from high-energy jets crossing the full hadronic calorimeter, or from cavern background;
- energy deposit in the calorimeters due to non-collision background and reconstructed as jets.

4.6 Analysis objects

As discussed in Section 4.4, physics objects are reconstructed from hits in the detector, which in the case of [MC](#) simulation are obtained from [GEANT4](#) simulations of the ATLAS detector.

The choice of working points for the identification and isolation algorithms, as well as kinematic requirements of physics objects, have been optimised prior my contribution to the analyses presented in this thesis. As already mentioned in Section 4.4, identification and isolation criteria serve as a first suppression of the [FNP](#) background.

There are two levels of object definition, which, as it will be described in the following sections, are used for different purposes: a looser level of selection, referred to as *loose* or *baseline*, defines a first collection of objects; while a tighter selection, referred to as *tight* or *signal*, further skims the collection of objects passing the baseline definition. The following sections contain details on the baseline and signal selections for leptons and jets.

Baseline objects

Electrons and muons Baseline electrons and muons are required to have $z_0 \sin \theta < 0.5$ and $p_T > 10$ GeV, respectively. Electrons must be inside the $|\eta| < 2.47$ region, while muons are reconstructed inside the $|\eta| < 2.5$ region. In addition, baseline electrons must pass the LooseAndBLayer working point for identification, while muons must satisfy the Medium working point.

Jets Baseline jets must pass the ANTIKT4EMTOPO algorithm and have $p_T > 20$ GeV. To maximise the efficiency of reconstruction, their calorimeter release must lie in a region with $|\eta| < 4.5$. At this level of selection, no flavour-tagging is applied.

Overlap Removal Baseline objects must pass the overlap removal procedure discussed earlier. This provides further cleaning from pile-up of underlying events and further suppression of [FNP](#) backgrounds.

Signal objects

Electrons and muons For signal electrons and muons, the main additional requirements regard the lepton isolation. For electrons only, the identification requirements are tightened and signal electrons must pass the Medium working point for the identification. Signal electrons and signal muons must pass the Tight efficiency working point for the isolation, described in Sections [4.4.2](#) and [4.4.3](#), respectively. Both signal electrons and signal muons are required to have $p_T > 10$ GeV. In addition, in order to suppress contributions from [FNP](#) background, the d_0 *significance*, defined as the ratio of the impact parameter d_0 and its uncertainty, is required to be less than 5 for signal electrons and less than 3 for signal muons.

Jets No additional cut on p_T is applied for signal jets compared to baseline jets. They need to have $|\eta| < 2.8$ and, if their p_T is greater than 120 GeV and they are within $|\eta| < 2.5$, they must pass a [JVT](#) algorithm at the Medium working point, as discussed in Section [4.4.4](#).

***b*-tagged jets** Signal jets can be *b*-tagged if they pass the MV2C10 algorithm at the 85%-efficiency working point, as in Section 4.4.5. Furthermore, the candidate *b*-jet must be within $|\eta| < 2.5$.

5

ANALYSIS STRATEGY FOR EWK SUSY SEARCHES WITH THREE-LEPTON FINAL STATES

This chapter presents the analysis strategy and key selection variables for the Run-2 ATLAS searches presented in this thesis for the production of $\tilde{\chi}_1^\pm$ and $\tilde{\chi}_2^0$ decaying to three-lepton final states via SM intermediate bosons (W , Z and h). A discussion on the techniques used for the statistical interpretation of the results is also presented.

5.1 Data and simulated samples

5.1.1 SUSY signals

The simplified models targeted by the analyses in this thesis have been already discussed in Section 2.2.2.3. However, as a reminder, the diagrams for the WZ and the Wh models are shown again in Figure 5.1, where now leptonic decays of the SM bosons are shown.

For both the Wh and WZ models, signal samples are examined for different values of the sparticle masses $m_{\tilde{\chi}_1^\pm/\tilde{\chi}_2^0} = m_{\tilde{\chi}_1^\pm} = m_{\tilde{\chi}_2^0}$ and $m_{\tilde{\chi}_1^0}$. Each SUSY scenario is a so-called *mass point* in the corresponding *signal grid*. The MADGRAPH generator, interfaced with PYTHIA for the simulation of the parton shower, is used for the MC production of all the signal samples. Moreover, to ensure that sufficiently large samples are produced with three leptons in the final state, dedicated filters are applied to the WZ and Wh points at generation level.

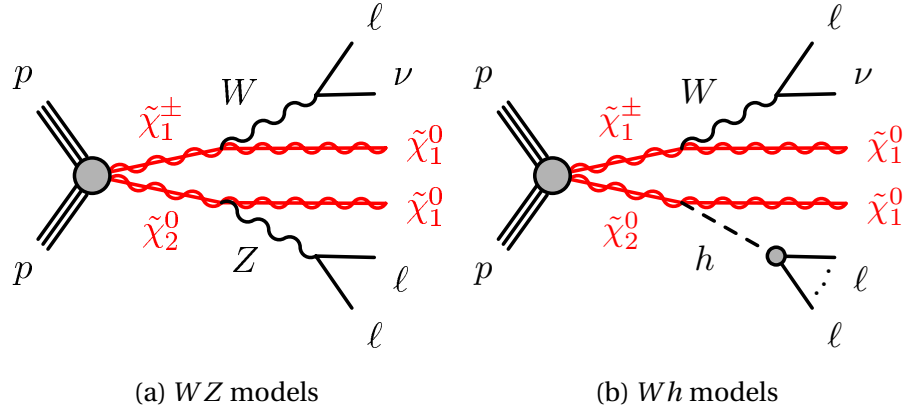


Figure 5.1: Diagrams for the production of chargino and neutralino, decaying to three-lepton final states via (a) *WZ* and (b) *Wh* bosons. The channel with exactly three light leptons in the final states is considered.

For the *Wh* benchmark points, only events where any *W* boson decays to a charged lepton ℓ ($\ell = e, \mu, \tau$) plus neutrino ν , and the Higgs boson decays to W^+W^- , ZZ or $\tau^+\tau^-$, are selected. Moreover, events are required to have at least three light leptons with truth-level $p_T > 7$ GeV. Similarly, for the *WZ* signal samples, only leptonic decays of the *W* and the *Z* bosons are considered, and events are required to have at least two light leptons with truth-level $p_T > 7$ GeV.

The particles mass ranges and corresponding typical cross sections for the considered signal samples considered in this thesis are summarised in Table 5.1.

Model	$m_{\tilde{\chi}_1^\pm/\tilde{\chi}_2^0}$ [GeV]	$m_{\tilde{\chi}_1^0}$ [GeV]	cross section [pb]
<i>Wh</i>	[150,425]	[0,100]	3.274-0.065
<i>WZ</i>	[100,800]	[0,400]	13.895-0.003

Table 5.1: Features of the MC samples for the targeted SUSY models *WZ* and *Wh*. In the last column, the ranges of nominal cross sections for the production of $\tilde{\chi}_1^\pm$ and $\tilde{\chi}_2^0$ at given $m_{\tilde{\chi}_1^\pm/\tilde{\chi}_2^0}$.

Signal benchmark points are used as reference signal models in what follows, and are labelled by the simplified model and the chosen values of the $m_{\tilde{\chi}_1^\pm/\tilde{\chi}_2^0}$ and $m_{\tilde{\chi}_1^0}$ parameters. For instance, the label "Wh(175, 0)" indicates the benchmark signal for the *Wh* model with $m_{\tilde{\chi}_1^\pm/\tilde{\chi}_2^0} = 175$ GeV and $m_{\tilde{\chi}_1^0} = 0$ GeV. A similar naming convention is maintained for the *WZ* signal samples.

5.1.2 Trigger strategy and data quality

In order to target final states with three leptons, all events are requested to pass trigger chains which require the presence of one or more light leptons. No pre-scale is applied to the chosen trigger chains, and low p_T thresholds are used for the leptons entering the trigger selection.

All analyses described in this thesis use a logical OR of available di-lepton (ee , $\mu\mu$ or $e\mu$) trigger chains, listed in Table 5.2. For the early Run-2 analysis discussed in Section 6.1, the single-lepton triggers listed in Table 5.3 were also used.

Year	Trigger signature	Trigger chains
2015	ee	HLT_2e12_lhloose_L12EM10VH
	$\mu\mu$	HLT_mu12_mu8noL1
	$e\mu$	HLT_e17_lhloose_mu14
2016	ee	HLT_2e17_lhvloose_nod0
	$\mu\mu$	HLT_mu22_mu8noL1
	$e\mu$	HLT_e17_lhloose_nod0_mu14
2017-2018	ee	HLT_2e17_lhvloose_nod0_L12EM15VHI HLT_2e24_lhvloose_nod0_L12EM20VH
	$\mu\mu$	HLT_mu22_mu8noL1
	$e\mu$	HLT_e17_lhloose_nod0_mu14

Table 5.2: Di-lepton trigger chains used for all analyses presented in this thesis, listed by year of data taking.

Year	Trigger signature	Trigger chains
2015	e	HLT_e24_lhmedium_L1EM20VH
		HLT_e60_lhmedium
		HLT_e120_lhloose
2015	μ	HLT_mu20_iloose_L1MU15
		HLT_mu40
2016	e	HLT_e26_lhtight_nod0_ivarloose
		HLT_e60_lhmedium_nod0
		HLT_e140_lhloose_nod0
	μ	HLT_mu26_ivarmedium
		HLT_mu50

Table 5.3: Single-lepton trigger chains used for the early Run-2 analysis presented in Section 6.1, listed by year of data taking.

The nomenclature of the trigger chains follows the conventions detailed in Sec-

tion 3.2.6. In the case of the di-electron trigger chain for the year 2017-2018, in order to recover inefficiencies of the $HLT_2e17_lhvlose_nod0_L12EM15VHI$ during some runs of the year 2017, the additional trigger chain $HLT_2e24_lhvlose_nod0_L12EM20VH$ was used in a logical OR for the ee trigger signature, as discussed in Ref. [125].

5.1.3 Standard Model backgrounds

Based on the presence, or not, of **FN**P leptons in the final states, the **SM** background processes for this analysis are grouped into two distinct categories:

- *Irreducible backgrounds*, with exactly three real light leptons and real E_T^{miss} ;
- *Reducible backgrounds*, in which at least one of the final-state leptons is **FN**P.

Table 5.4 shows a list of the background processes considered in these searches, grouped according to the above categorisation.

Type of background	Processes
Irreducible	$VV, VVV, t\bar{t}+V, t\bar{t}+H, VH$
Reducible	single-top, $t\bar{t}$, Z +jets, $Z + \gamma$, $W+W$

Table 5.4: **SM** processes which are significant background for the considered analyses, where $V = W, Z$.

Generators discussed in Section 4.2.1 are used for the generation of **SM** backgrounds. Unless otherwise specified, cross sections are calculated using **NLO** matrix elements.

Multi-boson (VV, VVV) [126] The production of two (VV) or three (VVV) vector bosons ($V=W, Z$), with W and Z decaying leptonically, constitute the main **SM** irreducible backgrounds in the searches. The SHERPA-2.2.1 and SHERPA-2.2.2 generators are used for the production of the **MC** samples for the di-boson and tri-boson production, respectively.

Higgs boson processes [127] This category includes **SM** processes that involve the production of a Higgs boson, such as single Higgs boson production via gluon-gluon fusion and Vector-Boson Fusion (**VBF**), the production of Higgs boson alongside a $t\bar{t}$

pair, or Higgs boson production in association with a W or Z boson. All the Higgs boson samples are generated using POWHEG, interfaced with PYTHIA for the simulation of the parton shower development.

$t\bar{t} + V$ The production of $t\bar{t}$ in association with a vector boson ($V = W, Z$) constitutes an important background process that contributes to the irreducible SM backgrounds. These events are generated using PYTHIA interfaced with the EVTGEN package.

Other top processes ($t\bar{t}$, single-top) [128] [129] The top quark decays virtually exclusively to a bottom quark and a W boson, which can in turn decay leptonically. Processes with a $t\bar{t}$ pair or single-top production can mimic the three-lepton signature due to the mis-reconstruction as lepton of a b -jet or a light jet and in-jet leptonic decays leading to an FNP lepton in the final state. These other top processes are produced with the POWHEG, interfaced with PYTHIA + EVTGEN for parton shower simulation.

$Z + \text{jets}$ and $Z + \gamma$ [130] Production of a vector boson Z in association with jets or photons is one of the most important reducible SM processes at low E_T^{miss} . Three-lepton final states are possible when an FNP lepton arises from a mis-reconstructed jet or a photon conversion. SHERPA is used for the simulation of $Z + \text{jets}$ and $Z + \gamma$ processes.

5.2 Strategy for the event selection

The event selection strategy for the searches in this thesis is based on a *cut-and-count approach*, where several requirements on specific selection variables are applied to define Signal Region (SR)s, which are enriched in the targeted SUSY signal, while SM contributions in the same region are adequately suppressed.

The definition of the SRs, and thus the choice of the cuts on the relevant selection variables, is based on the optimisation of the *expected significance* Z_n , which represents the level of rejection of the SM “background-only” hypothesis in favour of the “background+signal” hypothesis, as will be further discussed in Section 5.5. It is given

by:

$$Z_n = \sqrt{2} \operatorname{erf}^{-1}(1 - 2p), \quad (5.1)$$

where the function erf is the Gaussian error function, and p represents the probability that the observed data is given by a statistical fluctuation of the background, calculated from the expected number of signal events s , background events b , and the total uncertainty on the background σ_b . For the optimisation of the SRs in this thesis, a flat σ_b is assumed, equal to 30% if not stated otherwise. The significance Z_n is calculated numerically using the analysis tool ROOT [131]. Moreover, each selection is chosen such that at least one background event is left in all the SRs, to ensure robustness of results based on sufficient statistics in the final selections.

5.2.1 Selection variables

For the SR definitions applied in these analyses, events are split into categories according to the flavour and sign combinations of leptons, as explained below.

Firstly, events are classified based on whether at least one pair of Same-Flavour Opposite-Sign (SFOS) leptons is present. The SFOS category can be used for the SR optimisation targeting both the WZ and Wh models. In what follows, selections applied to SFOS events will be referred to as SFOS SRs. For the considered signals, in events not containing a SFOS pair, it is normally possible to find a pair of Same-Flavour Same-Sign (SFSS) leptons, plus an additional lepton. In the SR selections, this third lepton is required to be of Different-Flavour Opposite-Sign (DFOS) with respect to the leptons in the SFSS pair. In this way, contributions from events containing leptonically-decaying Z bosons are suppressed. This kind of selection, referred to as the DFOS SRs in the following, is used to target signals from the Wh models. Contrary to the WZ model, in the Wh signals the decays $h \rightarrow WW^*$ and $h \rightarrow \tau^+\tau^-$ can yield two DFOS leptons, one of which can be SFSS to that obtained via leptonic decay of the W boson coming from the $\tilde{\chi}_1^\pm$.

Once events have been divided into the SFOS and DFOS categories, other variables, described below, are used to further optimise the SRs.

Lepton p_T The transverse momentum p_T is already defined in Section 3.2.1. The transverse momentum of the i -th lepton in each event is labelled as $p_T^{\ell_i}$ ($i = 1, 2, 3$), where by convention leptons are sorted by descending values of their p_T . Similarly, ordered p_T values of the light jets are labelled $p_T^{j_n}$ ($n = 1, \dots, N$, where N is the total number of jets in the event).

The scalar sums of the transverse momenta of the three leptons (H_T^{lep}), or of the jets (H_T) are also introduced:

$$H_T = \sum_{n=1}^N |\vec{p}_T^{j_n}| \quad (5.2)$$

and

$$H_T^{\text{lep}} = \sum_{i=1}^3 |\vec{p}_T^{\ell_i}|. \quad (5.3)$$

E_T^{miss} significance The E_T^{miss} significance [132] measures the probability that the measured missing transverse momentum is due to the presence of some invisible particles in the events. It is obtained by a likelihood-based test of the hypothesis that the sum of transverse momenta of invisible particle is equal to 0, against the hypothesis of a non-zero value. In fact, low values of the E_T^{miss} significance are expected for those events where none of the involved particles decays into invisible states, whilst higher values are characteristic of events with prompt decays in invisible particles, such as the **SUSY** signal considered here.

Invariant and transverse masses In the case of the **SFOS** selection, the invariant mass of the **SFOS** lepton pair is given by:

$$m_{\ell\ell} = \sqrt{(E^{\ell_1} + E^{\ell_2})^2 - (\vec{p}^{\ell_1} + \vec{p}^{\ell_2})^2}. \quad (5.4)$$

It a good discriminant for processes in which the **SFOS** lepton pair originates from a Z boson decay. With three leptons in the events, there can be up to two lepton pairs which satisfy the **SFOS** requirement. The choice is made here to select as primary **SFOS** pair that with invariant mass closest to the nominal Z boson mass.

The invariant mass of the three leptons, called $m_{\ell\ell\ell}$, is also used, given by:

$$m_{\ell\ell\ell} = \sqrt{(E^{\ell_1} + E^{\ell_2})^2 + E^{\ell_3})^2 - (\vec{p}^{\ell_1} + \vec{p}^{\ell_2})^2 + \vec{p}^{\ell_3})^2}. \quad (5.5)$$

The p_T of the third lepton not in the primary SFOS pair and the transverse missing momentum can be combined to define a transverse mass m_T as follows:

$$m_T = \sqrt{2p_T^\ell E_T^{\text{miss}} - 2\vec{p}_T^\ell \cdot \vec{p}_T^{\text{miss}}}. \quad (5.6)$$

While often used as an estimator of the mass of the lepton's parent, in this context m_T provides good signal-to-background discrimination in the definition of the SR bins.

Angular variables A set of angular variables are used in the DFOS selection. These are schematically illustrated in Figure 5.2 and defined in the following:

- The ΔR distance between the DFOS lepton not in the SFSS pair (called ℓ_{DFOS}) and the lepton in the SFSS pair (called ℓ_{near}) closest in $\Delta\phi$ to the ℓ_{DFOS} itself. This is called $\Delta R_{\text{OS, near}}$;
- The $\Delta\phi$ separation between the SFSS leptons, called $\Delta\phi_{\text{SS}}$;
- The invariant mass constructed from the ℓ_{DFOS} and ℓ_{near} lepton pair, called $m_{\ell_{\text{DFOS}}+\ell_{\text{near}}}$.

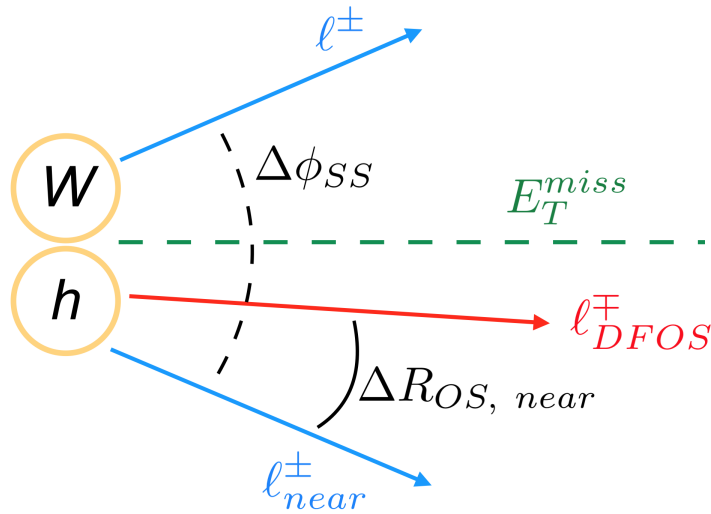


Figure 5.2: A schematic illustration of the angular variables defined for the DFOS selection. See text for more details.

5.3 Background estimation

The understanding of the SM background entering contributions in the SRs is crucial when inspecting data in the SRs (a procedure often referred to as *unblinding*). An insufficient characterisation of the background processes in the SRs could in fact lead to a “fake” excess in data, in case of an underestimation of the backgrounds, or hide an actual SUSY observation, in case of a background overestimation. Depending on the irreducible or reducible nature of the background processes, different techniques are used for their estimation.

5.3.1 Data-driven estimation of FNP backgrounds

When at least a FNP lepton is present in the event, data-driven methods are used for the estimation of those backgrounds in the SRs. In what follows, the methods used in this thesis are discussed.

5.3.1.1 Fake Factor method

The basic idea of the Fake Factor method is that, for a given selection, the total number of events with FNP leptons can be correlated to the number of events with leptons passing a *tight* and *loose* object definition. For the methods used in this thesis, the tight and loose selections are identified as the baseline and signal requirements described in Section 4.6.

For illustration, it is useful to consider first the case with just one lepton in the final state, when one can write:

$$\begin{pmatrix} N_T \\ N_L \end{pmatrix} = \begin{pmatrix} \epsilon_R & \epsilon_F \\ \bar{\epsilon}_R & \bar{\epsilon}_F \end{pmatrix} \begin{pmatrix} N_R \\ N_F \end{pmatrix}, \quad (5.7)$$

where N_T (N_L) is the number of events with one tight (loose) lepton, and N_F (N_R) is the number of events with a FNP (real) lepton. The quantities ϵ_R and ϵ_F express the *real-lepton efficiency* and the *fake-lepton efficiency*. These represent the probability that a prompt lepton, or a fake lepton, respectively, passes the tight selection. Similarly,

$\bar{\epsilon}_R = 1 - \epsilon_R$ and $\bar{\epsilon}_F = 1 - \epsilon_F$ give the probability that a prompt, or a fake lepton, fails to pass the tight selection.

From the relations defined in Equation 5.7, one can write the formula for the estimation of the number of events with an **FNP** lepton entering the selection:

$$\begin{aligned} N_T^F &= N_T - N_T^R \\ &= \frac{\epsilon_F}{\bar{\epsilon}_F} (N_L - \bar{\epsilon}_R N_R) \\ &= \frac{\epsilon_F}{\bar{\epsilon}_F} (N_L - N_L^R), \end{aligned} \quad (5.8)$$

where $N_T^F = \epsilon_F N_F$ is the number of **FNP** leptons that pass the tight selection. Similarly, N_T^R represents the number of real leptons that satisfy the tight requirements. The ratio $F = \epsilon_F / \bar{\epsilon}_F$ is referred to as Fake Factor (**FF**).

The simpler matrix relation in Equation 5.7 can be generalised to the more complex case with three leptons in the final state, when one needs to consider an 8×8 matrix, composed of real and fake lepton efficiencies for the eight possible combination of tight and loose leptons. These are TTT , LTT , TLT , TTL , LLT , LTL , TLL and LLL .

Extending from the one-lepton case, the formula for the estimation of the number of **FNP** background events with up to three **FNP** leptons is written as:

$$\begin{aligned} N_{TTT}^{FFF} &= N_{TTT} - N_{TTT}^{RRR} = F_1(N_{LTT} - N_{LTT}^{RRR}) + F_2(N_{TLT} - N_{TLT}^{RRR}) \\ &\quad + F_3(N_{TTL} - N_{TTL}^{RRR}) - F_1 F_2 (N_{LLT} - N_{LLT}^{RRR}) \\ &\quad - F_2 F_3 (N_{TLL} - N_{TLL}^{RRR}) - F_1 F_3 (N_{LTL} - N_{LTL}^{RRR}) \\ &\quad + F_1 F_2 F_3 (N_{LLL} - N_{LLL}^{RRR}), \end{aligned} \quad (5.9)$$

where F_i is the fake factor calculated for the i -th lepton. The other terms are the number of events with different lepton combinations, where the subscripts indicate if leptons are tight (T) or loose (L), and the superscripts indicate the **FNP** (F) or real (R) choices of leptons. For example, N_{TTT}^{FFF} is the number of events with three **FNP** leptons which pass the tight selection, N_{TTL}^{RRR} is the number of events with three real leptons, the first two of which pass the tight selection and the third passes the loose selection, but not the tight one; and so on for all the other terms. Terms entering the differences in Equation 5.9 are taken from data from which yields of those **MC** background processes that are not estimated by the method are subtracted.

Extraction of single-lepton fake factors

The tight and loose selection used to derive the formula for the estimation of the **FNP** leptons are based on the baseline and signal definitions given in Section 4.6. Electrons and muons are defined as tight if they satisfy the signal definition requirements, while they are counted as loose if they pass the baseline selection, but they fail to pass the signal criteria.

The **FF** are extracted in a dedicated region, defined so it is highly pure in **FNP** background. The **FF** can be written as:

$$F_i = \frac{N_T^{\text{data}} - N_T^{\text{others}}}{N_L^{\text{data}} - N_L^{\text{others}}}, \quad (5.10)$$

where N_T^{data} and N_T^{others} are the number of events in which the i -th lepton passes the tight selection, for data or for all the **MC** processes that are not estimated with the same data-driven method. Once the F_i are calculated, these enter the final **FNP** estimation through Equation 5.9. The **FF** are extracted separately for electrons and muons.

5.3.1.2 Matrix Method

The Matrix Method is based on the inversion of the matrix in Equation 5.7, in order to obtain an expression of the number of **FNP** leptons depending on the number of tight and loose leptons. For the single-lepton case, this results gives the equation:

$$N_T^{\text{F}} = \frac{\epsilon_{\text{F}}}{\epsilon_{\text{R}} - \epsilon_{\text{F}}} (N_T(\epsilon_{\text{R}} - 1) + \epsilon_{\text{R}} N_L), \quad (5.11)$$

where the ϵ_{R} and ϵ_{F} are again the real-lepton and the fake-lepton efficiencies, respectively.

As before, the Matrix Method can be generalised to higher number of fake leptons. In the case of three leptons in the final state, a 8×8 matrix is inverted in order to obtain a three-lepton counterpart of Equation 5.11.

The Matrix Method uses real-lepton and fake-lepton efficiencies for the derivation of the fake contribution. The real-lepton efficiencies can be calculated via a *tag-and-probe* technique. This selects a *tag* lepton which is required to pass the tight selection,

and an additional *probe* lepton. The invariant mass of the two leptons is required to be within ± 10 GeV of the Z boson mass, to ensure that the two selected objects are prompt leptons coming from the $Z \rightarrow \ell\ell$ decay. The real-lepton efficiency is then defined as the ratio between the number of probe leptons which pass the tight selection and those passing the loose requirements.

The extraction of the fake-lepton efficiencies follows a procedure which is very similar to the one applied for the calculation of the FFs. First, a fake-enriched Control Region (CR) is defined selecting events with at least one b -tagged jet and two same-sign leptons, comprising a muon with $p_T > 40$ GeV and an additional lepton which passes the loose selection. The fake-lepton efficiencies are calculated using loose leptons for reference, taking the ratio of the number of probes passing the tight selection to the number of those passing the loose definition.

5.3.2 Normalisation of irreducible background

Approximated values of the cross sections, detector effects and pile-up effects can affect the modelling of the irreducible background. A *semi-data-driven* technique is used to address a possible mis-modelling. A dedicated control region, referred to as CR, is defined. Its definition must select the targeted irreducible background with high purity, while keeping possible contaminations from the targeted SUSY signals as low as possible. A CR needs to be kinematically close to the relevant SRs, and must be kept *orthogonal* to the SRs, meaning that no kinematic overlap can occur between the CR and any of the SRs.

Expected yields of the targeted irreducible background are normalised to the observed data, in order to assign a Normalisation Factor (NF) to it. This is achieved by a fit in the CRs, referred to as *background-only fit*, based on the maximisation of a likelihood, built on the expected Poisson probability distributions of the observed data and expected background. A fit parameter μ is assigned to the irreducible background. This is fixed by the fit, and corresponds to the NF. The general form and use of likelihoods in this thesis are further discussed in Section 5.5, where other important aspects of the statistical interpretation of results are also detailed.

5.3.3 Validation of the background estimation

Methods and techniques used for the estimation of the main sources of background must be validated. This is done in dedicated Validation Region (**VR**), whose definition needs to be tailored to relevant backgrounds but also to ensure low contamination from the targeted **SUSY** signals. Similarly to the **CRs**, all the **VRs** are defined to be orthogonal to the **SRs**, while targeting a similar kinematic phase space. A **VR** does not need to be dominated by a specific process, but has to include other sources of backgrounds so to mimic the relative contribution of **SM** processes in the **SRs**. For illustration, the interplay between the **SRs**, **CRs** and **VRs** is shown schematically in Figure 5.3, where the orthogonality between all the different regions is achieved by applying cuts on just two observables.

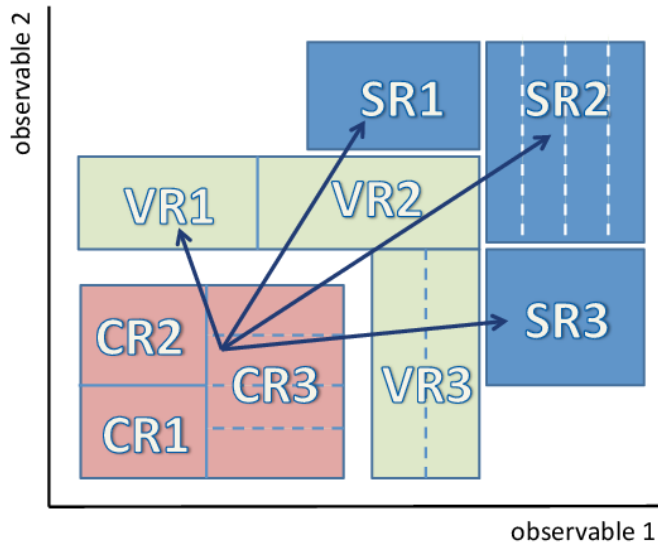


Figure 5.3: Illustration of the interplay between **CRs**, **VRs** and **SRs**. The arrows represent the extrapolation of **NFs** from the **CRs** to the **VRs** and **SRs**. [133]

5.4 Systematic uncertainties

Systematic uncertainties play an essential role in the interpretation of results and their statistical treatment. Several sources of systematic uncertainties are considered. Firstly, those linked to the calibration of physics objects and the resolution on measured kin-

ematic quantities, such as transverse momenta and E_T^{miss} . Such uncertainties are mainly due to detector effects: pile-up and non-linear response from calorimeter towers are examples of possible sources of said systematic uncertainties. Another source of uncertainty is given by the theoretical predictions of SM processes, such as dependencies on the QCD scale or the choice of PDFs, or assumptions on the value of α_s .

5.4.1 Detector-level uncertainties

Electrons and muons There are two kinds of uncertainties associated with electrons. The uncertainties on the energy scale originate from possible mis-calibrations of the ECal, while uncertainties on the energy resolution depend on the precision of calorimeter-based measurements of the energy of electrons. Electron energy scale and energy resolution uncertainties are extracted as a function of p_T and η , using calibration procedures based on the analysis of $Z \rightarrow ee$ and $J/\Psi \rightarrow ee$ decays [108].

Similarly to the electrons, detector-level uncertainties on the energy scale and the resolution for muons are estimated through calibrations using of $Z \rightarrow \mu\mu$ and $J/\Psi \rightarrow \mu$ decays. Contribution from the MS and the ID are considered [134].

Jets The Jet Energy Scale (JES) systematics are extracted from the calibration of MC samples using measured values of the jet energy as measured in test beams, and including contribution for in-situ calibration of Z +jets, γ +jets, multi-jet processes, pile-up effects and flavour tagging [135]. The Jet Energy Resolution (JER) uncertainty is obtained as the correction applied to the MC jet p_T distribution after applying a Gaussian smearing scale factor obtained from data to account for detector response effects [113].

In the jet identification, the JVT algorithm is also affected by systematic uncertainties. These are estimated from $Z(\rightarrow \mu\mu)$ +jets events, and are given by differences between data and MC, using both SHERPA and POWHEG to account for possible effects due to the parton shower model [116].

E_T^{miss} The uncertainties on the calibration of the objects entering the E_T^{miss} calculation in Equation 4.5 are propagated as uncertainty on the same E_T^{miss} . In addition, specific systematic uncertainties are extracted for the soft terms in the E_T^{miss} using data-to-

MC comparisons [124]. In particular, the $Z \rightarrow \mu\mu$ decay is used, which does not have any source of prompt E_T^{miss} . Disagreements between data and MC can arise in the distributions of the longitudinal and transverse projections of the soft term of Equation 4.5 onto the hard terms. These differences are taken as systematic deviations.

Pile-up Pile-up reweighting is based on the comparison of the pile-up profile between data and MC. Varying the distribution of the average number of interaction per bunch crossing by $\pm 10\%$ can introduce a systematic in the final pile-up-related event weight. The discrepancy between the nominal weight and the variation is taken as systematic uncertainty.

b-jet tagging Techniques for the identification of b - and c -jets are described in Section 4.4.5. Flavour-tagging algorithms carry systematic uncertainties coming from different sources, such as differences in the ratio of b and c quark between data and simulated events, as well as differences in the b -tagging algorithm efficiency between data and $t\bar{t}$ MC simulations [120].

5.4.2 Theory uncertainties

Theory systematic uncertainties are estimated to cover inaccuracies in the theoretical prediction of key parameters. Two main sources of theory uncertainties are considered:

QCD scale Variations arising from the the assumption on the normalisation scale μ_S and the factorisation scale μ_F . The uncertainties propagate to the calculation of the matrix elements in the perturbation theory and, therefore, to the final value of the cross-sections. Typically, QCD scale uncertainties are estimated by varying the normalisation and factorisation scales by a factor of two up and down;

α_s Experimental uncertainties on the estimation of α_s are considered, as well as uncertainties associated with the running of the strong coupling, used to calculate α_s at different energy scales;

PDFs Experimental uncertainties on the set of PDF used in the estimation of the matrix elements for the cross-section calculations. These are obtained following specific procedures for the considered PDF set and, generally, account for experimental errors on the data used for the extrapolation of the PDF. Theoretical uncertainties on the PDF arise from the running of the α_s , and are estimated by varying the value of the α_s and taking into account the differences in the calculated values of the PDF.

5.5 Statistical analysis of results

The statistical interpretation of the searches presented in this thesis is obtained using the HISTFITTER framework [133, 136], which provides all the packages and tools necessary both to perform the fits in the CRs (for the extraction of the NFs for the irreducible backgrounds) and to test the signal hypothesis and draw exclusion contours for the targeted SUSY models.

The fits are based on likelihoods, and systematic uncertainties are treated as *nuisance parameters*, labelled θ_j . This is done by describing each j -th systematic uncertainty as a Gaussian centred at $\theta_j^0 = 0$ and with width corresponding to the systematic variation itself. The fits in the HISTFITTER framework are based on the maximum likelihood approach. For instance, the case of the background-only fit, the likelihood is obtained from the Poisson probability distributions of the observed data, given the expected backgrounds, in all the CR bins. A fit parameter μ is then assigned to the targeted irreducible background as a NF, and constrained by maximising the likelihood simultaneously in all the CRs.

5.5.1 Hypothesis test

5.5.1.1 Likelihoods and test statistics

A key point of the statistical treatment of search results is to find a way to establish if the observations are compatible with the SM-only predictions or not.

The likelihood L is again the fundamental ingredient of the procedure, generally interpreted as a measure of the compatibility of the expected number of both back-

ground and chosen signal model with the observed number of events. In its general form, the likelihood can be written as the product of Poisson distributions P in the considered SRs and CRs:

$$\begin{aligned} L(n, \theta^0 | \mu_{\text{sig}} s, b, \theta) &= P_{\text{SR}} \times P_{\text{CR}} \times \prod_{j \in \text{NP}} G(\theta_j^0 - \theta_j) = \\ &= \prod_{k \in \text{SR}} P(n_k | \lambda_k(\mu_{\text{sig}} s, b, \theta)) \times \prod_{i \in \text{CR}} P(n_i | \lambda_i(\mu_{\text{sig}} s, b, \theta)) \times \prod_{j \in \text{NP}} G(\theta_j^0 - \theta_j), \end{aligned} \quad (5.12)$$

where $P_{\text{SR}} = \prod_{k \in \text{SR}} P(n_k | \lambda_k(\mu_{\text{sig}} s, b, \theta))$ and $P_{\text{CR}} = \prod_{i \in \text{CR}} P(n_i | \lambda_i(\mu_{\text{sig}} s, b, \theta))$ are products of Poisson distributions in the SRs and CRs, respectively, obtained from the observed data and *expectation functions* $\lambda_{i,k}$ which give the expected background events b and the expected signal s in all each region. The fit parameter μ_{sig} , the so-called *signal strength*, is assigned to the signal yields in all the regions as a scale factor, and is constrained by the fit. The last term in the product in Equation 5.12 is the Gaussian profiling of the systematic uncertainties (altogether labeled with the symbol θ).

The test of a hypothesis is done according to the Neyman-Pearson lemma, which affirms that the most powerful tool to probe a hypothesis is to define a *test statistics* as a ratio of likelihoods. The LHC experiments adopt a conventional formulation for the test statistics, $t_{\mu_{\text{sig}}}$, written as:

$$t_{\mu_{\text{sig}}} = -2 \ln \frac{L(\mu_{\text{sig}} | \hat{\theta})}{L(\hat{\mu}_{\text{sig}} | \hat{\theta})}, \quad (5.13)$$

where the numerator is a likelihood maximised only over the nuisance parameters θ , while at the denominator the likelihood is maximised looking at both the nuisance parameters θ and the signal strength μ_{sig} .

In general, the test statistics in Equation 5.13 can be used to build a pdf $f(t_{\mu} | \mu)$ of the t_{μ} under the assumption μ . The integral of the pdf $f(t_{\mu} | \mu)$ over the interval $[t_{\mu, \text{obs}}, +\infty]$, where $t_{\mu, \text{obs}}$ is the observed value of the test statistics, is called *p-value*. This is interpreted as the probability to obtain a test statistics greater than $t_{\mu, \text{obs}}$, therefore the probability that the observed data is consistent with hypothesis defined by the choice of μ , as shown in Figure 5.4. For the specific cases in this thesis, the parameter μ is replaced with the signal strength μ_{sig} , in order to test both the $\mu_{\text{sig}} = 0$ (SM-only) and the $\mu_{\text{sig}} = 1$ (SM+SUSY) hypotheses.

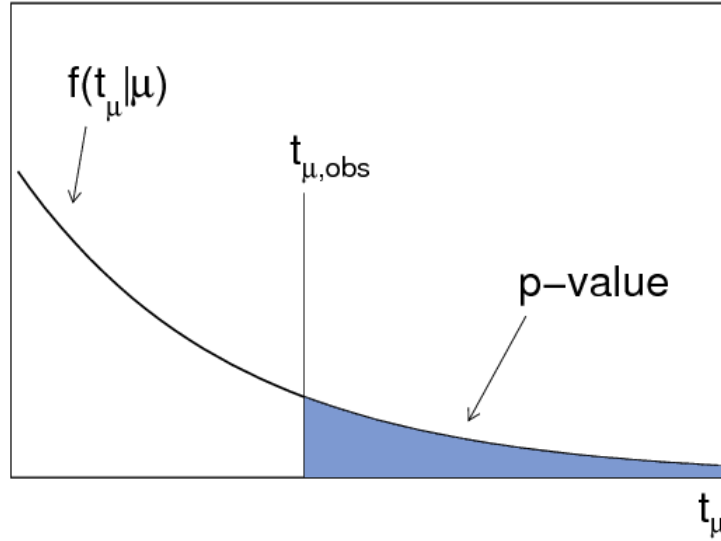


Figure 5.4: Definition of the p-value as the probability of the data to be consistent with the null hypothesis under which the pdf of the test statistics was built. [137]

The HISTFITTER framework allows the test of the **SM+SUSY** by taking direct inputs from the simulation of the **SUSY** models considered (*model-dependent fit*) or by assigning a given value to the signal yields (conventionally +1) in the **SRs** entering the calculation of the test statistics (*model-independent fit*).

5.5.1.2 Confidence levels

As it can only state if the **SM+SUSY** hypothesis is rejected or not, the p-value in itself is not adequate to assess consistency between the observations and the **SM**-only hypothesis. A more appropriate way to test both hypotheses at the same time is by building two pdfs for the test statistics q as in Equation 5.13, one for the **SM**-only hypothesis b and one for the **SM+SUSY** hypothesis $b + s$. These are shown in Figure 5.5. For the pdf $f(q|b)$, one can define the probability p_b , corresponding to the yellow area in in Figure 5.5, obtained as integral of $f(q|b)$ over the $[-\infty, q_{\text{obs}}]$ interval, and interpreted as the probability that the observation is not consistent with the **SM**-only hypothesis. At the same time, for the pdf $f(q|s + b)$, the probability p_{b+s} , the green area in Figure 5.5, is calculated as integral of $f(q|s + b)$ on the $[q_{\text{obs}}, +\infty]$ interval, and it is interpreted as the probability that the observations are consistent with the alternative hypothesis.

The probabilities p_b and p_{b+s} are then used to define the Confidence Level (**CL**), interpreted as the grade of rejection of the **SM+SUSY** model, in favour of the **SM** hypo-

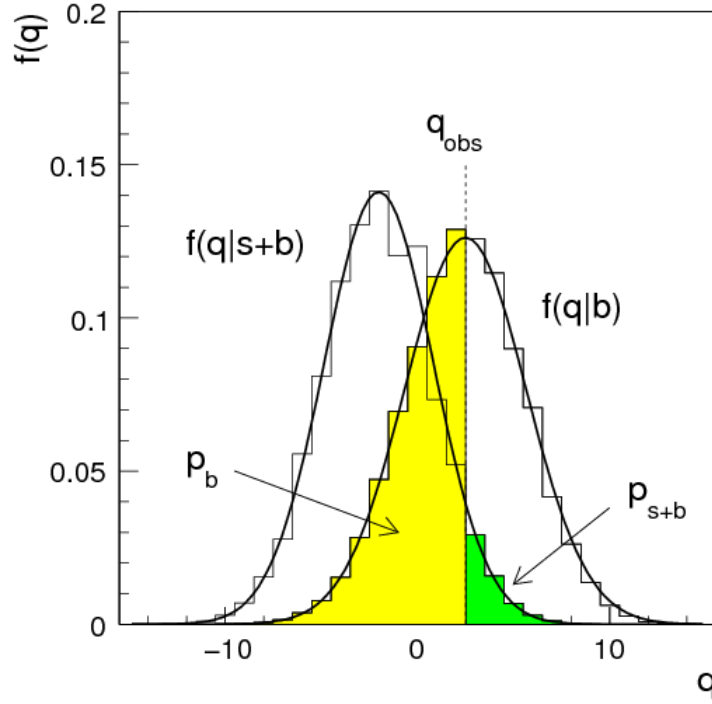


Figure 5.5: Definition of the p-values p_{b+s} and p_b , defined under the alternative hypothesis and the null hypothesis pdf, respectively. The test-statistics q corresponds to the likelihood ratio in Equation 5.13. [137]

thesis. It is expressed as:

$$CL_S = \frac{p_{b+s}}{1 - p_b}. \quad (5.14)$$

For sufficiently small values of the CL_S the alternative **SM+SUSY** is excluded and the observations are interpreted as a statistical fluctuation of the **SM** background. In this thesis, the convention is used that the **SM+SUSY** hypothesis is *excluded* if its calculated CL_S is less than 0.05.

6

RESULTS OF $\tilde{\chi}_1^\pm \tilde{\chi}_2^0$ SEARCHES WITH THREE-LEPTON AND E_T^{miss} FINAL STATES

In this chapter, results from the Run-2 ATLAS searches for $\tilde{\chi}_1^\pm \tilde{\chi}_2^0$ with three light leptons and missing transverse momentum in the final states to which I have made major contribution are presented. The considered dataset is the one recorded by the ATLAS experiment in proton-proton collisions at $\sqrt{s} = 13$ TeV between 2015-2018.

Firstly, results from an early Run-2 analysis of the first 36.1 fb^{-1} dataset collected by ATLAS between the year 2015 and 2016 is described concisely in Section 6.1. This initial work targeted the production of $\tilde{\chi}_1^\pm \tilde{\chi}_2^0$ decaying via Wh , as an early analysis in preparation for those with the full Run-2 dataset. It was included in the publication reported in Ref. [138].

Results for the searches for $\tilde{\chi}_1^\pm \tilde{\chi}_2^0$ via WZ and Wh decays to three light leptons plus E_T^{miss} using the full 139 fb^{-1} Run-2 dataset are described in Section 6.2. These results were published in the ATLAS conference note in Ref. [139], made public for LHCP2020. A paper is in preparation. The results are a significant improvement on previously published results and provide an important contribution to the comprehensive searches for electroweak SUSY signals by the ATLAS collaboration using the full Run-2 dataset.

6.1 Early Run-2 analysis searching for $\tilde{\chi}_1^\pm \tilde{\chi}_2^0$ via Wh

The early Run-2 analysis, published in Ref. [138], searched for $\tilde{\chi}_1^\pm \tilde{\chi}_2^0$ production with decays via Wh using the first 36.1 fb^{-1} collected by ATLAS between 2015-2016. A num-

ber of final states were considered: with the Higgs boson decaying to $b\bar{b}$ and the W decaying hadronically (full hadronic channel) or leptonically ($1\ell + bb$ channel); the one where $H \rightarrow \gamma\gamma$ and $W \rightarrow \ell\nu$ ($1\ell + \gamma\gamma$); and the fully leptonic channels, either with two same-sign leptons ($\ell^\pm\ell^\pm$) or three leptons (3ℓ) in the final state.

For this paper, I was the main analyser for the 3ℓ final state. I developed and optimised the **DFOS SRs**, and worked on the definition of the **CR** and **VR** for the corresponding background estimation, the estimation of the irreducible backgrounds and the statistical interpretation of the results.

Event selection

For this analysis, a logical OR combination of di-lepton and single-lepton trigger chains was considered. The trigger chains used are those un-prescaled with lowest available p_T thresholds, listed in Table 5.2 and Table 5.3. The trigger strategy and the object definitions were harmonised across the 3ℓ and the $\ell^\pm\ell^\pm$ channels, which shared also the same method for the estimation of the **FNP** background.

All the events entering the analysis were required to have exactly three light leptons with $p_T > 25$ GeV. Events were rejected if they contained any b -tagged jet. A cut on $m_{\ell\ell\ell} > 20$ GeV was used to provide rejection of low-mass resonances and **FNP** backgrounds, allowing the reduction of the total **SM** background by around the 40%, while selecting approximately the 90% of the target **SUSY** signal. The criteria listed above were referred to as the *preselection*.

The **SFOS** and **DFOS** flavour-sign categories, as discussed in Section 5.2.1, were used to define the **SRs**. Contrary to the one described in Section 5.2.1, the early Run-2 Wh analysis considered an alternative way of solving the possible ambiguity when more than one **SFOS** pair is present in the event. Instead of identifying the **SFOS** lepton pair as the one whose invariant mass is closest to the nominal Z boson mass, the third lepton not in the **SFOS** pair was chosen to be the one with the minimum value of transverse mass m_T^{\min} .

The **SR** definitions for this early analysis are listed in Table 6.1 and Table 6.2, for the **DFOS** and the **SFOS** selections, respectively.

Variable	SR3L-DFOS-0J	SR3L-DFOS-1Ja	SR3L-DFOS-1Jb
Flavour/sign	DFOS	DFOS	DFOS
$N_{\text{jets}} (p_{\text{T}} > 20 \text{ GeV})$	= 0	> 0	> 0
$E_{\text{T}}^{\text{miss}} [\text{GeV}]$	> 60	$\in [30, 100]$	> 100
$m_{\ell_{\text{DFOS}} + \ell_{\text{near}}} [\text{GeV}]$	< 90	< 60	< 70
$\Delta R_{\text{OS, near}}$	-	< 1.4	< 1.4
$\Delta\phi_{\text{SS}}$	-	-	< 2.8

Table 6.1: Definitions of the 3ℓ **DFOS** SRs used in the early Run-2 Wh analysis. [138]

Variable	SR3L-SFOS-0Ja	SR3L-SFOS-0Jb	SR3L-SFOS-1J
Flavour/sign	SFOS	SFOS	SFOS
$m_{\text{SFOS}}^{\text{min}} [\text{GeV}]$	> 20, $\notin [81.2, 101.2]$	> 20, $\notin [81.2, 101.2]$	> 20, $\notin [81.2, 101.2]$
$N_{\text{jets}} (p_{\text{T}} > 20 \text{ GeV})$	= 0	= 0	> 0
$E_{\text{T}}^{\text{miss}} [\text{GeV}]$	$\in [80, 120]$	> 120	> 110
$m_{\text{T}}^{\text{min}} [\text{GeV}]$	> 110	> 110	> 110

Table 6.2: Definitions of the 3ℓ **SFOS** SRs used in the early Run-2 Wh analysis. [138]

The **DFOS** selection used the jet multiplicity to select events with either no light jets (SR3L-DFOS-0J) or at least one light jet (SR3L-DFOS-1Ja,b). The **SRs** with at least one signal jet are then distinguished according to a binning in $E_{\text{T}}^{\text{miss}}$. Cuts on $m_{\ell_{\text{DFOS}} + \ell_{\text{near}}}$, $\Delta\phi_{\text{SS}}$ and $\Delta R_{\text{OS, near}}$ are also applied to some or all the **DFOS** SRs.

In the case of the **SFOS** selection, **SRs** were again defined based on their light-jet multiplicity (N_{jet}), selecting events with either no light jets (SR3L-SFOS-0Ja,b) or at least one light jet (SR3L-SFOS-aJ). The two zero-jet **SRs** are distinguished based on $E_{\text{T}}^{\text{miss}}$. A cut $m_{\text{T}}^{\text{min}} > 110 \text{ GeV}$ is used for all the three **SRs**, to suppress contribution from WZ background process.

Background estimation

A **CR** is defined in order to normalise the expected **MC** yields for the WZ background to the data, and find an **NF** to rescale contributions in the **SRs**. This is performed by the background-only fit procedure described in Section 5.3.2.

The CR3L-onZ-highMET region requires events to have a **SFOS** lepton pair with invariant mass $m_{\text{SFOS}}^{\text{min}}$ in the $[81.2, 101.2] \text{ GeV}$ interval. Events must also satisfy the requirement $E_{\text{T}}^{\text{miss}} > 80 \text{ GeV}$, and preselection cuts are applied. Full list of cuts used

for the definition of the CR3L-onZ-highMET CR is shown in Table 6.3. Contamination from the targeted SUSY signal model in the CR3L-onZ-highMET is $< 1\%$ for all the considered mass points. A NF of 1.11 ± 0.13 is extracted via the background-only fit. The E_T^{miss} distribution after the background-only fit in the CR is shown in Figure 6.1. For this and all the other distributions in this chapter, the last bin is an overflow bin, which thus includes entries above the shown x -axis range.

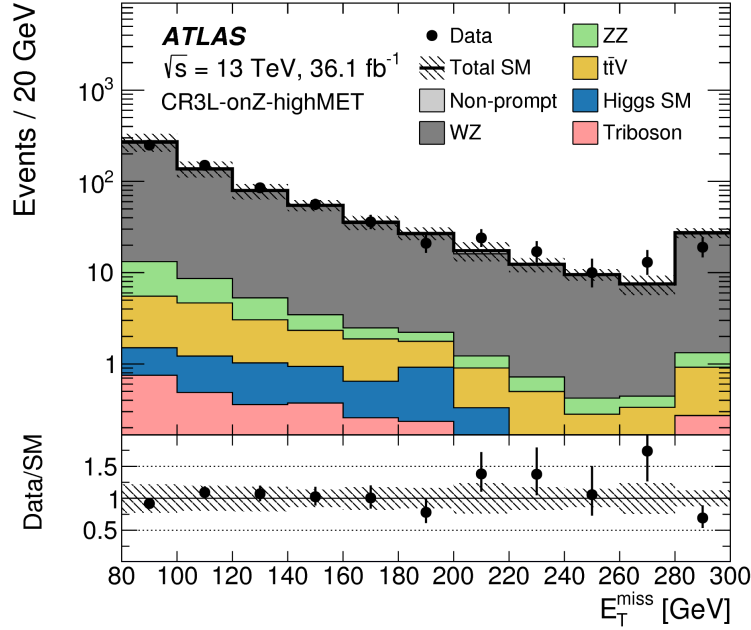


Figure 6.1: E_T^{miss} distribution in the CR3L-onZ-highMET, after background-only fit. All systematic and statistical uncertainties are considered. [138]

A VR was defined of the WZ background estimation, called VR3L-offZ-HighMET, which selects events in the SFOS flavour-sign category with $m_{\text{SFOS}}^{\text{min}} > 20$ GeV and outside the [81.2, 101.2] GeV interval. In addition, events must have $E_T^{\text{miss}} > 80$ GeV and $m_T^{\text{min}} < 110$ GeV. The latter cut ensures full orthogonality to the SRs and a very limited contamination by the targeted SUSY signal, of again the order of 1% or less for all the considered mass points. The definition of the VR3L-offZ-HighMET VR is shown in Table 6.3.

Data is compared to the SM predictions in the VR, after applying the extracted NF to the WZ background. In Figure 6.2 yields of $\ell^\pm \ell^\pm$ and 3ℓ validation regions are shown. The yields for VR3L-offZ-HighMET region are shown in last bin. The other two bins show results for two VRs used in the $\ell^\pm \ell^\pm$ analysis, not discussed in this thesis.

The FNP backgrounds are estimated with the data-driven Matrix Method tech-

Variable	CR3L-onZ-HighMET	VR3L-offZ-HighMET
Flavour/sign	SFOS	SFOS
$m_{\text{SFOS}}^{\text{min}}$ [GeV]	$\in [81.2, 101.2]$	$> 20, \notin [81.2, 101.2]$
$E_{\text{T}}^{\text{miss}}$ [GeV]	> 80	> 80
$m_{\text{T}}^{\text{min}}$ [GeV]	-	< 110

Table 6.3: List of cuts for the definition of the CR3L-onZ-HighMET **CR** and the VR3L-offZ-HighMET **VR**, used for the estimation and the validation of the WZ background in the early Run-2 $3\ell Wh$ search. Region definitions extracted from Ref. [138].

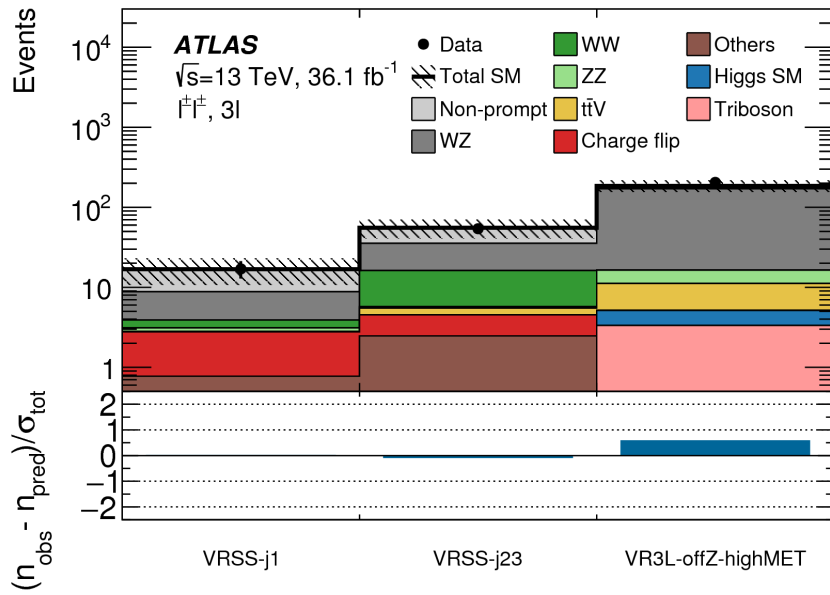


Figure 6.2: In the upper panel, yields of observed data and expected background in VR3L-offZ-HighMET (last bin), after the background-only fit. In the lower panel, the data on **SM** predictions ratio for all the regions are reported. Systematic and statistical uncertainties are considered. [138]

nique, discussed in Section 5.3.1.2. For completeness, validation of the data-driven estimation of the **FNP** backgrounds is briefly discussed in what follows, although I have not made major contribution to this part of the early Wh analysis.

A dedicated **VR**, named VRSS, was defined after selecting events with two same-sign leptons, providing high purity in **FNP** background. Comparison between data and the expected **SM** background in VRSS in the ee channel is shown in Figure 6.3, displaying good agreement everywhere.

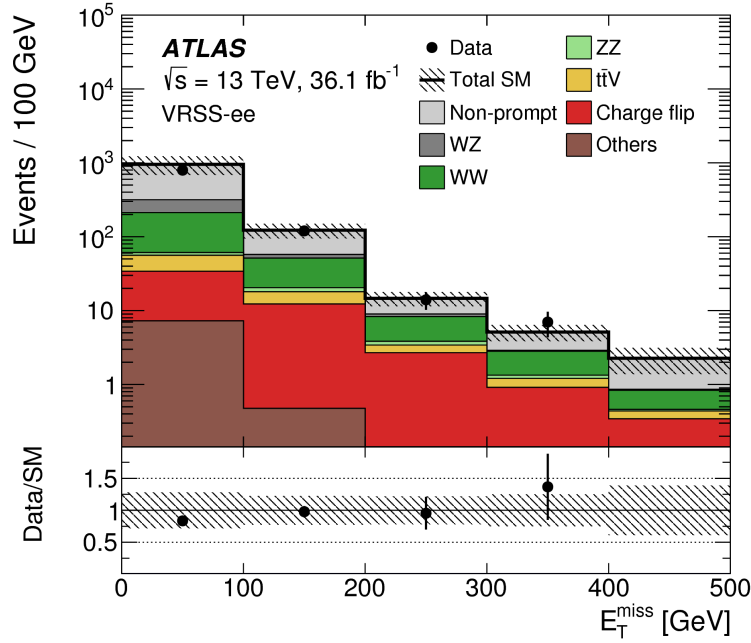


Figure 6.3: Distribution of E_T^{miss} in the VRSS-ee VR, used to demonstrate the goodness of the FNP background estimation for the multileptonic channels examined in the early Run-2 Wh analysis. [138]

Systematic uncertainties

Along with the detector and theory uncertainties, described in Section 5.4.1 and Section 5.4.2, a dedicated set of systematics uncertainties were evaluated for the data-driven method used for the FNP background estimation. These uncertainties are obtained by changing the definitions of the CR used for the extraction of the real-lepton and the fake-lepton efficiencies, as further discussed in Ref. [138].

The breakdown of all the systematics in the SR is shown in Table 6.4 and Table 6.5, for the DFOS and SFOS regions, respectively. As seen in Table 6.4 and Table 6.5, the detector and theoretical systematic uncertainties are dominant in most of the regions. In a few cases, they are comparable to the statistical uncertainties on the MC samples.

Results and statistical interpretation

Results in the SRs for the early Run-2 $Wh 3\ell$ analysis are shown in Table 6.6 and Table 6.7. These are compatible with SM expectations within uncertainties.

Distributions of relevant variables are shown in Figure 6.4, for SR3L-DFOS-0J, SR3L-

Uncertainty of region	SR3L-DFOS-0J	SR3L-DFOS-1Ja	SR3L-DFOS-1Jb
Total background expectation	2.05	8	1.7
Total background uncertainty	± 0.98	± 4	± 0.7
Systematic, experimental	± 0.8	± 4	± 0.5
Systematic, theoretical	± 0.11	± 0.25	± 0.16
Statistical, MC samples	± 0.6	± 1.2	± 0.4
Statistical, μ_{WZ}	± 0.022	± 0.12	± 0.06

Table 6.4: Uncertainties in units of number of events in the **DFOS SRs**. Different sources of uncertainties can correlate and the total does not necessarily correspond to the squared sum of all the contributions. The category "experimental" comprises the detector systematic uncertainties and the ones related to the **FNP** data-driven estimation. Numbers extracted from Ref. [138].

Uncertainty of region	SR3L-SFOS-0Ja	SR3L-SFOS-0Jb	SR3L-SFOS-1J
Total background expectation	3.8	2.37	11.5
Total background uncertainty	± 1.7	± 0.96	± 2.6
Systematic, experimental	± 1.7	± 0.8	± 2.0
Systematic, theoretical	± 0.15	± 0.22	± 1.5
Statistical, MC samples	± 0.6	± 0.4	± 0.9
Statistical, μ_{WZ}	± 0.3	± 0.24	± 0.9

Table 6.5: Uncertainties in units of number of events in the **SFOS SRs**. Different sources of uncertainties can correlate and the total does not necessarily correspond to the squared sum of all the contributions. The category "experimental" comprises the detector systematic uncertainties and the ones related to the **FNP** data-driven estimation. Numbers extracted from Ref. [138].

DFOS-1Jb and SR3L-SFOS-1J regions. These plots are so-called “N-1 distributions”, in which all the **SR** selection cuts but the one on the considered variable are applied. The arrows show the position and “direction” of the cut on the given variable, according to the **SR** definitions in Table 6.1 and Table 6.2.

Observation in the **SRs** are interpreted to give upper limits on the cross section multiplied by branching ratio, by testing the **SM**-only hypothesis through the model-independent procedure, described in Section 5.5.1. The observed and expected number of signal events, namely S_{obs}^{95} and S_{exp}^{95} , and the p-value p_0 are shown in Table 6.8.

The results in the **SRs** can also be used to extract exclusion limits on the masses of the chargino and neutralinos, $m_{\tilde{\chi}_1^\pm/\tilde{\chi}_2^0}$ and $m_{\tilde{\chi}_1^0}$. Due to the limited statistics available for this early analysis, the 3ℓ channel did not yet reach sufficient sensitivity to exclude

SR channels	SR3L-DFOS-0J	SR3L-DFOS-1Ja	SR3L-DFOS-1Jb
Observed events	0	7	1
Fitted bkg events	2.1 ± 1.0	8.3 ± 3.8	1.7 ± 0.7
WZ	0.18 ± 0.13	1.01 ± 0.27	0.54 ± 0.16
ZZ	0.0017 ± 0.0012	0.06 ± 0.02	0.03 ± 0.01
$t\bar{t} + V$	0.0013 ± 0.0013	0.79 ± 0.29	0.43 ± 0.16
Tribosons	0.52 ± 0.28	0.66 ± 0.22	0.23 ± 0.08
Higgs SM	0.39 ± 0.15	$0.1^{+0.5}_{-0.1}$	0.05 ± 0.04
FNP events	1.0 ± 0.9	5.6 ± 3.8	$0.4^{+0.6}_{-0.4}$

Table 6.6: Observed data and expected yields from the relevant **SM** backgrounds for the region SR3L-DFOS-0J, SR3L-DFOS-1Ja and SR3L-DFOS-1Jb. The $W+Z$ **NF** after the background-only fit is applied. The category ‘‘Higgs MC’’ comprises the **SM** $t\bar{t}H$ production. All uncertainties are considered and symmetrised around the nominal post-fit yields, negative errors are truncated at the zero event yields. Numbers extracted from Ref. [138].

SR channels	SR3L-SFOS-0Ja	SR3L-SFOS-0Jb	SR3L-SFOS-1J
Observed events	0	3	11
Fitted bkg events	3.8 ± 1.7	2.4 ± 0.96	11.5 ± 2.6
WZ	2.5 ± 1.2	2.0 ± 0.9	7.4 ± 2.3
ZZ	0.10 ± 0.04	0.07 ± 0.02	0.29 ± 0.09
$t\bar{t} + V$	0.09 ± 0.03	0.02 ± 0.01	1.9 ± 0.5
Tribosons	0.57 ± 0.29	0.16 ± 0.08	1.4 ± 0.4
Higgs SM	$0.24^{+0.25}_{-0.24}$	0.07 ± 0.07	0.07 ± 0.04
FNP events	$0.27^{+0.31}_{-0.27}$	$0.11^{+0.20}_{-0.11}$	$0.4^{+0.5}_{-0.4}$

Table 6.7: Observed data and expected yields from the relevant **SM** backgrounds for the region SR3L-SFOS-0Ja, SR3L-SFOS-0Jb and SR3L-SFOS-1J. The $W+Z$ **NF** after the background-only fit is applied. The category ‘‘Higgs MC’’ comprises the **SM** $t\bar{t}H$ production. All uncertainties are considered and symmetrised around the nominal post-fit yields, negative errors are truncated at the zero event yields. Numbers extracted from Ref. [138].

any signal points. However, results were used to set expected and observed 95% CL upper limits on the cross sections for different assumption on the $m_{\tilde{\chi}_1^\pm/\tilde{\chi}_2^0}$, but only considering mass points with $m_{\tilde{\chi}_1^\pm/\tilde{\chi}_2^0} - m_{\tilde{\chi}_1^0} = 130$ GeV. These upper limits for the 3ℓ channel are shown in Figure 6.5, together with results from all the other Wh search channels considered in Ref. [138]. From this one can see how the 3ℓ channel is sensitive to mass points along the kinematic edge $m_{\tilde{\chi}_1^\pm/\tilde{\chi}_2^0} - m_{\tilde{\chi}_1^0} = 130$ GeV, which is indeed more challenging for other channels.

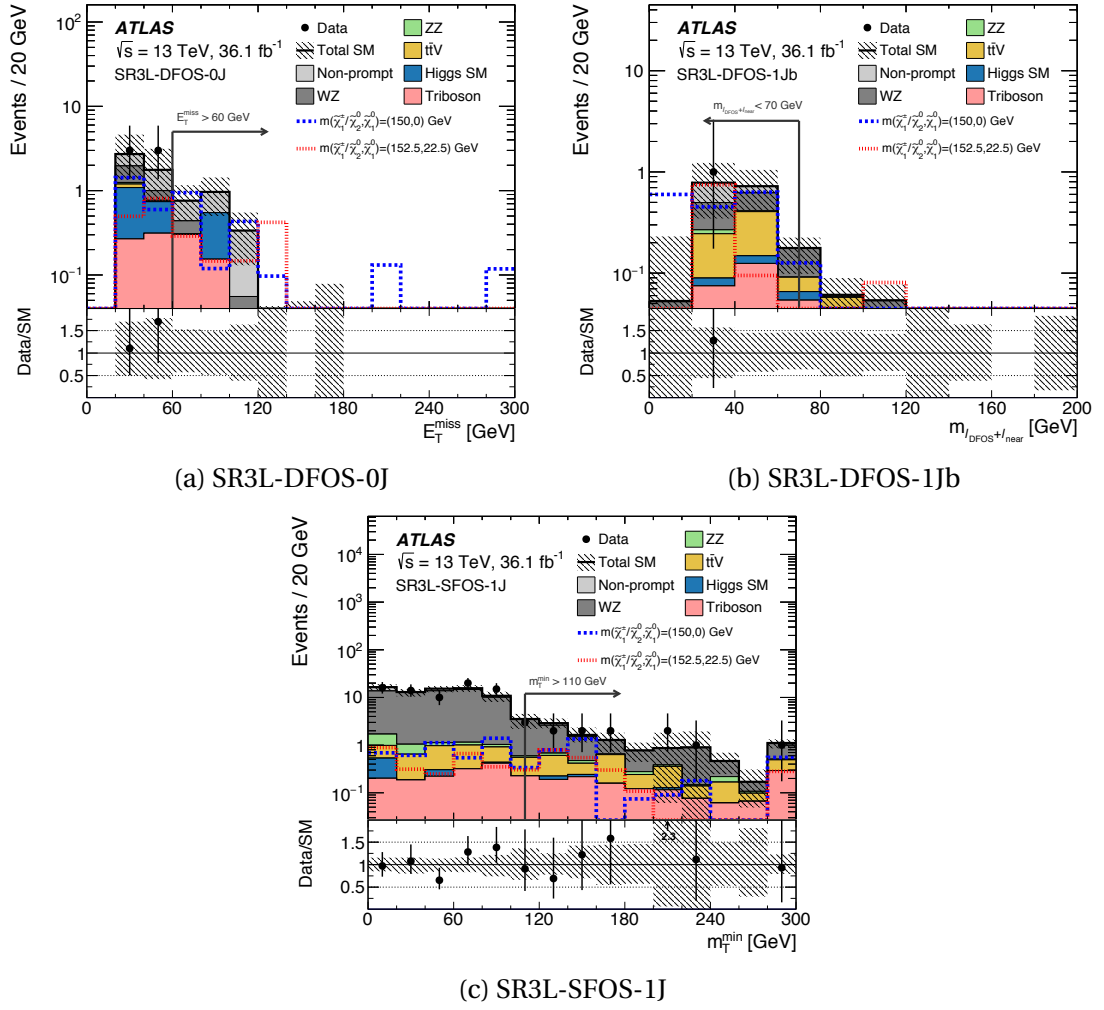


Figure 6.4: N-1 distributions of observed data and SM expectation for (a) the E_T^{miss} in the SR3L-DFOS-0J region, (b) the $m_{\ell_{\text{DFOS}}+\ell_{\text{near}}}$ in the SR3L-DFOS-1Jb region and (c) the m_T^{min} in the SR3L-SFOS-1J region. The lower panel shows the ratio between the observed data and the SM expectation. The SR selections but the cut on the shown variables are applied. Systematic and statistical uncertainties are considered. [138]

The improved analysis using the full Run-2 statistics was developed in order to target the region close to the kinematic edge $m_{\tilde{\chi}_1^\pm/\tilde{\chi}_2^0} - m_{\tilde{\chi}_1^0} = 130$ GeV. The analysis also extends results for decays via WZ bosons. This more extensive and sensitive analysis is the subject of the remainder of this chapter.

	σ_{vis} [fb]	S_{obs}^{95}	S_{exp}^{95}	p_0 -value
SR3L-SFOS-0Ja	0.08	3.0	$4.4_{-1.3}^{+1.9}$	0.47
SR3L-SFOS-0Jb	0.16	5.9	$5.0_{-1.2}^{+2.0}$	0.35
SR3L-SFOS-1J	0.26	9.2	$9.4_{-2.5}^{+3.8}$	0.50
SR3L-DFOS-0J	0.08	3.0	$3.8_{-0.9}^{+1.4}$	0.43
SR3L-DFOS-1Ja	0.25	9.0	$9.2_{-2.0}^{+3.3}$	0.50
SR3L-DFOS-1Jb	0.10	3.7	$4.0_{-0.5}^{+1.6}$	0.50

Table 6.8: The observed 95% CL upper limits on the visible cross-section σ_{vis} and the observed and expected number of events from BSM signal model S_{obs}^{95} and S_{exp}^{95} are shown in the first three columns for each SR. The correspondent discovery p_0 -value is reported in the last column. Systematic and statistical uncertainties are considered. [138]

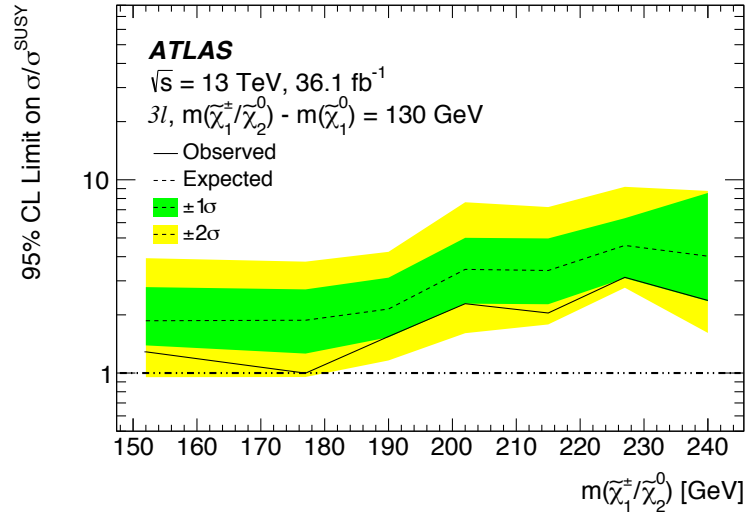
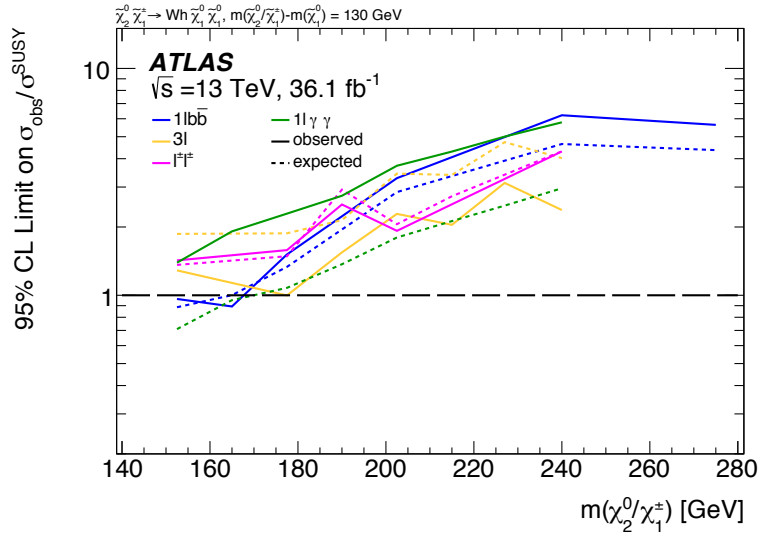
(a) 3ℓ (b) $1\ell + bb, 1\ell + \gamma\gamma, \ell^\pm \ell^\pm, 3\ell$

Figure 6.5: Observed and expected 95% CL upper limits on the cross-section for the (a) 3ℓ channel of searches of $\tilde{\chi}_1^\pm \tilde{\chi}_2^0$ via Wh decays and (b) in comparison to all the consider channels: full-hadronic, $1\ell + bb$, $1\ell + \gamma\gamma$ and $\ell^\pm \ell^\pm$. Different values of $m_{\tilde{\chi}_1^\pm/\tilde{\chi}_2^0}$ up to 240 GeV are considered, when $m_{\tilde{\chi}_1^\pm/\tilde{\chi}_2^0} - m_{\tilde{\chi}_1^0} = 130$ GeV. [138]

6.2 Full Run-2 analysis searching for $\tilde{\chi}_1^\pm \tilde{\chi}_2^0$ via WZ/Wh

In this section, the full Run-2 searches for the production of $\tilde{\chi}_1^\pm \tilde{\chi}_2^0$ decaying to three leptons and transverse missing momentum via intermediate WZ and Wh are described. For the WZ model, signals with sparticle mass spectra were considered which allow decays into either on-shell or off-shell intermediate SM bosons. For the Wh models only on-shell scenarios are considered. This analysis has been published as a conference note by the ATLAS collaboration [139] for the LHCP2020 conference. A journal paper is in preparation. In the following, plots extracted from the published conference note report the corresponding reference in the caption, while those without reference are provided as additional material.

My own work for this publication has focused on the on-shell WZ analysis and the Wh analysis, therefore the off-shell analysis is not discussed in this thesis and the reader is referred to Ref. [139] for details on that aspect of the search.

I was one of the main analysers of the on-shell models, particularly working on the optimisation and definition of the DFOS SR for the Wh channel, the data-driven FNP estimation for both on-shell WZ and Wh models, the validation of the $t\bar{t}$ background estimation, the background-only fit and the statistical interpretation of the results for on-shell WZ and Wh models.

6.2.1 Event selection

Events used in the analyses must have exactly three baseline leptons which also pass the signal object definition in Section 4.6, and pass the logical OR of the di-lepton trigger chains listed in Table 5.2.

As before, a set of initial selection criteria, the pre-selection, are applied. These select events with no b -tagged jets and $E_T^{\text{miss}} > 50$ GeV. Furthermore, in order to ensure the selection of events in the plateau of the trigger efficiencies, p_T threshold are applied to the two leading leptons. The first lepton must have $p_T > 25$ GeV, while the second lepton must have $p_T > 20$ GeV.

6.2.1.1 Signal region definitions

Like in the early Run-2 Wh analysis, events are divided into the **SFOS** and **DFOS** categories, with additional criteria which separate between events with a **SFOS** pair compatible with originating from a Z boson decay or not. Thus, three different selections are identified:

SR_{DFOS}^{Wh} selection: analogously to the early Run-2 Wh analysis, this selection vetoes the presence of a **SFOS** lepton pair and it targets Wh signal models. The **DFOS SRs** have been re-optimised fully for the full Run-2 analysis presented here;

SR_{SFOS}^{Wh} selection: events with an **SFOS** lepton pair, with invariant mass $m_{\ell\ell}$ outside the [75, 105] GeV interval. Two different $m_{\ell\ell}$ ranges are considered. The selection uses events with $m_{\ell\ell} < 75$ GeV, and events with $m_{\ell\ell} > 105$ GeV, independently optimised, both targeting the Wh models;

SR^{WZ} selection: events with an **SFOS** lepton pair, with invariant mass $m_{\ell\ell}$ in the [75, 105] GeV interval around the nominal mass of the Z boson. These **SRs** are optimised to be sensitive to the WZ models.

As I have not worked on the **SFOS SRs** optimisation, these will not be discussed in the same detail as for the regions for which I have myself developed the optimisation.

DFOS signal regions

The optimisation of the **DFOS SRs** is presented by considering three benchmark points for the Wh model: Wh(150,0), Wh(190,60), and Wh(200,25) (as a reminder, the first number in parentheses indicates the mass $m_{\tilde{\chi}_1^\pm/\tilde{\chi}_2^0}$, while the second one is $m_{\tilde{\chi}_1^0}$).

Following and improving the ideas developed for the early Run-2 analysis targeting Wh models, the definition of the **SRs** in the **DFOS** flavour-sign combination uses distances and angular variables to suppress the **SM** backgrounds. Furthermore, similarly again to what showed for the 36.1 fb⁻¹ analysis, the main contribution to the **SM** background entering the **DFOS** selection comes from the reducible background $t\bar{t}$. Non-negligible background contributions come from the production of three vector

bosons and from processes with a SM Higgs boson, mainly the production of a Higgs boson in association with a gauge boson $VH(V=W, Z)$.

Distribution of the light-jet multiplicity (n_{jets}) for events passing the preselection criteria and the DFOS requirement is shown in Figure 6.6. The plot clearly shows sensitivity to the Wh model for low light-jet multiplicities, contrary to some dominant SM backgrounds (e.g. $t\bar{t}$) which instead dominate the bins with at least 2 light jets.

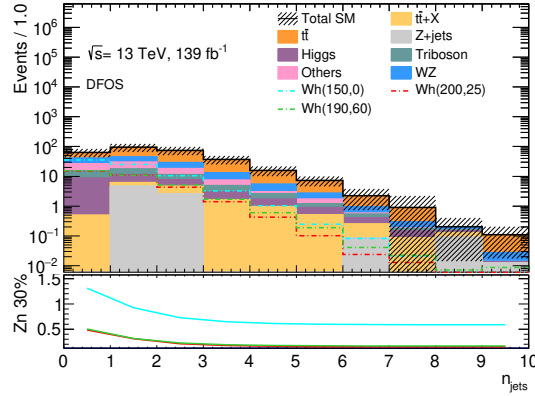


Figure 6.6: In the upper panel, the distributions of the number n_{jets} of light jets for events passing the preselection and the DFOS flavour-sign requirement. The sensitivities Z_n curves are calculated for possible upper cuts on the given variable and assuming a flat 30% total uncertainty on the SM background.

For this analysis, only events with low light-jet multiplicity are considered, indentifying two DFOS SRs: a first one selecting events with no light jets ($\text{SR}_{\text{DFOS}}^{\text{Wh}}-1$); and a second one selecting events with either one or two light jets ($\text{SR}_{\text{DFOS}}^{\text{Wh}}-2$). Each SR is then optimised looking at additional variables, as discussed in what follows.

As mentioned, the choice of selection variables and the SR optimisation follows and improves the SR definitions for the early Run-2 Wh analysis. One of the improvements is the use of $E_{\text{T}}^{\text{miss}}$ significance instead of $E_{\text{T}}^{\text{miss}}$ for the definition of the DFOS SRs. This choice is motivated by the distributions in Figure 6.7a and Figure 6.7b, obtained after selecting events passing the preselection criteria and the DFOS flavour-sign requirement. The distributions show, for all the shown Wh benchmark points, that the $E_{\text{T}}^{\text{miss}}$ significance provides a better discrimination of the signal against the background with respect to the $E_{\text{T}}^{\text{miss}}$.

As further motivation for the choice of $E_{\text{T}}^{\text{miss}}$ significance, the correlation plots between the $E_{\text{T}}^{\text{miss}}$ significance and $E_{\text{T}}^{\text{miss}}$ are shown in Figure 6.8a and Figure 6.8b, for the $t\bar{t}$

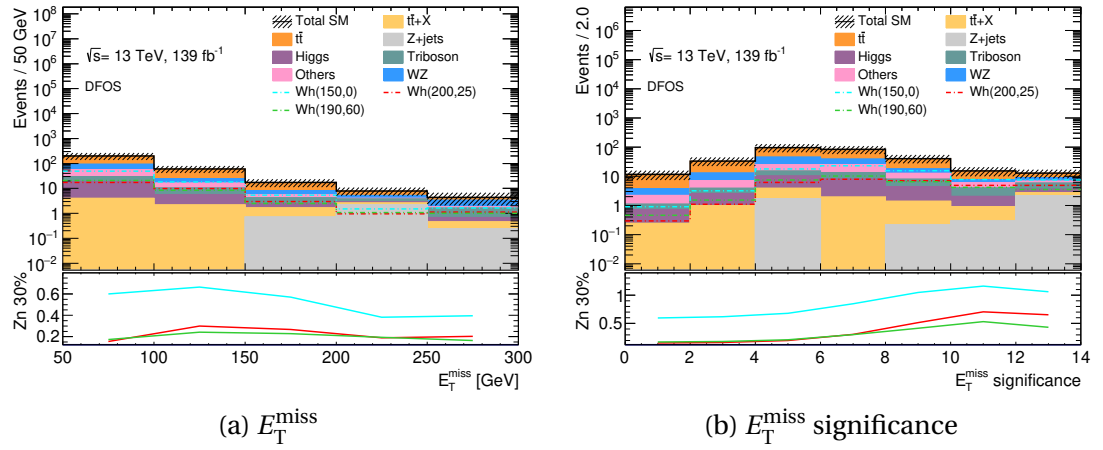


Figure 6.7: In the upper panels, the distributions of the E_T^{miss} and E_T^{miss} significance for events passing the pre-selection criteria and the DFOS flavour-sign selection. All the sensitivities Z_n curves are calculated for possible lower cuts on the given variables and assuming a flat 30% total uncertainty on the SM background.

background and the benchmark point Wh(175,0), respectively. They show that a cut on E_T^{miss} would be unnecessary, if E_T^{miss} significance were used instead.

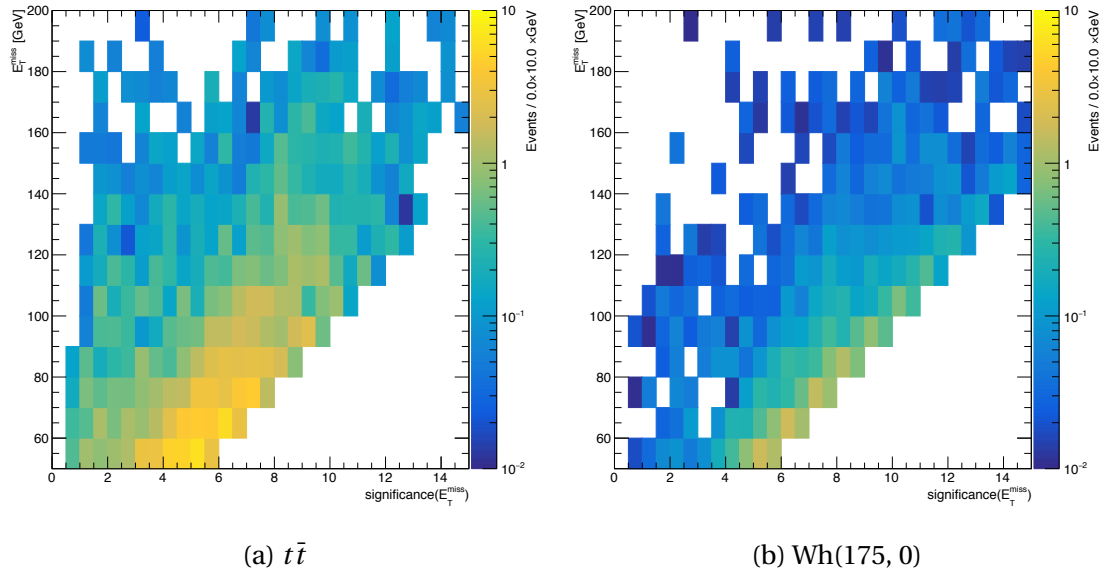


Figure 6.8: Correlation between E_T^{miss} and the E_T^{miss} significance variables for (a) the $t\bar{t}$ process and (b) the Wh signal point Wh(175, 0).

As before, the $\Delta R_{\text{OS, near}}$ distance and the p_T of the third lepton have been explored. Distribution of the $\Delta R_{\text{OS, near}}$ distance and the third lepton p_T are shown in Figure 6.9a and Figure 6.9b, respectively, for events passing the preselection and the DFOS flavour-sign requirement. As can be seen, both the variables provide good suppression of the SM backgrounds, particularly the WZ and $t\bar{t}$.

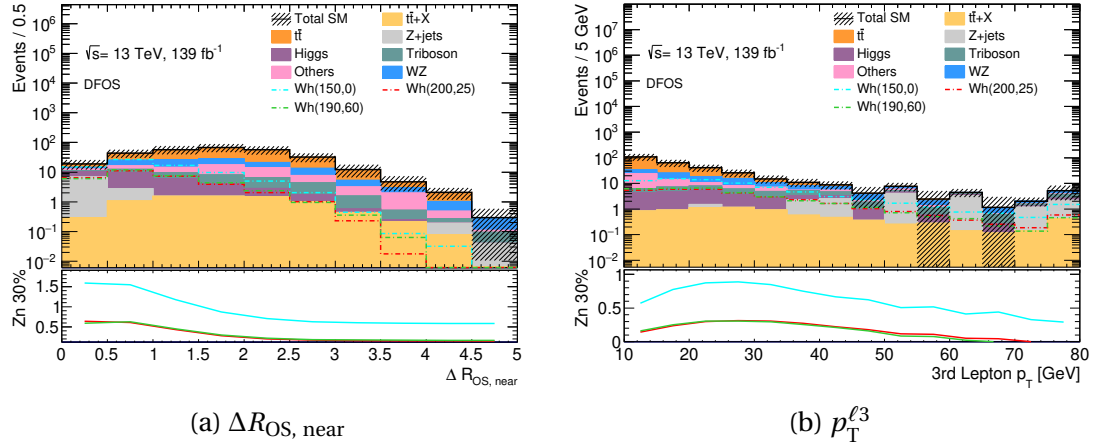


Figure 6.9: In the upper panels, the distributions of the $\Delta R_{OS, \text{near}}$ and the $p_T^{\ell 3}$ for events passing the pre-selection criteria and the DFOS flavour-sign selection. All the sensitivities Z_n curves but those in the $\Delta R_{OS, \text{near}}$ distribution are calculated for possible lower cuts on the given variables and assuming a flat 30% total uncertainty on the SM background.

The two DFOS SRs, $SR_{DFOS}^{Wh}-1$ and $SR_{DFOS}^{Wh}-2$, are defined in Table 6.9. The same selection variables are used in both cases, with different cuts, optimised for the specific selections. The N-1 distributions of SM backgrounds and benchmark Wh signal points in the SRs are shown in Figure 6.10. As anticipated, for the $SR_{DFOS}^{Wh}-1$, the p_T of the third lepton and the E_T^{miss} significance suppress contribution of $t\bar{t}$ and other irreducible background, while $\Delta R_{OS, \text{near}}$ helps reducing background from less dominant sources. For the $SR_{DFOS}^{Wh}-2$, all the chosen selection variables provide good suppression of $t\bar{t}$, WZ and FNP background. After the selections, the background processes with a Higgs boson are dominant in $SR_{DFOS}^{Wh}-1$, while the $t\bar{t}$ process and the FNP backgrounds constitute the main source of background in $SR_{DFOS}^{Wh}-2$.

Variable	Selection requirements	
	$SR_{DFOS}^{Wh}-1$	$SR_{DFOS}^{Wh}-2$
n_{jets}	= 0	$\in [1, 2]$
E_T^{miss} significance	> 8	> 8
$p_T^{\ell 3}$ [GeV]	> 15	> 20
$\Delta R_{OS, \text{near}}$	< 1.2	< 1.0

Table 6.9: Summary of the selection criteria for SRs targeting events with a DFOS lepton pair, for the Wh selection. Preselection criteria are applied. [139]

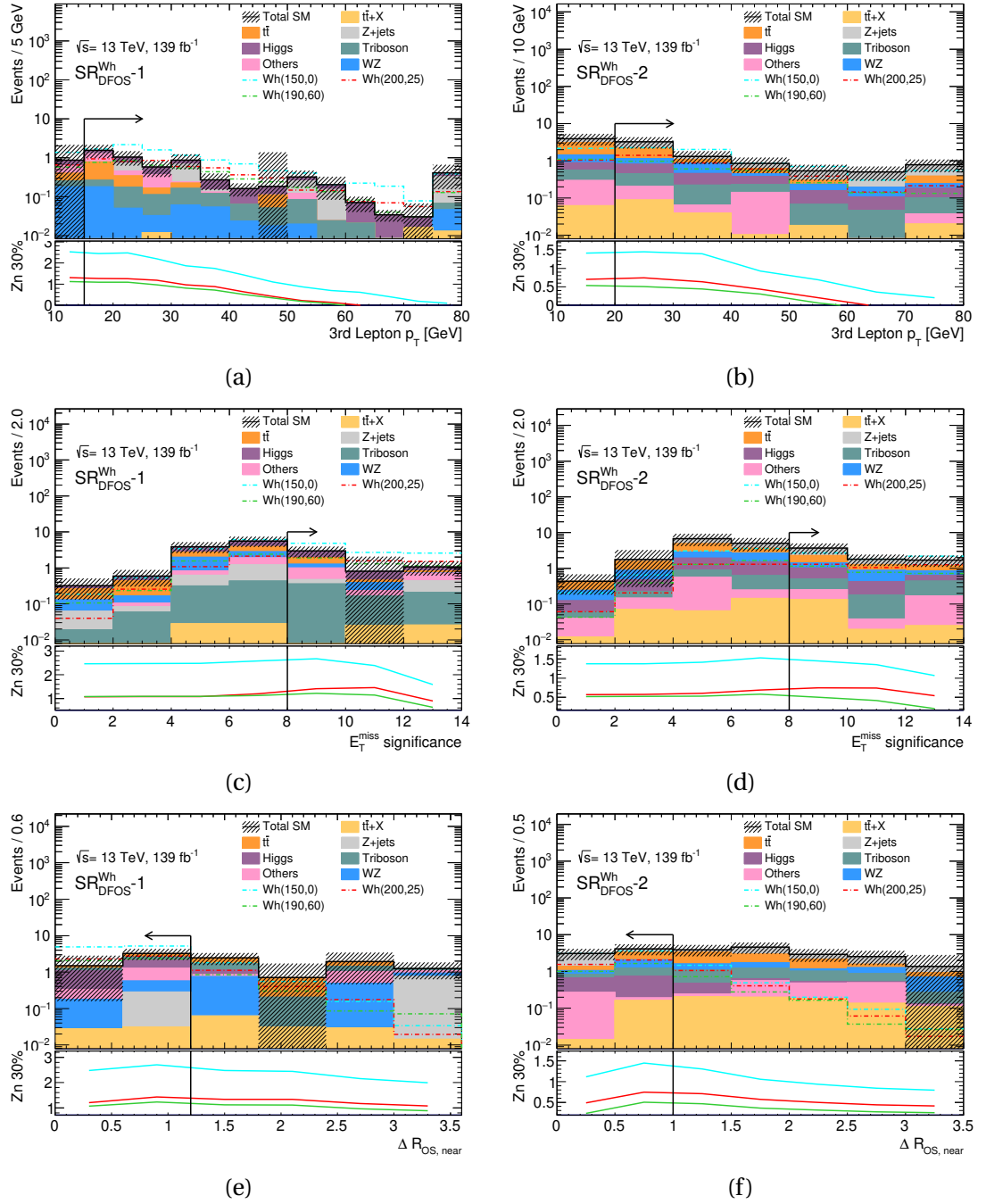


Figure 6.10: N-1 distributions for the $SR_{DFOS}^{Wh}-1$ (first column) and $SR_{DFOS}^{Wh}-2$ (second column) regions. The upper panels show the distribution for relevant background processes and chosen benchmark Wh signal points, the arrows show the position and the verse of the cuts on the p_T of the third lepton (first row), the E_T^{miss} significance (second row) and the $\Delta R_{OS, near}$ (third row). The significance Z_n is calculated assuming a flat 30% total uncertainty on the SM background.

SFOS signal regions

The invariant mass $m_{\ell\ell}$ is a good discriminator to target either the WZ or the Wh models, since it provides a good way to select events with the presence (or not) of a Z boson in the decay chains. Figure 6.11a and Figure 6.11b show the distributions of $m_{\ell\ell}$ for events passing the preselection criteria and the SFOS flavour-sign requirement. In both plots, the upper panels show distributions of the main SM background processes and reference mass points for the SUSY models. In the lower panels, the significance Z_n is calculated assuming 15% of uncertainty on the background, for a lower or an upper cut on the invariant mass $m_{\ell\ell}$, to show potential sensitivity for two WZ and Wh benchmark points, as indicated.

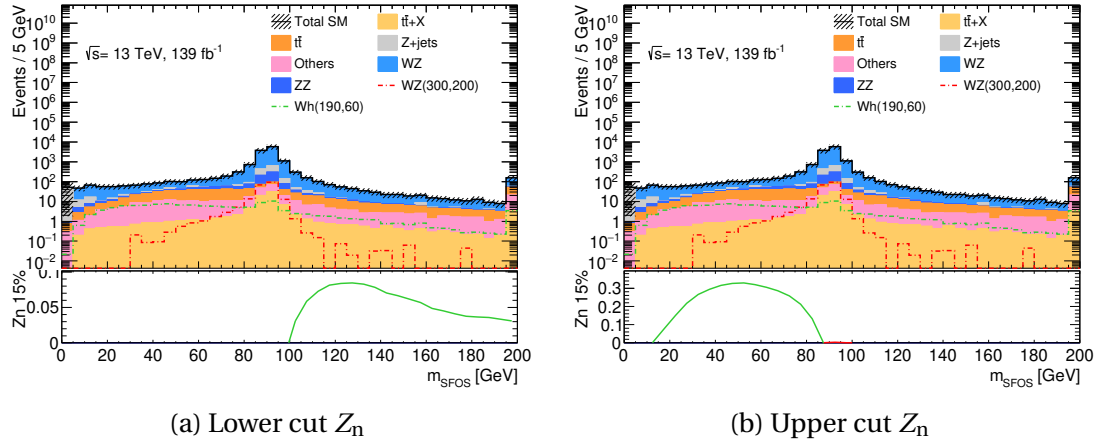


Figure 6.11: In the upper panels, the distributions of the $m_{\ell\ell}$ for events passing the preselection criteria and the SFOS requirement. In the lower pad, the sensitivity Z_n is calculated for (a) a lower cut and for (a) an upper cut on the shown variable. Sensitivity is calculated assuming a 10% flat total uncertainties on the SM background.

A cut on the SFOS invariant mass $m_{\ell\ell} > 12$ GeV is applied to suppress the low-mass (e.g. J/Ψ , and the Υ) resonances. A cut on the tripleton invariant mass $m_{\ell\ell\ell}$ is used to suppressed the contribution from FNP processes from the total SM background, requesting $|m_{\ell\ell\ell} - m_Z| > 15$ GeV, where m_Z is the nominal Z boson mass.

The presence of any ISR jet is exploited to boost the $\tilde{\chi}_1^\pm \tilde{\chi}_2^0$ system, resulting in a boosted kinematics for the physics objects in the final states. In such configuration, scenario with low mass-splitting, close to the kinematic edge $m_{\tilde{\chi}_1^\pm / \tilde{\chi}_2^0} - m_{\tilde{\chi}_1^0} = m_Z$, can be targeted. In both the SR^{WZ} and SR_{SFOS}^{Wh} selections, events are therefore split into three different categories: those with no the light jets ($n_{jets} = 0$); those, referred to as

low- H_T , with at least one jet and moderate hadronic activity, selected through H_T ($H_T < 200$ GeV); and those with at least one light jet and significant hadronic activity ($H_T > 200$ GeV), referred to as *high- H_T* .

The SRs in both the SR^{WZ} and the SR_{SFOS}^{Wh} selections are optimised in all the hadronic activity configurations separately, using a binning in m_T and E_T^{miss} . The motivation for the binning in m_T and E_T^{miss} used in the SFOS SRs is provided by the plots in Figure 6.12, where m_T distributions are shown for the SR^{WZ} selection with either $n_{jets} = 0$, labelled SR_{0j}^{WZ} , or in the high- H_T category, labelled $SR_{High-H_T}^{WZ}$.

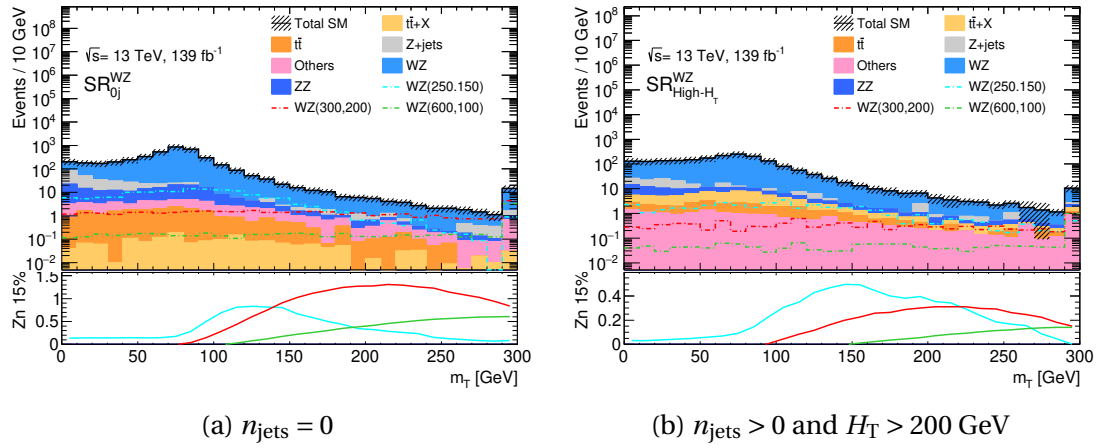


Figure 6.12: In the upper panels, the distributions of the m_T in the SR^{WZ} selection, split into categories of events with (a) $n_{jets} = 0$, and (b) $n_{jets} > 0$ and $H_T > 200$ GeV. In each lower panel, the sensitivity Z_n curve is calculated by assuming a 15% of total uncertainty on the SM background and for possible lower cuts on the shown variables.

A total of twenty SR bins are defined for the on-Z selection targeting the WZ model. Their definitions are shown in Table 6.10, accounting for all hadronic activity configurations described above.

As mentioned, similar strategy has been followed for the optimisation of the SR_{SFOS}^{Wh} SRs. Nevertheless, opposite to the SR^{WZ} SRs, the high- H_T category for the SR_{SFOS}^{Wh} selection did not show any significant contribution to the overall sensitivity for the Wh models. Moreover, for events with $m_{\ell\ell} > 105$ GeV, only the zero-jet category $n_{jets} = 0$ contributes significantly to the analysis.

Definitions of the SR_{SFOS}^{Wh} regions are listed in Table 6.11, showing a total of nineteen SR bins targeting the Wh model.

Selection requirements				
$n_{\text{jets}} = 0$				
m_T [GeV]	E_T^{miss} [GeV]			
[100,160]	SR ^{WZ} -1: [50,100]	SR ^{WZ} -2: [100,150]	SR ^{WZ} -3: [150,200]	SR ^{WZ} -4: > 200
> 160	SR ^{WZ} -5: [50,150]	SR ^{WZ} -6: [150,200]	SR ^{WZ} -7: [200,350]	SR ^{WZ} -8: > 350
$n_{\text{jets}} > 0, H_T < 200$ GeV				
m_T [GeV]	E_T^{miss} [GeV]			
[100,160]	SR ^{WZ} -9: [100,150]	SR ^{WZ} -10: [150,250]	SR ^{WZ} -11: [250,300]	SR ^{WZ} -12: > 300
> 160	SR ^{WZ} -13: [50,150]	SR ^{WZ} -14: [150,250]	SR ^{WZ} -15: [250,400]	SR ^{WZ} -16: > 400
$n_{\text{jets}} > 0, H_T > 200$ GeV, $H_T^{\text{lep}} < 350$ GeV				
m_T [GeV]	E_T^{miss} [GeV]			
> 100	SR ^{WZ} -17: [150,200]	SR ^{WZ} -18: [200,300]	SR ^{WZ} -19: [300,400]	SR ^{WZ} -20: > 400

Table 6.10: Summary of the selection criteria for SRs targeting events with at least one SFOS lepton pair and $m_{\ell\ell} \in [75, 105]$ GeV, for the SR^{WZ} search regions. Region selections are binned by m_T (rows) and E_T^{miss} for the two sets of regions, where each set has different n_{jets} , and H_T requirements. Preselection criteria are applied. [139]

Selection requirements				
$m_{\ell\ell} \leq 75$ GeV, $n_{\text{jets}} = 0$				
m_T [GeV]	E_T^{miss} [GeV]			
[0,100]	SR _{SFOS} ^{Wh} -1: [50,100]	SR _{SFOS} ^{Wh} -2: [100,150]	SR _{SFOS} ^{Wh} -3 > 150	
[100,160]	SR _{SFOS} ^{Wh} -4: [50,100]	SR _{SFOS} ^{Wh} -5: > 100		
> 160	SR _{SFOS} ^{Wh} -6: [50,100]	SR _{SFOS} ^{Wh} -7: > 100		
$m_{\ell\ell} \leq 75$ GeV, $n_{\text{jets}} > 0, H_T < 200$ GeV				
m_T [GeV]	E_T^{miss} [GeV]			
[0,50]	SR _{SFOS} ^{Wh} -8: [50,100]			
[50,100]	SR _{SFOS} ^{Wh} -9: [50,100]			
[0,100]	SR _{SFOS} ^{Wh} -10: [100,150]			SR _{SFOS} ^{Wh} -11: > 150
[100,160]	SR _{SFOS} ^{Wh} -12: [50,100]	SR _{SFOS} ^{Wh} -13: [100,150]	SR _{SFOS} ^{Wh} -14: > 150	
> 160	SR _{SFOS} ^{Wh} -15: [50,150]	SR _{SFOS} ^{Wh} -16: > 150		
$m_{\ell\ell} \geq 105$ GeV, $n_{\text{jets}} = 0$				
m_T [GeV]	E_T^{miss} [GeV]			
> 100	SR _{SFOS} ^{Wh} -17: [50,100]	SR _{SFOS} ^{Wh} -18: [100,200]	SR _{SFOS} ^{Wh} -19: > 200	

Table 6.11: Summary of the selection criteria for SRs targeting events with at least one SFOS lepton pair and $m_{\ell\ell} \notin [75, 105]$ GeV, for the Wh search regions. Region selections are binned by m_T (rows) and E_T^{miss} for the three sets of regions, where each set has different $m_{\ell\ell}$, n_{jets} , and H_T requirements. Preselection criteria are applied. [139]

6.2.2 Standard Model background estimation

As seen for the early Run-2 Wh analysis, also for the full Run-2 analysis background estimation methods are in place for the sources of irreducible and reducible back-

grounds. Table 6.12 summarises the various techniques used in this thesis for the estimation of the different **SM** background processes entering the **SRs**.

Process	Method
WZ	MC, normalised in CR
FNP (Z +jets)	Data-driven Fake Factor
$t\bar{t}$	MC, validated in VR
Others	MC

Table 6.12: Summary of the background estimation methods used for the full Run-2 analysis detailed in this thesis. The category "Others" includes the WW , ZZ , $t\bar{t}+V$ ($V=W,Z$), single-top and processes with a Higgs boson.

Additional details on the methods are discussed in the following. For the background estimation, I made major contribution by doing the **FNP** data-driven estimation, designing the validation of the $t\bar{t}$ background, and performing all the steps of the background-only fit for the irreducible background estimation.

FNP estimation

The Fake Factor method is used for the estimation of the **FNP** background from Z +jets process. The method is described in Section 5.3.1.1. A **CR**, named CRFF^{WZ} , is used for the extraction of the fake factors for electrons and muons, and it is chosen to select events with **FNP** contribution, against other **SM** backgrounds, as well as to emulate an **FNP** source composition similar to the one expected in the **SRs**.

The definition of the CRFF^{WZ} is shown in Table 6.13. While the regular preselection criteria are applied to all the other regions used in this analysis, they are not applied to CRFF^{WZ} , since they are optimised for the suppression of **FNP** background and would limit the available statistics for the extraction of the **FFs**. Events with an **SFOS** pair, no b -tagged jets and with $E_T^{\text{miss}} \in [20,50]$ GeV are selected. The **SFOS** leptons, labelled ℓ_{Z1} and ℓ_{Z2} , are used for the reconstruction of the invariant mass $m_{\ell\ell}$, required to be $\in [75,105]$ GeV, and are required to pass the signal object definition. Additional cuts on their p_T are applied to ensure selection in the plateau of the di-lepton trigger efficiencies. The trasverse mass m_T of the third lepton not in the **SFOS** pair is required to have $m_T < 20$ GeV. This latter lepton is assumed to be the **FNP** lepton and is used for the extraction of the fake factors.

The fake factors extracted from the CRFF^{WZ} are calculated as a function of the lepton p_T . FFs obtained from data after subtraction of prompt backgrounds are of the order of 0.1, except for leptons with $p_T > 50$ GeV. These are then used for the estimation of the FNP background in the regions, according to the procedure described in Section 5.3.1.1.

A set of dedicated systematic uncertainties are calculated for the FNP estimation. In the case of the Fake Factor method, two main sources are considered:

Statistical uncertainties on the FFs: these arise from the Poisson uncertainties associated with the counting of leptons that pass the tight or loose selection. The statistical errors on the FFs are treated as a correlated source of systematic uncertainty across all the SRs.

Closure test: the same method is used on MC simulation of Z+jets background, using FFs calculated purely from MC. The test is expected to produce results similar to prediction of out-of-the-box MC simulation of the same background in all the SRs. Possible discrepancies are associated to a different FNP source composition in the CRFF^{WZ} with respect to the SRs. In that case, discrepancies between the MC-based Fake Factor estimation and the MC-only expectations are taken as source of uncorrelated systematic uncertainty on the FNP background estimation.

The FNP estimation method is validated in a dedicated VR, named VRFF^{WZ} , defined in a kinematic region which does not overlap with any other region used in the analysis, and where the contribution from the FNP background is dominant. Events with a SFOS pair are selected and with $E_T^{\text{miss}} \in [50, 100]$ GeV. Additional cuts on $m_T < 20$ GeV and $m_{\ell\ell\ell} \in [105, 160]$ GeV are applied to select events with FNP leptons. The exact definition of the VRFF^{WZ} is shown in Table 6.13.

Distributions of the p_T of the third lepton in the FNP-VR are shown in Figure 6.13, for the four flavour channels eee , $ee\mu$, $\mu\mu e$ and $\mu\mu\mu$. The plots show good agreement in all the bins between data and the SM backgrounds, including the FNP background estimation.

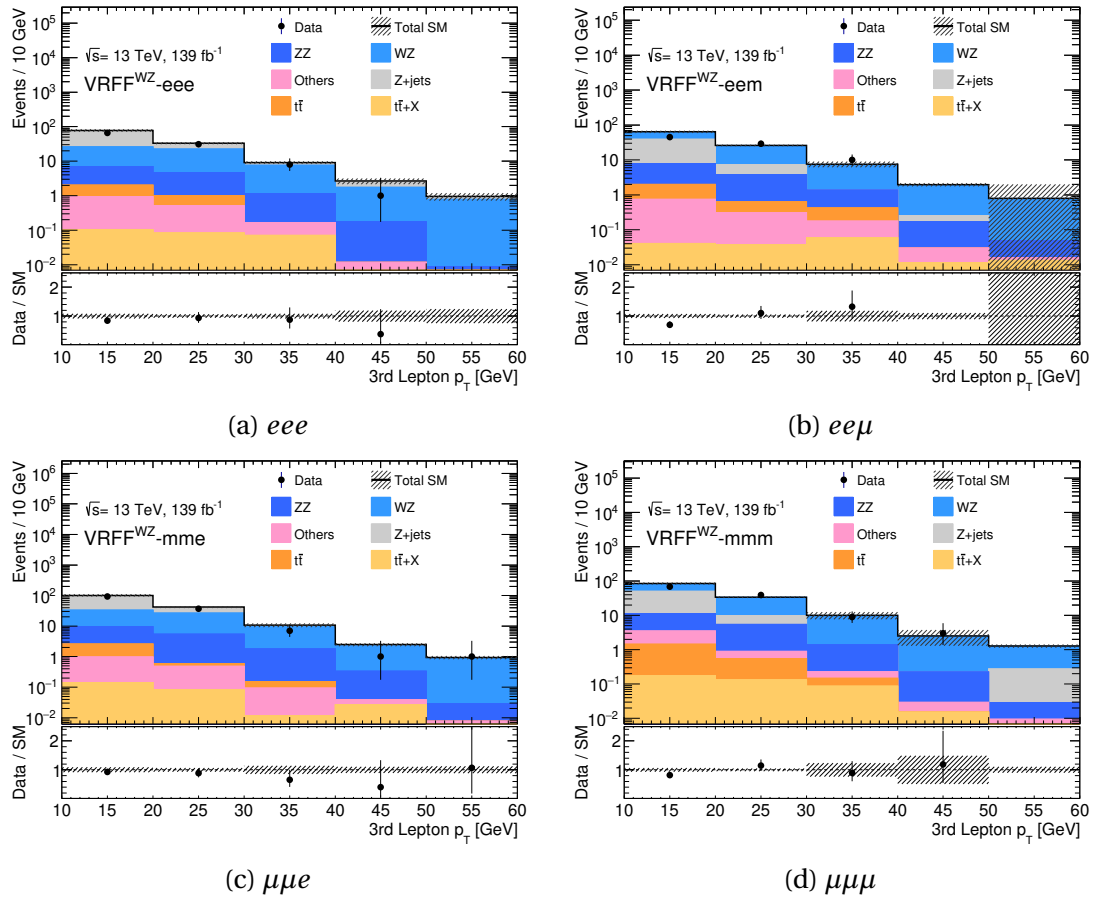


Figure 6.13: In the upper panels, the distribution of the p_T of the third lepton in the $VRRFF^{WZ}$, for two flavour channels (c) $\mu\mu e$ and (d) $\mu\mu\mu$. In the lower pad, ratio between data and **SM** prediction is shown. Systematic and statistical uncertainties are considered.

Validation of the $t\bar{t}$ background estimation

The **MC** modelling of the $t\bar{t}$ is validated in a dedicated **VR**, which select events with no **SFOS** lepton pairs and with either one or two b -tagged jets ($VRt\bar{t}^{WZ}$). By definition, the $VRt\bar{t}^{WZ}$ is orthogonal to all the **DFOS SRs**. Another region is also defined for the validation of the $t\bar{t}$ background. The additional $VRt\bar{t}_{inc}^{WZ}$ selects events in the **DFOS** selection and E_T^{miss} significance less than 8, but it does not apply any requirement on the b -tagged-jet multiplicity, approaching the zero- b -jets selection applied to the **SRs**. The exact definitions of the **VRs** for the $t\bar{t}$ background are shown Table 6.13.

Distribution of $\Delta R_{OS, near}$, E_T^{miss} and E_T^{miss} significance for the data and the **SM** prediction in the $VRt\bar{t}^{WZ}$ are shown in Figure 6.14 and Figure 6.15. Good agreement between data and **SM** expectations is observed which validates the **MC** modelling of the $t\bar{t}$ process.

Variable	VRt \bar{t}^{WZ}	VRt \bar{t}^{WZ}_{inc}	CRFF WZ	VRFF WZ
n_{SFOS}	= 0	= 0	≥ 1	≥ 1
n_{b-jets}	$\in [1, 2]$	-	= 0	= 0
$ m_{\ell\ell} - m_Z $ [GeV]	-	-	< 15	< 15
$p_T^{\ell_{Z1}}, p_T^{\ell_{Z2}}$ [GeV]	-	-	> 25, > 20	-
E_T^{miss} [GeV]	> 50	> 50	$\in [20, 50]$	$\in [50, 100]$
E_T^{miss} significance	-	< 8	-	-
m_T [GeV]	-	-	< 20	< 20
$m_{\ell\ell}$ [GeV]	-	-	-	$\in [105, 160]$

Table 6.13: Summary of the selection criteria for the CRs and VRs for $t\bar{t}$ and **FNP** estimation, for the SR WZ and SR $^{Wh}_{SFOS}$ selections. Preselection criteria are applied for VRt \bar{t}^{WZ} , VRt \bar{t}^{WZ}_{inc} and VRFF WZ regions. [139]

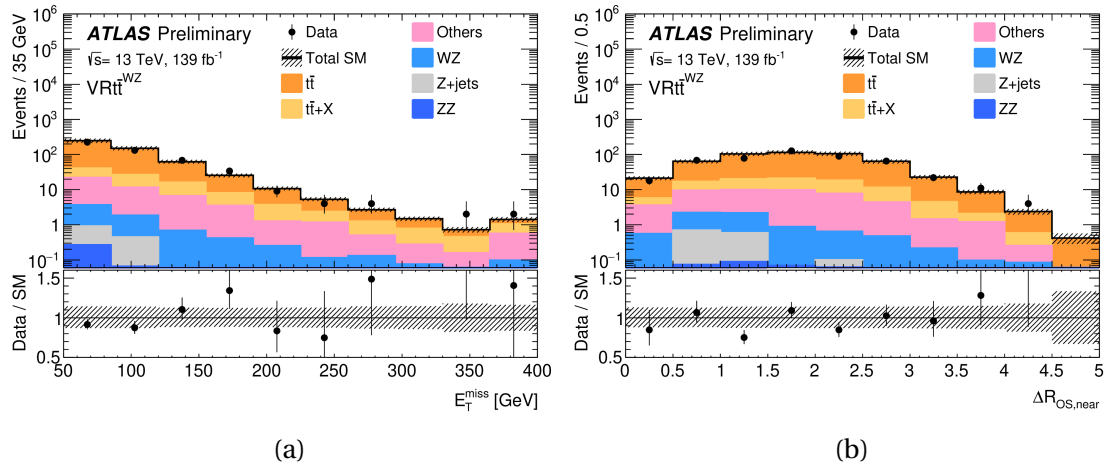


Figure 6.14: In the upper panels, the distribution of the (a) E_T^{miss} and (b) $\Delta R_{OS, near}$ in the VRt \bar{t}^{WZ} . In the lower pad, ratio between data and SM prediction is shown. Systematic and statistical uncertainties are considered. [139]

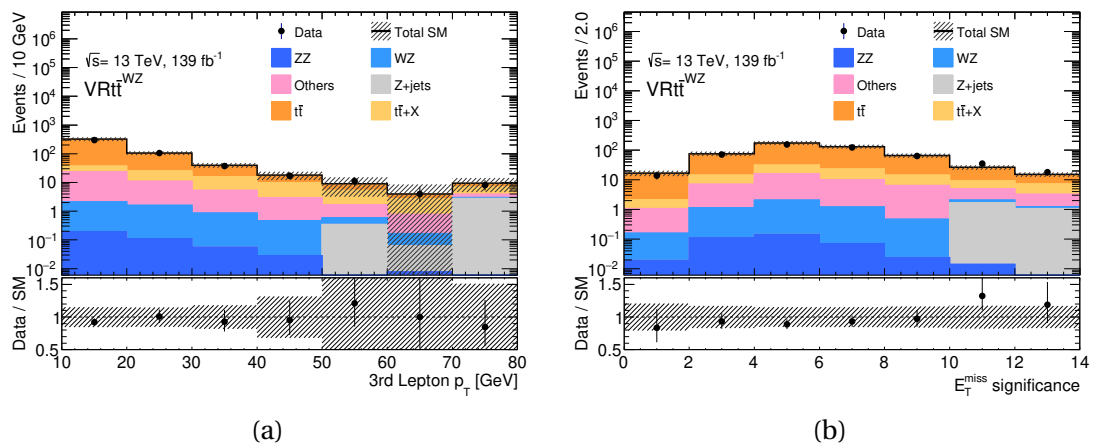


Figure 6.15: In the upper panels, the distribution of the (a) p_T of the third lepton and (b) E_T^{miss} significance in the VRt \bar{t}^{WZ} . In the lower pad, ratio between data and SM prediction is shown. Systematic and statistical uncertainties are considered.

In Figure 6.16 distributions are shown for the $\text{VRt}_{\text{inc}}^{\text{WZ}}$, including $E_{\text{T}}^{\text{miss}}$, $\Delta R_{\text{OS, near}}$ and the b -tagged jet multiplicity $n_{b\text{-jets}}$. Good agreement is again seen in all the distribution, validating the shape and normalisation of the $t\bar{t}$ process.

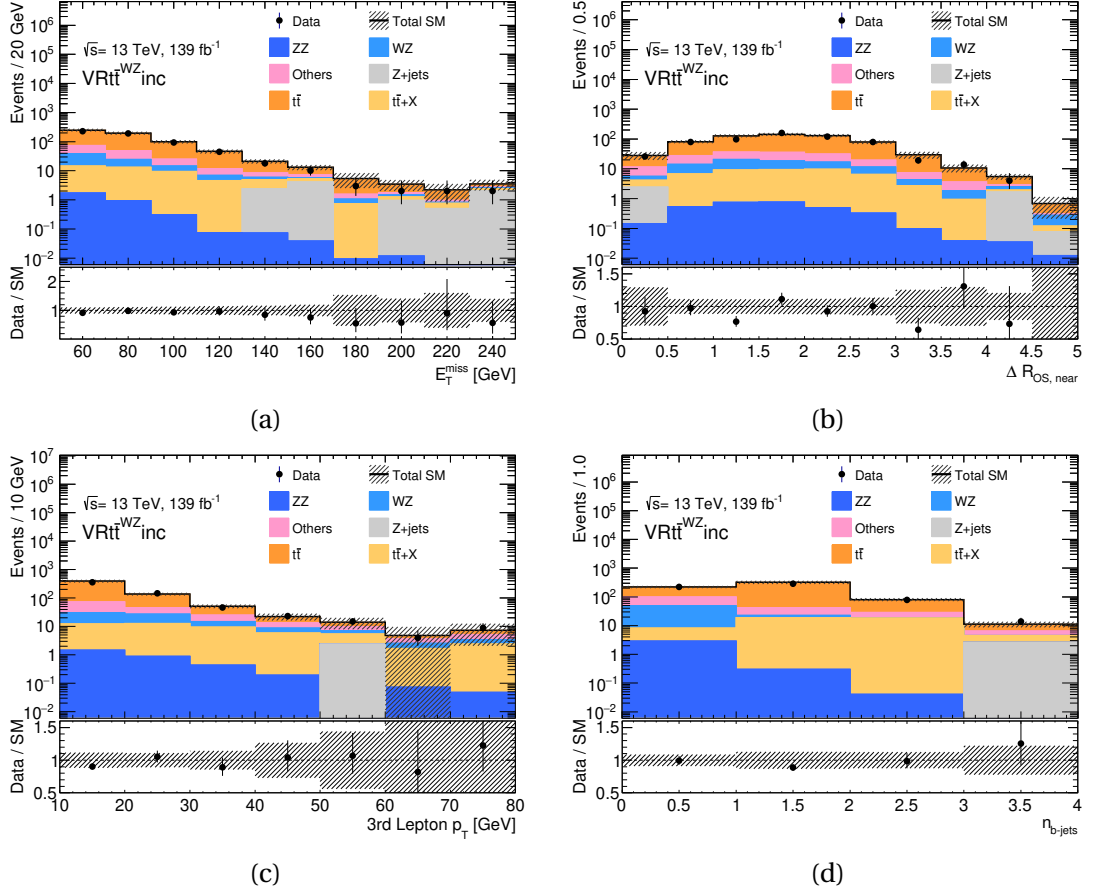


Figure 6.16: In the upper panels, the distribution of the (a) $E_{\text{T}}^{\text{miss}}$, (b) $\Delta R_{\text{OS, near}}$, (c) p_{T} of the third lepton and (d) the number $n_{b\text{-jets}}$ of b -tagged jets in the $\text{VRt}_{\text{inc}}^{\text{WZ}}$. In the lower pad, ratio between data and SM prediction is shown. Systematic and statistical uncertainties are considered.

WZ background estimation

As in the early Run-2 analysis, the irreducible background WZ is estimated in a dedicated CR, named CRWZ^{WZ} . The same hadronic binning in n_{jets} and H_{T} used in the SFOS SR definition are used for the binning of the CRWZ^{WZ} . In what follows, bins in n_{jets} and H_{T} for the CRWZ^{WZ} are labelled $\text{CRWZ}_{0j}^{\text{WZ}}$, $\text{CRWZ}_{\text{Low}H_{\text{T}}}^{\text{WZ}}$ and $\text{CRWZ}_{\text{High}H_{\text{T}}}^{\text{WZ}}$. In addition to the preselection criteria, events with a SFOS lepton pair with invariant mass $m_{\ell\ell} \in [75, 105]$ GeV are selected. Moreover, cuts on $E_{\text{T}}^{\text{miss}} \in [50, 100]$ GeV and $m_{\text{T}} \in [20, 100]$ GeV are applied. The exact definition of CRWZ^{WZ} is shown in Table 6.14.

Distributions of the m_T in all the hadronic binning in n_{jets} and H_T for the CRWZ^{WZ} , before the background-only fit, are shown in Figure 6.17. Some disagreement is noticeable in all the hadronic bins, particularly accentuated for the high- H_T region. The shape of the m_T distribution was further validated by data on background comparison for the $W + \gamma$ background, whose m_T distribution shape does not differ by that from WZ . I did not make any contribution to this aspect of the analysis, therefore the reader is remanded to Ref. [139] for further details and description of the method.

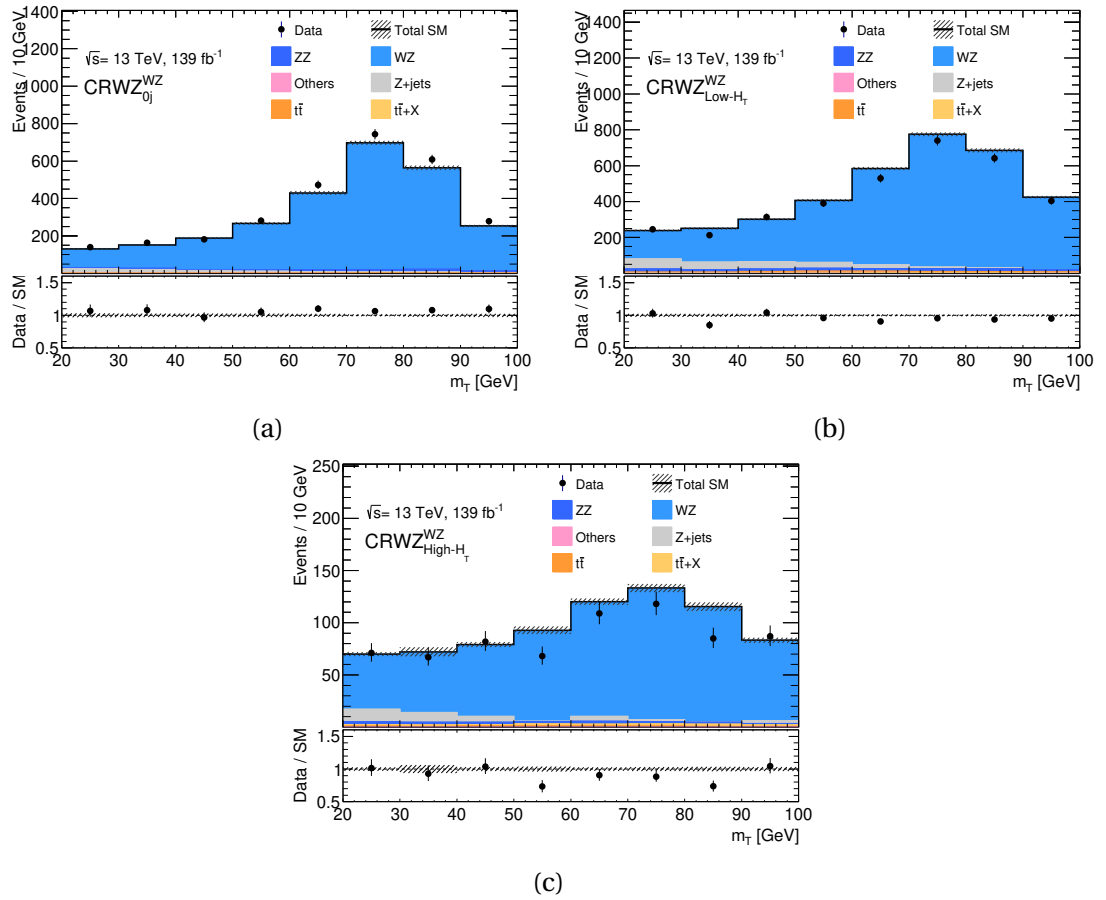


Figure 6.17: In the upper panels, distributions of m_T in the CRWZ^{WZ} , before the background-only fit. Events are selected in all the hadronic binning considered in the optimisation of the SRs: (a) $n_{\text{jets}} > 0$, (b) $n_{\text{jets}} = 0$ and $H_T < 200$ GeV, and (c) $n_{\text{jets}} > 0$ and $H_T > 200$ GeV. In the lower panels, data on background ratio is compared to the error band, including statistical and systematic uncertainties on the SM background.

A dedicated VR, called VRWZ^{WZ} , is introduced to test the NF extracted from the CRWZ^{WZ} . Contamination in the VRWZ^{WZ} from SUSY signals is of the order 1% or less for all the signal points not already excluded by previous equivalent searches. Also in this case, the VRWZ^{WZ} is split into the same bins in n_{jets} and H_T , as considered for the corresponding CR and the SR. The VRWZ^{WZ} definition is also shown in Table 6.14. The

m_T and the E_T^{miss} are used to keep all the regions in the analysis orthogonal.

Variable	CRWZ ^{WZ}			VRWZ ^{WZ}		
	0 jets	low- H_T	high- H_T	0 jets	low- H_T	high- H_T
n_{jets}	=0	≥ 1	≥ 1	=0	≥ 1	≥ 1
H_T [GeV]	-	< 200 GeV	> 200 GeV	-	< 200 GeV	> 200 GeV
n_{SFOS}		≥ 1			≥ 1	
m_T [GeV]		$\in [20, 100]$			$\in [20, 100]$	
$m_{\ell\ell}$ [GeV]		$\in [75, 105]$			$\in [75, 105]$	
$ m_{\ell\ell\ell} - m_Z $ [GeV]		> 15			> 15	
E_T^{miss} [GeV]		$\in [50, 100]$			> 100	

Table 6.14: Summary of the selection criteria for the CRs and VRs for WZ , for the SR^{WZ} and SR^{Wh}_{SFOS} selections. Preselection criteria are applied. In rows where only one value is given it applies to all regions. [139]

6.2.3 Systematic uncertainties

The detector systematic uncertainties considered in the analysis are those discussed in Section 5.4.1. The theory uncertainties on the MC modelling of the SM processes are described in Section 5.4.2. These are calculated for the $W+Z$ background for all the SFOS regions. For the DFOS SRs, theory uncertainties are calculated for the dominant VVV and the $t\bar{t}$ backgrounds. Furthermore, a set of dedicated systematic uncertainties are considered for the data-driven estimation of the FNP background, discussed in Section 6.2.2.

The plots in Figure 6.18 show the relative uncertainties for all the SR designed for the WZ and the Wh models. In the plots, the category ‘‘Experimental’’ includes all the detector systematics, ‘‘Modelling’’ refers to the theory uncertainties on the main SM background processes, ‘‘Fake’’ are the systematic uncertainties related to the FNP data-driven estimation, ‘‘Normalisation’’ are those on the NF extrapolated from the CR in the background-only fit, and ‘‘MC stats’’ are the uncertainties associated to the statistics available in the used MC samples for the SM background.

Experimental systematic uncertainties and statistical from the MC samples are dominant in most of the SR^{WZ} regions, except for the high- H_T bins, where the ‘‘Modelling’’ uncertainties for the WZ background become dominant. In the case of the low- $m_{\ell\ell}$ and high- $m_{\ell\ell}$ SRs, modelling of the $W+Z$ background is the dominant contribution to the uncertainties in most of the SR bins, while for the DFOS SRs, uncertainties on the FNP

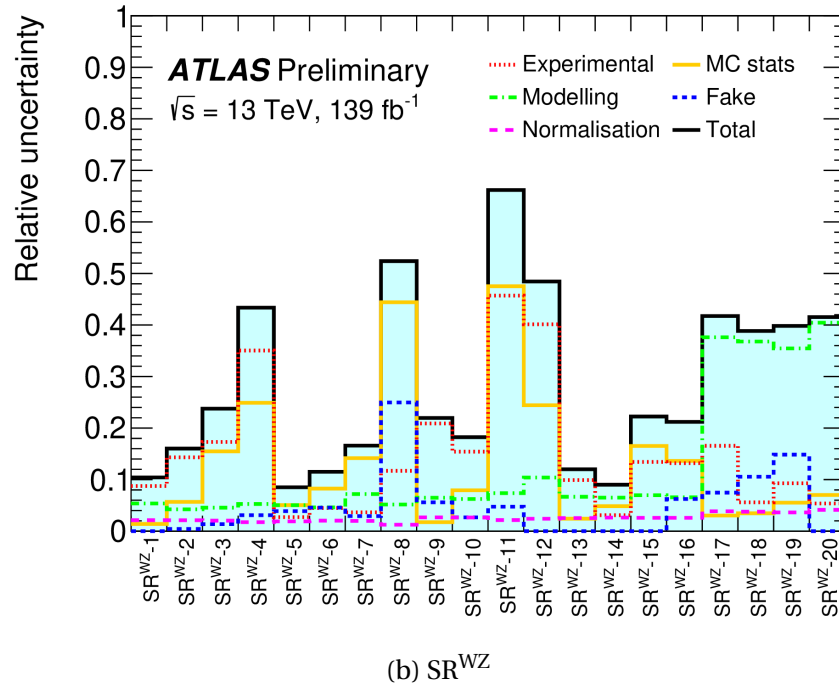
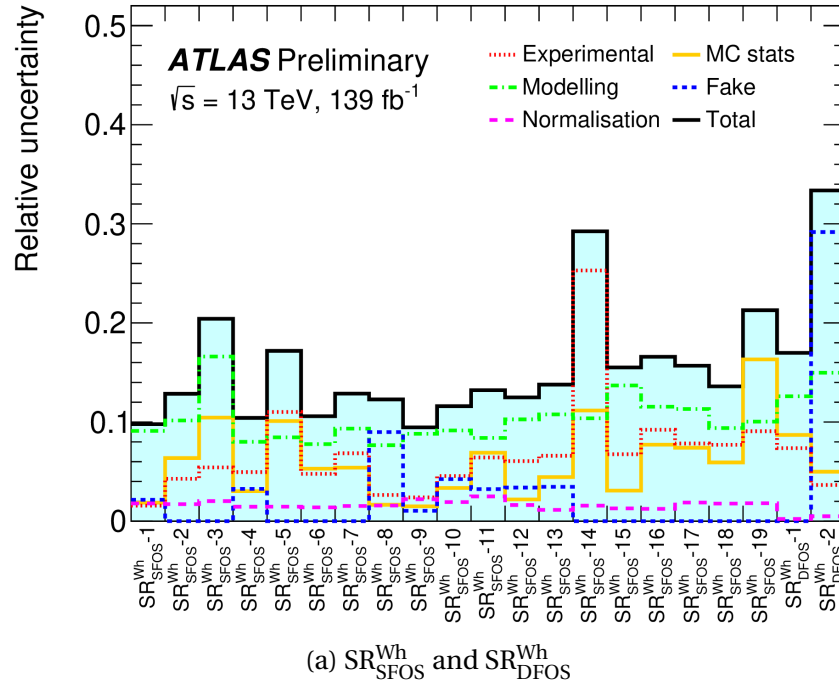


Figure 6.18: Relative uncertainties in the (a) SR_{SFO}^{Wh} and SR_{DFO}^{Wh} , and (b) the SR^{WZ} regions. All sources of systematics and statistical uncertainties considered in the analysis are reported. [139]

estimation become dominant in the $\text{SR}_{\text{DFOS}}^{\text{Wh}-2}$.

6.2.4 Background-only fit results

The background-only fit to data was performed simultaneously in all the bins in n_{jets} and H_T , producing three different NFs. The NFs extracted for the targeted WZ background are $\mu_{W+Z}^{\text{0jets}} = 1.07 \pm 0.02$, $\mu_{W+Z}^{\text{low-}H_T} = 0.94 \pm 0.03$ and $\mu_{W+Z}^{\text{high-}H_T} = 0.85 \pm 0.05$, for the $\text{CRWZ}_{0j}^{\text{WZ}}$, $\text{CRWZ}_{\text{Low}H_T}^{\text{WZ}}$ and $\text{CRWZ}_{\text{High}H_T}^{\text{WZ}}$, respectively.

Observed event yields in data and results from the background-only fit for all the VRs are summarised in Figure 6.19. In the first three bins, yields before the background-only fit in all the bins of the CRWZ^{WZ} , showing the relative differences between data and SM predictions, of the same order as the NFs extracted through the fit. The other bins show results in the VRs after the background-only fit. Good agreement between observed data and expected yields from SM backgrounds is seen in all the VRs within the error band, comprising statistical and systematic uncertainties on the background.

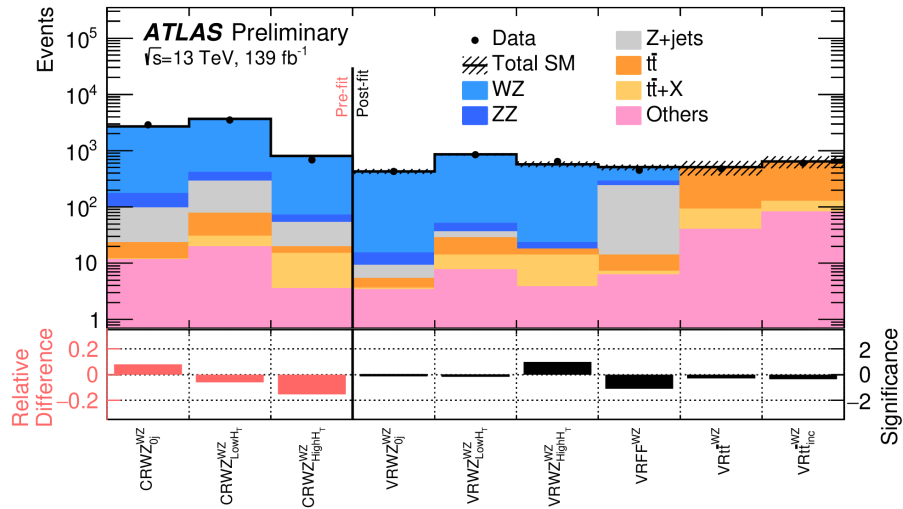


Figure 6.19: Data on SM predictions comparisons in all the CRs and VRs considered for the background estimation. In the upper panel, the yields of background processes and data in all the regions. In the lower panel, the comparison between data and SM prediction is expressed as relative difference (in red) for the CR, calculated before the background-only fit, and as significance for the VRs (in black), after the background-only fit. Statistical and systematic uncertainties on the SM backgrounds are considered. [139]

Results of the background-only fit are also shown in Figure 6.20 and Figure 6.21, where distributions of the m_T in all the bins in n_{jets} and H_T for the CRWZ^{WZ} and the

$VRWZ^{WZ}$ are presented. As desired, excellent agreement between data and SM predictions is seen everywhere in the $CRWZ^{WZ}$, and good agreement is found in all the hadronic categories of the $VRWZ^{WZ}$.

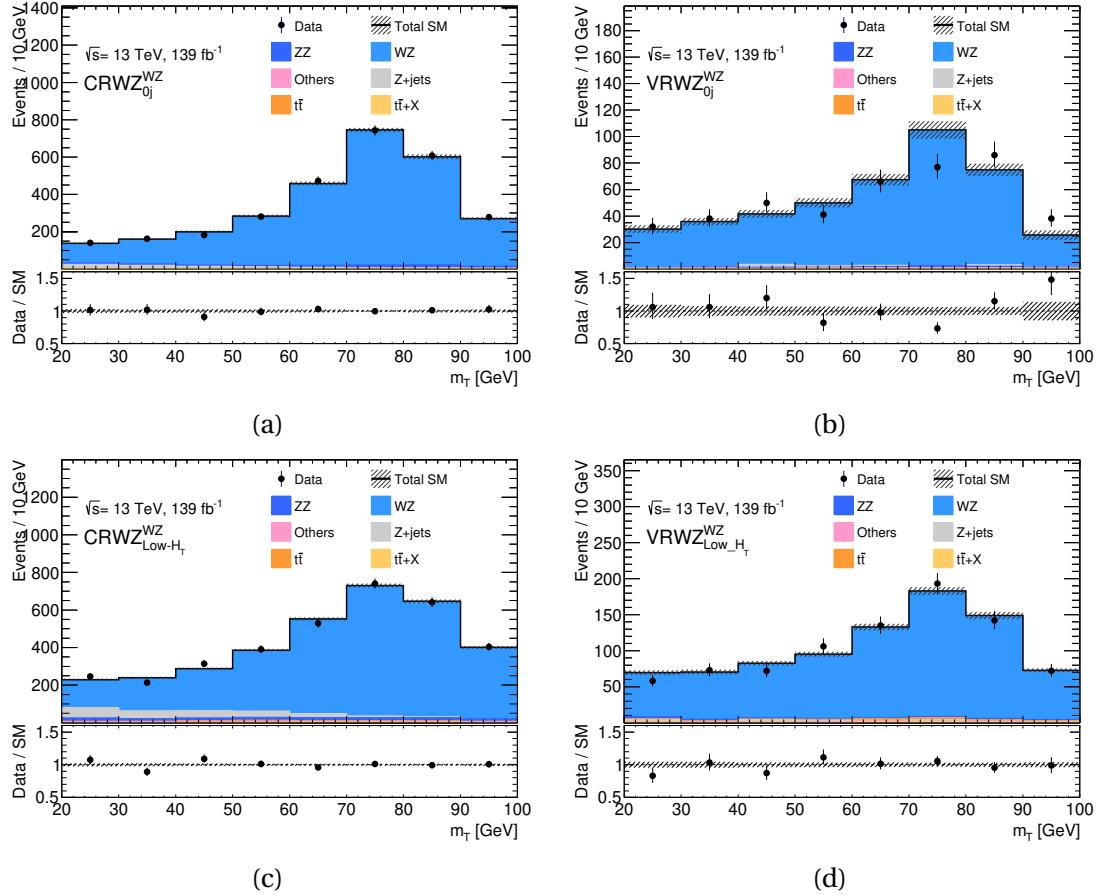


Figure 6.20: In the upper panels, distributions of m_T in the $CRWZ^{WZ}$ (left-hand column) and the $VRWZ^{WZ}$ (right-hand column), after the background-only fit. Events are selected in all the hadronic binning categories considered in the optimisation of the SRs $n_{jets} = 0$ (first row), and $n_{jets} > 0$ and $H_T < 200$ GeV (second row). In the lower panels, data on background ratio is compared to the error band, including statistical and systematic uncertainties on the SM background.

Finally, the effect of the simultaneous background-only fit in all the bins in n_{jets} and H_T is shown in Figure 6.22. The visible disagreement in the n_{jets} distribution before the background-only fit is fully recovered by applying the NFs, with clear benefit from the extraction of NFs for the different hadronic activity configurations considered.

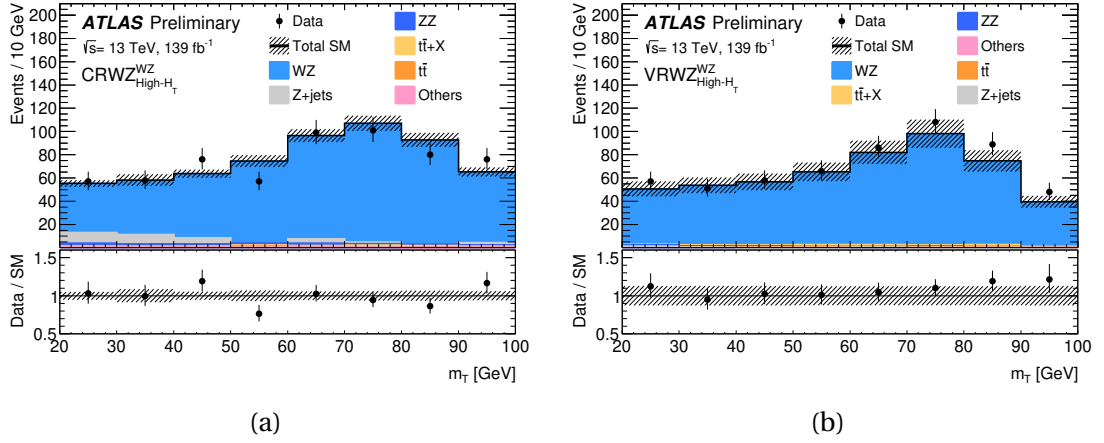


Figure 6.21: In the upper panels, distributions of m_T in the CRWZ^{WZ} (left-hand column) and the VRWZ^{WZ} (right-hand column), after the background-only fit. Events are selected in the hadronic binning category $n_{\text{jets}} > 0$ and $H_T > 200$ GeV considered in the optimisation of the SRs. In the lower panels, data on background ratio is compared to the error band, including statistical and systematic uncertainties on the SM background. [139]

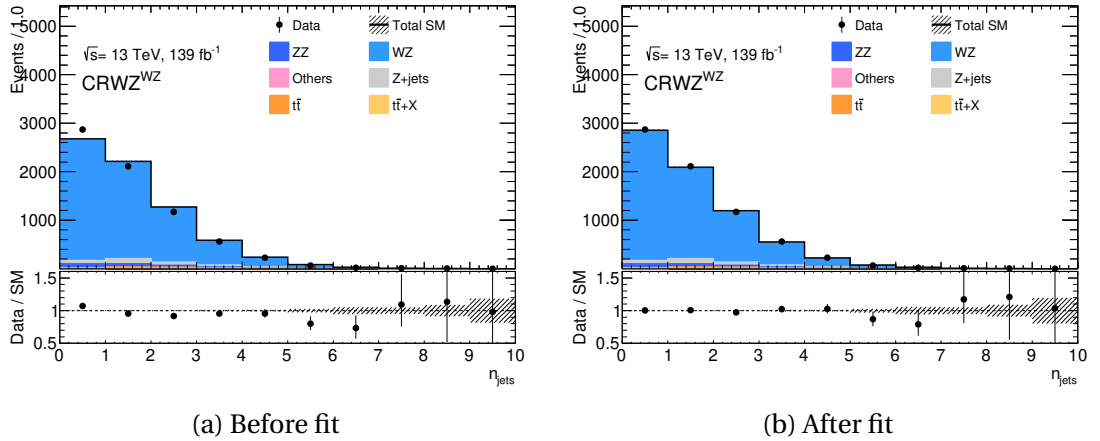


Figure 6.22: In the upper panels, distributions of n_{jets} in the CRWZ^{WZ}, (a) before and (b) after the background-only fit. In the lower panels, data on background ratio is compared to the error band, including statistical uncertainties on the SM background.

6.2.5 Results and statistical interpretation

The results in the SRs, after the background-only fit in the CRs, are summarised in Figure 6.23 and Figures 6.24, for the Wh and WZ models, respectively. In the upper panels, yields of observed data and SM predictions are shown, while the lower panels indicate the significance for each bin. No significant deviation with respect to the SM predictions is seen in any SR, although a mild 2σ deviation from the SM prediction is observed for the SR_{DFOS}^{Wh}-1 bin.

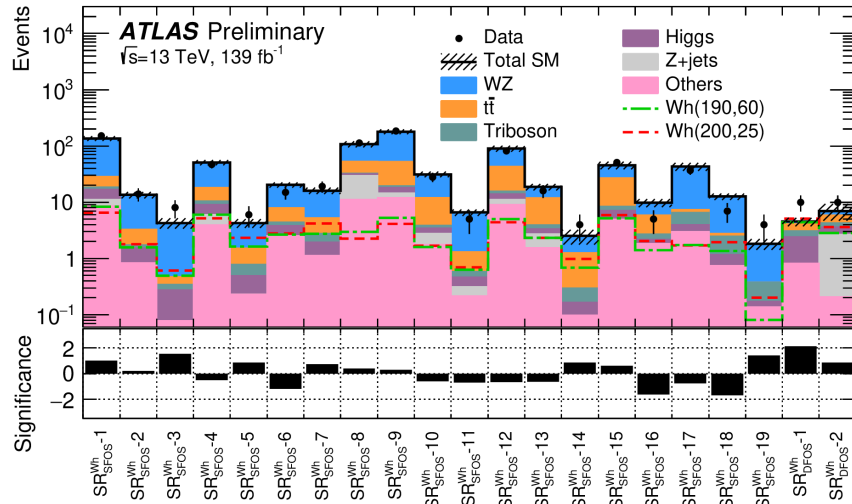


Figure 6.23: In the upper panels, the observed data and SM prediction yields in the SR targeting the Wh model. The lower panel show the significance for the data and SM expectation, accounting for the full set of systematic and statistical uncertainties. [139]

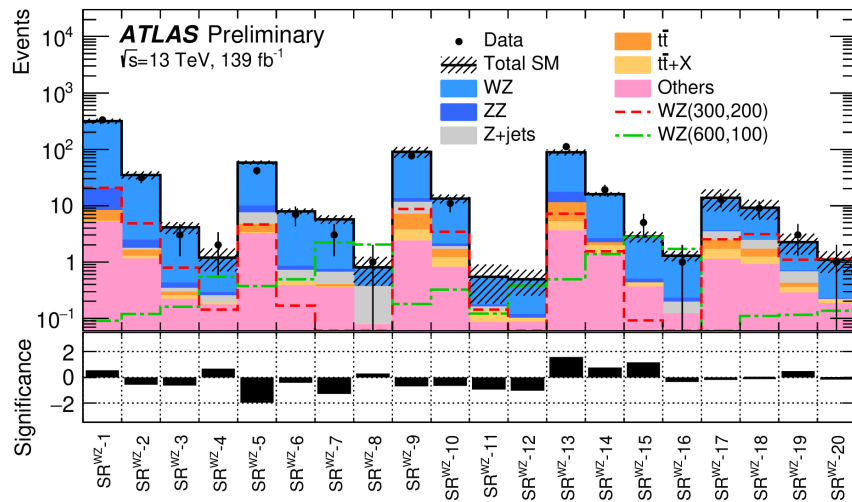


Figure 6.24: In the upper panels, the observed data and SM prediction yields in the SR targeting the WZ model. The lower panel show the significance for the data and SM expectation, accounting for the full set of systematic and statistical uncertainties. [139]

Results in the SRs are also presented as breakdown of the yields for all the SM backgrounds and the observed data in all the SRs. These are shown in Tables 6.15 and Table 6.16, for the Wh and WZ SRs, respectively.

Regions	SR _{SFOS} ^{Wh} -1	SR _{SFOS} ^{Wh} -2	SR _{SFOS} ^{Wh} -3	SR _{SFOS} ^{Wh} -4	SR _{SFOS} ^{Wh} -5	SR _{SFOS} ^{Wh} -6	SR _{SFOS} ^{Wh} -7
Observed	152	14	8	47	6	15	19
Fitted SM	136 ± 13	13.5 ± 1.7	4.3 ± 0.9	50 ± 5	4.3 ± 0.7	20.2 ± 2.1	16.0 ± 2.1
WZ	107 ± 12	10.2 ± 1.7	3.8 ± 0.8	32 ± 4	2.7 ± 0.6	12.3 ± 1.6	10.8 ± 1.7
$t\bar{t}$	10.3 ± 2.5	1.6 ± 0.6	0.13 ± 0.12	7.7 ± 1.9	0.74 ± 0.34	3.5 ± 1.0	2.5 ± 0.7
Z +jets	2.5 ± 2.9	0.00 ^{+0.02} _{0.00}	0.00 ^{+0.02} _{0.00}	2.0 ± 1.6	0.00 ^{+0.04} _{0.00}	0.00 ^{+0.04} _{0.00}	0.00 ^{+0.02} _{0.00}
Higgs	5.7 ± 0.6	0.69 ± 0.07	0.20 ± 0.03	3.12 ± 0.31	0.26 ± 0.05	1.29 ± 0.14	0.81 ± 0.09
VVV	1.9 ± 0.5	0.22 ± 0.07	0.07 ± 0.02	1.4 ± 0.4	0.28 ± 0.09	0.61 ± 0.18	0.83 ± 0.24
Others	8.6 ± 1.9	0.84 ± 0.11	0.08 ± 0.05	4.0 ± 0.5	0.23 ± 0.24	2.54 ± 0.22	1.11 ± 0.15
Regions	SR _{SFOS} ^{Wh} -8	SR _{SFOS} ^{Wh} -9	SR _{SFOS} ^{Wh} -10	SR _{SFOS} ^{Wh} -11	SR _{SFOS} ^{Wh} -12	SR _{SFOS} ^{Wh} -13	SR _{SFOS} ^{Wh} -14
Observed	113	184	28	5	82	16	4
Fitted SM	108 ± 13	180 ± 17	31 ± 4	6.6 ± 0.9	90 ± 11	18.7 ± 2.6	2.5 ± 0.7
WZ	54 ± 6	127 ± 13	19.3 ± 2.3	5.3 ± 0.8	47 ± 6	6.8 ± 1.7	1.26 ± 0.26
$t\bar{t}$	21 ± 6	33 ± 10	8.2 ± 2.3	0.7 ± 0.5	28 ± 8	8.0 ± 2.2	0.9 ± 0.5
Z +jets	19 ± 10	2.3 ± 1.9	1.0 ± 1.3	0.10 ± 0.21	2.1 ± 3.1	1.2 ± 0.7	0.00 ^{+0.12} _{0.00}
Higgs	1.91 ± 0.19	3.63 ± 0.35	0.67 ± 0.06	0.15 ± 0.02	2.98 ± 0.25	0.61 ± 0.07	0.07 ± 0.07
VVV	0.79 ± 0.24	1.4 ± 0.4	0.41 ± 0.13	0.12 ± 0.05	1.6 ± 0.5	0.56 ± 0.18	0.13 ± 0.05
Others	11.1 ± 2.2	12.2 ± 2.2	1.8 ± 0.4	0.22 ± 0.05	9.0 ± 1.1	1.6 ± 0.7	0.10 ± 0.05
Regions	SR _{SFOS} ^{Wh} -15	SR _{SFOS} ^{Wh} -16	SR _{SFOS} ^{Wh} -17	SR _{SFOS} ^{Wh} -18	SR _{SFOS} ^{Wh} -19	SR _{DFOS} ^{Wh} -1	SR _{DFOS} ^{Wh} -2
Observed	51	5	37	7	4	10	10
Fitted SM	46 ± 7	9.8 ± 1.6	43 ± 7	12.6 ± 1.7	1.8 ± 0.4	4.5 ± 0.8	7.0 ± 2.3
WZ	18.9 ± 2.2	3.9 ± 0.8	35 ± 6	9.8 ± 1.6	1.44 ± 0.32	0.44 ± 0.14	1.05 ± 0.20
$t\bar{t}$	18 ± 6	3.2 ± 1.3	1.00 ± 0.34	0.33 ± 0.17	0.00 ^{+0.01} _{0.00}	1.0 ± 0.6	1.7 ± 1.1
Z +jets	0.00 ^{+0.12} _{0.00}	0.00 ^{+0.20} _{0.00}	2.5 ± 2.0				
Higgs	2.06 ± 0.23	0.36 ± 0.05	1.02 ± 0.12	0.44 ± 0.05	0.05 ± 0.05	1.59 ± 0.22	0.96 ± 0.11
VVV	1.5 ± 0.4	0.53 ± 0.17	2.5 ± 0.7	1.3 ± 0.4	0.2 ± 0.1	0.66 ± 0.15	0.64 ± 0.16
Others	5.0 ± 0.6	1.8 ± 0.5	3.0 ± 0.7	0.73 ± 0.15	0.14 ± 0.05	0.81 ± 0.09	0.21 ± 0.07

Table 6.15: Observed and expected yields after the background-only fit in the SRs for the SR_{SFOS}^{Wh} and SR_{DFOS}^{Wh} selection. The “Others” category contains the single-top, WW, $t\bar{t}$ + V and rare top processes. Statistical and systematic uncertainties are presented. [139]

Regions	SR ^{WZ} -1	SR ^{WZ} -2	SR ^{WZ} -3	SR ^{WZ} -4	SR ^{WZ} -5	SR ^{WZ} -6	SR ^{WZ} -7
Observed	331	31	3	2	42	7	3
Fitted SM	314 ± 33	35 ± 6	4.1 ± 1.0	1.2 ± 0.5	58 ± 5	8.0 ± 0.9	5.8 ± 1.0
<i>WZ</i>	294 ± 31	32 ± 5	3.7 ± 0.9	0.9 ± 0.5	48 ± 4	7.1 ± 0.8	5.0 ± 0.9
<i>ZZ</i>	12.1 ± 3.1	0.66 ± 0.35	0.08 ± 0.04	0.04 ± 0.02	2.3 ± 0.6	0.12 ± 0.04	0.08 ± 0.03
<i>t\bar{t}</i>	2.8 ± 0.8	0.36 ± 0.26	0.04 ± 0.01	0.00 ± $\begin{smallmatrix} 0.01 \\ 0.00 \end{smallmatrix}$	1.4 ± 0.4	0.00 ± $\begin{smallmatrix} 0.01 \\ 0.00 \end{smallmatrix}$	0.04 ± 0.02
<i>Z+jets</i>	0.01 ± 0.01	0.14 ± 0.14	0.05 ± 0.06	0.06 ± 0.04	2.8 ± 2.3	0.3 ± 0.4	0.26 ± 0.17
<i>t\bar{t}+X</i>	0.16 ± 0.06	0.13 ± 0.05	0.03 ± 0.04	0.01 ± 0.01	0.10 ± 0.06	0.05 ± 0.03	0.01 ± 0.01
Others	5.1 ± 0.8	1.1 ± 0.4	0.21 ± 0.06	0.17 ± 0.06	3.2 ± 0.5	0.38 ± 0.11	0.34 ± 0.10
Regions	SR ^{WZ} -8	SR ^{WZ} -9	SR ^{WZ} -10	SR ^{WZ} -11	SR ^{WZ} -12	SR ^{WZ} -13	SR ^{WZ} -14
Observed	1	77	11	0	0	111	19
Fitted SM	0.8 ± 0.4	90 ± 19	13.4 ± 2.4	0.5 ± 0.4	0.49 ± 0.24	89 ± 11	16.0 ± 1.4
<i>WZ</i>	0.44 ± 0.32	77 ± 18	11.3 ± 2.4	0.37 ± 0.31	0.38 ± 0.22	72 ± 9	13.4 ± 1.3
<i>ZZ</i>	0.01 ± 0.01	1.9 ± 0.9	0.24 ± 0.13	0.01 ± 0.01	0.01 ± 0.01	5.8 ± 2.8	0.39 ± 0.18
<i>t\bar{t}</i>	0.00 ± $\begin{smallmatrix} 0.01 \\ 0.00 \end{smallmatrix}$	3.3 ± 0.9	0.45 ± 0.28	0.00 ± $\begin{smallmatrix} 0.01 \\ 0.00 \end{smallmatrix}$	0.00 ± $\begin{smallmatrix} 0.01 \\ 0.00 \end{smallmatrix}$	6.0 ± 1.4	0.24 ± 0.17
<i>Z+jets</i>	0.28 ± 0.20	4 ± 5	0.2 ± 0.4	0.02 ± 0.03	0.02 ± 0.03	0.02 ± 0.03	0.02 ± 0.03
<i>t\bar{t}+X</i>	0 ± 0	1.3 ± 0.4	0.40 ± 0.14	0.05 ± 0.04	0.02 ± 0.01	1.6 ± 0.5	0.56 ± 0.16
Others	0.08 ± 0.06	2.3 ± 0.5	0.79 ± 0.22	0.08 ± 0.05	0.08 ± 0.03	3.5 ± 0.7	1.37 ± 0.33
Regions	SR ^{WZ} -15	SR ^{WZ} -16	SR ^{WZ} -17	SR ^{WZ} -18	SR ^{WZ} -19	SR ^{WZ} -20	
Observed	5	1	13	9	3	1	
Fitted SM	2.8 ± 0.6	1.30 ± 0.28	14 ± 6	9.2 ± 3.5	2.3 ± 0.9	1.1 ± 0.5	
<i>WZ</i>	2.3 ± 0.6	1.07 ± 0.24	10 ± 5	6.7 ± 3.4	1.6 ± 0.8	0.9 ± 0.5	
<i>ZZ</i>	0.07 ± 0.04	0.04 ± 0.03	0.13 ± 0.06	0.10 ± 0.04	0.02 ± 0.01	0.02 ± 0.01	
<i>t\bar{t}</i>	0.00 ± $\begin{smallmatrix} 0.01 \\ 0.00 \end{smallmatrix}$	0.00 ± $\begin{smallmatrix} 0.01 \\ 0.00 \end{smallmatrix}$	0.77 ± 0.32	0.45 ± 0.26	0.00 ± $\begin{smallmatrix} 0.01 \\ 0.00 \end{smallmatrix}$	0.00 ± $\begin{smallmatrix} 0.01 \\ 0.00 \end{smallmatrix}$	
<i>Z+jets</i>	0.02 ± 0.02	0.07 ± 0.08	1 ± 1	0.7 ± 1.0	0.25 ± 0.34	0.02 ± 0.02	
<i>t\bar{t}+X</i>	0.07 ± 0.03	0.00 $\begin{smallmatrix} 0.03 \\ 0.00 \end{smallmatrix}$	0.53 ± 0.17	0.33 ± 0.10	0.07 ± 0.04	0.03 ± 0.02	
Others	0.37 ± 0.11	0.12 ± 0.04	1.1 ± 0.8	0.9 ± 0.7	0.27 ± 0.07	0.18 ± 0.05	

Table 6.16: Observed and expected yields after the background-only fit in the SRs for the SR^{WZ} selection. The “Others” category contains the single-top, WW, triboson, Higgs and rare top processes. Statistical and systematic uncertainties are presented. [139]

Finally, the distributions of kinematic variables for some of the **SR** bins are shown below. In Figure 6.25, the E_T^{miss} and m_T distributions are shown in the SR_{0j}^{WZ} regions, which selects events in the SR^{WZ} selection with $N_{\text{jet}} = 0$, along with distributions of the p_T of the third lepton and the $\Delta R_{\text{OS, near}}$ in the $SR_{\text{DFOS}}^{\text{Wh}}-1$ and $SR_{\text{DFOS}}^{\text{Wh}}-2$, respectively. As already seen in the results above, no significant deviation from the **SM** background predictions is visible for any of the m_T and E_T^{miss} bins, while a mild excess is seen in the region $SR_{\text{DFOS}}^{\text{Wh}}-1$.

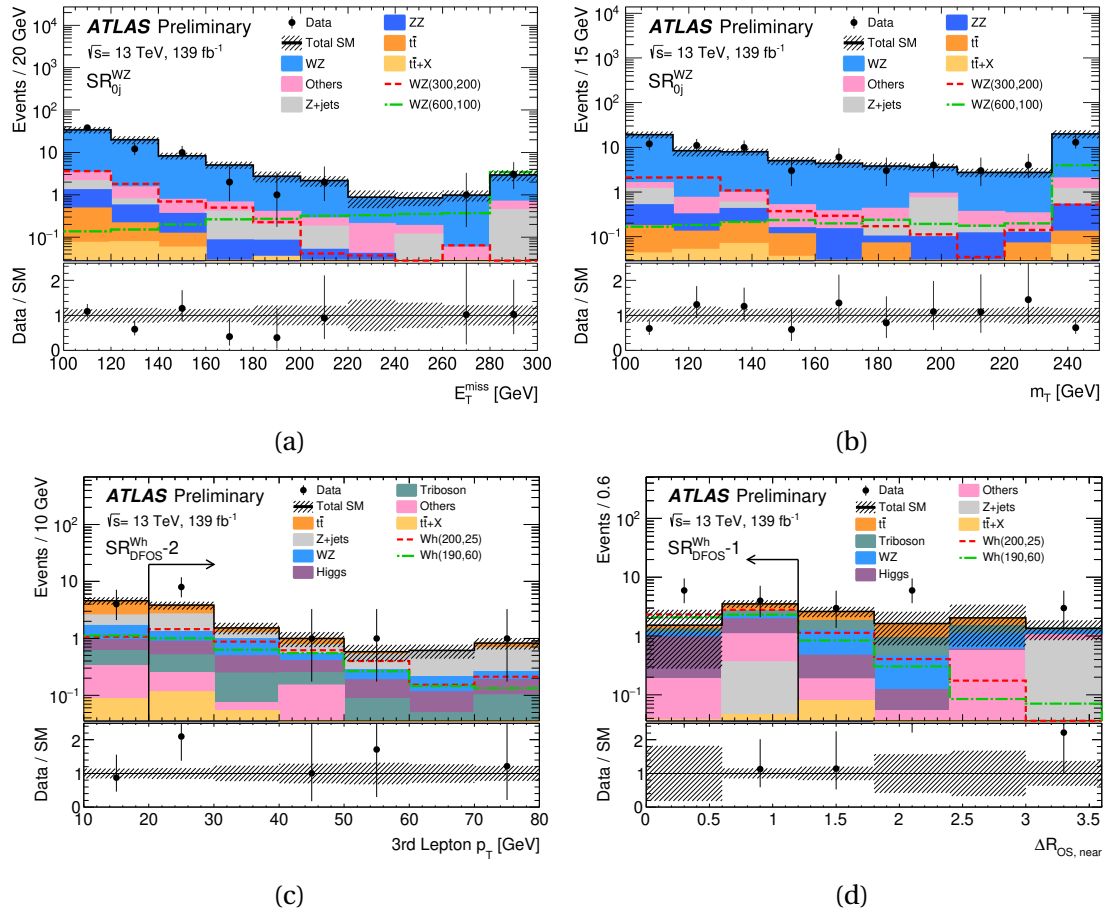


Figure 6.25: In the upper panels, data and **SM** background distributions of (a) E_T^{miss} and (b) m_T in the SR_{0j}^{WZ} selection, and (c) p_T of the 3rd lepton and (d) $\Delta R_{\text{OS, near}}$ in the $SR_{\text{DFOS}}^{\text{Wh}}-2$ and $SR_{\text{DFOS}}^{\text{Wh}}-1$ regions, respectively. In the lower panels, data on background ratio are compared to the error band, which includes all the statistical and systematic uncertainties on the background. [139]

For completeness, the N-1 distributions of all the other selection variables used in the definitions of $SR_{\text{DFOS}}^{\text{Wh}}-1$ and $SR_{\text{DFOS}}^{\text{Wh}}-2$ are shown in Figure 6.26. The mild excess in the region $SR_{\text{DFOS}}^{\text{Wh}}-1$ is again seen in some of the bins, particularly for $\Delta R_{\text{OS, near}} < 0.5$.

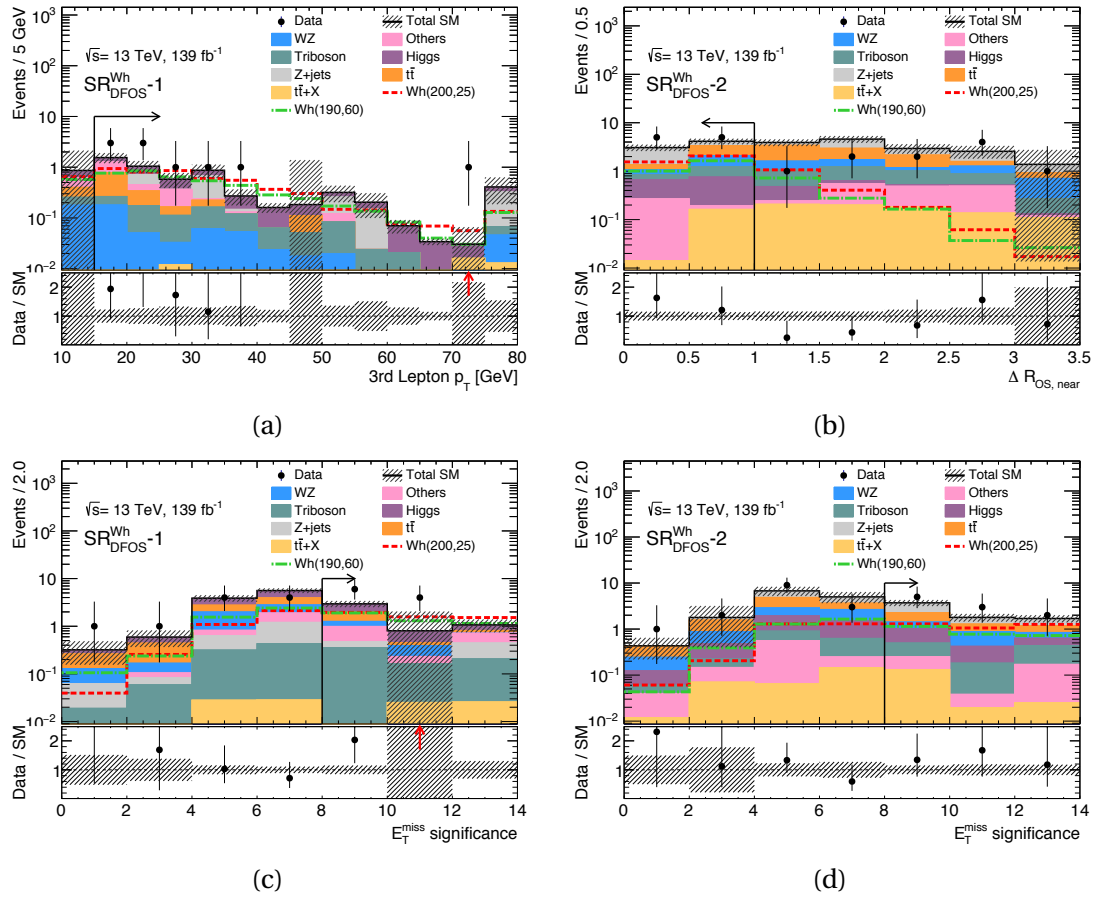


Figure 6.26: In the upper panels, data and SM background distributions of (a) the p_T of the 3rd lepton, (b) $\Delta R_{OS, near}$ and (c)-(d) E_T^{miss} significance, in the $SR_{DFOS}^{Wh}-1$ (first column) and $SR_{DFOS}^{Wh}-2$ (second column) regions. In the lower panels, data on background ratio are compared to the error band, which includes all the statistical and systematic uncertainties on the background.

Model-independent upper-limits

The model-independent fit is performed to set upper-limits on the number of observed and expected events. A set of dedicated *discovery regions* was identified for the purpose. These are defined to be sensitive to possible BSM physics, by not being optimised for any specific SUSY models, as done for the SRs considered in these searches. For this reason, binning in the SRs targeting the WZ and Wh models were relaxed, in order to consider more inclusive regions to use in a model-independent approach. A total of twelve discovery regions are defined in Table 6.17.

Upper-limits after the model-independent fit are shown in Table 6.18, which lists the upper limits on the observed (N_{obs}) and expected (N_{exp}) number of signal events, the CL value calculated under the SM-only hypothesis, and the p-value p_0 , calculated

SR ^{WZ} ($m_{\ell\ell} \in [75, 105]$ GeV)				
m_T [GeV]	$n_{\text{jets}} = 0$		$n_{\text{jets}} > 0$	
	E_T^{miss} [GeV]			
[100,160]	incSR ^{WZ} -1: [100,200]	incSR ^{WZ} -2: > 200	incSR ^{WZ} -3: [150,250]	incSR ^{WZ} -4: > 250
> 160	incSR ^{WZ} -5: > 200		incSR ^{WZ} -6: > 200	
SR ^{Wh} _{SFOS} ($m_{\ell\ell} \leq 75$ GeV)				
m_T [GeV]	$n_{\text{jets}} = 0$		$n_{\text{jets}} > 0$	
	E_T^{miss} [GeV]			
[0,100]	incSR ^{Wh} _{SFOS} -7: > 50		-	
[100, 160]	incSR ^{Wh} _{SFOS} -8: > 50		incSR ^{Wh} _{SFOS} -9: > 75	
> 160	incSR ^{Wh} _{SFOS} -10: > 50		incSR ^{Wh} _{SFOS} -11: > 75	
SR ^{Wh} _{DFOS}				
incSR ^{Wh} _{DFOS} -12: $n_{\text{jets}} \in [0, 2]$, $\Delta R_{\text{OS, near}} < 1.2$, 3rd lepton $p_T > 20$ GeV				

Table 6.17: Summary of the selection criteria for the inclusive SRs in the SR^{WZ}, SR^{Wh}_{SFOS} and SR^{Wh}_{DFOS} selections. [139]

under the SM-only hypothesis in each discovery region. In the case of the SR^{Wh}_{DFOS} selection, relaxing the binning in n_{jets} has had the effect to moderate the 2σ excess seen for the single bin SR^{Wh}_{DFOS}-1 down to 1.48σ for the inclusive DFOS bin incSR^{Wh}_{DFOS}-12. Similar deviations are seen for the inclusive incSR^{WZ}-6 (1.48σ) and incSR^{Wh}_{SFOS}-7 (1.27σ) regions.

SR	N_{obs}	N_{exp}	σ_{vis}^{95} [fb]	S_{obs}^{95}	S_{exp}^{95}	CLb	$p(s=0)$ (Z)
incSR ^{WZ} -1	34	38 ± 5	0.10	13.5	$15.7^{+6.7}_{-4.1}$	0.32	0.50 (0.00)
incSR ^{WZ} -2	2	1.2 ± 0.5	0.04	5.0	$4.0^{+1.6}_{-0.7}$	0.76	0.23 (0.73)
incSR ^{WZ} -3	4	6.5 ± 1.1	0.03	4.8	$6.5^{+2.6}_{-1.8}$	0.19	0.50 (0.00)
incSR ^{WZ} -4	25	31 ± 6	0.09	12.4	$15.4^{+6.0}_{-4.1}$	0.25	0.50 (0.00)
incSR ^{WZ} -5	1	5.2 ± 1.1	0.03	3.9	$5.8^{+2.2}_{-1.4}$	0.03	0.50 (0.00)
incSR ^{WZ} -6	23	16 ± 2	0.12	17.0	$10.3^{+3.9}_{-3.0}$	0.93	0.07 (1.48)
incSR ^{Wh} _{SFOS} -7	174	150 ± 14	0.41	57.6	$37.8^{+15.1}_{-10.6}$	0.90	0.10 (1.27)
incSR ^{Wh} _{SFOS} -8	53	55 ± 5	0.12	17.1	$18.3^{+7.4}_{-4.6}$	0.42	0.50 (0.00)
incSR ^{Wh} _{SFOS} -9	34	36 ± 4	0.10	13.8	$15.0^{+6.2}_{-4.2}$	0.40	0.50 (0.00)
incSR ^{Wh} _{SFOS} -10	56	55 ± 7	0.16	21.7	$20.5^{+8.3}_{-5.8}$	0.55	0.41 (0.22)
incSR ^{Wh} _{SFOS} -11	41	45 ± 6	0.11	15.5	$17.9^{+7.2}_{-4.8}$	0.34	0.50 (0.00)
incSR ^{Wh} _{DFOS} -12	18	11 ± 3	0.12	17.0	$10.5^{+4.2}_{-2.7}$	0.92	0.07 (1.48)

Table 6.18: Results of the model-independent fit in the discovery regions. The number of observed and expected yields, N_{obs} and N_{exp} , are after the background-only fit, for the inclusive discovery regions. Upper limits at 95% CL on the visible cross-section (σ_{vis}^{95}), the number of signal events (S_{obs}^{95}), and the expected number of signal events (S_{exp}^{95}) are shown. Finally, the CL value calculated for SM-only hypothesis and the correspondent p -value ($p(s=0)$) are listed. [139]

Model-dependent exclusion limits

In the absence of a significant deviation from the SM predictions, results have been interpreted as exclusion limits on the sparticle masses, independently for the WZ and Wh models targeted by the SRs.

The observed and expected exclusion limits for the WZ model are shown in Figure 6.27 and discussed in what follows.

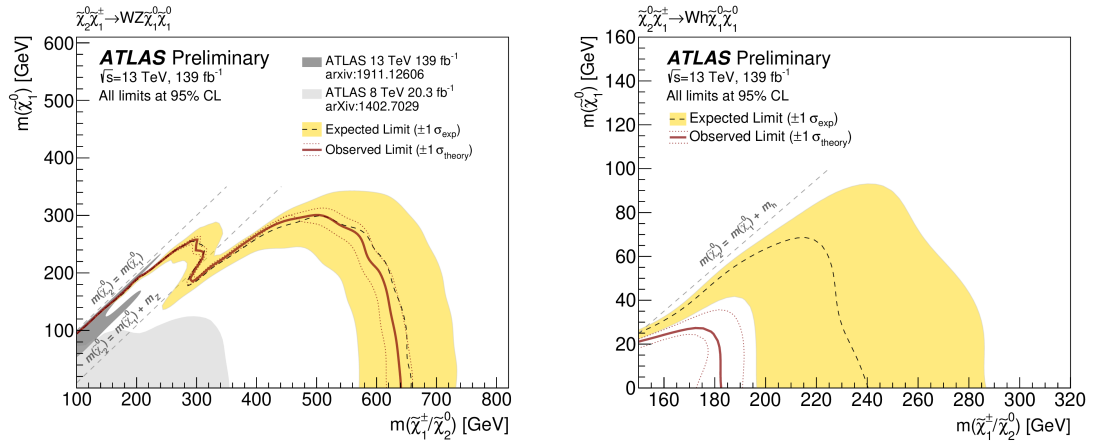


Figure 6.27: Observed (red solid line) and expected (dashed black line) exclusion limits on the masses $m_{\tilde{\chi}_1^\pm/\tilde{\chi}_2^0}$ and $m_{\tilde{\chi}_1^0}$ for the WZ and Wh models with three-lepton and missing transverse momentum in the final states. The yellow band corresponds to $\pm\sigma_{\text{exp}}$ systematic uncertainties. The dotted red lines represent the $\pm 1\sigma_{\text{theory}}$ uncertainties on the observed data from signal cross-section uncertainties. All limits are obtained at the 95% CL. On the left plot, the light and dark grey areas are the corresponding observed exclusion from similar analysis using the 8 TeV 20.3 fb^{-1} dataset [53] and the searches for compressed spectra using the 13 TeV 139 fb^{-1} dataset [140], respectively. [139]

In the case of the WZ model, results from the SR^{WZ} are considered for the $m_{\tilde{\chi}_1^\pm/\tilde{\chi}_2^0} > m_Z$, while limits on mass points with $m_{\tilde{\chi}_1^\pm/\tilde{\chi}_2^0} - m_{\tilde{\chi}_1^0} < m_Z$ are obtained via a combination of two set of results: those provided by the analysis targeting off-shell WZ -mediated decay, to which I did not make any contribution and it is described in [139], and the interpretation of the $\text{SR}_{\text{SFOS}}^{\text{Wh}}$ SRs for off-shell WZ points. Although being optimised to target the Wh scenario, the $\text{SR}_{\text{SFOS}}^{\text{Wh}}$ SRs have shown good sensitivity to the off-shell scenario of the WZ model, as shown in the left-hand plot of Figure 6.28.

Finally, in the right-hand plot in Figure 6.28, the observed and expected exclusion limits for the WZ model are shown, only for scenarios where WZ are on-shell, obtained from the results in the SR^{WZ} regions, dedicatedly optimised to be sensitive to

the WZ model. Overall, the results for the on-shell WZ analysis are able to exclude sparticle mass scenario up to $m_{\tilde{\chi}_1^\pm/\tilde{\chi}_2^0} = 640$ GeV (for a massless **LSP**), with a clear improvement with respect to previous equivalent analysis using $36.1 \text{ fb}^{-1} \sqrt{s} = 13$ TeV data [50]. Furthermore, the analysis reaches good sensitivity to models where the mass splitting is close to the kinematic edge $m_{\tilde{\chi}_1^\pm/\tilde{\chi}_2^0} - m_{\tilde{\chi}_1^0} = m_Z$, improving the exclusion of scenarios with compressed spectra and low-mass sparticles with respect to previous results from the ATLAS collaboration.

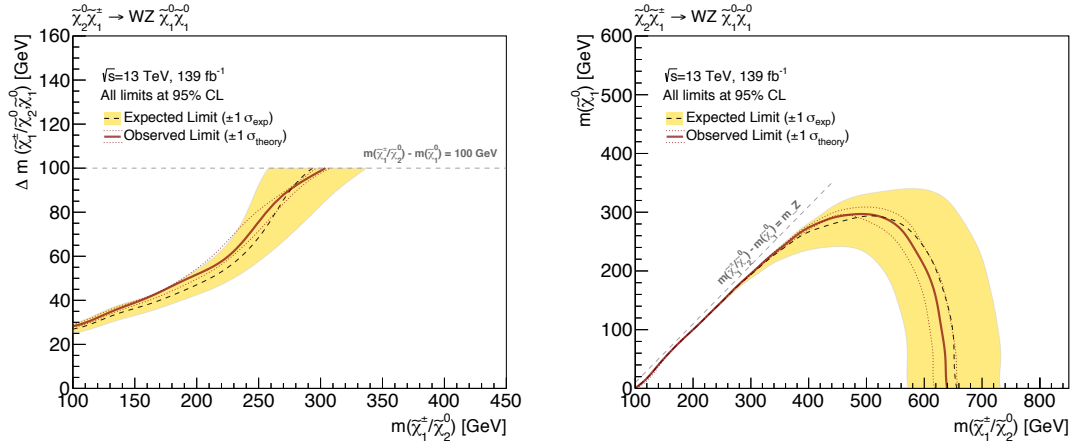


Figure 6.28: Observed (solid dark red line) and expected (dashed black line) limits on the masses of $\tilde{\chi}_1^\pm \tilde{\chi}_2^0$ and $\tilde{\chi}_1^0$ for WZ simplified models with three-lepton and missing transverse momentum in the final states. The yellow band corresponds to $\pm\sigma_{\text{exp}}$ systematic uncertainties. The dotted red lines represent the $\pm 1\sigma_{\text{theory}}$ uncertainties on the observed data from signal cross-section uncertainties. All limits are obtained at the 95% CL.

The observed and expected exclusion limits on the Wh model are shown in Figure 6.27. The limits are calculated at 95% CL, using results in the $\text{SR}_{\text{SFOS}}^{\text{Wh}}$ and $\text{SR}_{\text{DFOS}}^{\text{Wh}}$ regions. The analysis is able to exclude sparticle mass scenarios up to $m_{\tilde{\chi}_1^\pm/\tilde{\chi}_2^0} = 180$ GeV (for massless **LSP**), and shows sensitivity to signal models close to the kinematic edge $m_{\tilde{\chi}_1^\pm/\tilde{\chi}_2^0} - m_{\tilde{\chi}_1^0} = m_h$, as clear improvement of the equivalent early Run-2 analysis, described in Section 6.1. The difference between the observed and the expected limits is due to the mild excess in the $\text{SR}_{\text{DFOS}}^{\text{Wh}}$ -1 region, and it is consistent with the 2σ excess seen in this region. In particular, Figure 6.29 shows the expected sensitivity to the Wh model calculated for just the $\text{SR}_{\text{DFOS}}^{\text{Wh}}$ SRs, with reach expected exclusion for sparticle mass scenarios up to $m_{\tilde{\chi}_1^\pm/\tilde{\chi}_2^0} = 210$ GeV (for massless **LSP**).

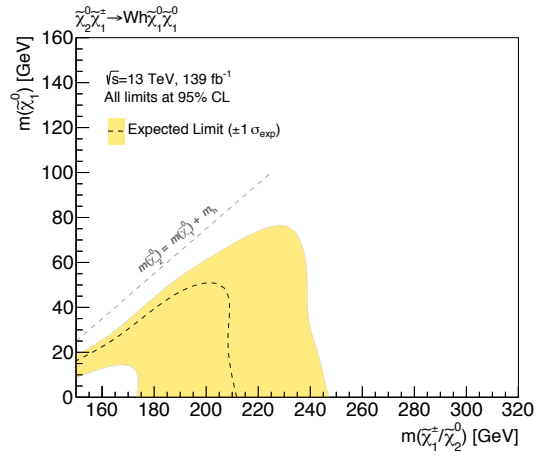


Figure 6.29: Observed (solid dark red line) and expected (dashed black line) limits on the masses of $\tilde{\chi}_1^\pm \tilde{\chi}_2^0$ and $\tilde{\chi}_1^0$ for Wh simplified models with three-lepton and missing transverse momentum in the final states. The yellow band corresponds to $\pm \sigma_{\text{exp}}$ systematic uncertainties. The dotted red lines represent the $\pm 1 \sigma_{\text{theory}}$ uncertainties on the observed data from signal cross-section uncertainties. All limits are obtained at the 95% CL.

7 | CONCLUSIONS AND OUTLOOK

In this thesis, analyses for the searches for $\tilde{\chi}_1^\pm \tilde{\chi}_2^0$ production by the ATLAS experiment with $\sqrt{s} = 13$ TeV proton-proton collisions at the LHC are presented. The targeted simplified models are those with intermediate SM bosons, WZ and Wh , decaying to final states with three light leptons and missing transverse momentum in the final states.

An early Run-2 analysis of 36.1 fb^{-1} data targeted only the Wh model in three-lepton final states. Although the analysis did not exclude any of the targeted SUSY scenario, it provided a training ground for the full Run-2 analysis, giving first hints of potential sensitivity for low-mass $\tilde{\chi}_1^\pm \tilde{\chi}_2^0$ and mass spectrum scenarios close to the kinematic edge $m_{\tilde{\chi}_1^\pm / \tilde{\chi}_2^0} - m_{\tilde{\chi}_1^0} = m_h$. In this search, I made major contribution as the main analyser of the three-lepton channel.

The full Run-2 analysis of 139 fb^{-1} collision data targeted both the Wh and WZ simplified models. I contributed to the analysis as one of the main analysers, with focus on Wh and on-shell WZ channels. No significant excess in data with respect to the SM predictions has been observed, although a mild excess of 2σ is seen for one of the Wh search bins. Results have been then interpreted as exclusion limits on the targeted simplified models. For the WZ signal scenario, masses for the $\tilde{\chi}_1^\pm$ and $\tilde{\chi}_2^0$ up to $m_{\tilde{\chi}_1^\pm / \tilde{\chi}_2^0} = 640$ GeV are excluded at 95% CL for massless $\tilde{\chi}_1^0$. This corresponds to an improvement of approximately 300 GeV with respect to previous equivalent analysis of 36.1 fb^{-1} data. For the Wh model, limits are set at 95% CL for masses up to $m_{\tilde{\chi}_1^\pm / \tilde{\chi}_2^0} = 180$ GeV for a massless $\tilde{\chi}_1^0$. The results for the standalone channel with three light leptons in the final states improve by approximately 30 GeV the Run-1 exclusion

obtained in combination with final states with hadronically decaying taus. Analysis results also show good sensitivity in **SUSY** scenarios with mass-splitting close to the diagonal $m_{\tilde{\chi}_1^\pm/\tilde{\chi}_2^0} - m_{\tilde{\chi}_1^0} = m_h$.

Despite no significant deviation from the **SM** has been observed, the searches for $\tilde{\chi}_1^\pm \tilde{\chi}_2^0$ with three-lepton final states provide an unique insight on the targeted **SUSY** scenarios, considerably improving the current exclusion limits and opening a window on the exploration of the challenging compressed scenarios for the sparticle mass spectrum. It will also provide a key contribution to the global fit of the **MSSM** [141], and provide inputs to the constraints on Dark Matter.

The summary plot in Figure 7.1 shows the most up-to-date expected and observed exclusion limits on the production of $\tilde{\chi}_1^\pm \tilde{\chi}_2^0$ decaying via intermediate bosons from the ATLAS collaboration, obtained from inputs of different analyses, including those described in this thesis.

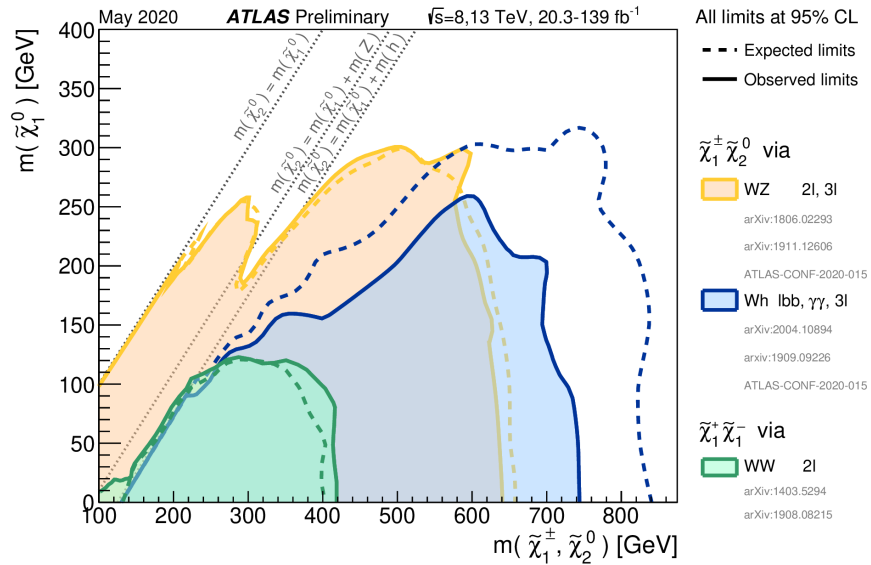


Figure 7.1: Observed and expected exclusion limits at 95% CL for the $\tilde{\chi}_1^\pm \tilde{\chi}_2^0$ searches via intermediate boson decays by the ATLAS experiment. [42]

The searches discussed in this thesis, and many other electroweak **SUSY** searches, will play a central role in the physics program of the ATLAS experiment during Run 3. In particular, the investigation of the Wh model in the three-lepton channel, which, although providing already compelling results with the full Run-2, can benefit from increased luminosity to target challenging low-mass scenarios, and from exploitation of some advanced **MVA**-based techniques, both at the event-reconstruction level and

as part of the analysis strategy.

Exploration of electroweak **SUSY** models will also have an important role in view of the High-Luminosity LHC (**HL-LHC**) upgrade [142]. Searches with leptons in the final states will benefit from the increased luminosity and improved analysis techniques which will be crucial in the hunt of elusive **SUSY** and other **BSM** scenarios. There is also scope to explore electroweak **SUSY** models also beyond the **LHC** era. Searches for production of charginos and neutralinos are part of the perspective physics programme of the main accelerator projects planned to start in the next few decades, both for linear e^+e^- collider [143] and circular hadronic colliders at $\sqrt{s} = 28$ TeV [144] and $\sqrt{s} = 100$ TeV [145].

In conclusion, the results of the searches presented in this thesis provide an essential contribution to understanding the most fundamental symmetry laws of the Universe, by also setting the ground for future and important developments in the hunt for New Physics.

A | PERFORMANCE OF THE HARDWARE-BASED TRACKING FOR TRIGGER UPGRADE FOR ATLAS

This appendix focuses on performance optimisation studies of a proposed tracking-based trigger upgrade of the ATLAS detector in view of the [HL-LHC](#), to which I made a contribution for my ATLAS authorship Qualification Task ([QT](#)).

A.1 The LHC and ATLAS upgrades for high-luminosity

The [HL-LHC](#) is the planned long-term upgrade of the [LHC](#), aimed at a dramatic increase of the instantaneous luminosity of the proton-proton collisions, essential preparation for the future physics programme of the [LHC](#) experiments [146]. Collisions at higher luminosity are important to open the chance to target rare processes not yet accessible at the luminosity currently planned for Run 3. Among other analyses, the increased luminosity will allow searches for elusive decays of the Higgs boson into leptons, di-Higgs production modes and heavy Higgs bosons. Also the [BSM](#) programme of the [LHC](#) experiments will benefit from the increased luminosity, as this will permit the exploration of challenging scenarios with low- p_T objects, particularly those with at least two light leptons and missing transverse energy in the final states. The main upgrades will particularly involve the injection complex, to allow more protons to populate the bunches in the beams. In particular, the [HL-LHC](#) is expected to collide protons at an instantaneous luminosity $\mathcal{L} = 7.5 \cdot 10^{34} \text{ cm}^{-2} \text{ s}^{-1}$, providing collisions at $\sqrt{s} = 14 \text{ TeV}$, and start operations in the year 2026 with the so-called Run 4 of data taking. In parallel with the [LHC](#) upgrades, The ATLAS detector is expected to go through a series

of upgrades, performed in stages [147, 148].

A first stage of upgrades will involve improvements in the electronic components of the TDAQ system and the CTP. In addition, New Small Wheels are expected to be installed in the end-cap regions to provide coincidence measurements to reject of events where forward objects fire mistakenly a muon trigger chain.

In view of the HL-LHC, a new full silicon tracking detector, the so-called Inner Tracker (ITk) [149], will replace the current ID. During LS1, the radiation damages occurred during Run 1 were partly recovered by the insertion and commissioning of the IBL. However, further radiation damages by the end of the Run 3 will inevitably require the full replacement of the current ID. The current design of the ITk comprises both silicon strips and pixel detectors arranged in the barrel and end-cap regions. In the barrel region, the $50 \times 50 \mu\text{m}^2$ pixels are arranged on an axial geometry around the beam axis, for a total of five layers in the barrel. In the end-cap region, the pixel modules are disposed in rings around the beam axis. Their position ensures a constant number of hits across all the η range, providing a coverage of the forward region $|\eta| < 4$. The silicon strip detector of the ITk comprises four double-layers silicon strip detectors in the barrel region and five disks in the end-cap, arranged in a cylindrical geometry around the beam axis. Overall, the strip detectors cover a region up to $|\eta| < 2.7$. The strips in the end-cap layers are distributed in a radial configuration, pointing at the beam axis and organised in rows for each of the five discs.

A.2 ATLAS TDAQ architecture for the Phase-II upgrade

Along with upgrades purely concerning the detector hardware and design, the architecture of the ATLAS TDAQ will be modified, due to the increased pile-up expected at HL-LHC. A schematic view of the proposed TDAQ structure for HL-LHC is visible in Figure A.1.

In one possible architecture, the Phase-II TDAQ structure is composed of three levels of event selection. At a very initial stage, L0 triggers are performed using features extracted from the calorimetry system and the muon chamber. The L0Calo uses hardware information to extract features of electron, photons, tau and jets. The com-

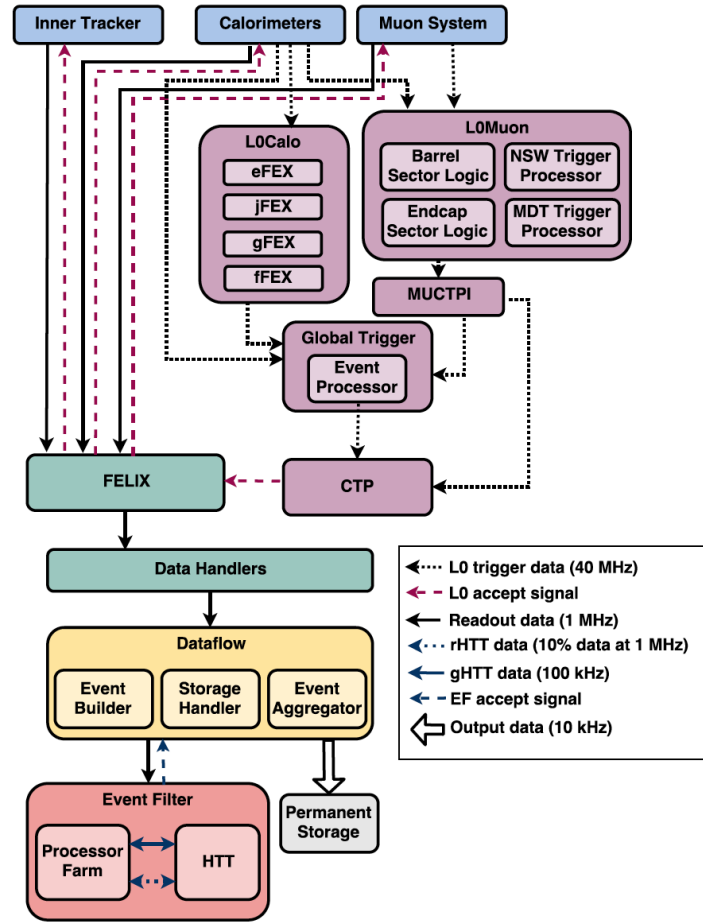


Figure A.1: Proposed structure of the TDAQ system for the ATLAS detector in view of the HL-LHC. Hits from the calorimetry system, the muon chambers and the inner tracker (in blue) are used in the trigger. The Level-0 (L0) of the trigger structure is represented in dark pink, while the Front-End Link eXchange (FELIX) and the Data Handlers are represented in green. Finally the Dataflow step and the Event Filter are represented in yellow and red, respectively. [148]

ponents able to perform such extraction are referred to as the electron Feature EXtractor (eFEX) and the jet Feature EXtractor (jFEX). In addition, L0Calo performs feature extraction for objects at low p_T in the forward region, using the forward Feature EXtractor (fFEX) component. The L0Muon uses hits from the MS from the RPCs and TGCs and comprises Trigger Processors for the MDTs and the New Small Wheel (NSW). It is interfaced to the CTP through the MUon Central Trigger Processor Interface (MUCTPI). The Global Trigger is another component at the L0 of the TDAQ. It uses the granularity of the calorimeter towers to perform almost-offline algorithms on trigger objects reconstructed by L0Calo and L0Muon. The information is finally passed to the CTP that makes a final decision whether an event passes the L0 trigger step. If it

does, the decision is passed to the Trigger, Timing Control system (TTC) that will allow full readout of detector-wide information.

If an event passes the L0 trigger, it is passed through the Readout sub-system which comprises the FELIX and subsequently the Data Handler. The Readout sub-system collects and processes the specific inputs from the ATLAS sub-detector before being transferred to the Dataflow sub-system stream. The Dataflow sub-system is formed by the Event Handler, the Storage Handler and the Event Aggregator, where information from the Readouts is buffered and aggregated to form the event stream.

With the Data Acquisition (DAQ) as described, the event rate at this stage would still be approximately of the order of 1 MHz, too high to be managed by the CERN storage facilities. For this reason, all components of the DAQ are connected to an Event Filter (EF) system. The EF consists of both CPU-based and hardware-based trigger processing that make a further filter decision of the events before storing them permanently in the facilities. The EF uses information from the ITk to reconstruct tracks and vertexes and uses tracking information to make a decision on whether to accept or not the events. The use of tracking information is essential at this step. The main scope of the upgraded architecture of the TDAQ is to lower the event rate so as to meet storage limitations, while maintaining the same physics acceptance as in Run-1.

A.3 The Hardware-based Tracking for Trigger for the HL-LHC

The proposed Hardware-based Tracking for Trigger (HTT) system is composed of Associative Memory (AM) Application Specific Integrated Circuits (ASICs) for pattern recognition and Field Programmable Arrays (FPGAs) for track fitting, managed within a module called Pattern Recognition Mezzanine (PRM). It takes part in the EF step of the Phase-II architecture of the TDAQ. The pattern recognition and the track fitting steps are consecutive and provide information to the EF to decide whether an event can be stored or not. The EF can ask the HTT to perform two different types of tracking, according to the kind of trigger signature that needs to be tested. In one case, the HTT is requested to perform a regional tracking (rHTT) in specific RoIs, designed around those trigger ob-

jects identified by the **L0** detectors with available track information, typically electrons, muons or jets. The **rHTT** is able to reduce the event rate down to 400 kHz. The other possibility is to run a global tracking (**gHTT**) across all the η scan of the **ITk**. The **gHTT** generally provides better resolutions and purity than the **rHTT**, giving the possibility to the **EF** to make trigger decisions using information regarding lepton isolation, primary vertex reconstruction or *b*-jet-tagging, but with longer processing times.

Generally, the way **HTT** reconstructs tracks from hits in the **ITk** is based on pattern recognition. For both the **rHTT** and the **gHTT** configurations, hits from consecutive silicon strips and pixel modules of the **ITk** are initially clustered and aggregated in so-called *superstrips*. A sequence of superstrips is called a pattern, characterised by coordinates measured by the silicon modules of the **ITk** arranged in eight layers of the detector. Each pixel layer and each side of the double-sided strip layers count as a layer in the pattern identification. When a hit pattern is identified, this is compared to candidate template patterns, which are pre-created patterns obtained from simulated samples of single-muon events and stored in the **FPGAs** in collection called *pattern banks*. This operation is handled by the **AM ASICs**. After a hit pattern is matched to a template pattern, track parameters are extracted from pattern coordinates via a track fit in the **FPGAs** in the **PRM**. At this point, the response of the **HTT** changes according to the original request from the **EF**: the **rHTT** releases the informations back to the **EF**. If the **gHTT** is requested, the track fit is extended to the remaining layers of **ITk** to give best parameter resolutions.

A.3.1 Track fitting in HTT

After the pattern recognition and matching, the track parameters are extracted from the coordinates of the superstrip hits that form the matched pattern. A linear correlation is assumed between the hit coordinates and track parameters. One can write:

$$p_i = \sum_{j=1}^N C_{ij} x_j + q_i, \quad (\text{A.1})$$

where N indicates the total number of hit coordinates or layers in the pattern recognition, p_i are the track parameters, x_j are the superstrip coordinates and the (C_{ij}, q_i) are fit parameters. As a reminder, the track parameters are those fully describing a track:

curvature, η , ϕ , d_0 and z_0 . Generally, the values of the constants depend on the position of the pattern and they are related to which modules of the detector have recorded hits for the pattern recognition. A sequence of tracker modules hit by the pattern matched is called a *sector*, which is identified by specific and unique values of (C_{ij}, q_i) . Therefore, track parameters can be extrapolated looking at all the sectors that describe the modules the pattern passes through. Finally, the track with minimum χ^2 is selected as the reconstructed track.

A full coverage of all the sectors in the [ITk](#) is key for an accurate extraction of the track parameters. Generally, this is obtained by training all the possible sectors with simulated single-muon events, so that pre-defined fit parameters can be obtained and stored.

The track fit presents some limitation due to the available hardware. In fact, one would require as many sectors as possible to be stored in specific *sector banks* in the [FPGAs](#), so that full coverage and high statistics for the extrapolation of the fit constants can be ensured throughout the track fit procedure. Nevertheless, this is subject to compelling hardware limitations, since the available storage space would hardly permit a large number of sectors to be saved. Approximately, the [FPGAs](#) are expected to contain not much more than 3000 sectors for the track-fitting step. In the following, a possible strategy to reduce the needed storage space for sector bank files is described.

A.3.2 Reduction of storage space needed by track-fitting step

This section presents the core of my qualification task. As a reminder, the size of the sector banks is limited by the hardware storage capacities. Therefore, there is the need to reduce the size of the sector banks, without affecting performance and coverage of the [HTT](#).

All the studies have been performed over ten thousand simulated single-muon events with p_T of at least 4 GeV. The studies described here were performed by analysing the track fit efficiencies, calculated by using fitted tracks with a $\chi^2 < 40$, and residuals of the track parameters, calculated as difference between the fitted track parameters and the true values from simulation. The reconstruction resolution is calculated as Root Mean Square ([RMS](#)). When not specified, the nominal average interactions per

bunch crossing for HL-LHC of $\langle\mu\rangle = 200$ is assumed by injection of simulated jets in the events.

At first, the reduction of the size of the sector banks was attempted by reducing the size of the single-muon training samples. Different numbers of training events were explored. In the following, results for sector banks trained with one million and fifteen millions muons are shown. The RMS on the residuals for the reconstruction of the η are shown in Table A.1.

Number of training muons	Number of sectors	Efficiency	RMS on η
1 million	3392	$99.11 \pm 0.26 \%$	0.002452
15 million	5183	$99.31 \pm 0.29 \%$	0.002340

Table A.1: Sector numbers, efficiency and RMS on η comparison between two sector banks trained with one million and fifteen million simulated single-muons events.

Reducing the number of training muons corresponds to a reduction of the number of sectors, as expected. Reducing the number of training muons from fifteen million to one million reduces the number of sectors to be stored in the FPGAs by approximately 35%. Although no substantial difference is seen in terms of efficiency, a reduction of 4-5 % of RMS is found. Therefore, the results suggest a clear loss in reconstruction performance, and simply reducing the number of training muons is not a viable strategy to meet the hardware limitations.

An alternative way was tested. Instead of reducing the training size of the sectors, sector banks trained with the highest available amount of muons were used. The production of the sector banks used around 30×10^6 muons in the training. Contrary to what was done for the results in Table A.1, the full-statistics sector banks were skimmed by applying a requirement on the number of training muons per sector, discarding those which do not fulfil the criterium. Applying a lower cut on the number of training muons presents a few advantages:

- The size of the bank file is reduced by a cut that can be optimised according to the required performances in the RoIs and as a function of training muon kinematic variables:
- The lower cut on the number of training muons will skim just those sectors which were trained with fewer particles.

Different lower cuts have been tested and compared to each other, in two different η intervals and with or without pile-up. Different η intervals were used to test the validity of the strategy at different RoIs. In all the cases, patterns are required to hit eight layers, one from the pixel modules and seven from the strips of the ITk.

In a first stage, sectors were produced in the $[0.1, 0.3]$ η interval. Pile-up is assumed to be the nominal $\langle\mu\rangle = 200$ of the HL-LHC. Resolutions for the five reconstructed track parameters are shown in Figure A.2 and Figure A.3, for a test on ten thousand single-muon events with p_T between 4 and 400 GeV.

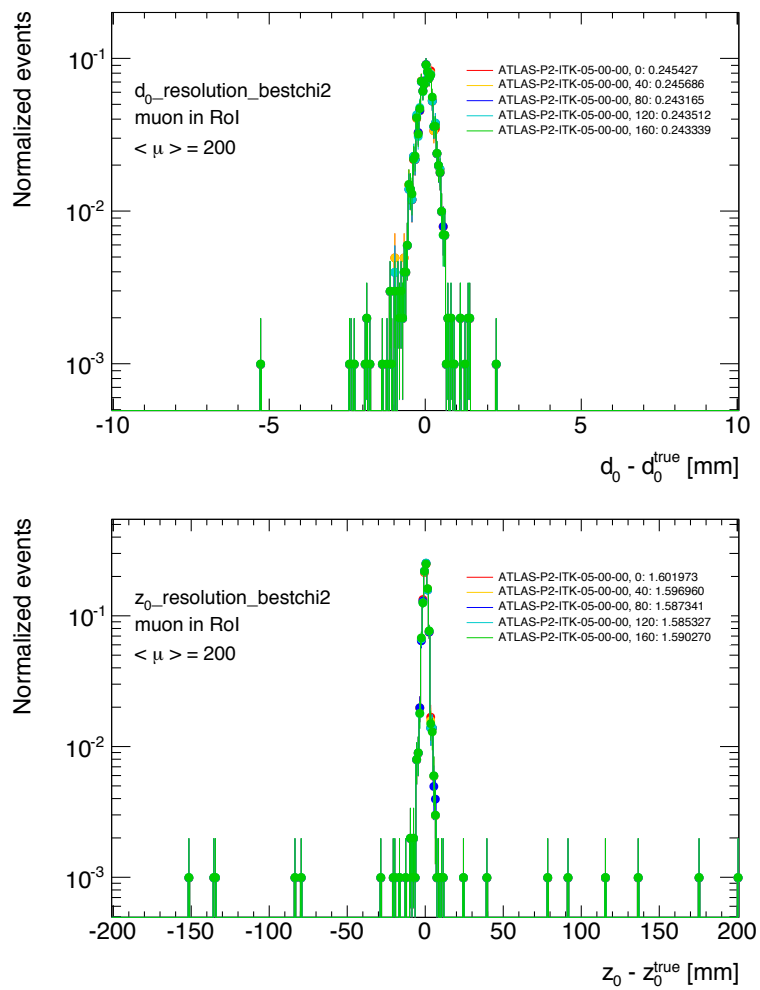


Figure A.2: Resolution of d_0 and z_0 , calculated as RMS. Calculated over ten thousand simulated single-muon events passing through ITk and requiring at least one pixel layer and seven strip layers to be hit by the particles. The targeted region is the $[0.1, 0.3]$ η interval. Pile-up is assumed to be the nominal of the HL-LHC, $\langle\mu\rangle = 200$.

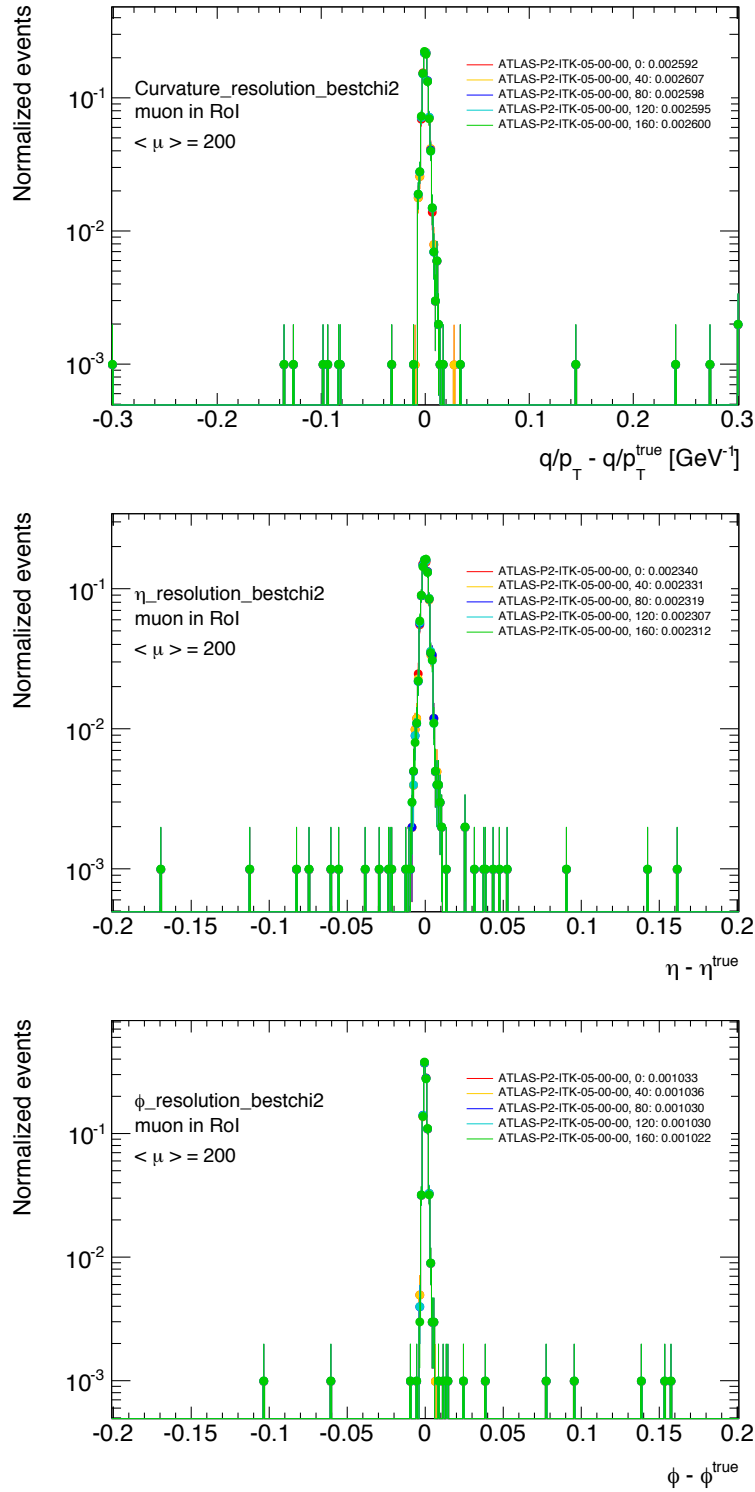


Figure A.3: Resolution of curvature, η and ϕ , calculated as RMS. Calculated over ten thousand simulated single-muon events passing through ITk and requiring at least one pixel layer and seven strip layers to be hit by the particles. The targeted region is the [0.1, 0.3] η interval. Pile-up is assumed to be the nominal of the HL-LHC, $\langle \mu \rangle = 200$.

As seen in Figure A.2 and Figure A.3, no clear difference in resolution is noticed for any of the track parameters, when comparing five different lower cuts on the number of training muons: 0, 40, 80, 120, 160. Efficiencies and number of sectors are shown in Table A.2. A lower cut at 40 on the number of training muons reduces the sample size by 35%, without any tangible effect on resolution and efficiencies.

# muon cuts	Number of sectors	Efficiency	RMS on η
0	5183	99.7 %	0.002340
40	3702	99.5 %	0.002331
80	3203	99.3 %	0.002319
120	2936	98.9 %	0.002307
160	2696	98.6 %	0.002312

Table A.2: Sector numbers, efficiency and RMS on η for the five cuts on the number of training muons considered in the studies. The η range considered is between 0.1-0.3 and pile-up from soft-scattering collisions assumed to be the nominal of the HL-LHC, $\langle\mu\rangle = 200$.

The same performance studies have been performed in the [0.7, 0.9] η interval. In this case, the method is tested in a different RoI and without any effects due to additional pile-up jets. Results are shown in Figure A.4 and Figure A.5.

Similarly to the results in the [0.1, 0.3] η interval, in Figure A.4 and Figure A.5 no drastic change in resolution is noticed for any track parameter. This is also reflected in Table A.3, although results indicate a tighter cut in the [0.7, 0.9] η interval might be needed with respect to the first case analysed.

# muon cuts	Number of sectors	Efficiency	RMS on η
0	8185	97.9 %	0.001160
40	5039	97.7 %	0.001154
80	3988	97.3 %	0.001144
120	3337	96.7 %	0.001145
160	2877	96.0 %	0.001142

Table A.3: Sector numbers, efficiency and RMS on η for the five cuts on the number of training muons considered in the studies. The η range considered is between 0.7-0.9 and no pile-up from soft-scattering collisions is considered.

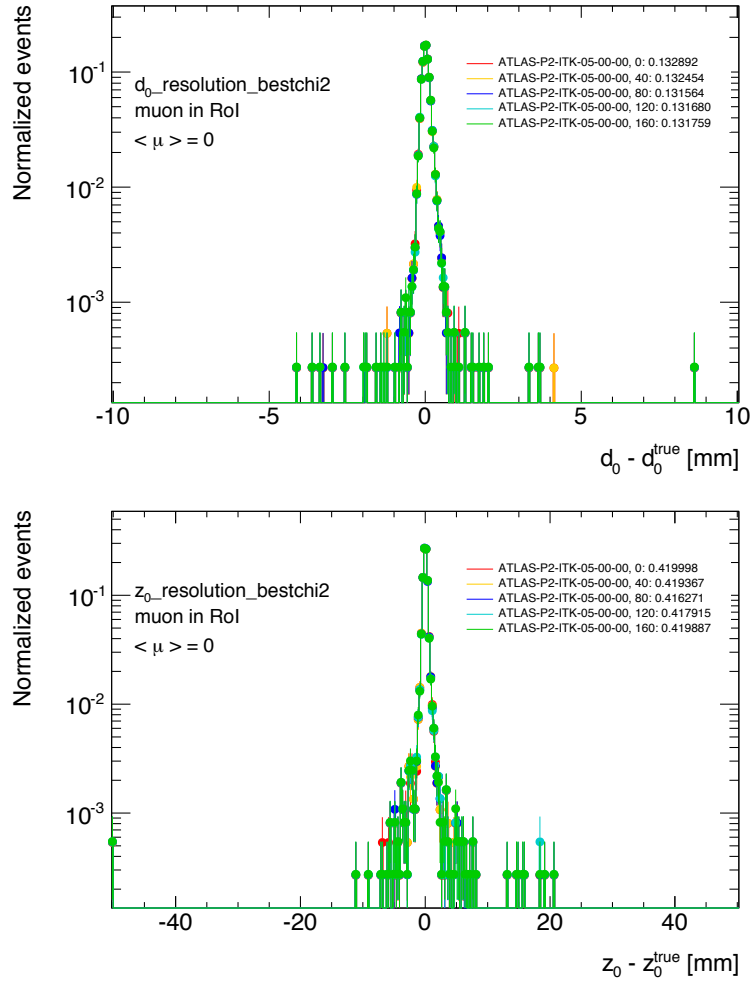


Figure A.4: Resolution of d_0 and z_0 , calculated as RMS. Calculated over ten thousand simulated single-muon events passing through ITk and requiring at least one pixel layer and seven strip layers to be hit by the particles. The targeted region is the $[0.7, 0.9]$ η interval. No pile-up is considered, $\langle \mu \rangle = 0$.

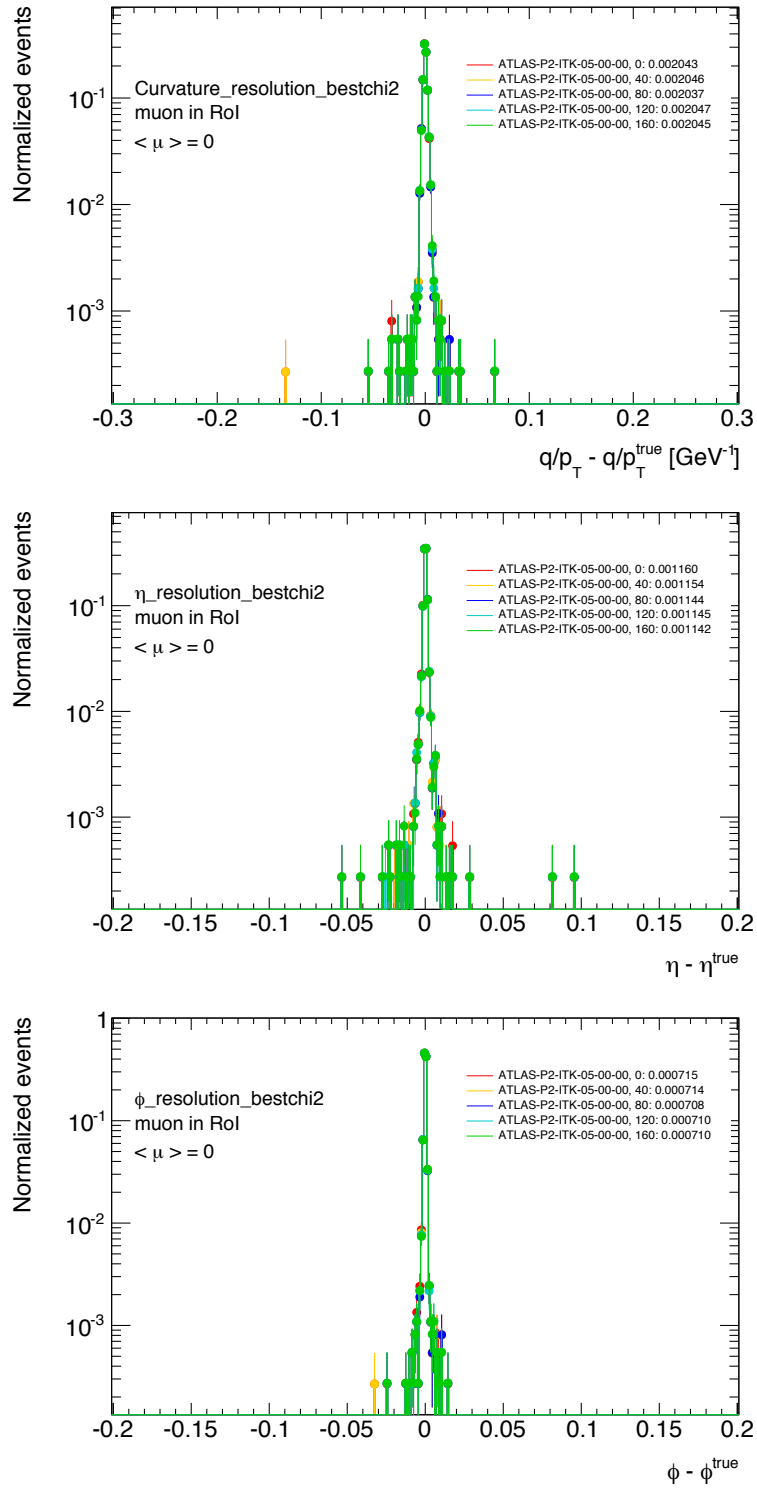


Figure A.5: Resolution of curvature, η , ϕ , calculated as RMS. Calculated over ten thousand simulated single-muon events passing through ITK and requiring at least one pixel layer and seven strip layers to be hit by the particles. The targeted region is the $[0.7, 0.9]$ η interval. No pile-up is considered, $\langle \mu \rangle = 0$.

A.3.3 Exploring the low- p_T range

At this point, only muons with $p_T > 4$ GeV have been tested. Performance studies have been performed for low p_T muons, to test the robustness of the sector reduction strategy even a low p_T . The studies presented in Section A.3.2 have been repeated for the $0.7 < |\eta| < 0.9$ interval, but for single-muon events with $p_T > 2$ GeV and 1 GeV. No pile-up is considered. As a consequence of lowering the p_T range, more training muons are needed for the production of the sector banks. Sixty and ninety million training muons were used to cover the RoI coverage and statistics for the sector bank production in the two p_T ranges [2, 400] GeV and [1, 400] GeV, respectively. Residual plots for the track parameters are shown in Figure A.6 and Figure A.7, for the [2, 400] GeV p_T range, and Figure A.8 and Figure A.9, or the [1, 400] GeV p_T range.

As Figure A.6-A.9 show, no substantial loss of resolution on the track parameter is observed, for all the considered lower cuts on the training muons and independently on the muon p_T range. As done in Section A.3.2, the impact of the reduction of the number of sectors on the efficiencies was calculated. Results for the two p_T ranges are shown in Table A.4 and Table A.5, respectively.

# muon cuts	Number of sectors	Efficiency	RMS on η
0	15521	98.23 %	0.001079
40	10119	98.20 %	0.001078
80	8632	98.15 %	0.001079
120	7792	98.10 %	0.001080
160	7213	98.07 %	0.001081

Table A.4: Sector numbers, efficiency and RMS on η for the five cuts on the number of training muons considered in the studies. The η range considered is between 0.7-0.9 and no pile-up from soft-scattering collisions is considered. Numbers refer to analysis of ten thousand muons with p_T between 2 GeV and 400 GeV.

# muon cuts	Number of sectors	Efficiency	RMS on η
0	31601	98.78 %	0.001092
40	18992	98.75 %	0.001093
80	15695	98.72 %	0.001092
120	13877	98.66 %	0.001093
160	12691	98.61 %	0.001093

Table A.5: Sector numbers, efficiency and [RMS](#) on η for the five cuts on the number of training muons considered in the studies. The η range considered is between 0.7-0.9 and no pile-up from soft-scattering collisions is considered. Numbers refer to analysis on ten thousand muons with p_T between 1 GeV and 400 GeV.

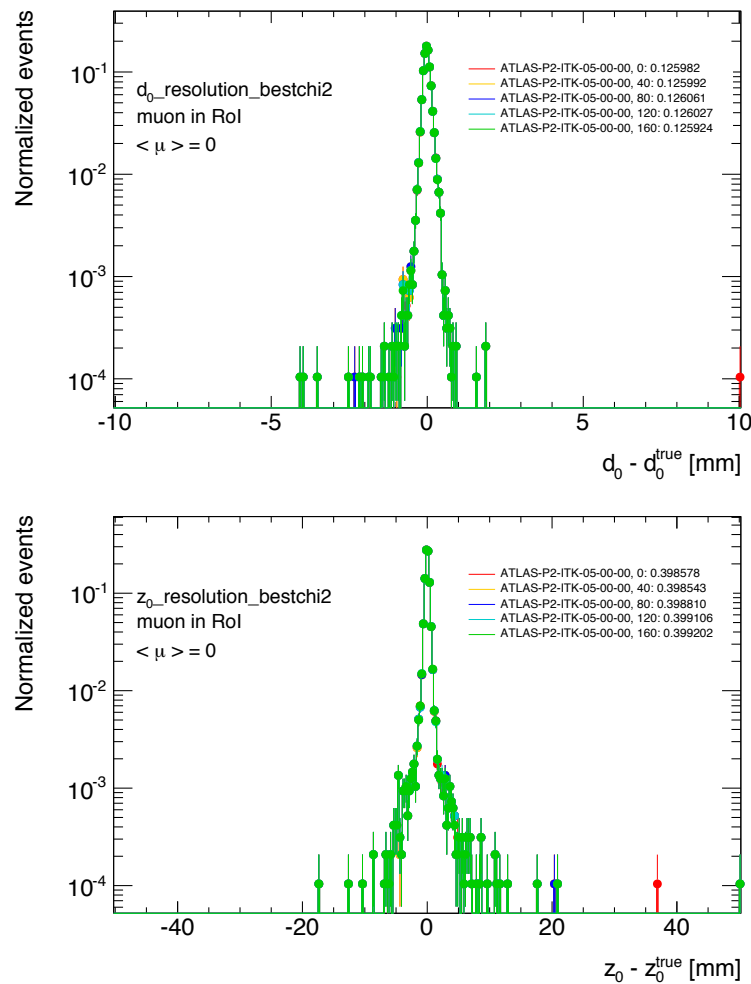


Figure A.6: Resolution of d_0 and z_0 , calculated as [RMS](#). Calculated over ten thousand simulated single-muon events passing through *ITk* and requiring at least one pixel layer and seven strip layers to be hit by the particles. The muon p_T range is [2, 400] GeV. The targeted region is the [0.7, 0.9] η interval. No pile-up is considered, $\langle \mu \rangle = 0$.

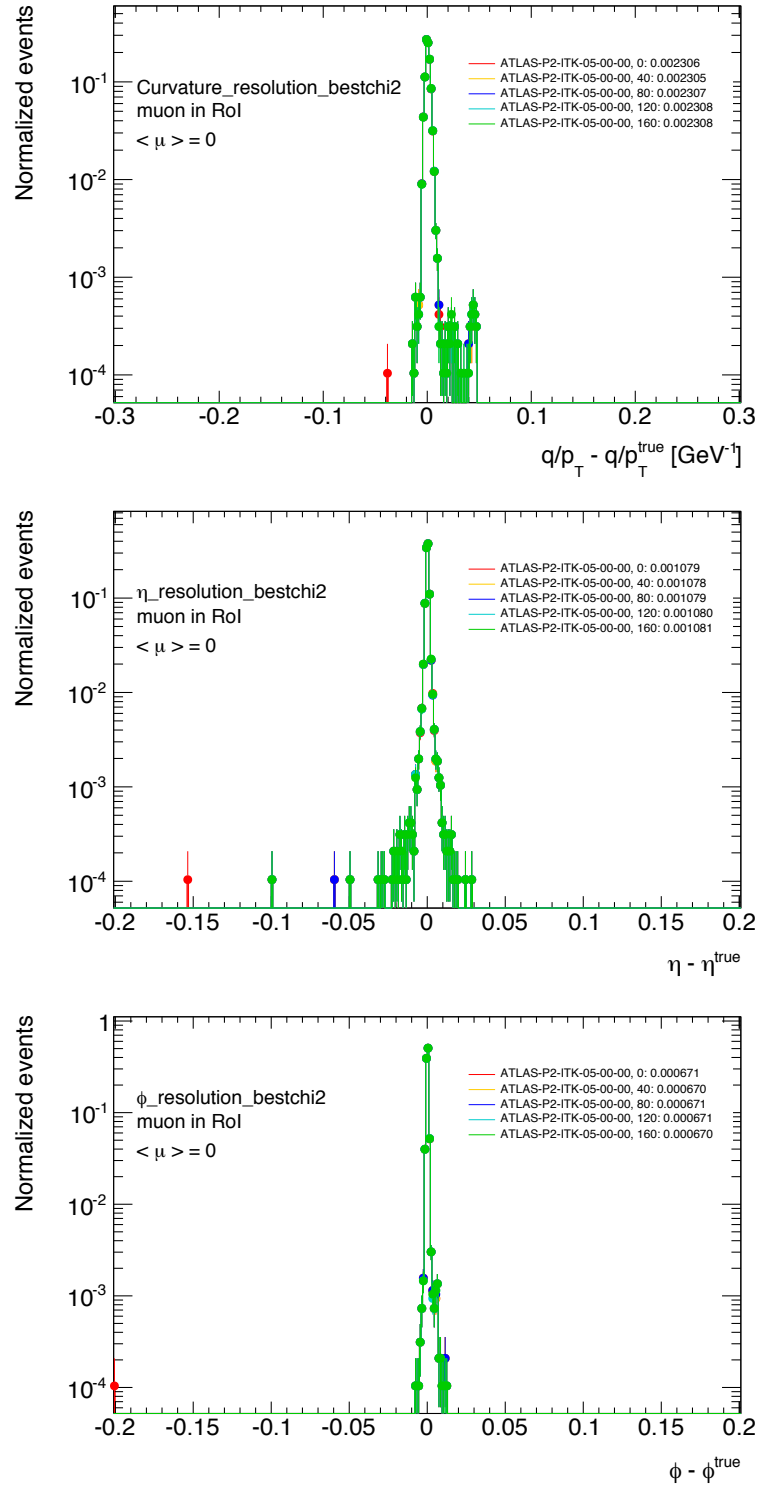


Figure A.7: Resolution of curvature, η , ϕ , calculated as RMS. Calculated over ten thousand simulated single-muon events passing through *ITk* and requiring at least one pixel layer and seven strip layers to be hit by the particles. The muon p_T range is [2, 400] GeV. The targeted region is the [0.7, 0.9] η interval. No pile-up is considered, $\langle \mu \rangle = 0$.

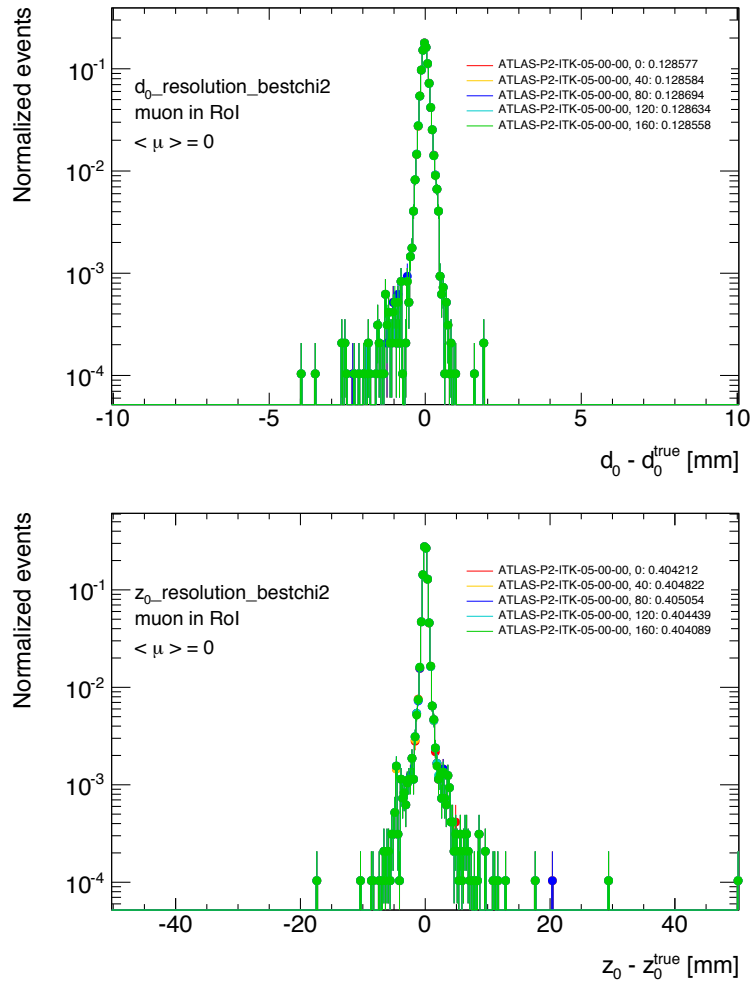


Figure A.8: Resolution of d_0 and z_0 , calculated as RMS. Calculated over ten thousand simulated single-muon events passing through ITk and requiring at least one pixel layer and seven strip layers to be hit by the particles. The muon p_T range is [1, 400] GeV. The targeted region is the [0.7, 0.9] η interval. No pile-up is considered, $\langle \mu \rangle = 0$.

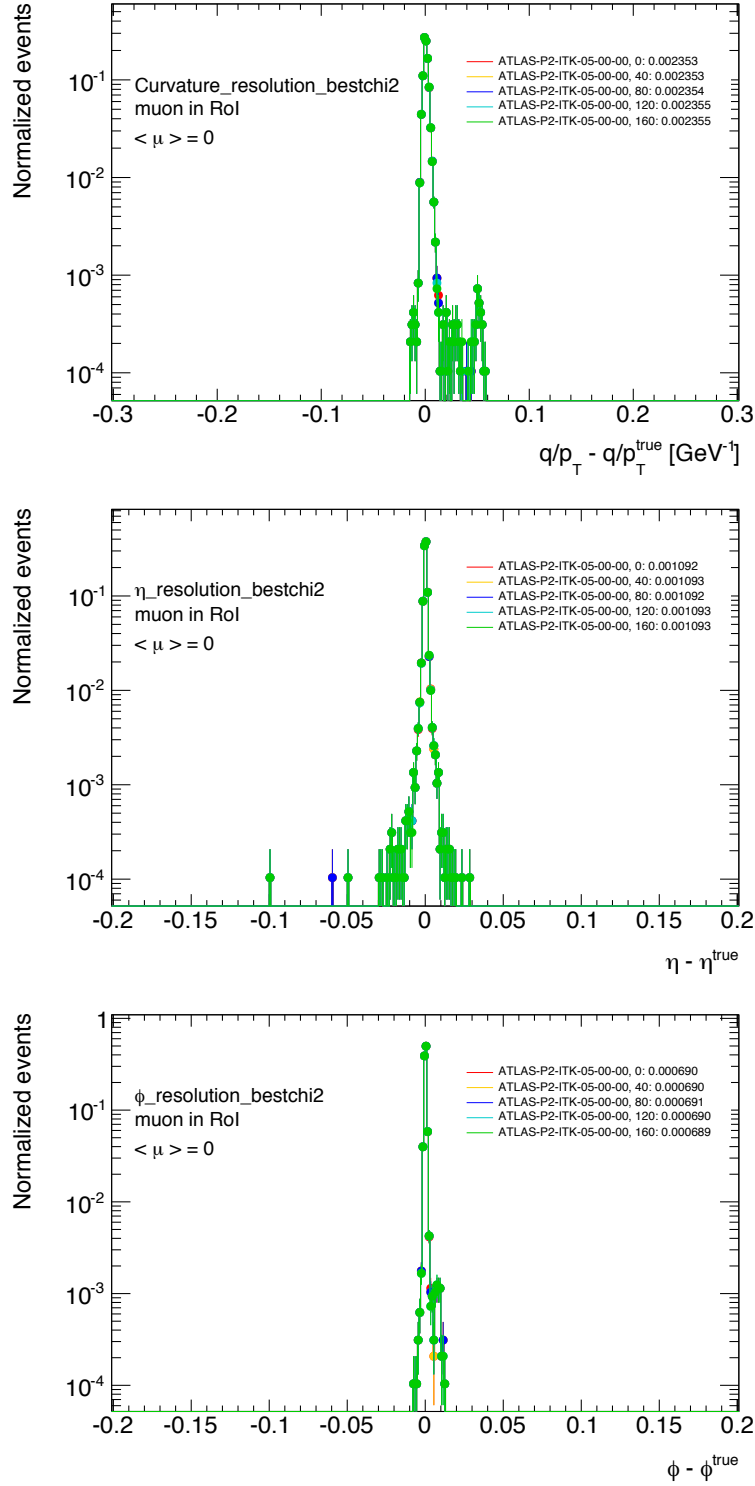


Figure A.9: Resolution of curvature, η , ϕ , calculated as RMS. Calculated over ten thousand simulated single-muon events passing through *ITk* and requiring at least one pixel layer and seven strip layers to be hit by the particles. The muon p_T range is [1, 400] GeV. The targeted region is the [0.7, 0.9] η interval. No pile-up is considered, $\langle \mu \rangle = 0$.

As seen in Table A.4 and Table A.5, although clear evidence that the strategy can be extended to the low- p_T case and no important loss of efficiency and resolution is noticeable across all the cuts tested. In particular, due to the increased statistics, at a lower p_T threshold, a tighter cut on the number of training muons is needed for a substantial suppression of the number of sectors. This is shown also in Figure A.10, where the distribution of the average number of training muons per sector as a function of the lepton p_T is presented for all three p_T ranges considered in the studies.

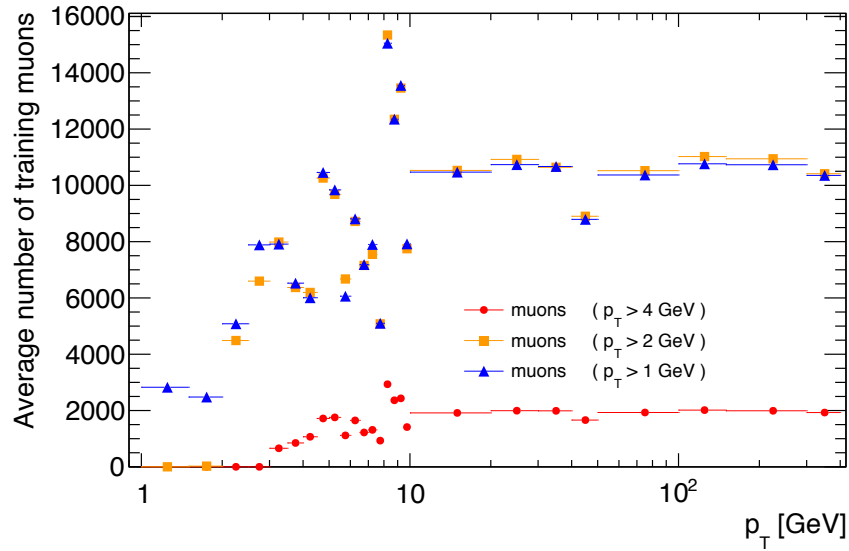


Figure A.10: Profiling of the number of training muons against their p_T . The three p_T ranges between 4 GeV-400 GeV, 2 GeV-400 GeV and 1 GeV-400 GeV are shown.

A.4 Conclusions

In view of the HL-LHC operations of the ATLAS detector, the realisation of the full silicon *ITk* will open the window to several improvements of the trigger strategy and permit an efficient reconstruction of those events that are in the interest of the physics reach of the whole experiment. The proposed *HTT* uses information given by the *ITk* to skim events and improve the acceptance of interesting events. It uses hits in the pixel and strip modules of the *ITk* to reconstruct track parameters by fit in specific sectors. Sectors are trained with simulated muons and stored in specific files, and provide the fit parameters necessary for the extraction of key track variables. The size of the sector banks affects the performances of the *HTT*, and its size needs to meet demanding hardware limitations in terms of storage space. For my ATLAS authorship *QT*, I studied

a possible strategy to suppress the number of sectors, while maintaining performance and [HTT](#) efficiency. It was found that a lower cut on the number of training muons for the stored sectors reduces the number of sectors, without substantial loss of performance of the track fitting. The strategy, originally tested for muons with a p_T of at least 4 GeV, has shown potential extension to the low- p_T case, leaving room for further studies on a cut on the number of training muons as a function of the lepton p_T .

In conclusion, the overall [HTT](#) strategy shows clear benefit to the future ATLAS searches with leptons in the final stage, particularly those which target scenarios with low- p_T objects. Regarding the models and results presented in this thesis, the upgraded ATLAS trigger strategy in view of the [HL-LHC](#) will certainly allow the analysis of new challenging, compressed mass-splitting scenarios as well as open a window into the exploration of new phenomena not yet observed.

LIST OF ACRONYMS

LEP Large Electron-Positron collider

EWK Electroweak

QED Quantum Electrodynamics

QCD Quantum Chromodynamics

QFT Quantum Field Theory

BEH Brout-Englert-Higgs

LSP Lightest Supersymmetric Particle

SM Standard Model

SUSY Supersymmetry

MSSM Minimal Supersymmetric Standard Model

BSM Beyond the Standard Model

WIMP Weakly Interacting Massive Particle

ISR Initial State Radiation

FSR Final State Radiation

LS long shutdown

LS1	first long shutdown
LS2	second long shutdown
CERN	European Organization for Nuclear Research
LHC	Large Hadron Collider
HL-LHC	High-Luminosity LHC
RF	Radio-frequency
PSB	Proton Synchrotron Booster
PS	Proton Synchrotron
SPS	Super Proton Synchrotron
ID	Inner Detector
IBL	Insertable B-Layer
SCT	Semiconductor Tracker
TRT	Transition Radiation Tracker
ECal	Electromagnetic Calorimeter
EMEC	Electromagnetic End-cap Calorimeter
HCal	Hadronic Calorimeter
HEC	Hadronic End-cap Calorimeter
LAr	Liquid Argon
TileCal	Tile Calorimeter
FCal	Forward Calorimeter
MS	Muon Spectrometer
MDTs	Monitored Drift Tubes
CSCs	Cathod Strip Chambers

RPCs Resistive Plate Chambers

TGCs Thin Gap Chambers

HLT High-Level Trigger

L1 Level-1

L0 Level-0

TDAQ Trigger and Data Acquisition

CTP Central Trigger Processor

ROS Read-Out Systems

RoI Region of Interests

FTF Fast Track Finder

NSW New Small Wheel

ITk Inner TracKer

RMS Root Mean Square

QT Qualification Task

eFEX electron Feature EXtractor

jFEX jet Feature EXtractor

fFEX forward Feature EXtractor

MUCTPI MUon Central Trigger Processor Interface

TTC Trigger, Timing Control system

DAQ Data Acquisition

FELIX Front-End Link eXchange

EF Event Filter

HTT Hardware-based Tracking for Trigger

AM	Associative Memory
ASICs	Application Specific Integrated Circuits
FPGAs	Field Programmable Arrays
PRM	Pattern Recognition Mezzanine
rHTT	regional tracking
gHTT	global tracking
MC	Monte Carlo
FNP	Fake or Non-Prompt
VBF	Vector-Boson Fusion
SR	Signal Region
CR	Control Region
VR	Validation Region
SFOS	Same-Flavour Opposite-Sign
SFSS	Same-Flavour Same-Sign
DFOS	Different-Flavour Opposite-Sign
NF	Normalisation Factor
FF	Fake Factor
JVT	Jet Vertex Tagger
JES	Jet Energy Scale
JER	Jet Energy Resolution
PDF	Parton Distribution Functions
pdf	Probability Density Function
CL	Confidence Level

LO Leading Order

NLO Next-to-Leading Order

NNLO Next-to-Next-Leading Order

NLL Next-to-Leading-Logarithm

NNLL Next-Next-to-Leading-Logarithm

RDO Raw Data Objects

AOD Analysis Object Data

AFII ATLFastII

NEWT New Tracking

RoI Region of Interest

LH Likelihood

LCW Local Cluster Weight

MVA Multi-Variate Analysis

BDT Boosted Decision Trees

LIST OF FIGURES

2.1	Particle content of the SM. The six quarks (u, d, s, c, b and t) are shown in purple, the six leptons ($e, \mu, \tau, \nu_e, \nu_\mu$ and ν_τ) displayed in green, while the gauge bosons (g, γ, Z and W) and Higgs boson (H) are shown in red and yellow, respectively. Values of masses, electric charge and spin are also given for each particle. [2]	4
2.2	One-loop supersymmetric contributions to the anomalous magnetic momentum of the muon, involving chargino and sneutrino (left) and neutralino and smuon (right). [9]	9
2.3	The complex scalar potential $V(\phi)$ in the Brout-Englert-Higgs mechanism, shown in function of the real and imaginary components of the complex scalar field ϕ . The potential presents a set of vacuum expectation values, lying on the same complex plane. [18]	13
2.4	The reconstructed mass of the Higgs boson, at the time of its first observation in 2012. On the left, the distribution of the four-lepton invariant mass from the $H \rightarrow ZZ^* \rightarrow 4\ell$ decay, as observed by ATLAS. On the right, the analogous distribution from the $H \rightarrow \gamma\gamma$ channel as measured by CMS.[19, 20]	15
2.5	Fermionic one-loop correction to the mass of Higgs boson.	15
2.6	Rotation curves for the spiral galaxy NGC 3198. Observed data show agreement with the model which assumes a uniform distribution of matter across the core of the galaxy and the halo. [23]	16

2.7	Running of the interaction couplings in the SM as a function of the energy scale, where α_1 corresponds to the electromagnetic force coupling, α_2 the strong force coupling and α_3 the weak force coupling. [24]	17
2.8	Bosonic one-loop correction to the mass of Higgs boson.	18
2.9	Running of the couplings in the MSSM as a function of the energy scale, where α_1 corresponds to the electromagnetic force coupling, α_2 the strong force coupling and α_3 the weak force coupling. [24]	20
2.10	Scalar cubic coupling in the MSSM. Interaction couplings a of Higgs bosons to squark and sleptons are part of the MSSM parameters. [27]	22
2.11	Channels for the production of gauginos and sleptons with hadronic initial states, with both contributions from s -channels mediated by gauge bosons and t -channels. In these diagrams, $\tilde{C}_i^\pm = \tilde{\chi}_i^\pm$ ($i=1, 2$) and $\tilde{N}_j^0 = \tilde{\chi}_j^0$ ($j=1, 2, 3, 4$). [27]	26
2.12	Typical cross-sections for the production of sparticles at the LHC as a function of their masses. The assumed centre of mass energy is $\sqrt{s} = 13$ TeV.	26
2.13	Diagram for the production of chargino and neutralino, with decays via W and Z bosons.	28
2.14	Diagram for the production of chargino and neutralino, with decays via W bosons and the Higgs boson h	29
2.15	Observed and expected exclusion limits on the mass of the top-squark. The dataset corresponds to 20.3 fb^{-1} data at $\sqrt{s} = 8$ TeV and 139 fb^{-1} data at $\sqrt{s} = 13$ TeV in proton-proton collisions at the LHC, recorded by the ATLAS experiment. Limits are set at the 95% of confidence level. [42]	30
2.16	Observed and expected exclusion limits on the masses of the gluino. The dataset corresponds to 20.3 fb^{-1} data at $\sqrt{s} = 8$ TeV and 139 fb^{-1} data at $\sqrt{s} = 13$ TeV in proton-proton collisions at the LHC, recorded by the ATLAS experiment. Limits are set at the 95% of confidence level. [42]	31
2.17	Observed and expected exclusion limits on the masses of sleptons. The dataset corresponds to 139 fb^{-1} data at $\sqrt{s} = 13$ TeV in proton-proton collisions at the LHC, recorded by the ATLAS experiment. Limits are set at the 95% of confidence level. [45]	32

- 2.18 Observed and expected exclusion limits on the masses of charginos and neutralinos decaying via intermediate sleptons. The proton-proton collision data was recorded by the ATLAS experiment at $\sqrt{s} = 8$ TeV and $\sqrt{s} = 13$ TeV. All the limits but those for the $\tilde{\chi}_1^\pm \tilde{\chi}_2^0$ production are obtained by targeting channels with two leptons in the final states. Searches for $\tilde{\chi}_1^\pm \tilde{\chi}_2^0$ are presented as a combination of the three light lepton and two lepton channels. Limits are set at the 95% of confidence level. [42] 33
- 2.19 Observed and expected exclusion limits on the masses of $\tilde{\chi}_1^\pm$ and $\tilde{\chi}_2^0$ and $\tilde{\chi}_1^0$ for the Wh models. The dataset corresponds to 20.3 fb^{-1} data collected at $\sqrt{s} = 8$ TeV proton-proton collisions by the ATLAS experiment. Exclusion limits are obtained through a combination of channels with three light leptons, one leptonic τ and two light leptons and two leptonic τ and a light lepton. Limits are set at the 95% of confidence level. [53] 34
- 2.20 Observed and expected exclusion limits on the masses of $\tilde{\chi}_1^\pm$ and $\tilde{\chi}_2^0$ and $\tilde{\chi}_1^0$ for the WZ model. The dataset corresponds to 36.1 fb^{-1} of proton-proton collision data collected at $\sqrt{s} = 13$ TeV by the ATLAS experiment. Exclusion limits are obtained by combining the three-lepton and two-lepton channels. All limits are set at the 95% of confidence level. [50] 34
- 2.21 Observed and expected exclusion limits on the masses of $\tilde{\chi}_1^\pm$ and $\tilde{\chi}_2^0$ and $\tilde{\chi}_1^0$ for the Wh and the WZ models. The dataset corresponds to 35.9 fb^{-1} of proton-proton collision data collected at $\sqrt{s} = 13$ TeV by the CMS experiment. Exclusion limits are shown for channels with one lepton plus photons, the two leptons and at least three leptons in the final states, and the two-lepton and three-lepton channels, for the Wh and the WZ models, respectively. All limits are set at the 95% of confidence level. [52] 35
- 2.22 Summary of observed and exclusion limits on the masses of $\tilde{\chi}_1^\pm$ and $\tilde{\chi}_2^0$ and $\tilde{\chi}_1^0$ for the WZ , Wh and WW models. The datasets correspond to 36.1 fb^{-1} data collected in 13-TeV proton-proton collisions at the LHC by the ATLAS experiment. Limits are obtained by combining the three-lepton and two-lepton channels. Limits are set at the 95% of confidence level. [42] 36
- 3.1 A schematic view of the CERN acceleration complex. [56] 39

3.2	Cumulative integrated luminosity delivered to the ATLAS experiment during the data taking years in Run 1 and Run 2, as measured by the LUCID2 detector. [65]	40
3.3	A schematic view of the main components of the ATLAS detector. [59]	41
3.4	Delivered and recorded luminosity as measured by the ATLAS experiment during the LHC Run-2. [65]	42
3.5	Schematic view of the magnet system of the ATLAS detector. [66]	44
3.6	Digital-graphic representation of the ATLAS tracker detector.	45
3.7	Schematic view of the calorimetry system of the ATLAS detector. [59]	47
3.8	Sketch of the setup of the barrel module of the ECal of the ATLAS detector. Each of the modules is split into three different components with increasing granularity. [59]	48
3.9	Schematic view of the muon system of the ATLAS detector. [59]	50
3.10	Schematic description of the ATLAS TDAQ system architecture used in Run 2. [70]	52
4.1	Schematic representation of the data flow in the ATLAS ATHENA framework prior to physics analysis.	56
4.2	Proton PDF as measured by the H1 and ZEUS deep inelastic scattering experiments, at a scale of $\mu_f^2 = 10 \text{ GeV}^2$. The xu_v and xu_d represent the PDF of valence up-quarks and down-quarks. PDF for the gluons, xg , and the sea-quarks $xS = 2x(\bar{U} + \bar{D})$, are scaled down by a factor of 20. Experimental and modelling uncertainties are included. [78]	57
4.3	Distribution of the mean number of interactions per bunch crossing, $\langle \mu \rangle$, for the different years of data-taking in Run 2. [65]	61
4.4	Performance of the working points for the LH-based identification of electrons. The upper panel shows efficiencies in data for the three working points: the Loose (blue) presents the highest efficiency with respect to the Medium (red) and Tight (tight). The lower panel shows the ratio between data and MC. Only data collected between 2015-2017 is used. Statistical and systematic uncertainties are considered. [108]	66

4.5	Performance of the working points for isolation of electrons. The upper panel shows efficiencies in data for different working points. The lower panel shows the ratio between data and MC. Only data collected between 2015-2016 is used, and only statistical uncertainties are shown. [106]	67
4.6	Performance of the working points for the identification of muons. Upper panel shows efficiencies in data and MC for the Medium working point. The lower panel shows ration between data and MC. Only data collected in 2015 is used for a total of 3.2 fb^{-1} . Statistical and systematic uncertainties are considered. [110]	70
4.7	Pictorial representation of the general behaviour of the ANTIKT4EMTOPO algorithm, showing all the possible clustering configurations. Instances of clusters with high momentum and conical reconstructed shape are shown as blue and red cones. An example of isolated low-momentum clusters are represented in cyan and pink. Finally, an instance of a low-momentum cluster in proximity of a high-energy deposit is shown in magenta. [115]	72
4.8	The fraction of jets as a function of the discriminant of the MV2, namely D_{MV2} . Distribution for the background c -jets (green) and light-jets (red) and the signal b -jets (blue) are shown. [120]	74
5.1	Diagrams for the production of chargino and neutralino, decaying to three-lepton final states via (a) WZ and (b) Wh bosons. The channel with exactly three light leptons in the final states is considered.	80
5.2	A schematic illustration of the angular variables defined for the DFOS selection. See text for more details.	86
5.3	Illustration of the interplay between CRs, VRs and SRs. The arrows represent the extrapolation of NFs from the CRs to the VRs and SRs. [133]	91
5.4	Definition of the p-value as the probability of the data to be consistent with the null hypothesis under which the pdf of the test statistics was built. [137]	96
5.5	Definition of the p-values p_{b+s} and p_b , defined under the alternative hypothesis and the null hypothesis pdf, respectively. The test-statistics q corresponds to the likelihood ratio in Equation 5.13. [137]	97

- 6.1 E_T^{miss} distribution in the CR3L-onZ-highMET, after background-only fit. All systematic and statistical uncertainties are considered. [138] 101
- 6.2 In the upper panel, yields of observed data and expected background in VR3L-offZ-HighMET (last bin), after the background-only fit. In the lower panel, the data on SM predictions ratio for all the regions are reported. Systematic and statistical uncertainties are considered. [138] 102
- 6.3 Distribution of E_T^{miss} in the VRSS- ee VR, used to demonstrate the goodness of the FNP background estimation for the multileptonic channels examined in the early Run-2 Wh analysis. [138] 103
- 6.4 N-1 distributions of observed data and SM expectation for (a) the E_T^{miss} in the SR3L-DFOS-0J region, (b) the $m_{\ell_{\text{DFOS}}+\ell_{\text{near}}}$ in the SR3L-DFOS-1Jb region and (c) the m_T^{min} in the SR3L-SFOS-1J region. The lower panel shows the ratio between the observed data and the SM expectation. The SR selections but the cut on the shown variables are applied. Systematic and statistical uncertainties are considered. [138] 106
- 6.5 Observed and expected 95% CL upper limits on the cross-section for the (a) 3ℓ channel of searches of $\tilde{\chi}_1^\pm \tilde{\chi}_2^0$ via Wh decays and (b) in comparison to all the consider channels: full-hadronic, $1\ell + bb$, $1\ell + \gamma\gamma$ and $\ell^\pm \ell^\pm$. Different values of $m_{\tilde{\chi}_1^\pm/\tilde{\chi}_2^0}$ up to 240 GeV are considered, when $m_{\tilde{\chi}_1^\pm/\tilde{\chi}_2^0} - m_{\tilde{\chi}_1^0} = 130$ GeV. [138] 108
- 6.6 In the upper panel, the distributions of the number n_{jets} of light jets for events passing the preselection and the DFOS flavour-sign requirement. The sensitivities Z_n curves are calculated for possible upper cuts on the given variable and assuming a flat 30% total uncertainty on the SM background. 111
- 6.7 In the upper panels, the distributions of the E_T^{miss} and E_T^{miss} significance for events passing the pre-selection criteria and the DFOS flavour-sign selection. All the sensitivities Z_n curves are calculated for possible lower cuts on the given variables and assuming a flat 30% total uncertainty on the SM background. 112
- 6.8 Correlation between E_T^{miss} and the E_T^{miss} significance variables for (a) the $t\bar{t}$ process and (b) the Wh signal point $Wh(175, 0)$ 112

- 6.9 In the upper panels, the distributions of the $\Delta R_{\text{OS, near}}$ and the $p_{\text{T}}^{\ell 3}$ for events passing the pre-selection criteria and the DFOS flavour-sign selection. All the sensitivities Z_{n} curves but those in the $\Delta R_{\text{OS, near}}$ distribution are calculated for possible lower cuts on the given variables and assuming a flat 30% total uncertainty on the SM background. 113
- 6.10 N-1 distributions for the $\text{SR}_{\text{DFOS}}^{\text{Wh}}-1$ (first column) and $\text{SR}_{\text{DFOS}}^{\text{Wh}}-2$ (second column) regions. The upper panels show distribution for relevant background processes and chosen benchmark Wh signal points, the arrows show the position and the verse of the cuts on the p_{T} of the third lepton (first row), the $E_{\text{T}}^{\text{miss}}$ significance (second row) and the $\Delta R_{\text{OS, near}}$ (third row). The significance Z_{n} is calculated assuming a flat 30% total uncertainty on the SM background. 114
- 6.11 In the upper panels, the distributions of the $m_{\ell\ell}$ for events passing the preselection criteria and the SFOS requirement. In the lower pad, the sensitivity Z_{n} is calculated for (a) a lower cut and for (a) an upper cut on the shown variable. Sensitivity is calculated assuming a 10% flat total uncertainties on the SM background. 115
- 6.12 In the upper panels, the distributions of the m_{T} in the SR^{WZ} selection, split into categories of events with (a) $n_{\text{jets}} = 0$, and (b) $n_{\text{jets}} > 0$ and $H_{\text{T}} > 200$ GeV. In each lower panel, the sensitivity Z_{n} curve is calculated by assuming a 15% of total uncertainty on the SM background and for possible lower cuts on the shown variables. 116
- 6.13 In the upper panels, the distribution of the p_{T} of the third lepton in the VRFF^{WZ} , for two flavour channels (c) $\mu\mu e$ and (d) $\mu\mu\mu$. In the lower pad, ratio between data and SM prediction is shown. Systematic and statistical uncertainties are considered. 120
- 6.14 In the upper panels, the distribution of the (a) $E_{\text{T}}^{\text{miss}}$ and (b) $\Delta R_{\text{OS, near}}$ in the $\text{VRt}\bar{\text{t}}^{\text{WZ}}$. In the lower pad, ratio between data and SM prediction is shown. Systematic and statistical uncertainties are considered. [139] 121

- 6.15 In the upper panels, the distribution of the (a) p_T of the third lepton and (b) E_T^{miss} significance in the $\text{VRt}\bar{t}^{\text{WZ}}$. In the lower pad, ratio between data and SM prediction is shown. Systematic and statistical uncertainties are considered. 121
- 6.16 In the upper panels, the distribution of the (a) E_T^{miss} , (b) $\Delta R_{\text{OS, near}}$, (c) p_T of the third lepton and (d) the number $n_{b\text{-jets}}$ of b -tagged jets in the $\text{VRt}\bar{t}^{\text{WZ}}$. In the lower pad, ratio between data and SM prediction is shown. Systematic and statistical uncertainties are considered. 122
- 6.17 In the upper panels, distributions of m_T in the CRWZ^{WZ} , before the background-only fit. Events are selected in all the hadronic binning considered in the optimisation of the SRs: (a) $n_{\text{jets}} > 0$, (b) $n_{\text{jets}} = 0$ and $H_T < 200$ GeV, and (c) $n_{\text{jets}} > 0$ and $H_T > 200$ GeV. In the lower panels, data on background ratio is compared to the error band, including statistical and systematic uncertainties on the SM background. 123
- 6.18 Relative uncertainties in the (a) $\text{SR}_{\text{SFOS}}^{\text{Wh}}$ and $\text{SR}_{\text{DFOS}}^{\text{Wh}}$, and (b) the SR^{WZ} regions. All sources of systematics and statistical uncertainties considered in the analysis are reported. [139] 125
- 6.19 Data on SM predictions comparisons in all the CRs and VRs considered for the background estimation. In the upper panel, the yields of background processes and data in all the regions. In the lower panel, the comparison between data and SM prediction is expressed as relative difference (in red) for the CR, calculated before the background-only fit, and as significance for the VRs (in black), after the background-only fit. Statistical and systematic uncertainties on the SM backgrounds are considered. [139] 126
- 6.20 In the upper panels, distributions of m_T in the CRWZ^{WZ} (left-hand column) and the VRWZ^{WZ} (right-hand column), after the background-only fit. Events are selected in all the hadronic binning categories considered in the optimisation of the SRs $n_{\text{jets}} = 0$ (first row), and $n_{\text{jets}} > 0$ and $H_T < 200$ GeV (second row). In the lower panels, data on background ratio is compared to the error band, including statistical and systematic uncertainties on the SM background. 127

- 6.21 In the upper panels, distributions of m_T in the CRWZ^{WZ} (left-hand column) and the VRWZ^{WZ} (right-hand column), after the background-only fit. Events are selected in the hadronic binning category $n_{\text{jets}} > 0$ and $H_T > 200$ GeV considered in the optimisation of the SRs. In the lower panels, data on background ratio is compared to the error band, including statistical and systematic uncertainties on the SM background. [139] 128
- 6.22 In the upper panels, distributions of n_{jets} in the CRWZ^{WZ}, (a) before and (b) after the background-only fit. In the lower panels, data on background ratio is compared to the error band, including statistical uncertainties on the SM background. 128
- 6.23 In the upper panels, the observed data and SM prediction yields in the SR targeting the Wh model. The lower panel show the significance for the data and SM expectation, accounting for the full set of systematic and statistical uncertainties. [139] 129
- 6.24 In the upper panels, the observed data and SM prediction yields in the SR targeting the WZ model. The lower panel show the significance for the data and SM expectation, accounting for the full set of systematic and statistical uncertainties. [139] 129
- 6.25 In the upper panels, data and SM background distributions of (a) E_T^{miss} and (b) m_T in the SR_{0j}^{WZ} selection, and (c) p_T of the 3rd lepton and (d) $\Delta R_{\text{OS, near}}$ in the $SR_{\text{DFOS}}^{\text{Wh}}-2$ and $SR_{\text{DFOS}}^{\text{Wh}}-1$ regions, respectively. In the lower panels, data on background ratio are compared to the error band, which includes all the statistical and systematic uncertainties on the background. [139] 132
- 6.26 In the upper panels, data and SM background distributions of (a) the p_T of the 3rd lepton, (b) $\Delta R_{\text{OS, near}}$ and (c)-(d) E_T^{miss} significance, in the $SR_{\text{DFOS}}^{\text{Wh}}-1$ (first column) and $SR_{\text{DFOS}}^{\text{Wh}}-2$ (second column) regions. In the lower panels, data on background ratio are compared to the error band, which includes all the statistical and systematic uncertainties on the background. 133

- 6.27 Observed (red solid line) and expected (dashed black line) exclusion limits on the masses $m_{\tilde{\chi}_1^\pm/\tilde{\chi}_2^0}$ and $m_{\tilde{\chi}_1^0}$ for the WZ and Wh models with three-lepton and missing transverse momentum in the final states. The yellow band corresponds to $\pm\sigma_{\text{exp}}$ systematic uncertainties. The dotted red lines represent the $\pm 1\sigma_{\text{theory}}$ uncertainties on the observed data from signal cross-section uncertainties. All limits are obtained at the 95% CL. On the left plot, the light and dark grey areas are the corresponding observed exclusion from similar analysis using the 8 TeV 20.3 fb⁻¹ dataset [53] and the searches for compressed spectra using the 13 TeV 139 fb⁻¹ dataset [140], respectively. [139] 135
- 6.28 Observed (solid dark red line) and expected (dashed black line) limits on the masses of $\tilde{\chi}_1^\pm\tilde{\chi}_2^0$ and $\tilde{\chi}_1^0$ for WZ simplified models with three-lepton and missing transverse momentum in the final states. The yellow band corresponds to $\pm\sigma_{\text{exp}}$ systematic uncertainties. The dotted red lines represent the $\pm 1\sigma_{\text{theory}}$ uncertainties on the observed data from signal cross-section uncertainties. All limits are obtained at the 95% CL. 136
- 6.29 Observed (solid dark red line) and expected (dashed black line) limits on the masses of $\tilde{\chi}_1^\pm\tilde{\chi}_2^0$ and $\tilde{\chi}_1^0$ for Wh simplified models with three-lepton and missing transverse momentum in the final states. The yellow band corresponds to $\pm\sigma_{\text{exp}}$ systematic uncertainties. The dotted red lines represent the $\pm 1\sigma_{\text{theory}}$ uncertainties on the observed data from signal cross-section uncertainties. All limits are obtained at the 95% CL. 137
- 7.1 Observed and expected exclusion limits at 95% CL for the $\tilde{\chi}_1^\pm\tilde{\chi}_2^0$ searches via intermediate boson decays by the ATLAS experiment. [42] 139
- A.1 Proposed structure of the TDAQ system for the ATLAS detector in view of the HL-LHC. Hits from the calorimetry system, the muon chambers and the inner tracker (in blue) are used in the trigger. The L0 of the trigger structure is represented in dark pink, while the FELIX and the Data Handlers are represented in green. Finally the Dataflow step and the Event Filter are represented in yellow and red, respectively. [148] 143

- A.2 Resolution of d_0 and z_0 , calculated as RMS. Calculated over ten thousand simulated single-muon events passing through ITk and requiring at least one pixel layer and seven strip layers to be hit by the particles. The targeted region is the $[0.1, 0.3]$ η interval. Pile-up is assumed to be the nominal of the HL-LHC, $\langle\mu\rangle = 200$ 148
- A.3 Resolution of curvature, η and ϕ , calculated as RMS. Calculated over ten thousand simulated single-muon events passing through ITk and requiring at least one pixel layer and seven strip layers to be hit by the particles. The targeted region is the $[0.1, 0.3]$ η interval. Pile-up is assumed to be the nominal of the HL-LHC, $\langle\mu\rangle = 200$ 149
- A.4 Resolution of d_0 and z_0 , calculated as RMS. Calculated over ten thousand simulated single-muon events passing through ITk and requiring at least one pixel layer and seven strip layers to be hit by the particles. The targeted region is the $[0.7, 0.9]$ η interval. No pile-up is considered, $\langle\mu\rangle = 0$ 151
- A.5 Resolution of curvature, η , ϕ , calculated as RMS. Calculated over ten thousand simulated single-muon events passing through ITk and requiring at least one pixel layer and seven strip layers to be hit by the particles. The targeted region is the $[0.7, 0.9]$ η interval. No pile-up is considered, $\langle\mu\rangle = 0$. . 152
- A.6 Resolution of d_0 and z_0 , calculated as RMS. Calculated over ten thousand simulated single-muon events passing through ITk and requiring at least one pixel layer and seven strip layers to be hit by the particles. The muon p_T range is $[2, 400]$ GeV. The targeted region is the $[0.7, 0.9]$ η interval. No pile-up is considered, $\langle\mu\rangle = 0$ 154
- A.7 Resolution of curvature, η , ϕ , calculated as RMS. Calculated over ten thousand simulated single-muon events passing through ITk and requiring at least one pixel layer and seven strip layers to be hit by the particles. The muon p_T range is $[2, 400]$ GeV. The targeted region is the $[0.7, 0.9]$ η interval. No pile-up is considered, $\langle\mu\rangle = 0$ 155

-
- A.8 Resolution of d_0 and z_0 , calculated as RMS. Calculated over ten thousand simulated single-muon events passing through ITk and requiring at least one pixel layer and seven strip layers to be hit by the particles. The muon p_T range is [1, 400] GeV. The targeted region is the [0.7, 0.9] η interval. No pile-up is considered, $\langle\mu\rangle = 0$ 156
- A.9 Resolution of curvature, η , ϕ , calculated as RMS. Calculated over ten thousand simulated single-muon events passing through ITk and requiring at least one pixel layer and seven strip layers to be hit by the particles. The muon p_T range is [1, 400] GeV. The targeted region is the [0.7, 0.9] η interval. No pile-up is considered, $\langle\mu\rangle = 0$ 157
- A.10 Profiling of the number of training muons against their p_T . The three p_T ranges between 4 GeV-400 GeV, 2 GeV-400 GeV and 1 GeV-400 GeV are shown. . . . 158

LIST OF TABLES

2.1	Summary of the main properties of the SM leptons. [4]	6
2.2	Summary of the main properties of the SM quarks. [4]	7
2.3	List of the supermultiplets in the MSSM. Chiral and gauge multiplets are shown. In the case of leptons and quarks, only one generation is reported; two additional sets of chiral supermultiplets are to be considered to account for a total of three families of fermions and SUSY counterparts. [27]	20
2.4	The MSSM parameters introduced by the soft SUSY breaking. Only first generation of scalar quarks and leptons are considered in this table.	21
4.1	Working points for isolation of electrons used in the analyses described here. [108]	67
4.2	Working points for isolation of electrons used in the analyses described here. [110]	71
5.1	Features of the MC samples for the targeted SUSY models WZ and Wh . In the last column, the ranges of nominal cross sections for the production of $\tilde{\chi}_1^\pm$ and $\tilde{\chi}_2^0$ at given $m_{\tilde{\chi}_1^\pm/\tilde{\chi}_2^0}$	80
5.2	Di-lepton trigger chains used for all analyses presented in this thesis, listed by year of data taking.	81
5.3	Single-lepton trigger chains used for the early Run-2 analysis presented in Section 6.1, listed by year of data taking.	81
5.4	SM processes which are significant background for the considered analyses, where $V = W, Z$	82
6.1	Definitions of the 3ℓ DFOS SRs used in the early Run-2 Wh analysis. [138] . .	100

6.2	Definitions of the 3ℓ SFOS SRs used in the early Run-2 Wh analysis. [138] . . .	100
6.3	List of cuts for the definition of the CR3L-onZ-HighMET CR and the VR3L-offZ-HighMET VR, used for the estimation and the validation of the WZ background in the early Run-2 $3\ell Wh$ search. Region definitions extracted from Ref. [138].	102
6.4	Uncertainties in units of number of events in the DFOS SRs. Different sources of uncertainties can correlate and the total does not necessarily correspond to the squared sum of all the contributions. The category "experimental" comprises the detector systematic uncertainties and the ones related to the FNP data-driven estimation. Numbers extracted from Ref. [138].	104
6.5	Uncertainties in units of number of events in the SFOS SRs. Different sources of uncertainties can correlate and the total does not necessarily correspond to the squared sum of all the contributions. The category "experimental" comprises the detector systematic uncertainties and the ones related to the FNP data-driven estimation. Numbers extracted from Ref. [138].	104
6.6	Observed data and expected yields from the relevant SM backgrounds for the region SR3L-DFOS-0J, SR3L-DFOS-1Ja and SR3L-DFOS-1Jb. The $W+Z$ NF after the background-only fit is applied. The category "Higgs MC" comprises the SM $t\bar{t}H$ production. All uncertainties are considered and symmetrised around the nominal post-fit yields, negative errors are truncated at the zero event yields. Numbers extracted from Ref. [138].	105
6.7	Observed data and expected yields from the relevant SM backgrounds for the region SR3L-SFOS-0Ja, SR3L-SFOS-0Jb and SR3L-SFOS-1J. The $W+Z$ NF after the background-only fit is applied. The category "Higgs MC" comprises the SM $t\bar{t}H$ production. All uncertainties are considered and symmetrised around the nominal post-fit yields, negative errors are truncated at the zero event yields. Numbers extracted from Ref. [138].	105
6.8	The observed 95% CL upper limits on the visible cross-section σ_{vis} and the observed and expected number of events from BSM signal model S_{obs}^{95} and S_{exp}^{95} are shown in the first three columns for each SR. The correspondent discovery p_0 -value is reported in the last column. Systematic and statistical uncertainties are considered. [138]	107

6.9	Summary of the selection criteria for SRs targeting events with a DFOS lepton pair, for the Wh selection. Preselection criteria are applied. [139]	113
6.10	Summary of the selection criteria for SRs targeting events with at least one SFOS lepton pair and $m_{\ell\ell} \in [75, 105]$ GeV, for the SR^{WZ} search regions. Region selections are binned by m_T (rows) and E_T^{miss} for the two sets of regions, where each set has different n_{jets} , and H_T requirements. Preselection criteria are applied. [139]	117
6.11	Summary of the selection criteria for SRs targeting events with at least one SFOS lepton pair and $m_{\ell\ell} \notin [75, 105]$ GeV, for the Wh search regions. Region selections binned by m_T (rows) and E_T^{miss} for the three sets of regions, where each set has different $m_{\ell\ell}$, n_{jets} , and H_T requirements. Preselection criteria are applied. [139]	117
6.12	Summary of the background estimation methods used for the full Run-2 analysis detailed in this thesis. The category "Others" includes the WW , ZZ , $t\bar{t}+V$ ($V=W, Z$), single-top and processes with a Higgs boson.	118
6.13	Summary of the selection criteria for the CRs and VRs for $t\bar{t}$ and FNP estimation, for the SR^{WZ} and $SR_{\text{SFOS}}^{\text{Wh}}$ selections. Preselection criteria are applied for $VR_{\text{t}}^{\bar{t}WZ}$, $VR_{\text{inc}}^{\bar{t}WZ}$ and $VR_{\text{FF}}^{\text{WZ}}$ regions. [139]	121
6.14	Summary of the selection criteria for the CRs and VRs for WZ , for the SR^{WZ} and $SR_{\text{SFOS}}^{\text{Wh}}$ selections. Preselection criteria are applied. In rows where only one value is given it applies to all regions. [139]	124
6.15	Observed and expected yields after the background-only fit in the SRs for the $SR_{\text{SFOS}}^{\text{Wh}}$ and $SR_{\text{DFOS}}^{\text{Wh}}$ selection. The "Others" category contains the single-top, WW , $t\bar{t}+V$ and rare top processes. Statistical and systematic uncertainties are presented. [139]	130
6.16	Observed and expected yields after the background-only fit in the SRs for the SR^{WZ} selection. The "Others" category contains the single-top, WW , tri-boson, Higgs and rare top processes. Statistical and systematic uncertainties are presented. [139]	131
6.17	Summary of the selection criteria for the inclusive SRs in the SR^{WZ} , $SR_{\text{SFOS}}^{\text{Wh}}$ and $SR_{\text{DFOS}}^{\text{Wh}}$ selections. [139]	134

6.18	Results of the model-independent fit in the discovery regions. The number of observed and expected yields, N_{obs} and N_{exp} , are after the background-only fit, for the inclusive discovery regions. Upper limits at 95% CL on the visible cross-section (σ_{vis}^{95}), the number of signal events (S_{obs}^{95}), and the expected number of signal events (S_{exp}^{95}) are shown. Finally, the CL value calculated for SM-only hypothesis and the correspondent p -value ($p(s = 0)$) are listed. [139]	134
A.1	Sector numbers, efficiency and RMS on η comparison between two sector banks trained with one million and fifteen million simulated single-muons events.	147
A.2	Sector numbers, efficiency and RMS on η for the five cuts on the number of training muons considered in the studies. The η range considered is between 0.1-0.3 and pile-up from soft-scattering collisions assumed to be the nominal of the HL-LHC, $\langle\mu\rangle = 200$	150
A.3	Sector numbers, efficiency and RMS on η for the five cuts on the number of training muons considered in the studies. The η range considered is between 0.7-0.9 and no pile-up from soft-scattering collisions is considered.	150
A.4	Sector numbers, efficiency and RMS on η for the five cuts on the number of training muons considered in the studies. The η range considered is between 0.7-0.9 and no pile-up from soft-scattering collisions is considered. Numbers refer to analysis of ten thousand muons with p_{T} between 2 GeV and 400 GeV.	153
A.5	Sector numbers, efficiency and RMS on η for the five cuts on the number of training muons considered in the studies. The η range considered is between 0.7-0.9 and no pile-up from soft-scattering collisions is considered. Numbers refer to analysis on ten thousand muons with p_{T} between 1 GeV and 400 GeV.	154

BIBLIOGRAPHY

- [1] M. Thomson, *Modern particle physics*. Cambridge University Press, New York, 2013.
- [2] A. Arbuzov, *Quantum Field Theory and the Electroweak Standard Model*,. <https://cds.cern.ch/record/2315477>. 35 pages.
- [3] A. Einstein, *The Foundation of the General Theory of Relativity*, [Annalen Phys.](#) **49** no. 7, (1916) 769–822.
- [4] Particle Data Group Collaboration, *Review of Particle Physics*, [Phys. Rev. D](#) **98** (2018) 030001. <https://link.aps.org/doi/10.1103/PhysRevD.98.030001>.
- [5] A. Pich, *The Standard Model of Electroweak Interactions*, pp. , 1–50. 2012. [arXiv:1201.0537 \[hep-ph\]](#).
- [6] M. Maggiore, *A Modern introduction to quantum field theory*. 9, 2005.
- [7] D. Hanneke, S. Fogwell, and G. Gabrielse, *New Measurement of the Electron Magnetic Moment and the Fine Structure Constant*, [Phys. Rev. Lett.](#) **100** (2008) 120801, [arXiv:0801.1134 \[physics.atom-ph\]](#).
- [8] Muon g-2 Collaboration, *Final Report of the Muon E821 Anomalous Magnetic Moment Measurement at BNL*, [Phys. Rev. D](#) **73** (2006) 072003, [arXiv:hep-ex/0602035](#).

- [9] E. Kpatcha, I. n. Lara, D. E. López-Fogliani, C. Muñoz, and N. Nagata, *Explaining muon $g - 2$ data in the $\mu\nu$ SSM*, [arXiv:1912.04163](https://arxiv.org/abs/1912.04163) [hep-ph].
- [10] S. Glashow, *Partial Symmetries of Weak Interactions*, *Nucl. Phys.* **22** (1961) 579–588.
- [11] S. Weinberg, *A Model of Leptons*, *Phys. Rev. Lett.* **19** (1967) 1264–1266.
- [12] S. Glashow, J. Iliopoulos, and L. Maiani, *Weak Interactions with Lepton-Hadron Symmetry*, *Phys. Rev. D* **2** (1970) 1285–1292.
- [13] M. Gell-Mann, *The interpretation of the new particles as displaced charge multiplets*, *Nuovo Cim.* **4** no. S2, (1956) 848–866.
- [14] K. Nishijima, *Charge Independence Theory of V Particles*, *Prog. Theor. Phys.* **13** no. 3, (1955) 285–304.
- [15] F. Englert and R. Brout, *Broken Symmetry and the Mass of Gauge Vector Mesons*, *Phys. Rev. Lett.* **13** (1964) 321–323.
- [16] P. W. Higgs, *Broken Symmetries and the Masses of Gauge Bosons*, *Phys. Rev. Lett.* **13** (1964) 508–509.
- [17] G. Guralnik, C. Hagen, and T. Kibble, *Global Conservation Laws and Massless Particles*, *Phys. Rev. Lett.* **13** (1964) 585–587.
- [18] J. Ellis, *Higgs Physics*, <https://cds.cern.ch/record/1638469>. 52 pages, 45 figures, Lectures presented at the ESHEP 2013 School of High-Energy Physics, to appear as part of the proceedings in a CERN Yellow Report.
- [19] ATLAS Collaboration, *Observation of a new particle in the search for the Standard Model Higgs boson with the ATLAS detector at the LHC*, *Phys. Lett. B* **716** (2012) 1–29, [arXiv:1207.7214](https://arxiv.org/abs/1207.7214) [hep-ex].
- [20] CMS Collaboration, *Observation of a New Boson at a Mass of 125 GeV with the CMS Experiment at the LHC*, *Phys. Lett. B* **716** (2012) 30–61, [arXiv:1207.7235](https://arxiv.org/abs/1207.7235) [hep-ex].

- [21] ATLAS, CMS Collaboration, *Measurements of the Higgs boson production and decay rates and constraints on its couplings from a combined ATLAS and CMS analysis of the LHC pp collision data at $\sqrt{s} = 7$ and 8 TeV*, *JHEP* **08** (2016) 045, [arXiv:1606.02266](https://arxiv.org/abs/1606.02266) [hep-ex].
- [22] Planck Collaboration, *Planck 2018 results. VI. Cosmological parameters*, [arXiv:1807.06209](https://arxiv.org/abs/1807.06209) [astro-ph.CO].
- [23] T. S. Van Albada, K. Begeman, R. Sancisi, and J. N. Bahcall, *Distribution of dark matter in the spiral galaxy NGC 3198*, *Astrophys. J.; (United States)*.
- [24] H. P. D. Gross and F. Wilczek, *The nobel prize in physics 2004 - popular information*,. <https://www.nobelprize.org/prizes/physics/2004/popular-information/>.
- [25] R. Haag, J. T. Lopuszanski, and M. Sohnius, *All Possible Generators of Supersymmetries of the s Matrix*, *Nucl. Phys. B* **88** (1975) 257.
- [26] S. R. Coleman and J. Mandula, *All Possible Symmetries of the S Matrix*, *Phys. Rev.* **159** (1967) 1251–1256.
- [27] S. P. Martin, *A Supersymmetry primer*, pp. , 1–153. 2010. [arXiv:hep-ph/9709356](https://arxiv.org/abs/hep-ph/9709356).
- [28] P. Fayet, *Supersymmetry and Weak, Electromagnetic and Strong Interactions*, *Phys. Lett. B* **64** (1976) 159.
- [29] G. R. Farrar and P. Fayet, *Phenomenology of the Production, Decay, and Detection of New Hadronic States Associated with Supersymmetry*, *Phys. Lett. B* **76** (1978) 575–579.
- [30] S. Dimopoulos and D. W. Sutter, *The Supersymmetric flavor problem*, *Nucl. Phys.* **B452** (1995) 496–512, [arXiv:hep-ph/9504415](https://arxiv.org/abs/hep-ph/9504415) [hep-ph].
- [31] A. H. Chamseddine, R. L. Arnowitt, and P. Nath, *Locally Supersymmetric Grand Unification*, *Phys. Rev. Lett.* **49** (1982) 970.
- [32] J. R. Ellis, D. V. Nanopoulos, and K. Tamvakis, *Grand Unification in Simple Supergravity*, *Phys. Lett. B* **121** (1983) 123–129.

- [33] M. Dine and A. E. Nelson, *Dynamical supersymmetry breaking at low-energies*, *Phys. Rev. D* **48** (1993) 1277–1287, [arXiv:hep-ph/9303230](#).
- [34] L. Randall and R. Sundrum, *A Large mass hierarchy from a small extra dimension*, *Phys. Rev. Lett.* **83** (1999) 3370–3373, [arXiv:hep-ph/9905221](#).
- [35] Super-Kamiokande Collaboration, *Search for proton decay into three charged leptons in 0.37 megaton-years exposure of the Super-Kamiokande*, *Phys. Rev. D* **101** no. 5, (2020) 052011, [arXiv:2001.08011 \[hep-ex\]](#).
- [36] LHC New Physics Working Group Collaboration, *Simplified Models for LHC New Physics Searches*, *J. Phys. G* **39** (2012) 105005, [arXiv:1105.2838 \[hep-ph\]](#).
- [37] J. Alwall, P. Schuster, and N. Toro, *Simplified Models for a First Characterization of New Physics at the LHC*, *Phys. Rev. D* **79** (2009) 075020, [arXiv:0810.3921 \[hep-ph\]](#).
- [38] ATLAS Collaboration, *Search for a scalar partner of the top quark in the all-hadronic $t\bar{t}$ plus missing transverse momentum final state at $\sqrt{s}=13$ TeV with the ATLAS detector*, [arXiv:2004.14060 \[hep-ex\]](#).
- [39] ATLAS Collaboration, *Search for new phenomena with top quark pairs in final states with one lepton, jets, and missing transverse momentum in pp collisions at $\sqrt{s} = 13$ TeV with the ATLAS detector*, Tech. Rep. ATLAS-CONF-2020-003, CERN, Geneva, Feb, 2020. <http://cds.cern.ch/record/2711489>.
- [40] CMS Collaboration, *Search for direct top squark pair production in events with one lepton, jets, and missing transverse momentum at 13 TeV with the CMS experiment*, *JHEP* **05** (2020) 032, [arXiv:1912.08887 \[hep-ex\]](#).
- [41] CMS Collaboration, *Search for top squark pair production in a final state with two tau leptons in proton-proton collisions at $\sqrt{s} = 13$ TeV*, *JHEP* **02** (2020) 015, [arXiv:1910.12932 \[hep-ex\]](#).
- [42] ATLAS Collaboration, *SUSY May 2020 Summary Plot Update*, Tech. Rep. ATL-PHYS-PUB-2020-013, CERN, Geneva, May, 2020. <http://cds.cern.ch/record/2718947>.

- [43] ATLAS Collaboration, *Search for squarks and gluinos in final states with jets and missing transverse momentum using 139 fb^{-1} of $\sqrt{s} = 13 \text{ TeV}$ pp collision data with the ATLAS detector*, Tech. Rep. ATLAS-CONF-2019-040, CERN, Geneva, Aug, 2019. <http://cds.cern.ch/record/2686254>.
- [44] CMS Collaboration, *Search for supersymmetry in proton-proton collisions at 13 TeV in final states with jets and missing transverse momentum*, *JHEP* **10** (2019) 244, [arXiv:1908.04722](https://arxiv.org/abs/1908.04722) [hep-ex].
- [45] ATLAS Collaboration, *Search for electroweak production of charginos and sleptons decaying into final states with two leptons and missing transverse momentum in $\sqrt{s} = 13 \text{ TeV}$ pp collisions using the ATLAS detector*, *Eur. Phys. J. C* **80** no. 2, (2020) 123, [arXiv:1908.08215](https://arxiv.org/abs/1908.08215) [hep-ex].
- [46] CMS Collaboration, *Search for supersymmetric partners of electrons and muons in proton-proton collisions at $\sqrt{s} = 13 \text{ TeV}$* , *Phys. Lett. B* **790** (2019) 140–166, [arXiv:1806.05264](https://arxiv.org/abs/1806.05264) [hep-ex].
- [47] ATLAS Collaboration, *Search for direct stau production in events with two hadronic τ -leptons in $\sqrt{s} = 13 \text{ TeV}$ pp collisions with the ATLAS detector*, *Phys. Rev. D* **101** no. 3, (2020) 032009, [arXiv:1911.06660](https://arxiv.org/abs/1911.06660) [hep-ex].
- [48] CMS Collaboration, *Search for direct pair production of supersymmetric partners to the τ lepton in proton-proton collisions at $\sqrt{s} = 13 \text{ TeV}$* , *Eur. Phys. J. C* **80** no. 3, (2020) 189, [arXiv:1907.13179](https://arxiv.org/abs/1907.13179) [hep-ex].
- [49] ATLAS Collaboration, *Search for the electroweak production of supersymmetric particles in $\sqrt{s} = 8 \text{ TeV}$ pp collisions with the ATLAS detector*, *Phys. Rev. D* **93** no. 5, (2016) 052002, [arXiv:1509.07152](https://arxiv.org/abs/1509.07152) [hep-ex].
- [50] ATLAS Collaboration, *Search for electroweak production of supersymmetric particles in final states with two or three leptons at $\sqrt{s} = 13 \text{ TeV}$ with the ATLAS detector*, *Eur. Phys. J. C* **78** no. 12, (2018) 995, [arXiv:1803.02762](https://arxiv.org/abs/1803.02762) [hep-ex].
- [51] CMS Collaboration, *Searches for pair production of charginos and top squarks in final states with two oppositely charged leptons in proton-proton collisions at $\sqrt{s} = 13 \text{ TeV}$* , *JHEP* **11** (2018) 079, [arXiv:1807.07799](https://arxiv.org/abs/1807.07799) [hep-ex].

- [52] CMS Collaboration, *Combined search for electroweak production of charginos and neutralinos in proton-proton collisions at $\sqrt{s} = 13$ TeV*, *JHEP* **03** (2018) 160, [arXiv:1801.03957](https://arxiv.org/abs/1801.03957) [[hep-ex](#)].
- [53] ATLAS Collaboration, *Search for direct production of charginos and neutralinos in events with three leptons and missing transverse momentum in $\sqrt{s} = 8$ TeV pp collisions with the ATLAS detector*, *JHEP* **04** (2014) 169, [arXiv:1402.7029](https://arxiv.org/abs/1402.7029) [[hep-ex](#)].
- [54] CMS Collaboration, *Searches for electroweak production of charginos, neutralinos, and sleptons decaying to leptons and W, Z, and Higgs bosons in pp collisions at 8 TeV*, *Eur. Phys. J.* **C74** no. 9, (2014) 3036, [arXiv:1405.7570](https://arxiv.org/abs/1405.7570) [[hep-ex](#)].
- [55] L. Evans and P. Bryant, *LHC Machine*, *JINST* **3** (2008) S08001.
- [56] E. Mobs, *The CERN accelerator complex - 2019. Complexe des accélérateurs du CERN - 2019.*, <http://cds.cern.ch/record/2684277>. General Photo.
- [57] W. Herr and B. Muratori, *Concept of luminosity*, in *CERN Accelerator School and DESY Zeuthen: Accelerator Physics*. 2003.
- [58] J. Wenninger, *Operation and Configuration of the LHC in Run 2.*, <https://cds.cern.ch/record/2668326>.
- [59] ATLAS Collaboration, *The ATLAS Experiment at the CERN Large Hadron Collider*, *JINST* **3** (2008) S08003.
- [60] CMS Collaboration, *The CMS Experiment at the CERN LHC*, *JINST* **3** (2008) S08004.
- [61] LHCb Collaboration, *The LHCb Detector at the LHC*, *JINST* **3** (2008) S08005.
- [62] ALICE Collaboration, *The ALICE experiment at the CERN LHC*, *JINST* **3** (2008) S08002.
- [63] G. Avoni et al., *The new LUCID-2 detector for luminosity measurement and monitoring in ATLAS*, *JINST* **13** no. 07, (2018) P07017.

- [64] ATLAS Collaboration, *Luminosity determination in pp collisions at $\sqrt{s} = 13$ TeV using the ATLAS detector at the LHC*, Tech. Rep. ATLAS-CONF-2019-021, CERN, Geneva, Jun, 2019. <http://cds.cern.ch/record/2677054>.
- [65] ATLAS Collaboration, *Online luminosity measurements*, Accessed October 2019. twiki.cern.ch/twiki/bin/view/AtlasPublic/LuminosityPublicResultsRun2.
- [66] J. Goodson, *Magnet systems*, Accessed October 2019. <http://www.jetgoodson.com/images/thesisImages/magnetSystems.png>.
- [67] K. Potamianos, *The upgraded Pixel detector and the commissioning of the Inner Detector tracking of the ATLAS experiment for Run-2 at the Large Hadron Collider*, PoS (2015) 261, [arXiv:1608.07850](https://arxiv.org/abs/1608.07850) [physics.ins-det].
- [68] F. Hügging, *The ATLAS Pixel Insertable B-layer (IBL)*, *Nuclear Instruments and Methods in Physics Research Section A: Accelerators, Spectrometers, Detectors and Associated Equipment* **650** no. 1, (2011) 45 – 49. <http://www.sciencedirect.com/science/article/pii/S0168900210028937>. International Workshop on Semiconductor Pixel Detectors for Particles and Imaging 2010.
- [69] ATLAS Collaboration, *Performance of the ATLAS Trigger System in 2010*, *Eur. Phys. J. C* **72** (2012) 1849, [arXiv:1110.1530](https://arxiv.org/abs/1110.1530) [hep-ex].
- [70] ATLAS Collaboration, *Performance of the ATLAS Trigger System in 2015*, *Eur. Phys. J. C* **77** no. 5, (2017) 317, [arXiv:1611.09661](https://arxiv.org/abs/1611.09661) [hep-ex].
- [71] ATLAS Collaboration, *ATLAS Computing: technical design report*. Technical Design Report ATLAS. CERN, Geneva, 2005. <https://cds.cern.ch/record/837738>.
- [72] G. Barrand et al., *GAUDI - A software architecture and framework for building HEP data processing applications*, *Comput. Phys. Commun.* **140** (2001) 45–55.
- [73] M. Dobbs and J. B. Hansen, *The HepMC C++ Monte Carlo event record for High Energy Physics*, *Comput. Phys. Commun.* **134** (2001) 41–46.

- [74] V. Gribov and L. Lipatov, *Deep inelastic $e p$ scattering in perturbation theory*, Sov. J. Nucl. Phys. **15** (1972) 438–450.
- [75] A. Buckley et al., *General-purpose event generators for LHC physics*, *Phys. Rept.* **504** (2011) 145–233, [arXiv:1101.2599 \[hep-ph\]](#).
- [76] F. Brasse, *The H1 detector at HERA*, in *26th International Conference on High-energy Physics*. 1992.
- [77] ZEUS Collaboration, *The ZEUS experiment at HERA*, in *1st German-Polish Symposium on Particles and Fields*. 1992.
- [78] H1, ZEUS Collaboration, *Combination of measurements of inclusive deep inelastic $e^\pm p$ scattering cross sections and QCD analysis of HERA data*, *Eur. Phys. J. C* **75** no. 12, (2015) 580, [arXiv:1506.06042 \[hep-ex\]](#).
- [79] Y. L. Dokshitzer, *Calculation of the Structure Functions for Deep Inelastic Scattering and $e^+ e^-$ Annihilation by Perturbation Theory in Quantum Chromodynamics.*, Sov. Phys. JETP **46** (1977) 641–653.
- [80] G. Altarelli and G. Parisi, *Asymptotic Freedom in Parton Language*, *Nucl. Phys. B* **126** (1977) 298–318.
- [81] R. D. Ball et al., *Parton distributions with LHC data*, *Nucl. Phys. B* **867** (2013) 244–289, [arXiv:1207.1303 \[hep-ph\]](#).
- [82] NNPDF Collaboration, *Parton distributions for the LHC Run II*, *JHEP* **04** (2015) 040, [arXiv:1410.8849 \[hep-ph\]](#).
- [83] S. Catani, F. Krauss, R. Kuhn, and B. R. Webber, *QCD matrix elements + parton showers*, *JHEP* **11** (2001) 063, [arXiv:hep-ph/0109231 \[hep-ph\]](#).
- [84] M. L. Mangano, M. Moretti, and R. Pittau, *Multijet matrix elements and shower evolution in hadronic collisions: $W b\bar{b} + n$ jets as a case study*, *Nucl. Phys.* **B632** (2002) 343–362, [arXiv:hep-ph/0108069 \[hep-ph\]](#).
- [85] A. Kupco, *Cluster hadronization in HERWIG 5.9*, pp. , 292–300. 1998. [arXiv:hep-ph/9906412 \[hep-ph\]](#).

- [86] B. Andersson, S. Mohanty, and F. Soderberg, *Recent developments in the Lund model*, 2002. [arXiv:hep-ph/0212122](https://arxiv.org/abs/hep-ph/0212122) [hep-ph].
- [87] ATLAS Collaboration, *ATLAS Pythia 8 tunes to 7 TeV datas*, Tech. Rep. ATL-PHYS-PUB-2014-021, CERN, Geneva, Nov, 2014. <http://cds.cern.ch/record/1966419>.
- [88] P. Z. Skands, *Tuning Monte Carlo Generators: The Perugia Tunes*, *Phys. Rev. D* **82** (2010) 074018, [arXiv:1005.3457](https://arxiv.org/abs/1005.3457) [hep-ph].
- [89] ATLAS Collaboration, *Measurement of the Z/γ^* boson transverse momentum distribution in pp collisions at $\sqrt{s} = 7$ TeV with the ATLAS detector*, *JHEP* **09** (2014) 145, [arXiv:1406.3660](https://arxiv.org/abs/1406.3660) [hep-ex].
- [90] T. Sjöstrand, S. Ask, J. R. Christiansen, R. Corke, N. Desai, P. Ilten, S. Mrenna, S. Prestel, C. O. Rasmussen, and P. Z. Skands, *An Introduction to PYTHIA 8.2*, *Comput. Phys. Commun.* **191** (2015) 159–177, [arXiv:1410.3012](https://arxiv.org/abs/1410.3012) [hep-ph].
- [91] T. Gleisberg, S. Hoeche, F. Krauss, M. Schonherr, S. Schumann, F. Siegert, and J. Winter, *Event generation with SHERPA 1.1*, *JHEP* **02** (2009) 007, [arXiv:0811.4622](https://arxiv.org/abs/0811.4622) [hep-ph].
- [92] Sherpa Collaboration, *Event Generation with Sherpa 2.2*, *SciPost Phys.* **7** no. 3, (2019) 034, [arXiv:1905.09127](https://arxiv.org/abs/1905.09127) [hep-ph].
- [93] M. Bahr et al., *Herwig++ Physics and Manual*, *Eur. Phys. J. C* **58** (2008) 639–707, [arXiv:0803.0883](https://arxiv.org/abs/0803.0883) [hep-ph].
- [94] F. Maltoni and T. Stelzer, *MadEvent: Automatic event generation with MadGraph*, *JHEP* **02** (2003) 027, [arXiv:hep-ph/0208156](https://arxiv.org/abs/hep-ph/0208156).
- [95] S. Alioli, P. Nason, C. Oleari, and E. Re, *A general framework for implementing NLO calculations in shower Monte Carlo programs: the POWHEG BOX*, *JHEP* **06** (2010) 043, [arXiv:1002.2581](https://arxiv.org/abs/1002.2581) [hep-ph].
- [96] D. Lange, *The EvtGen particle decay simulation package*, *Nucl. Instrum. Meth. A* **462** (2001) 152–155.

- [97] CDF Collaboration, *The Underlying Event in Hard Scattering Processes*, eConf **C010630** (2001) P501, [arXiv:hep-ph/0201192](https://arxiv.org/abs/hep-ph/0201192).
- [98] ATLAS Collaboration, *Simulation of Pile-up in the ATLAS Experiment*, *J. Phys. Conf. Ser.* **513** (2014) 022024.
- [99] GEANT4 Collaboration, *GEANT4: A Simulation toolkit*, *Nucl. Instrum. Meth. A* **506** (2003) 250–303.
- [100] ATLAS Collaboration, *The simulation principle and performance of the ATLAS fast calorimeter simulation FastCaloSim*, Tech. Rep. ATL-PHYS-PUB-2010-013, CERN, Geneva, Oct, 2010. <http://cds.cern.ch/record/1300517>.
- [101] T. Cornelissen, M. Elsing, I. Gavrilenko, W. Liebig, E. Moyses, and A. Salzburger, *The new ATLAS track reconstruction (NEWT)*, *J. Phys. Conf. Ser.* **119** (2008) 032014.
- [102] R. Fruhwirth, *Application of Kalman filtering to track and vertex fitting*, *Nuclear Instruments and Methods in Physics Research Section A: Accelerators, Spectrometers, Detectors and Associated Equipment* **262** no. 2, (1987) 444 – 450.
- [103] ATLAS Collaboration, *Reconstruction of primary vertices at the ATLAS experiment in Run 1 proton–proton collisions at the LHC*, *Eur. Phys. J. C* **77** no. 5, (2017) 332, [arXiv:1611.10235](https://arxiv.org/abs/1611.10235) [physics.ins-det].
- [104] ATLAS Collaboration, *Expected Performance of the ATLAS Experiment - Detector, Trigger and Physics*, [arXiv:0901.0512](https://arxiv.org/abs/0901.0512) [hep-ex].
- [105] ATLAS Collaboration, *Electron efficiency measurements with the ATLAS detector using 2012 LHC proton–proton collision data*, *Eur. Phys. J. C* **77** no. 3, (2017) 195, [arXiv:1612.01456](https://arxiv.org/abs/1612.01456) [hep-ex].
- [106] ATLAS Collaboration, *Electron reconstruction and identification in the ATLAS experiment using the 2015 and 2016 LHC proton–proton collision data at $\sqrt{s} = 13$ TeV*, *The European Physical Journal C* **79** no. 8, (2019). <http://dx.doi.org/10.1140/epjc/s10052-019-7140-6>.

- [107] W. Lampl, S. Laplace, D. Lelas, et al., *Calorimeter Clustering Algorithms: Description and Performance*, Tech. Rep. ATL-LARG-PUB-2008-002. ATL-COM-LARG-2008-003, CERN, Geneva, Apr, 2008.
<http://cds.cern.ch/record/1099735>.
- [108] ATLAS Collaboration, *Electron and photon performance measurements with the ATLAS detector using the 2015-2017 LHC proton-proton collision data*, **JINST** **14** no. 12, (2019) P12006, [arXiv:1908.00005](https://arxiv.org/abs/1908.00005) [hep-ex].
- [109] ATLAS Collaboration, *Measurement of the muon reconstruction performance of the ATLAS detector using 2011 and 2012 LHC proton-proton collision data*, **Eur. Phys. J.** **C74** no. 11, (2014) 3130, [arXiv:1407.3935](https://arxiv.org/abs/1407.3935) [hep-ex].
- [110] ATLAS Collaboration, *Muon reconstruction performance of the ATLAS detector in proton-proton collision data at $\sqrt{s} = 13$ TeV*, **The European Physical Journal C** **76** (2016). <http://dx.doi.org/10.1140/epjc/s10052-016-4120-y>.
- [111] P. Mukhopadhyay and B. B. Chaudhuri, *A survey of Hough Transform*, **Pattern Recognition** **48** no. 3, (2015) 993 – 1010. <http://www.sciencedirect.com/science/article/pii/S0031320314003446>.
- [112] ATLAS Collaboration, *Topological cell clustering in the ATLAS calorimeters and its performance in LHC Run 1*, **Eur. Phys. J.** **C77** (2017) 490, [arXiv:1603.02934](https://arxiv.org/abs/1603.02934) [hep-ex].
- [113] ATLAS Collaboration, *Jet energy measurement and its systematic uncertainty in proton-proton collisions at $\sqrt{s} = 7$ TeV with the ATLAS detector*, **Eur. Phys. J.** **C75** (2015) 17, [arXiv:1406.0076](https://arxiv.org/abs/1406.0076) [hep-ex].
- [114] ATLAS Collaboration, *Hadronic calibration of the ATLAS liquid argon end-cap calorimeter in the pseudorapidity region $1.6 < |\eta| < 1.8$ in beam tests*, **Nucl. Instrum. Meth.** **A531** (2004) 481–514, [arXiv:physics/0407009](https://arxiv.org/abs/physics/0407009) [physics].
- [115] M. Cacciari, G. P. Salam, and G. Soyez, *The anti- k_t jet clustering algorithm*, **JHEP** **04** (2008) 063, [arXiv:0802.1189](https://arxiv.org/abs/0802.1189) [hep-ph].

- [116] ATLAS Collaboration, *Tagging and suppression of pileup jets with the ATLAS detector*, Tech. Rep. ATLAS-CONF-2014-018, CERN, Geneva, May, 2014.
<https://cds.cern.ch/record/1700870>.
- [117] ATLAS Collaboration, *Identification and rejection of pile-up jets at high pseudorapidity with the ATLAS detector*, *Eur. Phys. J.* **C77** no. 9, (2017) 580, [arXiv:1705.02211](https://arxiv.org/abs/1705.02211) [hep-ex]. [Erratum: *Eur. Phys. J.* C77,no.10,712(2017)].
- [118] ATLAS Collaboration, *Performance of b -Jet Identification in the ATLAS Experiment*, *JINST* **11** no. 04, (2016) P04008, [arXiv:1512.01094](https://arxiv.org/abs/1512.01094) [hep-ex].
- [119] ATLAS Collaboration, *Optimisation and performance studies of the ATLAS b -tagging algorithms for the 2017-18 LHC run*, Tech. Rep. ATL-PHYS-PUB-2017-013, CERN, Geneva, Jul, 2017.
<https://cds.cern.ch/record/2273281>.
- [120] ATLAS Collaboration, *ATLAS b -jet identification performance and efficiency measurement with $t\bar{t}$ events in pp collisions at $\sqrt{s} = 13$ TeV*, *Eur. Phys. J.* **C79** no. 11, (2019) 970, [arXiv:1907.05120](https://arxiv.org/abs/1907.05120) [hep-ex].
- [121] ATLAS Collaboration, *Identification and energy calibration of hadronically decaying tau leptons with the ATLAS experiment in pp collisions at $\sqrt{s}=8$ TeV*, *Eur. Phys. J.* **C75** no. 7, (2015) 303, [arXiv:1412.7086](https://arxiv.org/abs/1412.7086) [hep-ex].
- [122] ATLAS Collaboration, *Reconstruction of hadronic decay products of tau leptons with the ATLAS experiment*, *Eur. Phys. J.* **C76** no. 5, (2016) 295, [arXiv:1512.05955](https://arxiv.org/abs/1512.05955) [hep-ex].
- [123] ATLAS Collaboration, *Measurement of the tau lepton reconstruction and identification performance in the ATLAS experiment using pp collisions at $\sqrt{s} = 13$ TeV*, Tech. Rep. ATLAS-CONF-2017-029, CERN, Geneva, May, 2017.
<https://cds.cern.ch/record/2261772>.
- [124] ATLAS Collaboration, *Performance of missing transverse momentum reconstruction with the ATLAS detector using proton-proton collisions at $\sqrt{s} = 13$ TeV*, *Eur. Phys. J.* **C78** no. 11, (2018) 903, [arXiv:1802.08168](https://arxiv.org/abs/1802.08168) [hep-ex].

- [125] ATLAS Collaboration, *Performance of electron and photon triggers in ATLAS during LHC Run 2*, *Eur. Phys. J. C* **80** no. 1, (2020) 47, [arXiv:1909.00761 \[hep-ex\]](#).
- [126] ATLAS Collaboration, *Multi-Boson Simulation for 13 TeV ATLAS Analyses*, Tech. Rep. ATL-PHYS-PUB-2017-005, CERN, Geneva, May, 2017. <https://cds.cern.ch/record/2261933>.
- [127] H. B. Hartanto, B. Jager, L. Reina, and D. Wackerroth, *Higgs boson production in association with top quarks in the POWHEG BOX*, *Phys. Rev. D* **91** no. 9, (2015) 094003, [arXiv:1501.04498 \[hep-ph\]](#).
- [128] S. Frixione, P. Nason, and G. Ridolfi, *A Positive-weight next-to-leading-order Monte Carlo for heavy flavour hadroproduction*, *JHEP* **09** (2007) 126, [arXiv:0707.3088 \[hep-ph\]](#).
- [129] S. Alioli, P. Nason, C. Oleari, and E. Re, *NLO single-top production matched with shower in POWHEG: s- and t-channel contributions*, *JHEP* **09** (2009) 111, [arXiv:0907.4076 \[hep-ph\]](#). [Erratum: *JHEP* 02, 011 (2010)].
- [130] ATLAS Collaboration, *ATLAS simulation of boson plus jets processes in Run 2*, Tech. Rep. ATL-PHYS-PUB-2017-006, CERN, Geneva, May, 2017. <https://cds.cern.ch/record/2261937>.
- [131] R. Brun and F. Rademakers, *ROOT: An object oriented data analysis framework*, *Nucl. Instrum. Meth. A* **389** (1997) 81–86. <https://root.cern.ch>.
- [132] ATLAS Collaboration, *Object-based missing transverse momentum significance in the ATLAS detector*, Tech. Rep. ATLAS-CONF-2018-038, CERN, Geneva, Jul, 2018. <https://cds.cern.ch/record/2630948>.
- [133] M. Baak, G. J. Besjes, D. Côté, A. Koutsman, J. Lorenz, and D. Short, *HistFitter software framework for statistical data analysis*, *The European Physical Journal C* **75** no. 4, (2015) 153.
- [134] ATLAS Collaboration, *Measurement of the muon reconstruction performance of the ATLAS detector using 2011 and 2012 LHC proton-proton collision data*, *Eur. Phys. J. C* **74** no. 11, (2014) 3130, [arXiv:1407.3935 \[hep-ex\]](#).

- [135] ATLAS Collaboration, *Jet energy scale measurements and their systematic uncertainties in proton-proton collisions at $\sqrt{s} = 13$ TeV with the ATLAS detector*, *Phys. Rev.* **D96** no. 7, (2017) 072002, [arXiv:1703.09665 \[hep-ex\]](#).
- [136] J. M. Lorenz, M. Baak, G. J. Besjes, D. Côté, A. Koutsman, and D. Short, *HistFitter - A flexible framework for statistical data analysis*, *Journal of Physics: Conference Series* **608** (2015) 012049.
- [137] G. Cowan, K. Cranmer, E. Gross, and O. Vitells, *Asymptotic formulae for likelihood-based tests of new physics*, *Eur. Phys. J.* **C71** (2011) 1554, [arXiv:1007.1727 \[physics.data-an\]](#). [Erratum: *Eur. Phys. J.* **C73**,2501(2013)].
- [138] ATLAS Collaboration, *Search for chargino and neutralino production in final states with a Higgs boson and missing transverse momentum at $\sqrt{s} = 13$ TeV with the ATLAS detector*, *Phys. Rev. D* **100** no. 1, (2019) 012006, [arXiv:1812.09432 \[hep-ex\]](#).
- [139] ATLAS Collaboration, *Search for chargino-neutralino pair production in final states with three leptons and missing transverse momentum in $\sqrt{s} = 13$ TeV p - p collisions with the ATLAS detector*, Tech. Rep. ATLAS-CONF-2020-015, CERN, Geneva, Jun, 2020. <https://cds.cern.ch/record/2719521>.
- [140] ATLAS Collaboration, *Searches for electroweak production of supersymmetric particles with compressed mass spectra in $\sqrt{s} = 13$ TeV pp collisions with the ATLAS detector*, *Phys. Rev. D* **101** no. 5, (2020) 052005, [arXiv:1911.12606 \[hep-ex\]](#).
- [141] GAMBIT Collaboration, *A global fit of the MSSM with GAMBIT*, *Eur. Phys. J. C* **77** no. 12, (2017) 879, [arXiv:1705.07917 \[hep-ph\]](#).
- [142] ATLAS Collaboration, *Prospects for searches for staus, charginos and neutralinos at the high luminosity LHC with the ATLAS Detector*, Tech. Rep. ATL-PHYS-PUB-2018-048, CERN, Geneva, Dec, 2018. <http://cds.cern.ch/record/2651927>.

- [143] CLIC Collaboration, *The Compact Linear Collider (CLIC) - 2018 Summary Report*, [arXiv:1812.06018](https://arxiv.org/abs/1812.06018) [physics.acc-ph].
- [144] A. Aboubrahim and P. Nath, *Supersymmetry at a 28 TeV hadron collider: HE-LHC*, *Phys. Rev. D* **98** no. 1, (2018) 015009, [arXiv:1804.08642](https://arxiv.org/abs/1804.08642) [hep-ph].
- [145] T. Golling et al., *Physics at a 100 TeV pp collider: beyond the Standard Model phenomena*, *CERN Yellow Rep. no. 3*, (2017) 441–634, [arXiv:1606.00947](https://arxiv.org/abs/1606.00947) [hep-ph].
- [146] CMS and ATLAS Collaboration, *Report on the Physics at the HL-LHC and Perspectives for the HE-LHC*, Tech. Rep. [arXiv:1902.10229](https://arxiv.org/abs/1902.10229), CERN, Geneva, 2019. <https://cds.cern.ch/record/2651134>.
- [147] ATLAS Collaboration, *Technical Design Report for the Phase-I Upgrade of the ATLAS TDAQ System*, Tech. Rep. CERN-LHCC-2013-018. ATLAS-TDR-023, Sep, 2013. <https://cds.cern.ch/record/1602235>.
- [148] ATLAS Collaboration, *Technical Design Report for the Phase-II Upgrade of the ATLAS TDAQ System*, Tech. Rep. CERN-LHCC-2017-020. ATLAS-TDR-029, CERN, Geneva, Sep, 2017. <https://cds.cern.ch/record/2285584>.
- [149] ATLAS Collaboration, *Technical Design Report for the ATLAS Inner Tracker Strip Detector*, Tech. Rep. CERN-LHCC-2017-005. ATLAS-TDR-025, CERN, Geneva, Apr, 2017. <https://cds.cern.ch/record/2257755>.